

© 2015 Freddy Thanh-Son Nguyen

OPTICAL COHERENCE TOMOGRAPHY AND TARGETED MULTI-MODAL PROTEIN
MICROSPHERES FOR CANCER IMAGING

BY

FREDDY THANH-SON NGUYEN

DISSERTATION

Submitted in partial fulfillment of the requirements
for the degree of Doctor of Philosophy in Chemistry
in the Graduate College of the
University of Illinois at Urbana-Champaign, 2015

Urbana, Illinois

Doctoral Committee:

Professor Martin Gruebele, Chair
Professor Stephen A. Boppart, Director of Research
Professor Catherine J. Murphy
Professor Kenneth S. Suslick
Professor Michael S. Strano, Massachusetts Institute of Technology

ABSTRACT

The field of biomedical optics has grown quickly over the last two decades as various technological advances have helped increase the acquisition speeds and the sensitivity limits of the technology. During this time, optical coherence tomography (OCT) has been explored for a wide number of clinical applications ranging from cardiology to oncology to primary care. In this thesis, I describe the design and construction of an intraoperative clinical OCT system that can be used to image and classify breast cancer tumor margins as normal, close, or positive. I also demonstrate that normal lymph nodes can be distinguished from reactive or metastatic lymph nodes by looking at the difference in scattering intensity between the cortex and the capsule of the node. Despite the advances of OCT in the detection and diagnosis of breast cancer, this technology is still limited by its field of view and can only provide structural information about the tissue. Structural OCT would benefit from added contrast via sub-cellular or biochemical components via the use of contrast agents and functional OCT modalities.

As with most other optical imaging techniques, there is a trade off between the imaging field of view and the high-resolution microscopic imaging. In this thesis, I demonstrate for the first time that MM-OCT can be used as a complimentary technique to wide field imaging modalities, such as magnetic resonance imaging (MRI) or fluorescence imaging, using targeted multi-modal protein microspheres. By using a single contrast agent to bridge the wide field and microscopic imaging modalities, a wide field imaging technique can be used to initially localize the contrast agent at the site of interest to guide the location of the MM-OCT imaging to provide a microscopic view. In addition to multi-modal contrast, the microspheres were functionalized with RGD peptides that can target various cancer cell lines.

The cancer cells readily endocytosed bound protein microspheres, revealing the possibility that these protein microspheres could also be used as therapeutic agents. These investigations furthered the utility of the OCT technology for cancer imaging and diagnosis.

ACKNOWLEDGEMENTS

There are many individuals that I would like to take this opportunity to give my utmost thanks and gratitude for contributing to my development as a scientist and future physician-scientist, getting me through the highs and the lows, providing sage advice and moral support, and for continuing to believe in me throughout this arduous process. Without this support, this work would not have been possible.

First, I would like to thank Prof. Stephen Boppart for being my research mentor throughout these many years and for being understanding of the unique challenges of training as a physician-scientist, allowing me to pursue my medical training in tandem to my graduate research training. I want to thank Prof. Boppart for continuing to challenge me scientifically in both challenging and successful times of my research and always providing critical feedback. He provided a research lab environment that was truly interdisciplinary that included individuals and expertise crossing the fields of engineering, chemistry, physics, and medicine. Without this environment, I would not have had the opportunity to work with a group of highly talented individuals at the forefront of so many different disciplines. He has contributed tremendously to my development as a critical scientist in all aspects of being a scientist. He had been gracious enough to provide feedback and encourage me to apply for research grants and fellowships. I was fortunate enough to have had Prof. Boppart support me financially through his grants, the chemistry department through teaching assistantships, and the United States Department of Defense through a Congressionally Directed Medical Research Program Breast Cancer Predoctoral Fellowship (BC073292). He has also always supported me to present my research at national and international conferences, to publish, to apply for grants, and to explore new avenues of research. I particularly want to thank for him

helping me stay grounded and focused on my thesis research while giving me the freedom and the resources to pursue all of my research ideas. I also want to thank him for allowing me to also pursue my outside interests in particular in founding of the American Physician Scientists Association and for allowing me to advocate on behalf of physician-scientist trainees.

I also want to thank Prof. Boppart for giving me the unique opportunity to work with so many of our collaborators and for giving me the support to pursue and expand on new collaborations. In particular, I want to thank Prof. Michael Strano for exploring initial ideas of using single wall carbon nanotubes as potential contrast agents for OCT, and Prof. Kenneth Suslick for providing his lab and resources to learn about the synthesis of protein microspheres. I would like to thank the many individuals at Carle Foundation Hospital (Urbana, IL) who have been involved in the clinical studies, in particular, the surgeons, oncologists, and pathologists: Dr. Uretz Oliphant, Dr. Jan Kotynek, Dr. John Brockenbrough, Dr. Kendrith Rowland, Dr. Patricia Johnson, Dr. Frank Bellafiore. I also want to thank Dr. Gabriel Popescu over the years since our time at MIT for moral support and for allowing me to collaborate with him on his research when he came to UIUC.

Of course, some of the most important people I would like to thank who were there with me every day in the lab providing scientific guidance on their respective expertise, and allowing me to pick their brains day in and day out. I want to thank Eric Chaney for having been part of my research projects, teaching me about doing in vitro and in vivo research, and providing support during all of those cell and animal experiments. I want to thank both Eric Chaney and Adam Zysk for their camaraderie as we worked together to establish and expand our research projects at Carle Foundation Hospital. These projects have helped provide a very different perspective in the research we were doing and a new motivation in directing the

research we were pursuing. Over the years, I also wanted to thank other fellow lab members who contributed to my scientific development, shared their expertise and enthusiasm, and for collaborating with me on various projects: Dr. Amy Oldenburg, Dr. Daniel Marks, Dr. Renu John, Dr. Adam Zysk, Dr. Tyler Ralston, Dr. Xing Liang, and Adeel Ahmad.

I want to take this opportunity to also thank Dr. Martin Gruebele, the chair of my thesis committee, for always believing in me and providing sage advice and support throughout my PhD training. I want to thank all the members of my thesis committee for providing the critical feedback on my thesis research, for continuously challenging me throughout this process, and for graciously extending their time and resources towards my scientific development. I also want to thank the members of the microscopy suite and animal facilities at the Beckman Institute, and the Roy J. Carver Biotechnology Center for access to their research staff and facilities to make my thesis research possible. I also want to thank the Medical Scholars Program for giving me the opportunity to pursue my MD/PhD training at the University of Illinois.

Lastly, I want to personally thank my parents and friends for their support throughout this long, arduous, and challenging process. I want to thank them for always being there, listening to my difficulties, encouraging me, and always believing in me. In particular, I want to thank Dr. Daniel Heller, a long-time friend and collaborator, for being a great friend, scientific colleague, and always entertaining my random ideas. I want to thank Dr. Joseph Bast, Dr. Bidhan Das, Jessica Peters, and Adrienne Barry for celebrating my successes and helping me get through the challenging times. I also want to thank the people who helped get me started in science and are some of my greatest supporters: Dr. Robert Curl, Dr. Bruce Johnson, Dr. Carter Kittrell, and Dr. Ramachandra Dasari.

TABLE OF CONTENTS

CHAPTER 1 OPTICAL COHERENCE TOMOGRAPHY	1
1.1 Introduction	1
1.2 Optical Coherence Tomography in Cancer	1
1.2.1 Breast Cancer	2
1.2.2 Optical Coherence Tomography in Breast Cancer	3
1.3 Optical Coherence Tomography in Cardiovascular Applications	5
1.3.1 Atherosclerosis	6
1.3.2 Optical Coherence Tomography in Atherosclerosis	6
1.4 Importance of the Alpha (v) Beta (3) Integrin Receptor in Angiogenesis, Cancer, and Atherosclerosis	7
1.5 Optical Coherence Tomography	8
1.6 Functional Extensions of OCT	14
1.6.1 Magnetomotive Optical Coherence Tomography	15
1.7 Contrast Agents in OCT	18
1.8 Summary	18
1.9 References	21
CHAPTER 2 OPTICAL COHERENCE TOMOGRAPHY IN TUMOR MARGIN ASSESSMENT	40
2.1 Introduction	40
2.1.1 Tumor Margin Assessment and Local Recurrence	40
2.1.2 Intraoperative Margin Assessment	40
2.2 Portable Clinical Spectral Domain Optical Coherence Tomography System	42
2.3 Clinical Study	44
2.3.1 Patient Information	45
2.4 OCT Image Processing & Evaluation Protocol	45
2.5 Histology Image Evaluation Protocol	46
2.6 Training Data Set	46
2.7 Study Data Set	49
2.8 Conclusions	57
2.9 References	58

CHAPTER 3 OPTICAL COHERENCE TOMOGRAPHY IN LYMPH NODE

ASSESSMENT	64
3.1 Introduction	64
3.1.1 Clinical Importance of Lymph Node Assessment	64
3.1.2 Mapping of Lymph Nodes	64
3.1.3 Current and Experimental Nodal Assessment Techniques	65
3.2 Portable Clinical Spectral-Domain Optical Coherence Tomography System	66
3.3 Clinical Study	67
3.3.1 Specimen Information	68
3.4 OCT Image Processing & Evaluation Protocol	69
3.5 Histopathological Image Evaluation Protocol	70
3.6 OCT Images of Normal, Reactive, and Metastatic Lymph Nodes	70
3.6.1 Identification of Normal Nodes from Reactive and Metastatic Lymph Nodes	76
3.6.2 Potential Clinical Impact	77
3.7 Conclusions	78
3.8 References	79
CHAPTER 4 PROTEIN MICROSPHERES	83
4.1 Introduction	83
4.2 Protein Microspheres	86
4.3 Protein Microsphere Synthesis	90
4.3.1 Encapsulation of Particles in the Oil Core of the Protein Microspheres	92
4.3.2 Embedding Particles in the Protein Shell of the Microspheres	94
4.3.3 Emulsification of the Protein Microspheres	94
4.3.4 Protein Microsphere Washing and Purification	96
4.3.5 Surface Functionalization of Protein Microspheres using Layer-By-Layer Adhesion	97
4.4 Scanning Electron Microscopy of Protein Microspheres	98
4.5 Transmission Electron Microscopy of Protein Microspheres	107
4.6 Size Distribution of Protein Microspheres	109
4.7 Conclusions	115
4.8 References	116

CHAPTER 5 PROTEIN MICROSPHERES AS CONTRAST AGENTS	122
5.1 Introduction	122
5.1.1 Previous Uses of Protein Microspheres as Imaging Agents	122
5.2 Protein Microspheres as Magnetic Contrast Agents	123
5.2.1 Iron Oxide-filled Microspheres under MM-OCT	125
5.2.2 Quantification of Encapsulated Iron Oxide using MRI	132
5.3 Protein Microspheres as Fluorescent Contrast Agents	144
5.3.1 Protein Microspheres under the Wide-field Fluorescence Imaging System	150
5.3.2 Loading Capacity of Iron Oxide and Dye	156
5.4 Conclusions	165
5.5 References	166
CHAPTER 6 <i>IN VITRO</i> TARGETING OF PROTEIN MICROSPHERES IN CANCER	171
6.1 Introduction	171
6.1.1 Previous Studies on Layering of Protein Microspheres using RGD sequence	173
6.1.2 Initial Studies using RGD-coated Protein Microspheres	173
6.2 Quantifying the Expression of $\alpha_v\beta_3$ Integrin Receptors on Cells using Indirect Immunofluorescence Staining and Flow Cytometry	175
6.3 Targeting of the RGD-coated Microspheres to the $\alpha_v\beta_3$ Integrin Receptor <i>In Vitro</i>	185
6.4 <i>In Vitro</i> Uptake of Microspheres by Cancer Cells	200
6.5 Conclusions	206
6.6 References	207
CHAPTER 7 FUTURE DIRECTIONS AND CONCLUSIONS	212
7.1 Optical Coherence Tomography in Breast Cancer	212
7.2 Protein Microspheres	214
7.3 <i>In Vitro</i> Targeting of Protein Microspheres	217
7.4 <i>Ex Vivo</i> and <i>In Vivo</i> Targeting of Protein Microspheres in Cancer Animal Models ...	218
7.5 <i>Ex Vivo</i> and <i>In Vivo</i> Targeting of Protein Microspheres in Atherosclerosis	224
7.6 Conclusions	228
7.7 References	229

CHAPTER 1

OPTICAL COHERENCE TOMOGRAPHY

1.1 Introduction

Optical coherence tomography (OCT) is a high-resolution microscopic optical imaging technique that yields real-time multi-dimensional images of subsurface tissue structure [1-7]. OCT is the optical analogue to ultrasound imaging but uses light waves instead of sound waves to create images. Near-infrared light enables micron-scale resolution, providing images on the same resolution scale as histopathology. OCT is based on a Michelson interferometer and, when combined with a sample scanning mechanism, forms cross-sectional images. Since its introduction in 1991 as a method for the non-invasive imaging of the retina [7], OCT has capitalized on technological advances, resulting in significant increases in data acquisition speeds [8], added functional modalities [9-11], and new contrast agents [12, 13]. OCT has been evaluated in a large number of clinical applications including ophthalmology, cardiovascular disease, and oncology [14], to name a few.

1.2 Optical Coherence Tomography in Cancer

In recent years, the development of OCT technology for applications in the field of oncology has progressed rapidly. As newer scanning probes such as endoscopes, handheld probes, catheter probes, and needle based probes have been developed, the reach of OCT imaging continues to expand. For example, the development of specialized endoscopic probes enabled researchers to use OCT to assess lesions in the ear, nose, and throat [15-17]. OCT has

been successfully developed for imaging and assessing lesions in the laryngeal mucosa, oral cavity, oropharynx, vocal folds, and nasal mucosa [18-21]. OCT can also be used to detect malignancies in the gastrointestinal tract [22-25], and had a 78% accuracy rate for detecting dysplasia in patients with Barrett's esophagus [26]. In the cervix, neoplastic changes in chromatin and nuclear morphologies contributed to significantly elevated OCT scattering observed in abnormal cervical epithelium compared to normal epithelium [27-29]. The potential applications of OCT in breast cancer are discussed in greater detail later in this chapter and in Chapters 2 and 3.

1.2.1 Breast Cancer

Breast cancer is the second leading cause of cancer deaths in women and continues to be the most widely diagnosed type of cancer each year in women. Earlier detection, diagnosis, and treatment of breast cancer continue to be the most important factors in determining the patient's prognosis. Breast cancer afflicts a strikingly large number of women: 207,090 new cases of invasive breast cancer and 54,010 cases of *in situ* breast cancer were estimated for 2010, making it the most widely diagnosed cancer in women second only to skin cancer [30]. The number of deaths attributed to breast cancer (39,840 expected in 2010 – second only to lung cancer) has started to decrease over the last few years, largely attributed to the effectiveness of breast cancer screening [30]. Increased awareness about breast cancer and an increase in breast cancer screening has led to improved detection of breast cancer lesions at earlier stages, resulting in smaller breast lesions and a decreased likelihood of lymph node involvement and cancer metastasis. The management and treatment of breast cancer has continued to improve as evidenced by gradual increases in the five year survival rates for all stages of breast cancer [31]. Currently, patients who elect for lumpectomies or mastectomies

typically have a sentinel lymph node dissection (SLND), which may be accompanied by the resection of additional axillary lymph nodes via axillary lymph node dissection (ALND) to help stage disease progression [31]. The staging of breast cancer is currently based on three main criteria: the size of the primary tumor, the infiltration of lymph nodes by cancer cells, and the subsequent metastasis of cancer cells to other sites. Cancer metastasis is the spread of cancer cells from the primary tumor site to another organ site via the cardiovascular or lymphatic system. The medical community has used the status of lymph nodes as one of the major criteria in determining the metastatic state of the cancer. In breast cancer applications, OCT could prove to be an invaluable tool in guiding the surgical removal of tumors, the assessment of lymph nodes prior to resection, and potentially the real time staging of the cancer.

1.2.2 Optical Coherence Tomography in Breast Cancer

OCT was first evaluated for imaging breast cancer tumor margins in an NMU-carcinogen-induced rat mammary model [4]. In human breast tissue, the penetration depth of OCT is approximately 1-2 mm. The density of cells and sub-cellular scatterers such as the nuclei determine the penetration depth of OCT. High scattering signals observed in OCT images are often attributed to a combination of the increase in nuclear-to-cytoplasm (N/C) ratio and the increase in cellular density often found during the focal proliferation of cancer cells [29, 32]. Tissue comprised primarily of adipocytes can be imaged up to depths of 2 mm compared to cell-dense tumor tissue, which can be imaged up to depths of 1 mm. The penetration depths of OCT in these tissue types are comparable to the currently accepted margin widths of 1-2 mm that classify tumor margins as positive, close, and negative. Compared to the current standard of care, which calls for the pathological evaluation of

stained fixed or frozen sections, OCT can provide an assessment of the tumor margin in minutes. This real time feedback would allow surgeons to immediately resect additional tissues if necessary.

In the assessment of lymph nodes, OCT was first evaluated in a rat animal model and *ex vivo* human lymph nodes using an laboratory based OCT system centered at 800 nm [33]. These initial laboratory based studies demonstrated that OCT could penetrate through the lymph node capsule, and assess sub-capsular morphological changes in the cortex of the node. These differences in scattering intensities can be used to distinguish normal nodes from reactive and metastatic nodes. By being able to image through the capsule, OCT can assess the nodal status without compromising the structural integrity of the lymph node. Currently the primary purpose for resecting lymph nodes during breast cancer surgeries is for disease staging. A significant portion of the resected lymph nodes (> 50-75%) is classified as normal based on histopathological analysis. The risk for developing lymphedema could be vastly decreased by reducing the number of non-diagnostic or normal lymph nodes surgically removed during sentinel lymph node and axillary lymph node dissection procedures.

Needle-based OCT probes have previously been used to provide access to deeper breast lesions a few millimeters beneath the tissue surface [34-36]. These needle probes are fiber based and can provide real-time information for guided lesion biopsy or for placement of localization wires [34, 36]. Currently there are significant difficulties in guiding needle biopsies using ultrasound and x-ray imaging techniques due to sub-optimal contrast and only two-dimensional images provided to guide the needle. Coupling an OCT probe to the tip of the biopsy needle could provide real-time diagnostic information that could facilitate guiding the biopsy needle. Reports identified diagnostically significant information within the optical

backscattering and refractive index signals of the breast tissue, which can distinguish various breast tissue types [4, 37, 38]. These same diagnostic properties can be extracted from individual axial scans that comprise an OCT image, or from spatial information provided by the OCT image itself [36-38].

These studies represent the first demonstrations of OCT in the field of breast cancer. By enabling surgeons to rapidly visualize tissue morphology beneath the surface and over large surface areas while preserving tissue structure, OCT has the potential to become an invaluable tool for the surgical guidance of breast cancer surgeries. The intraoperative use of OCT in the assessment of tumor margins and lymph nodes during breast conserving surgeries will be further discussed in Chapters 2 and 3.

1.3 Optical Coherence Tomography in Cardiovascular Applications

Over the past decade, OCT has been extensively explored for various cardiovascular applications. OCT, spectroscopic OCT, and polarization sensitive OCT have been used to examine the structural integrity of the coronary artery [39-51]. The development of catheter-based probes, increased acquisition speeds, and the introduction of functional extensions of OCT have greatly increased the potential value of this technology for cardiovascular applications. Newer probes can integrate the OCT sample-arm optics into existing intravascular catheters for both forward and radial OCT imaging [47, 52].

Intravascular OCT has been successfully used in the characterization and visualization of cardiac interventions, such as percutaneous coronary intervention (PCI) and stent implantations [39, 41, 44, 46, 49, 50, 53, 54]. In cases of chronic total occlusion of a coronary artery, OCT can be used to guide the guide wire and decreases the chances of perforating the

artery and causing dissection of the intima [55, 56]. In the application of stent placement, OCT imaging can give surgeons a real-time visualization of stent apposition [40, 57], as well as provide greater information about stent integrity, neointimal proliferation, and neovascularization [58-60]. High-resolution *in vivo* OCT imaging can be used in real-time to guide the optimal placement and deployment of stents, assess the overexpansion of stents, identify post-stenting vessel injuries [40, 61], and assess stent failures such as restenosis and stent thrombosis.

1.3.1 Atherosclerosis

Atherosclerosis is a condition in which materials such as cellular waste, fatty substances, cholesterol, calcium, and fibrin accumulate within the inner lining of an artery. Atherosclerosis currently accounts for over 75% of cardiovascular diseases (CVDs) including strokes, which make up 18% of CVDs [62]. Vulnerable plaques are often caused by an inflammatory response and are found in medium- to large-sized arteries. Plaques are a key component in the development of atherosclerosis and CVDs in general. Recent research has focused not only on the detection of plaques but also more importantly on their potential for rupture. Distinguishing characteristics of vulnerable plaques include a thin fibrous cap, a large lipid pool, and an increase in macrophage activity. The greatest risk posed by plaques is the sudden rupture of the fibrous cap and resulting blockage of vessels downstream from the site of the plaque, which can lead to strokes and heart attacks.

1.3.2 Optical Coherence Tomography in Atherosclerosis

The ability to locate and assess the status of atherosclerotic lesions is an increasingly important issue [62]. Cardiovascular OCT imaging can be used to visualize vulnerable plaques in the coronary or carotid arteries and evaluate their potential for progression or

rupture. This assessment would be performed after suspicious areas had been localized using other imaging modalities such as CT, ultrasound, or fluoroscopy. Intravascular OCT imaging is limited by the tissue penetration depth and blood-induced signal attenuation, which can be reduced with saline flushes or vascular balloon occlusion prior to OCT imaging [44].

OCT has been demonstrated for the *in vivo* quantification of activated macrophage content in plaques and for the differentiation of plaque type [50, 63]. Plaque identification has been demonstrated with high sensitivity and specificity (fibrous tissue – 87%, 97%; fibrocalcific– 95%, 100%; lipid-rich – 92%, 94%). The OCT-quantified macrophage density located underneath the fibrous cap has been directly correlated with the patient’s clinical presentation. The presence of activated macrophages near the endothelial layer is thought to contribute to the instability of a vulnerable plaque [49, 63, 64]. OCT has been used to characterize the attenuation and layer thickness changes associated with arterial wall components such as the intima, media, lipid-rich regions, and calcifications [58, 65-67].

1.4 Importance of the Alpha (v) Beta (3) Integrin Receptor in Angiogenesis, Cancer, and Atherosclerosis

Angiogenesis is the development and growth of new blood vessels and occurs during the formation of tumors and in the development of atherosclerosis. New blood vessel formation is needed to support the growth of tumors larger than a few millimeters in size. Integrin receptors – heterodimer transmembrane proteins – have been widely reported as key players in angiogenesis and the proliferation of cancer metastases. With over 25 known integrin receptors, the one that has been targeted for the work presented in this thesis is the $\alpha_v\beta_3$ integrin receptor because it has been well characterized to be upregulated during the

angiogenesis process that would accompany inflammatory processes but in particular in cancer [68, 69] and atherosclerosis [70-72]. Integrins mediate cell-substrate adhesion and are often overexpressed in cancer cells, particularly in metastatic cancer cells. These circulating tumor cells may metastasize to other organ systems via the cardiovascular or lymphatic system. The $\alpha_v\beta_3$ integrin receptor has been known to be overexpressed in the development of tumor angiogenesis, cancer metastasis, and atherosclerosis. The arginine-glycine-aspartate or RGD sequence motif can be used as a label to target angiogenesis, cancer cells [73-109], and atherosclerotic plaques [70-72, 110-116]. During tumor angiogenesis, newly formed vessels surrounding the tumor are often leaky, tortuous, and highly unstructured. The blood flow is slower and not necessarily unidirectional in this random and disordered network of vessels. This environment could potentially be beneficial for trapping larger particles such as protein microspheres at the tumor site.

1.5 Optical Coherence Tomography

OCT is analogous to ultrasound employing the backscattered light waves instead of the backscattered sounds waves to create the OCT image. OCT or low coherence interferometry (LCI) can be performed using a Michelson type interferometer. A light source with low temporal coherence is split into two beams: a reference arm and a sample arm. The interference of the back reflections from the two arms is collected at the photodetector. Only back reflections that are within the coherence length will provide constructive interference. The coherence length determines the axial resolution along the depth of the OCT image. Using the optical coherence gating, all of the other back reflections not within the coherence length of the reflection coming back from the reference arm will be neglected. Using this

gating method, the localization of individual scatters in the sample can be resolved. The transverse resolution of OCT is determined by the objective used to focus the OCT beam onto the sample. Time-domain OCT systems physically scan the reference arm to move the optical coherence gate up and down along the axial direction. The development of spectral-domain OCT or swept-source OCT combined with faster detection systems has increased the OCT imaging speeds by several orders of magnitude [117-122].

For the intraoperative assessment of tumor margins and lymph nodes discussed in Chapters 2-3, I designed and built a portable spectral-domain OCT system using a super luminescent diode (SLD) (Model SLD1C, B&W Tek, Inc., Newark, Delaware) centered at 1310 nm with a bandwidth of 92 nm. Light is first passed through an optical circulator (CIRC-3-31-P-BB-10-6:3 port, Gould Fiber Optics, Millersville, Maryland) and into a 95/5 fiber-optic splitter (Gould Fiber Optics, Millersville, Maryland) that divides the light into a sample and reference arm. The sample arm focuses ~4.75 mW of light onto a 35.0 μm spot size (transverse resolution) using a 60 mm achromatic lens. A 60 mm focal length achromatic lens in the sample arm focuses 4.75 mW of light to a 35 μm spot (transverse resolution). The confocal parameter was 1.47 mm to closely match the OCT image depth of 2.0 mm. The broad bandwidth source yields an axial resolution of 8.2 μm in air or 5.9 μm in tissue. Reflected light from the sample and reference arms is passed through polarization controllers (FPC-2, Fiber Control, Holmdel, New Jersey), coupled into an interferometer, spectrally dispersed by a diffraction grating (53004BK01-148R, Richardson Gratings, Newport Corporation, Rochester, New York, 1000 grooves / mm and blazed for 1310 nm), and focused onto an Indium Gallium Arsenide (InGaAs) line camera (SU1024LE-1.7T1-0500, Sensors Unlimited, Inc., Goodrich Corporation, Princeton, New Jersey) with a 150 mm singlet lens.

Camera exposure times range from 24.4 μs to 408.4 μs , corresponding with measured signal-to-noise ratios of 96 dB to 116 dB. The imaging system acquires OCT images at a rate of $\sim 5,000$ axial scans per second or up to $\sim 8-9$ images per second (~ 600 axial scans / 10 mm). The sample is laterally scanned under the OCT beam using an automated translation stage. Data are collected using a high-speed data acquisition card with a 5 MHz sampling rate and 12-bit quantizer (PCI-6111E, National Instruments Corporation, Austin, Texas) in a dual Xeon processor (3.20 GHz) computer with 1 GB of RAM. Acquisition and processing time for an OCT image was ~ 5 seconds / image. The OCT hardware and data acquisition are controlled by custom software written in LabVIEW and interfaced with a data processing sequence written in Matlab/C++.

Due to the non-linear response from optical components, a cubic spline interpolation and resampling technique is implemented to resample the spectrum into a more uniform frequency space [123]. The most optimal spline interpolation parameters were calculated using data collected by placing a perfect reflector placed at the focus of the sample arm while the reference arm was moved through a range of optical path lengths corresponding to the full depth of the OCT image. The collected data was compiled to create a Modulation Transfer Function (MTF). The spline interpolation parameters were optimized to give the flattest MTF possible. The up-sampled data was re-indexed in the frequency domain using the spline interpolation. Lastly, an inverse Fourier transform was taken to bring the data from the spectral-domain back to the time-domain producing a traditional two-dimensional OCT image.

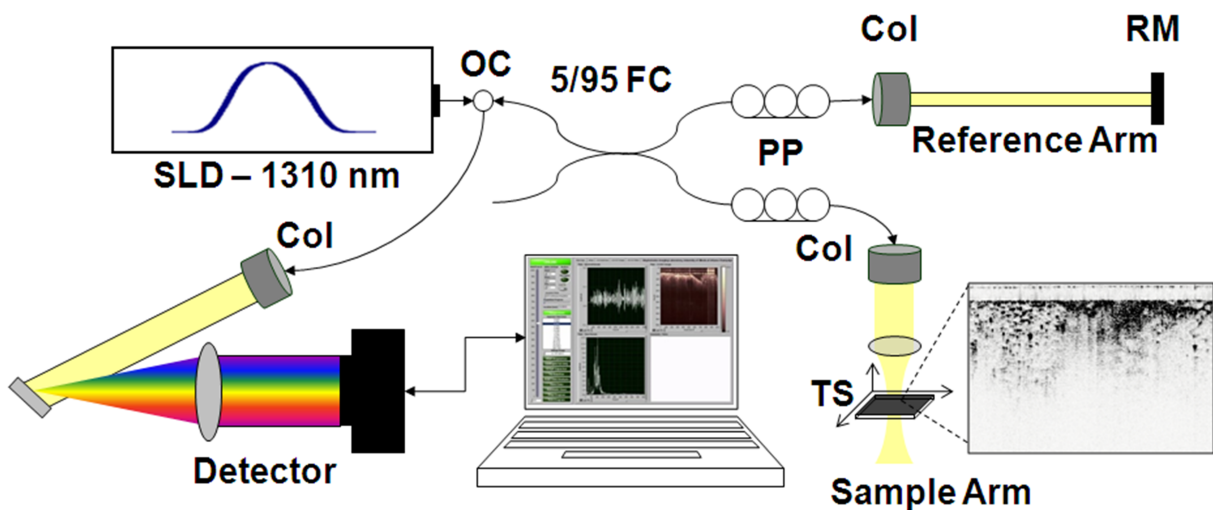
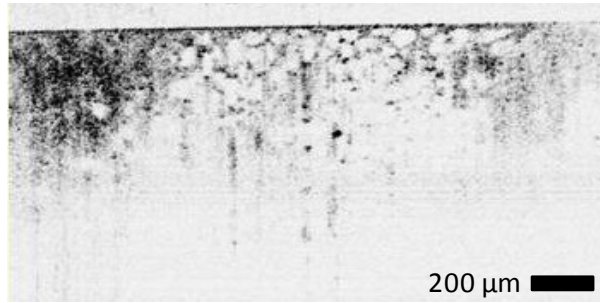


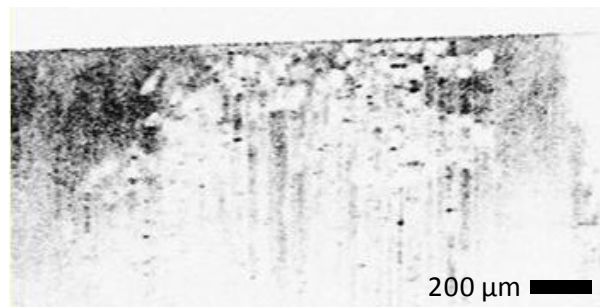
Figure 1.1: Schematic of the clinical spectral-domain optical coherence tomography (SD-OCT) system. Light from a superluminescent diode (SLD) ($\lambda=1310$ nm) is directed into an optical circulator (OC) and to a fiber coupler (FC) that splits 5% of the light to the reference arm mirror (RM) and 95% of the light to the sample arm containing focusing optics and an automated x-y translation stage (TS). Light is collimated through fiber collimators (Col). Reflected light from each arm is coupled through polarization paddles (PP), interfered within the fiber coupler, and spectrally dispersed onto a line camera.

During the development of the clinical instrument, several issues were considered and addressed which affect the overall performance of the system ranging from the choice of the laser source (power vs. bandwidth), the confocal parameter and transverse resolution of the sample arm, the penetration depth, the performance of the spectrometer, and the SNR of the system. The bandwidth of the optical light source was a more dominant contributor to increasing the axial resolution than the power of the light source. In order to validate the clinical OCT system, the same human breast cancer sample was imaged under the clinical SD-OCT system (1310 nm CW, 90 nm BW, 116 dB SNR, 5000 lines / sec acquisition rate), the laboratory-based time-domain OCT (TD-OCT) system (800 nm CW, 120 nm BW, 106 dB SNR, 10 lines/sec acquisition rate), and the laboratory-based SD-OCT system (800 nm CW, 120 nm BW, 96 dB SNR, 29000 lines / sec acquisition rate). The results show that although the resolution of the clinical SD-OCT system is lower than in the 800 nm systems (this is expected due to the smaller bandwidth) there was still remarkable agreement between the three systems in identifying the tumor margin in the sample (Figure 1.2).

The penetration depth of OCT is determined by several factors including the wavelength and power of the light used, and the density distribution of scatterers in the path of the light. OCT is largely performed using light in the NIR region where forward directed scattering dominates and there is minimal absorption by major biological components such as hemoglobin, water, melanin, to name a few. This therapeutic window is 600-1300 nm. The density and types of scatterers in the sample also affect the OCT penetration depth since OCT detects single scattering events. As the density of scatterers or as the penetration depth increases, the number of multiple scattering events increase thereby decreasing the signal to noise ratio and OCT penetration depth.



(a) Laboratory Bench-Based System (800 nm,time-domain OCT)



(b) Laboratory Bench-Based System (800 nm,spectral-domain OCT)



(c) Clinical Portable System (1300 nm,spectral-domain OCT)

Figure 1.2: OCT images of the same tissue sample across three different OCT systems. The laboratory bench-based system uses a Ti:Sapphire laser centered at 800 nm, which feeds into a time-domain OCT system (a) and a spectral-domain OCT system (b). The clinical portable system uses a 1300 nm SLD and is a spectral-domain OCT system (c).

1.6 Functional Extensions of OCT

As the field of OCT has matured, there has been a greater push to develop strategies that would improve the molecular and cellular sensitivity of OCT [12, 13, 124-133]. There are two main methods for adding molecular information to the field of OCT imaging. The first is through the extension of the coherence gating to detect non-structural phenomenon. For example, pump-probe OCT uses a pump-probe source to probe the ground state absorption of molecules [127]. Nonlinear Interferometric Vibrational Imaging (NIVI) probes the molecular vibrations of the sample using an interferometer setup to detect the coherent anti-Stokes Raman scattering (CARS) signals [129, 133]. In CARS imaging, the specimen is probed with both a pump frequency and a Stokes frequency, where the difference between the two frequencies is the Raman resonance frequency of interest [129]. The anti-Stokes pulse can then be measured. NIVI is able to measure both the amplitude and phase of the CARS signal, which allows researchers to filtering out the nonresonant background [129]. Under magnetomotive OCT (MM-OCT), an external magnetic field is modulated during OCT imaging causing the magnetic particles to physically displace nearby scatterers [13, 132]. MM-OCT can detect these changes in the displacement of the scatterers. Another functional extension of OCT is spectroscopic OCT (S-OCT), which provides quantitative information about the presence of near infrared region (NIR) dyes in the specimen or other strongly absorbing particles in the wavelength region of the OCT light [128, 134, 135]. With polarization-sensitive OCT (PS-OCT), the tissue birefringence is measured by detecting the change in the polarization of the back-scattered light caused by the specimen [124]. Changes in the ordered structure such as the actin filaments in muscle tissue or of collagen in skin has been thought to be attributed to the birefringence signal that can be measured with PS-OCT.

1.6.1 Magnetomotive Optical Coherence Tomography

MM-OCT is a novel method that was recently developed for providing additional contrast to OCT [10, 132, 136-139]. A solenoid placed just above the sample can induce a magnetic field strength ranging from 600 to 900 Gauss dependent on the driving voltage. This particular geometry allows the OCT imaging beam to pass through the central bore of the solenoid. Under this configuration, the magnetic field gradient is primarily in the axial direction along the same path as the OCT imaging beam and all radial components of the magnetic field are considered to be negligible within the OCT imaging volume.

Magnetomotion occurs when the applied magnetic field exerts a force on the magnetic particle along the axial direction (Figure 1.3). The motion of the magnetic particle physically displaces nearby scatterers, detected as a change in the OCT interferogram (Figure 1.3). The amplitude of the displacement is determined by the concentration of magnetic particles and the viscoelastic properties of the medium. Both higher magnetization and higher concentrations of the magnetic particle result in larger displacements of nearby scatterers. As the stiffness of the medium increases, the amplitude of the displacement decreases.

Using difference imaging, an OCT image is taken when the magnetic field is turned on and a second OCT image is taken when the magnetic field is turned off. The magnetomotive function can be added to either time-domain or spectral-domain OCT systems. In the case of time-domain MM-OCT, the field is turned off and on at each axial scan position along the transverse direction. Under spectral-domain MM-OCT, two images are acquired: one with the magnetic field modulated and the second OCT image with the field off. A sample schematic diagram of a time-domain MM-OCT system is depicted in Figure 1.4.

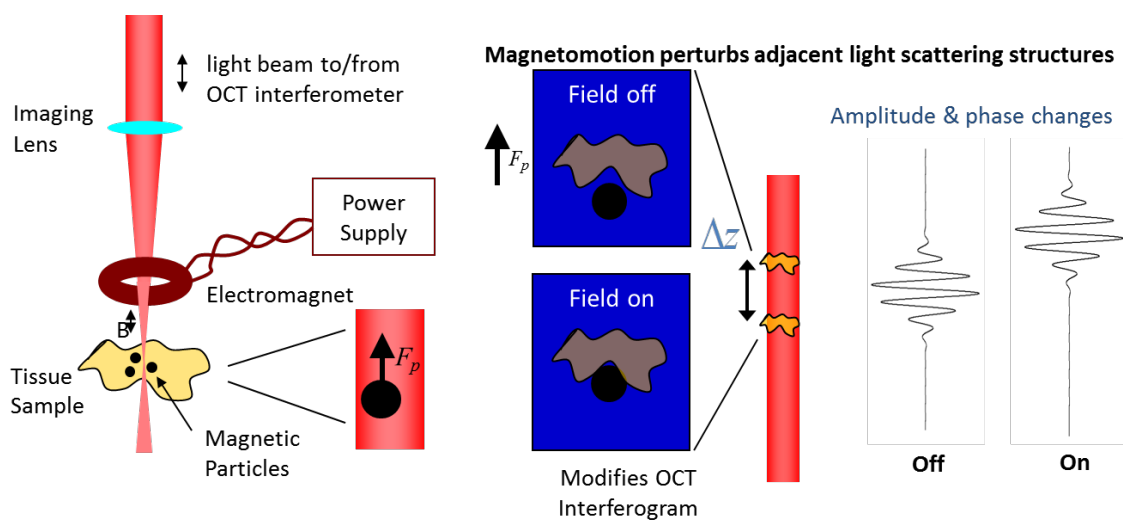


Figure 1.3: Magnetomotion in Magnetomotive Optical Coherence Tomography (MM-OCT) (courtesy of Amy Oldenburg).

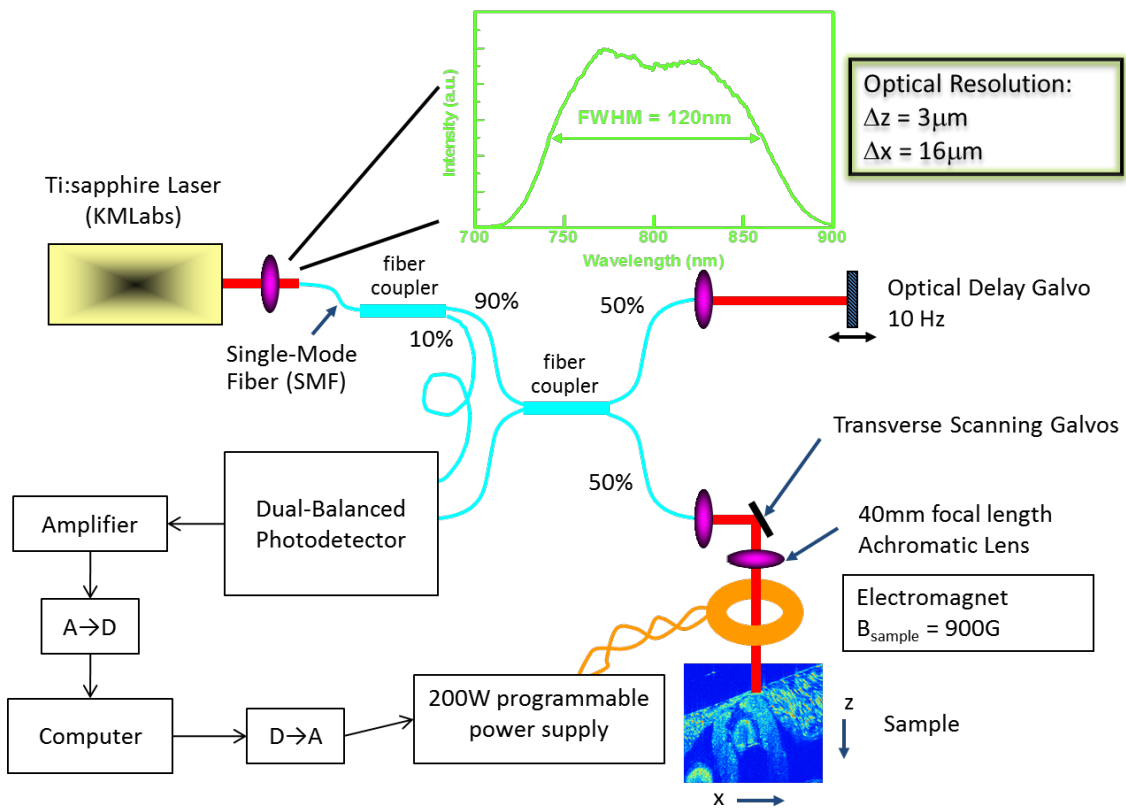


Figure 1.4: Schematic of a time-domain Magnetomotive OCT (MM-OCT) system.

1.7 Contrast Agents in OCT

The second method for extending the molecular sensitivity of OCT is through the development and use of exogenous contrast agents. Many different types of contrast agents have been developed for OCT and related imaging modalities that span a range of sizes and structures [140]. Protein microspheres have been modified for OCT imaging by incorporating gold nanoparticles into their protein shell to increase optical scattering [141]. Encapsulating iron oxide into protein microspheres provides MM-OCT contrast [142]. A more detailed discussion on the development of protein microspheres and protein microspheres as a contrast agent can be found in Chapters 4-5. Gold nanoshells, another class of OCT contrast agent, exhibit a large backscattering cross-section, which contributes significant OCT contrast in tissue phantoms at concentrations near 10^9 mL^{-1} [143, 144]. Hollowed-out gold nanocubes called nanocages (37 nm in size) can be detected at 1 nM concentrations using OCT [145]. Gold nanorods that are less than 45 nm in size provide absorption-based OCT contrast and can be detected at concentrations of 30 ppm [146]. Magnetic iron oxide nanoparticles were the first contrast agents to be developed for use with MM-OCT. These nanoparticles are perturbed using an externally modulated magnetic field which causes the physical displacement or magnetomotion of nearby scatterers providing the MM-OCT contrast previously described [132].

1.8 Summary

OCT is an interferometric imaging technique that provides real-time, high-resolution cross-sectional images of samples. OCT has been used in a wide number of biomedical

applications and has shown to be most successful in ophthalmology, cardiovascular applications, and oncology. Within the field of oncology, OCT has been shown to be quite successful in identifying tumor lesions in a number of clinical fields primarily because of the increased scattering observed with tumor cells. This increased scattering is largely attributed to the increased chromatin and increased nuclei to cytoplasmic (N/C) ratio commonly found in rapidly dividing cancer cells. The use of OCT for assessing tumor margins during breast conserving surgeries will be further discussed in Chapter 2. The intraoperative assessment of lymph nodes using OCT will be described and discussed in Chapter 3.

The endogenous OCT contrast is dependent on backscattered light provided by the sample, which is interfered with the light from the reference arm. The larger the change in refractive indices at boundary surfaces, the stronger the reflections detected by OCT. Many advances have increased the acquisition speed and resolution of the core OCT imaging technology. The most novel advances have been in the translation of OCT from a purely cellular imaging technique towards a molecular imaging technique. Molecular contrast can enhance OCT and is provided by new functional extensions such as pump-probe OCT or spectroscopic OCT, or with contrast agents. The use of contrast agents is potentially much more advantageous as it provides a method for adding exogenous contrast to samples, completely independent of the endogenous contrast from the specimen.

The development of protein microspheres as a targeted multi-modal contrast agent will be discussed in Chapters 4-5. The *in vitro* targeting and cellular uptake of RGD-coated and non-coated microspheres will be addressed in Chapter 6. Preliminary *ex vivo* and *in vivo* targeting studies of protein microspheres to the $\alpha_v\beta_3$ integrin receptors will be discussed.

Chapter 7 will focus on the future directions and conclusions of the work presented in this thesis.

1.9 References

1. Boppart SA, Bouma BE, Pitris C, Southern JF, Brezinski ME, Fujimoto JG. *In vivo* cellular optical coherence tomography imaging. *Nat Med*, 1998. 4 (7): p. 861-5.
2. Boppart SA, Bouma BE, Pitris C, Tearney GJ, Southern JF, Brezinski ME, Fujimoto JG. Intraoperative assessment of microsurgery with three-dimensional optical coherence tomography. *Radiology*, 1998. 208 (1): p. 81-6.
3. Boppart SA, Deutsch TF, Rattner DW. Optical imaging technology in minimally invasive surgery. Current status and future directions. *Surg Endosc*, 1999. 13 (7): p. 718-22.
4. Boppart SA, Luo W, Marks DL, Singletary KW. Optical coherence tomography: Feasibility for basic research and image-guided surgery of breast cancer. *Breast Cancer Res Treat*, 2004. 84 (2): p. 85-97.
5. Bouma BE, Tearney GJ. Handbook of optical coherence tomography. 2002, New York: Marcel Dekker. x, 741 p.
6. Fujimoto JG, Pitris C, Boppart SA, Brezinski ME. Optical coherence tomography: An emerging technology for biomedical imaging and optical biopsy. *Neoplasia*, 2000. 2 (1-2): p. 9-25.
7. Huang D, Swanson EA, Lin CP, Schuman JS, Stinson WG, Chang W, Hee MR, Flotte T, Gregory K, Puliafito CA, Et Al. Optical coherence tomography. *Science*, 1991. 254 (5035): p. 1178-81.
8. Huber R, Adler DC, Fujimoto JG. Buffered fourier domain mode locking: Unidirectional swept laser sources for optical coherence tomography imaging at 370,000 lines/s. *Opt Lett*, 2006. 31 (20): p. 2975-7.

9. De Boer JF, Milner TE, Van Gemert MJ, Nelson JS. Two-dimensional birefringence imaging in biological tissue by polarization-sensitive optical coherence tomography. *Opt Lett*, 1997. 22 (12): p. 934-6.
10. Oldenburg AL, Crecea V, Rinne SA, Boppart SA. Phase-resolved magnetomotive OCT for imaging nanomolar concentrations of magnetic nanoparticles in tissues. *Opt Express*, 2008. 16 (15): p. 11525-39.
11. Xu C, Vinegoni C, Ralston TS, Luo W, Tan W, Boppart SA. Spectroscopic spectral-domain optical coherence microscopy. *Opt Lett*, 2006. 31 (8): p. 1079-81.
12. Lee TM, Oldenburg AL, Sitafalwalla S, Marks DL, Luo W, Toublan FJ, Suslick KS, Boppart SA. Engineered microsphere contrast agents for optical coherence tomography. *Opt Lett*, 2003. 28 (17): p. 1546-8.
13. Yang C. Molecular contrast optical coherence tomography: A review. *Photochem Photobiol*, 2005. 81 (2): p. 215-37.
14. Zysk AM, Nguyen FT, Oldenburg AL, Marks DL, Boppart SA. Optical coherence tomography: A review of clinical development from bench to bedside. *J Biomed Opt*, 2007. 12 (5): p. 051403.
15. Herz PR, Chen Y, Aguirre AD, Schneider K, Hsiung P, Fujimoto JG, Madden K, Schmitt J, Goodnow J, Petersen C. Micromotor endoscope catheter for *in vivo*, ultrahigh-resolution optical coherence tomography. *Opt Lett*, 2004. 29 (19): p. 2261-3.
16. Tran PH, Mukai DS, Brenner M, Chen Z. *In vivo* endoscopic optical coherence tomography by use of a rotational microelectromechanical system probe. *Optics Letters*, 2004. 29 (11): p. 1236-8.

17. Xie T, Xie H, Fedder GK, Pan Y. Endoscopic optical coherence tomography with a modified microelectromechanical systems mirror for detection of bladder cancers. *Applied Optics*, 2003. 42 (31): p. 6422-6426.
18. Luerssen K, Lubatschowski H, Ursinus K, Gasse H, Koch R, Ptok M. [optical coherence tomography in the diagnosis of vocal folds]. *HNO*, 2006. 54 (8): p. 611-5.
19. Mahmood U, Ridgway J, Jackson R, Guo S, Su J, Armstrong W, Shibuya T, Crumley R, Chen Z, Wong B. *In vivo* optical coherence tomography of the nasal mucosa. *Am J Rhinol*, 2006. 20 (2): p. 155-9.
20. Ridgway JM, Armstrong WB, Guo S, Mahmood U, Su J, Jackson RP, Shibuya T, Crumley RL, Gu M, Chen Z. *In vivo* optical coherence tomography of the human oral cavity and oropharynx. *Archives of Otolaryngology- Head and Neck Surgery*, 2006. 132 (10): p. 1074-1081.
21. Bibas AG, Podoleanu AG, Cucu RG, Bonmarin M, Dobre GM, Ward VM, Odell E, Boxer A, Gleeson MJ, Jackson DA. 3-d optical coherence tomography of the laryngeal mucosa. *Clin Otolaryngol Allied Sci*, 2004. 29 (6): p. 713-20.
22. Brand S, Poneris JM, Bouma BE, Tearney GJ, Compton CC, Nishioka NS. Optical coherence tomography in the gastrointestinal tract. *Endoscopy*, 2000. 32 (10): p. 796-803.
23. Jackle S, Gladkova N, Feldchtein F, Terentieva A, Brand B, Gelikonov G, Gelikonov V, Sergeev A, Fritscher-Ravens A, Freund J, Seitz U, Soehendra S, Schrodern N. *In vivo* endoscopic optical coherence tomography of the human gastrointestinal tract--toward optical biopsy. *Endoscopy*, 2000. 32 (10): p. 743-9.

24. Pitris C, Jessor C, Boppart SA, Stamper D, Brezinski ME, Fujimoto JG. Feasibility of optical coherence tomography for high-resolution imaging of human gastrointestinal tract malignancies. *Journal of Gastroenterology*, 2000. 35 (2): p. 87-92.
25. Tearney GJ, Brezinski ME, Southern JF, Bouma BE, Boppart SA, Fujimoto JG. Optical biopsy in human gastrointestinal tissue using optical coherence tomography. *American Journal of Gastroenterology*, 1997. 92 (10): p. 1800-4.
26. Isenberg G, Sivak MV, Jr., Chak A, Wong RC, Willis JE, Wolf B, Rowland DY, Das A, Rollins A. Accuracy of endoscopic optical coherence tomography in the detection of dysplasia in barrett's esophagus: A prospective, double-blinded study. *Gastrointest Endosc*, 2005. 62 (6): p. 825-31.
27. Escobar PF, Belinson JL, White A, Shakhova NM, Feldchtein FI, Kareta MV, Gladkova ND. Diagnostic efficacy of optical coherence tomography in the management of preinvasive and invasive cancer of uterine cervix and vulva. *Int J Gynecol Cancer*, 2004. 14 (3): p. 470-4.
28. Zuluaga AF, Follen M, Boiko I, Malpica A, Richards-Kortum R. Optical coherence tomography: A pilot study of a new imaging technique for noninvasive examination of cervical tissue. *American Journal of Obstetrics and Gynecology*, 2005. 193 (1): p. 83-88.
29. Drezek R, Guillaud M, Collier T, Boiko I, Malpica A, Macaulay C, Follen M, Richards-Kortum R. Light scattering from cervical cells throughout neoplastic progression: Influence of nuclear morphology, DNA content, and chromatin texture. *J Biomed Opt*, 2003. 8 (1): p. 7-16.
30. *Cancer facts & figures 2010*; American Cancer Society: Atlanta, 2010.

31. *Breast cancer facts & figures 2009-2010*; American Cancer Society: Atlanta, 2010.
32. Arifler D, Guillaud M, Carraro A, Malpica A, Follen M, Richards-Kortum R. Light scattering from normal and dysplastic cervical cells at different epithelial depths: Finite-difference time-domain modeling with a perfectly matched layer boundary condition. *J Biomed Opt*, 2003. 8 (3): p. 484-94.
33. Luo W, Nguyen FT, Zysk AM, Ralston TLS, Brockenbrough J, Marks DL, Oldenburg AL, Boppart SA. Optical biopsy of lymph node morphology using optical coherence tomography. *Technology in Cancer Research & Treatment*, 2005. 4 (5): p. 539-547.
34. Goldberg BD, Iftimia NV, Bressner JE, Pitman MB, Halpern E, Bouma BE, Tearney GJ. Automated algorithm for differentiation of human breast tissue using low coherence interferometry for fine needle aspiration biopsy guidance. *J Biomed Opt*, 2008. 13 (1): p. 014014.
35. Hsiung PL, Phatak DR, Chen Y, Aguirre AD, Fujimoto JG, Connolly JL. Benign and malignant lesions in the human breast depicted with ultrahigh resolution and three-dimensional optical coherence tomography. *Radiology*, 2007. 244 (3): p. 865-74.
36. Zysk AM, Adie SG, Armstrong JJ, Leigh MS, Paduch A, Sampson DD, Nguyen FT, Boppart SA. Needle-based refractive index measurement using low-coherence interferometry. *Opt Lett*, 2007. 32 (4): p. 385-7.
37. Zysk AM, Boppart SA. Computational methods for analysis of human breast tumor tissue in optical coherence tomography images. *J Biomed Opt*, 2006. 11 (5): p. 054015.
38. Zysk AM, Chaney EJ, Boppart SA. Refractive index of carcinogen-induced rat mammary tumours. *Phys Med Biol*, 2006. 51 (9): p. 2165-77.

39. Bouma BE, Tearney GJ. Clinical imaging with optical coherence tomography. *Academic Radiology*, 2002. 9 (8): p. 942-53.
40. Bouma BE, Tearney GJ, Yabushita H, Shishkov M, Kauffman CR, DeJoseph Gauthier D, Macneill BD, Houser SL, Aretz HT, Halpern EF, Jang IK. Evaluation of intracoronary stenting by intravascular optical coherence tomography. *Heart*, 2003. 89 (3): p. 317-20.
41. Chau AH, Chan RC, Shishkov M, Macneill B, Iftimia N, Tearney GJ, Kamm RD, Bouma BE, Kaazempur-Mofrad MR. Mechanical analysis of atherosclerotic plaques based on optical coherence tomography. *Ann Biomed Eng*, 2004. 32 (11): p. 1494-503.
42. Fujimoto JG, Boppart SA, Tearney GJ, Bouma BE, Pitris C, Brezinski ME. High resolution *in vivo* intra-arterial imaging with optical coherence tomography. *Heart*, 1999. 82 (2): p. 128-33.
43. Gupta M, Rollins AM, Izatt JA, Efimov IR. Imaging of the atrioventricular node using optical coherence tomography. *Journal of Cardiovascular Electrophysiology*, 2002. 13 (1): p. 95.
44. Jang IK, Bouma BE, Kang DH, Park SJ, Park SW, Seung KB, Choi KB, Shishkov M, Schlendorf K, Pomerantsev E, Houser SL, Aretz HT, Tearney GJ. Visualization of coronary atherosclerotic plaques in patients using optical coherence tomography: Comparison with intravascular ultrasound. *Journal of the American College of Cardiology*, 2002. 39 (4): p. 604-9.
45. Jang IK, Tearney GJ, Macneill B, Takano M, Moselewski F, Iftima N, Shishkov M, Houser S, Aretz HT, Halpern EF, Bouma BE. *In vivo* characterization of coronary

- atherosclerotic plaque by use of optical coherence tomography. *Circulation*, 2005. 111 (12): p. 1551-5.
46. Macneill BD, Jang IK, Bouma BE, Iftimia N, Takano M, Yabushita H, Shishkov M, Kauffman CR, Houser SL, Aretz HT, DeJoseph D, Halpern EF, Tearney GJ. Focal and multi-focal plaque macrophage distributions in patients with acute and stable presentations of coronary artery disease. *Journal of the American College of Cardiology*, 2004. 44 (5): p. 972-9.
 47. Tearney GJ, Brezinski ME, Boppart SA, Bouma BE, Weissman N, Southern JF, Swanson EA, Fujimoto JG. Images in cardiovascular medicine. Catheter-based optical imaging of a human coronary artery. *Circulation*, 1996. 94 (11): p. 3013.
 48. Tearney GJ, Bouma BE. Method and apparatus for determination of atherosclerotic plaque type by measurement of tissue optical properties. *PCT International Patent Application*, 2002.
 49. Tearney GJ, Yabushita H, Houser SL, Aretz HT, Jang IK, Schlendorf KH, Kauffman CR, Shishkov M, Halpern EF, Bouma BE. Quantification of macrophage content in atherosclerotic plaques by optical coherence tomography. *Circulation*, 2003. 107 (1): p. 113-9.
 50. Yabushita H, Bouma BE, Houser SL, Aretz HT, Jang IK, Schlendorf KH, Kauffman CR, Shishkov M, Kang DH, Halpern EF, Tearney GJ. Characterization of human atherosclerosis by optical coherence tomography. *Circulation*, 2002. 106 (13): p. 1640-5.

51. Yelbuz TM, Choma MA, Thrane L, Kirby ML, Izatt JA. Optical coherence tomography: A new high-resolution imaging technology to study cardiac development in chick embryos. *Circulation*, 2002. 106 (22): p. 2771-4.
52. Zuluaga AF, Bouma BE. Multi-channel optical coupler for spinning catheter. *PCT International Patent Application*, 2003.
53. Brezinski ME, Tearney GJ, Bouma BE, Boppart SA, Hee MR, Swanson EA, Southern JF, Fujimoto JG. Imaging of coronary artery microstructure (*in vitro*) with optical coherence tomography. *American Journal of Cardiology*, 1996. 77 (1): p. 92-3.
54. Brezinski ME, Tearney GJ, Weissman NJ, Boppart SA, Bouma BE, Hee MR, Weyman AE, Swanson EA, Southern JF, Fujimoto JG. Assessing atherosclerotic plaque morphology: Comparison of optical coherence tomography and high frequency intravascular ultrasound. *Heart*, 1997. 77 (5): p. 397-403.
55. Takeda Y, Katoh O. Oct-guided wiring technique for chronic total coronary occlusion, in *Optical coherence tomography in cardiovascular research*, Regar E, Van Leeuwen TG, and Serruys PW, Editors. 2007, Informa Healthcare. p. 183-190.
56. Tanigawa J, Katoh O, Di Mario C. Chronic total occlusion: Do we need intravascular imaging guidance?, in *Optical coherence tomography in cardiovascular research*, Regar E, Van Leeuwen TG, and Serruys PW, Editors. 2007, Informa Healthcare. p. 171-182.
57. Jang IK, Tearney G, Bouma B. Visualization of tissue prolapse between coronary stent struts by optical coherence tomography: Comparison with intravascular ultrasound. *Circulation*, 2001. 104 (22): p. 2754.

58. Kume T, Akasaka T, Kawamoto T, Watanabe N, Toyota E, Neishi Y, Sukmawan R, Sadahira Y, Yoshida K. Assessment of coronary intima--media thickness by optical coherence tomography: Comparison with intravascular ultrasound. *Circ J*, 2005. 69 (8): p. 903-7.
59. Kume T, Akasaka T, Kawamoto T, Watanabe N, Toyota E, Sukmawan R, Sadahira Y, Yoshida K. Visualization of neointima formation by optical coherence tomography. *Int Heart J*, 2005. 46 (6): p. 1133-6.
60. Regar E, Van Beusekom HM, Van Der Giessen WJ, Serruys PW. Images in cardiovascular medicine. Optical coherence tomography findings at 5-year follow-up after coronary stent implantation. *Circulation*, 2005. 112 (23): p. e345-e346.
61. Surmely J-F, Takeda Y, Ito T, Suzuki T. Acute oct findings after stenting, in *Optical coherence tomography in cardiovascular research*, Regar E, Van Leeuwen TG, and Serruys PW, Editors. 2007, Informa Healthcare. p. 153-160.
62. *Heart disease and stroke statistics - 2005 update*; American Heart Association: Dallas, Texas, 2005.
63. Tearney GJ, Jang IK, Bouma BE. Optical coherence tomography for imaging the vulnerable plaque. *Journal of Biomedical Optics*, 2006. 11 (2): p. 021002.
64. Macneill BD, Bouma BE, Yabushita H, Jang IK, Tearney GJ. Intravascular optical coherence tomography: Cellular imaging. *J Nucl Cardiol*, 2005. 12 (4): p. 460-5.
65. Kume T, Akasaka T, Kawamoto T, Okura H, Watanabe N, Toyota E, Neishi Y, Sukmawan R, Sadahira Y, Yoshida K. Measurement of the thickness of the fibrous cap by optical coherence tomography. *Am Heart J*, 2006. 152 (4): p. 755 e1-4.

66. Van Der Meer FJ, Faber DJ, Baraznji Sassoon DM, Aalders MC, Pasterkamp G, Van Leeuwen TG. Localized measurement of optical attenuation coefficients of atherosclerotic plaque constituents by quantitative optical coherence tomography. *IEEE Transactions on Medical Imaging*, 2005. 24 (10): p. 1369-76.
67. Van Der Meer FJ, Faber DJ, Perree J, Pasterkamp G, Baraznji Sassoon D, Van Leeuwen TG. Quantitative optical coherence tomography of arterial wall components. *Lasers in Medical Science*, 2005. 20 (1): p. 45-51.
68. Liu Z, Wang F, Chen X. Integrin alpha(v)beta(3)-targeted cancer therapy. *Drug Dev Res*, 2008. 69 (6): p. 329-339.
69. Gasparini G, Brooks PC, Biganzoli E, Vermeulen PB, Bonoldi E, Dirix LY, Ranieri G, Miceli R, Cheresch DA. Vascular integrin alpha(v)beta3: A new prognostic indicator in breast cancer. *Clin Cancer Res*, 1998. 4 (11): p. 2625-34.
70. Burtea C, Laurent S, Murariu O, Rattat D, Toubreau G, Verbruggen A, Vanstherem D, Vander Elst L, Muller RN. Molecular imaging of alpha v beta 3 integrin expression in atherosclerotic plaques with a mimetic of rgd peptide grafted to gd-dtpa. *Cardiovasc Res*, 2008. 78 (1): p. 148-57.
71. Hoshiga M, Alpers CE, Smith LL, Giachelli CM, Schwartz SM. Alpha-v beta-3 integrin expression in normal and atherosclerotic artery. *Circ Res*, 1995. 77 (6): p. 1129-35.
72. Maile LA, Busby WH, Nichols TC, Bellinger DA, Merricks EP, Rowland M, Veluvolu U, Clemmons DR. A monoclonal antibody against alpha v beta 3 integrin inhibits development of atherosclerotic lesions in diabetic pigs. *Sci Transl Med*, 2010. 2 (18): p. 18ra11.

73. Juliano RL, Varner JA. Adhesion molecules in cancer: The role of integrins. *Curr Opin Cell Biol*, 1993. 5 (5): p. 812-8.
74. Glukhova M, Deugnier MA, Thiery JP. Tumor progression: The role of cadherins and integrins. *Mol Med Today*, 1995. 1 (2): p. 84-9.
75. Varner JA, Cheresch DA. Integrins and cancer. *Curr Opin Cell Biol*, 1996. 8 (5): p. 724-30.
76. Christofidou-Solomidou M, Bridges M, Murphy GF, Albelda SM, Delisser HM. Expression and function of endothelial cell alpha v integrin receptors in wound-induced human angiogenesis in human skin/scid mice chimeras. *Am J Pathol*, 1997. 151 (4): p. 975-83.
77. Pasqualini R, Koivunen E, Ruoslahti E. Alpha v integrins as receptors for tumor targeting by circulating ligands. *Nat Biotechnol*, 1997. 15 (6): p. 542-6.
78. Bader BL, Rayburn H, Crowley D, Hynes RO. Extensive vasculogenesis, angiogenesis, and organogenesis precede lethality in mice lacking all alpha v integrins. *Cell*, 1998. 95 (4): p. 507-19.
79. Clezardin P. Recent insights into the role of integrins in cancer metastasis. *Cell Mol Life Sci*, 1998. 54 (6): p. 541-8.
80. Eliceiri BP, Cheresch DA. The role of alpha v integrins during angiogenesis. *Mol Med*, 1998. 4 (12): p. 741-50.
81. Short SM, Talbott GA, Juliano RL. Integrin-mediated signaling events in human endothelial cells. *Molecular Biology of the Cell*, 1998. 9 (8): p. 1969-80.

82. Eliceiri BP, Cheresh DA. The role of alpha v integrins during angiogenesis: Insights into potential mechanisms of action and clinical development. *J Clin Invest*, 1999. 103 (9): p. 1227-30.
83. Haubner R, Wester HJ, Reuning U, Senekowitsch-Schmidtke R, Diefenbach B, Kessler H, Stocklin G, Schwaiger M. Radiolabeled alpha (v) beta (3) integrin antagonists: A new class of tracers for tumor targeting. *J Nucl Med*, 1999. 40 (6): p. 1061-71.
84. Castel S, Pagan R, Mitjans F, Piulats J, Goodman S, Jonczyk A, Huber F, Vilaro S, Reina M. Rgd peptides and monoclonal antibodies, antagonists of alpha(v)-integrin, enter the cells by independent endocytic pathways. *Lab Invest*, 2001. 81 (12): p. 1615-26.
85. Eliceiri BP, Cheresh DA. Adhesion events in angiogenesis. *Curr Opin Cell Biol*, 2001. 13 (5): p. 563-8.
86. Felding-Habermann B, O'toole TE, Smith JW, Fransvea E, Ruggeri ZM, Ginsberg MH, Hughes PE, Pampori N, Shattil SJ, Saven A, Mueller BM. Integrin activation controls metastasis in human breast cancer. *Proc Natl Acad Sci U S A*, 2001. 98 (4): p. 1853-8.
87. Liotta LA, Kohn EC. The microenvironment of the tumour-host interface. *Nature*, 2001. 411 (6835): p. 375-9.
88. Hynes RO. A reevaluation of integrins as regulators of angiogenesis. *Nat Med*, 2002. 8 (9): p. 918-21.
89. Janssen ML, Oyen WJ, Dijkgraaf I, Massuger LF, Frielink C, Edwards DS, Rajopadhye M, Boonstra H, Corstens FH, Boerman OC. Tumor targeting with

- radiolabeled alpha(v)beta(3) integrin binding peptides in a nude mouse model. *Cancer Res*, 2002. 62 (21): p. 6146-51.
90. Nisato RE, Tille JC, Jonczyk A, Goodman SL, Pepper MS. Alpha v beta 3 and alpha v beta 5 integrin antagonists inhibit angiogenesis *in vitro*. *Angiogenesis*, 2003. 6 (2): p. 105-19.
91. Jin H, Varner J. Integrins: Roles in cancer development and as treatment targets. *Br J Cancer*, 2004. 90 (3): p. 561-5.
92. Takagi J. Structural basis for ligand recognition by rgd (arg-gly-asp)-dependent integrins. *Biochem Soc Trans*, 2004. 32 (Pt3): p. 403-6.
93. Ginsberg MH, Partridge A, Shattil SJ. Integrin regulation. *Curr Opin Cell Biol*, 2005. 17 (5): p. 509-16.
94. Vellon L, Menendez JA, Lupu R. Alpha v beta 3 integrin regulates heregulin (hrg)-induced cell proliferation and survival in breast cancer. *Oncogene*, 2005. 24 (23): p. 3759-73.
95. Yamaguchi H, Wyckoff J, Condeelis J. Cell migration in tumors. *Curr Opin Cell Biol*, 2005. 17 (5): p. 559-64.
96. Bach-Gansmo T, Danielsson R, Saracco A, Wilczek B, Bogsrud TV, Fangberget A, Tangerud A, Tobin D. Integrin receptor imaging of breast cancer: A proof-of-concept study to evaluate 99mTc-nc100692. *J Nucl Med*, 2006. 47 (9): p. 1434-9.
97. Benedetto S, Pulito R, Crich SG, Tarone G, Aime S, Silengo L, Hamm J. Quantification of the expression level of integrin receptor alpha(v)beta 3 in cell lines and mr imaging with antibody-coated iron oxide particles. *Magn Reson Med*, 2006. 56 (4): p. 711-6.

98. Montet X, Montet-Abou K, Reynolds F, Weissleder R, Josephson L. Nanoparticle imaging of integrins on tumor cells. *Neoplasia*, 2006. 8 (3): p. 214-22.
99. Arnaout MA, Goodman SL, Xiong JP. Structure and mechanics of integrin-based cell adhesion. *Curr Opin Cell Biol*, 2007. 19 (5): p. 495-507.
100. Takada Y, Ye X, Simon S. The integrins. *Genome Biol*, 2007. 8 (5): p. 215.
101. Takagi J. Structural basis for ligand recognition by integrins. *Curr Opin Cell Biol*, 2007. 19 (5): p. 557-64.
102. White DE, Muller WJ. Multifaceted roles of integrins in breast cancer metastasis. *J Mammary Gland Biol Neoplasia*, 2007. 12 (2-3): p. 135-42.
103. Avraamides CJ, Garmy-Susini B, Varner JA. Integrins in angiogenesis and lymphangiogenesis. *Nat Rev Cancer*, 2008. 8 (8): p. 604-17.
104. Garmy-Susini B, Varner JA. Roles of integrins in tumor angiogenesis and lymphangiogenesis. *Lymphat Res Biol*, 2008. 6 (3-4): p. 155-63.
105. Ginsberg MH, Schwarzbauer JE. Cell-to-cell contact and extracellular matrix. *Curr Opin Cell Biol*, 2008. 20 (5): p. 492-4.
106. Hodivala-Dilke K. Alpha v beta 3 integrin and angiogenesis: A moody integrin in a changing environment. *Curr Opin Cell Biol*, 2008. 20 (5): p. 514-9.
107. Santra S, Kaittanis C, Grimm J, Perez JM. Drug/dye-loaded, multifunctional iron oxide nanoparticles for combined targeted cancer therapy and dual optical/magnetic resonance imaging. *Small*, 2009. 5 (16): p. 1862-8.
108. Brooks SA, Lomax-Browne HJ, Carter TM, Kinch CE, Hall DM. Molecular interactions in cancer cell metastasis. *Acta Histochem*, 2010. 112 (1): p. 3-25.

109. Ruegg C, Alghisi GC. Vascular integrins: Therapeutic and imaging targets of tumor angiogenesis. *Recent Results Cancer Res*, 2010. 180: p. 83-101.
110. Antonov AS, Kolodgie FD, Munn DH, Gerrity RG. Regulation of macrophage foam cell formation by alpha v beta 3 integrin: Potential role in human atherosclerosis. *Am J Pathol*, 2004. 165 (1): p. 247-58.
111. Bishop GG, Mcpherson JA, Sanders JM, Hesselbacher SE, Feldman MJ, Mcnamara CA, Gimple LW, Powers ER, Mousa SA, Sarembock IJ. Selective alpha(v)beta(3)-receptor blockade reduces macrophage infiltration and restenosis after balloon angioplasty in the atherosclerotic rabbit. *Circulation*, 2001. 103 (14): p. 1906-11.
112. Camenisch G, Pisabarro MT, Sherman D, Kowalski J, Nagel M, Hass P, Xie MH, Gurney A, Bodary S, Liang XH, Clark K, Beresini M, Ferrara N, Gerber HP. Angptl3 stimulates endothelial cell adhesion and migration via integrin alpha v beta 3 and induces blood vessel formation *in vivo*. *J Biol Chem*, 2002. 277 (19): p. 17281-90.
113. Khurana R, Simons M, Martin JF, Zachary IC. Role of angiogenesis in cardiovascular disease: A critical appraisal. *Circulation*, 2005. 112 (12): p. 1813-24.
114. Moiseeva EP. Adhesion receptors of vascular smooth muscle cells and their functions. *Cardiovasc Res*, 2001. 52 (3): p. 372-86.
115. Tam SH, Sassoli PM, Jordan RE, Nakada MT. Abciximab (reopro, chimeric 7e3 fab) demonstrates equivalent affinity and functional blockade of glycoprotein iib/iiiA and alpha(v)beta 3 integrins. *Circulation*, 1998. 98 (11): p. 1085-91.
116. Weng S, Zemany L, Standley KN, Novack DV, La Regina M, Bernal-Mizrachi C, Coleman T, Semenkovich CF. Beta 3 integrin deficiency promotes atherosclerosis and

- pulmonary inflammation in high-fat-fed, hyperlipidemic mice. *Proc Natl Acad Sci U S A*, 2003. 100 (11): p. 6730-5.
117. An L, Guan G, Wang RK. High-speed 1310 nm-band spectral domain optical coherence tomography at 184,000 lines per second. *J Biomed Opt*, 2011. 16 (6): p. 060506.
 118. De Boer JF, Cense B, Park BH, Pierce MC, Tearney GJ, Bouma BE. Improved signal-to-noise ratio in spectral-domain compared with time-domain optical coherence tomography. *Opt Lett*, 2003. 28 (21): p. 2067-9.
 119. Yun S, Tearney G, Bouma B, Park B, De Boer J. High-speed spectral-domain optical coherence tomography at 1.3 μm wavelength. *Opt Express*, 2003. 11 (26): p. 3598-604.
 120. Choma M, Sarunic M, Yang C, Izatt J. Sensitivity advantage of swept source and fourier domain optical coherence tomography. *Opt Express*, 2003. 11 (18): p. 2183-9.
 121. Yun S, Tearney G, De Boer J, Iftimia N, Bouma B. High-speed optical frequency-domain imaging. *Opt Express*, 2003. 11 (22): p. 2953-63.
 122. Yun SH, Tearney G, De Boer J, Bouma B. Pulsed-source and swept-source spectral-domain optical coherence tomography with reduced motion artifacts. *Opt Express*, 2004. 12 (23): p. 5614-24.
 123. Ralston TS, Marks DL, Scott Carney PS, Boppart SA. Interferometric synthetic aperture microscopy. *Nat Phys*, 2007. 3 (2): p. 129-134.
 124. Roth JE, Izatt JA, Rollins AM. Method and apparatus for polarization-sensitive optical coherence tomography. *PCT Int. Appl.*, 2002.

125. Lazebnik M, Marks DL, Potgieter K, Gillette R, Boppart SA. Functional optical coherence tomography for detecting neural activity through scattering changes. *Opt Lett*, 2003. 28 (14): p. 1218-20.
126. Toublan FJ, Suslick KS, Boppart SA, Lee TM, Oldenburg AL. Modification of protein microspheres for biomedical application. *Polymer Preprints*, 2003. 44: p. 185.
127. Rao KD, Choma MA, Yazdanfar S, Rollins AM, Izatt JA. Molecular contrast in optical coherence tomography by use of a pump-probe technique. *Opt Lett*, 2003. 28 (5): p. 340-2.
128. Xu C, Ye J, Marks DL, Boppart SA. Near-infrared dyes as contrast-enhancing agents for spectroscopic optical coherence tomography. *Opt Lett*, 2004. 29 (14): p. 1647-9.
129. Marks DL, Boppart SA. Nonlinear interferometric vibrational imaging. *Phys Rev Lett*, 2004. 92 (12): p. 123905.
130. Yang C, Choma MA, Lamb LE, Simon JD, Izatt JA. Protein-based molecular contrast optical coherence tomography with phytochrome as the contrast agent. *Opt Lett*, 2004. 29 (12): p. 1396-8.
131. Yang C, McGuckin LE, Simon JD, Choma MA, Applegate BE, Izatt JA. Spectral triangulation molecular contrast optical coherence tomography with indocyanine green as the contrast agent. *Opt Lett*, 2004. 29 (17): p. 2016-8.
132. Oldenburg AL, Gunther JR, Boppart SA. Imaging magnetically labeled cells with magnetomotive optical coherence tomography. *Opt Lett*, 2005. 30 (7): p. 747-9.
133. Bredfeldt JS, Vinegoni C, Marks DL, Boppart SA. Molecularly sensitive optical coherence tomography. *Opt Lett*, 2005. 30 (5): p. 495-7.

134. Storen T, Royset A, Svaasand LO, Lindmo T. Functional imaging of dye concentration in tissue phantoms by spectroscopic optical coherence tomography. *J Biomed Opt*, 2005. 10 (2): p. 024037.
135. Xu C, Kamalabadi F, Boppart SA. Comparative performance analysis of time-frequency distributions for spectroscopic optical coherence tomography. *Appl Opt*, 2005. 44 (10): p. 1813-22.
136. John R, Boppart SA. Magnetomotive molecular nanoprobe. *Curr Med Chem*, 2011. 18 (14): p. 2103-14.
137. John R, Nguyen FT, Kolbeck KJ, Chaney EJ, Marjanovic M, Suslick KS, Boppart SA. Targeted multifunctional multimodal protein-shell microspheres as cancer imaging contrast agents. *Mol Imaging Biol*, 2012. 14 (1): p. 17-24.
138. John R, Rezaeipoor R, Adie SG, Chaney EJ, Oldenburg AL, Marjanovic M, Haldar JP, Sutton BP, Boppart SA. *In vivo* magnetomotive optical molecular imaging using targeted magnetic nanoprobe. *Proc Natl Acad Sci U S A*, 2010. 107 (18): p. 8085-90.
139. Oldenburg AL, Toublan FJ, Suslick KS, Wei A, Boppart SA. Magnetomotive contrast for *in vivo* optical coherence tomography. *Opt Express*, 2005. 13 (17): p. 6597-614.
140. Boppart SA, Oldenburg AL, Xu C, Marks DL. Optical probes and techniques for molecular contrast enhancement in coherence imaging. *J Biomed Opt*, 2005. 10 (4): p. 41208.
141. Lee TM, Oldenburg AL, Sitafalwalla S, Marks DL, Luo W, Toublan FJ, Suslick KS, Boppart SA. Engineered microsphere contrast agents for optical coherence tomography. *Optics Letters*, 2003. 28 (17): p. 1546-8.

142. Toublan FJ. *Methods to tailor protein microspheres for biomedical applications* [dissertation]. Urbana, IL: University of Illinois at Urbana-Champaign; 2005.
143. Oldenburg SJ, Averitt RD, Westcott SL, Halas NJ. Nanoengineering of optical resonances. *Chemical Physics Letters*, 1998. 288 (2): p. 243-247.
144. Agrawal A, Huang S, Wei Haw Lin A, Lee MH, Barton JK, Drezek RA, Pfefer TJ. Quantitative evaluation of optical coherence tomography signal enhancement with gold nanoshells. *J Biomed Opt*, 2006. 11 (4): p. 041121.
145. Chen J, Saeki F, Wiley BJ, Cang H, Cobb MJ, Li ZY, Au L, Zhang H, Kimmey MB, Li X, Xia Y. Gold nanocages: Bioconjugation and their potential use as optical imaging contrast agents. *Nano Lett*, 2005. 5 (3): p. 473-7.
146. Oldenburg AL, Hansen MN, Zweifel DA, Wei A, Boppart SA. Plasmon-resonant gold nanorods as low backscattering albedo contrast agents for optical coherence tomography. *Optics Express*, 2006. 14 (15): p. 6724-6738.

CHAPTER 2 OPTICAL COHERENCE TOMOGRAPHY IN TUMOR MARGIN ASSESSMENT

2.1 Introduction

2.1.1 Tumor Margin Assessment and Local Recurrence

As lumpectomy rates increase over time, the definition of a clean surgical margin continues to change. A recent study of radiation oncologists reported that 45.9% defined negative margins as no cancer cells at the inked margins; whereas, 7.4% defined them as no cells within 1 mm, and 21.8% believed them as no cells within 2 mm [1]. As more studies correlated the width of uninvolved margins to local recurrence [2, 3], more aggressive approach towards breast conservation allow surgeons to use 2 mm, or even 1 mm, to define a clean margin. The same survey of radiation oncologists reported that 31% of respondents defined a close margin as having no cells within 1 mm, and an additional 38% defined it to be no cells within 2 mm of the inked surface [1].

Despite this debate, the key predictor of local recurrence is the margin status [4-15]. A positive margin, the presence of disease on the inked surface, occurs in at least 30-35% of surgical cases, and an additional 10-15% are classified as close margins (< 2 mm) [14]. Local recurrence rates for breast conserving therapy followed by radiation were reported in 2-28% of cases with positive margins, 2-16% with close margins (< 2 mm), and 2-8% with negative margins [14] which would be higher in the absence of radiation therapy [5, 7, 16, 17].

2.1.2 Intraoperative Margin Assessment

Currently, no real-time non-destructive intraoperative method exists to rapidly assess the microscopic status of lumpectomy margins as a standard of care [18, 19]. Several

techniques have been investigated including frozen section analysis (FSA), touch prep cytology, radiography, radiofrequency (RF) spectroscopy, and Raman spectroscopy. FSA has a sensitivity of 73.08% and a specificity of 98.32% compared to paraffin section analysis (PSA) in breast cancer [18]. FSA is not widely accepted as part of a standard of care due to difficulties in performing frozen sections on adipose tissue, added time (~20-30 minutes), increased operating room time, and increased costs associated with further pathology evaluation. The most significant disadvantage with FSA is the inability to be performed over the entire surface area of the tissue specimen, sharing the same sampling rate limitation as PSA in sampling only 10-15% of the surface area [20].

Touch prep cytology can rapidly assess the entire surface area, addressing the sampling rate issue while preserving the integrity of the specimen, and making it a promising technique for identifying positive margins. This technique reported sensitivities of 75% and specificities of 82.8% [20]. The major disadvantages include the need for tumor cells at the surface, and their detachment. Touch prep cytology does not provide information about the presence of cancer cells beneath the surface and therefore is unable to determine close and negative margins.

Intraoperative radiography of specimens provides surgeons with the ability to visualize margins in depth by displaying two-dimensional x-ray projections. However, the low reported sensitivity and specificity of 49% and 73%, respectively [21], are primarily due to the inability to identify diffuse microscopic processes, especially where the tumor boundary is poorly defined [22].

RF spectroscopy provides a bulk measurement over a circular area (0.7 cm diameter) and within a 100 μm depth [23]. With low sensitivity (71%) and specificity (68%) [23],

shallow penetration depth, and low resolution, detection within 1-2 mm for margin classification is limited. Raman spectroscopy, which extracts chemical information, was reported to have a sensitivity of 100%, a specificity of 100%, and an overall accuracy of 93% in identifying carcinomas [24]. Despite high sensitivity and specificity, this technique may have limited clinical utility because the required point measurements with long 1 second acquisition times per point prevent sampling of large surface areas.

2.2 Portable Clinical Spectral Domain Optical Coherence Tomography System

A clinical spectral-domain OCT (SD-OCT) system (Figure 2.1) was constructed to assess surgical margins from lumpectomy specimens. This OCT system was previously described in detail previously in Chapter 1 Section 5. The system employs a super-luminescent diode (SLD) (Model SLD1C, B&W Tek, Inc., Newark, Delaware), with an optical spectrum centered at 1310 nm and a bandwidth of 92 nm. Approximately 4.75 mW of light is focused onto a 35 μm spot (transverse resolution) on the sample. The broad bandwidth source yields an axial resolution of 8.2 μm in air or 5.9 μm in tissue. The depth-of-field of the lens (1.47 mm) closely matches the penetration depth of OCT in human breast tissue. The camera exposure time ranges from 24.4 μs to 408.4 μs , corresponding to measured signal-to-noise ratios of 96 dB to 116 dB. OCT images are acquired at a rate of $\sim 5,000$ axial scans per second or up to ~ 8 -9 images per second (~ 600 axial scans / 10 mm). Acquisition and processing time for an OCT image was ~ 5 seconds / image. The data is assembled, processed as previously described, and displayed as a two-dimensional image.

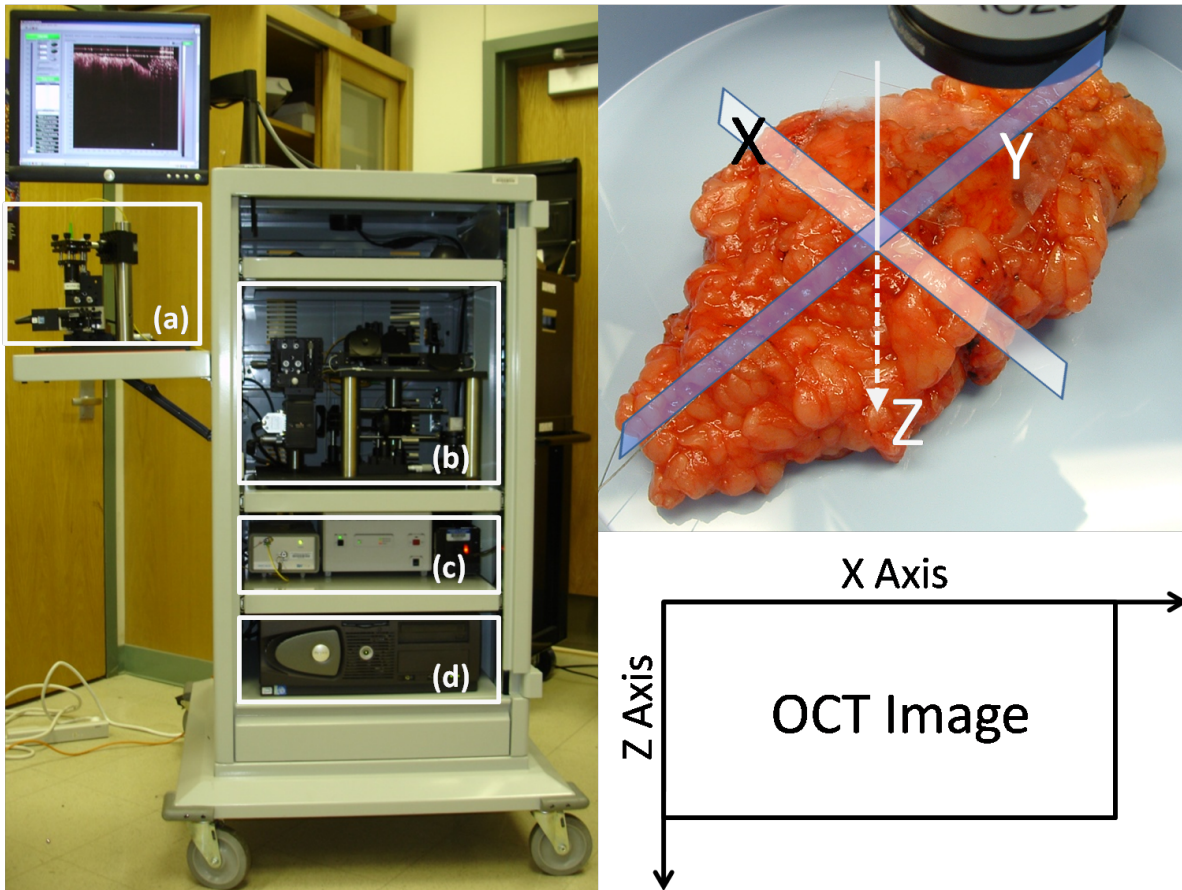


Figure 2.1: Photograph of the clinical SD-OCT system housed in a standard endoscopy cart (left). This system is portable for use in various surgical suites. Resected surgical specimens are placed on the sample-arm stage (a). The detector and reference arm (b) are located within the cart, along with the light source and hardware controllers (c) and computer (d). OCT images (shown in later figures) represent two dimensional cross-sectional planes (x-z) oriented perpendicular to the tissue surface (right). Multiple OCT images can be acquired by stepping the beam in the y direction.

2.3 Clinical Study

Patients identified and recruited for this study had primary breast tumors (both *in situ* and invasive carcinoma) in need of surgical resection by breast-conserving surgery, as determined by physicians at Carle Foundation Hospital and Carle Clinic Association, Urbana, Illinois, based on pre-operative radiological films, biopsy results, or other relevant diagnostic information. Patients undergoing mastectomy were excluded due to decreased likelihood of positive or close margins. No patients were excluded due to age or race. Patients were informed and consented prior to surgery per protocols approved by institutional review boards at the University of Illinois at Urbana-Champaign and Carle Foundation Hospital.

After surgical tissue resection but prior to margin assessment by the radiologist or pathologist, the initial lumpectomy specimen was imaged in the operating room using OCT (Figure 2.1). A series of 10-20 parallel images were taken over a 1.0 x 1.0 cm area. The researchers involved in image acquisition varied between imaging sessions and neither the surgeon nor staff disclosed any information about the specimen during the imaging sessions. Regions selected for OCT were based on suspicious visual or palpable findings as determined by the researchers, or were the entry-exit sites of localization guide wires. Following OCT imaging, one imaging site per specimen was marked with ink for correlation with histopathology, and the specimen was returned to surgical staff for standard processing and pathological margin assessment. In addition to histology sections acquired for diagnostic purposes as part of a standard of care, sections co-registered with intraoperative OCT were acquired, stained, and correlated.

2.3.1 Patient Information

A total of 37 female patients were enrolled in the study. The training set consisted of 17 patients with a mean age of 62 (range from 44 to 82) and the study set consisted of 20 patients with a mean age of 66 (range from 41 to 84). Their diagnoses, based on pathological findings and tumor margin assessments, included 15 cases of ductal carcinoma *in situ*, 1 case of lobular carcinoma *in situ*, 2 cases of infiltrating ductal carcinoma, 9 cases of invasive ductal carcinoma, 1 case of invasive papillary carcinoma, 2 cases of invasive mammary carcinoma, and 1 case of atypical ductal hyperplasia. The majority had more than one diagnosis classification associated with their histopathological assessment. An additional two patients in the training set and two in the study set were consented but subsequently excluded from the study and OCT imaging due to changes in surgery schedules or procedures.

2.4 OCT Image Processing & Evaluation Protocol

All OCT images were processed with the same standardization method and displayed on the same intensity scale [25]. OCT images were initially evaluated in real-time by one of several researchers trained on the characteristic features found on OCT of breast tissue to ensure that the images were of sufficient quality for evaluation and to ensure that a subset of the images collected contained diagnostic features. Using criteria established from the training set, a single researcher during a single session, several months after the data sets were acquired, evaluated all OCT images and identified normal or abnormal features. Since the OCT imaging depth is approximately within the same 2 mm range that pathologist used to define a close margin, OCT images with abnormal features were classified as positive. The observed OCT image features were thought to be indicative of either invasive or *in situ*

carcinoma. OCT margin assessment was made using the entire set of available OCT images (10-20 images) taken at each imaging site and was correlated with the respective histological section from that site.

2.5 Histology Image Evaluation Protocol

Histology sections were acquired from marked areas imaged in the operating room with OCT. All tissue sections were stained with hematoxylin and eosin (H&E) and some were additionally immunohistochemically stained as determined by the pathologists and the pathology staff. Histology slides were digitized using a light microscope at 4X magnification and stitched together (Adobe Photoshop) to produce a single image. The compiled montage was oriented based on inked borders for later correlation to OCT images. A board-certified pathologist classified the H&E-stained histology images either as invasive carcinoma, *in situ* carcinoma, other non-normal tissue, or normal tissue. Margins identified as carcinoma or other non-normal tissues were considered to be positive. The pathologist was blind to the OCT images and results so that an independent and unbiased assessment of the histology slide corresponding to the matching OCT image set could be made.

2.6 Training Data Set

An initial training data set of 78 OCT images from 17 patients (min = 2, max = 10, avg = 5 images / specimen) were used to establish standard imaging protocols, co-registration procedures, and image evaluation criteria of the surgical margins. Representative images shown in Figure 2.2 include normal adipose tissue (Figure 2.2a), surgical artifacts of surface

blood (Figure 2.2b) and cauterized tissue (Figure 2.2c), areas that appear duct-like in shape (Figure 2.2d and Figure 2.2e), and areas of highly scattering cells with spatially heterogeneous scattering intensity (Figure 2.2f). These results were confirmed by gross visual findings or by histopathological analysis. Histopathological analysis reported DCIS involvement for the specimen imaged in Figure 2.2f.

The training data set findings were used to establish methodologies used in subsequent analyses for identifying positive margins. These criteria include the presence or absence of high-intensity scatterers, the location of these scatterers throughout the tissue, the heterogeneous/homogeneous spatial distribution of scattering intensity, and the morphological characteristics of these regions of interest. Surgical artifacts that could interfere with OCT evaluation such as surface blood and cauterized tissue appeared as contiguous and highly scattering areas, remained localized to the immediate surface, and were quickly identified visually in the imaging field. In Figure 2.2b, a thin film ($< 100 \mu\text{m}$) of homogeneous scatterers represented a bloody surface, while in Figure 2.2c, the cauterized tissue produced a highly scattering area which was observed within $\sim 300 \mu\text{m}$ of the tissue surface. The region of interest in Figure 2.2d had both a high scattering intensity and a more heterogeneous composition indicative of cancerous tissue. In Figure 2.2d, the presence of highly scattering regions deep in the margin, instead of localized to the immediate surface, suggested that these features were intrinsic to the tissue architecture rather than a result of the surgical procedure.

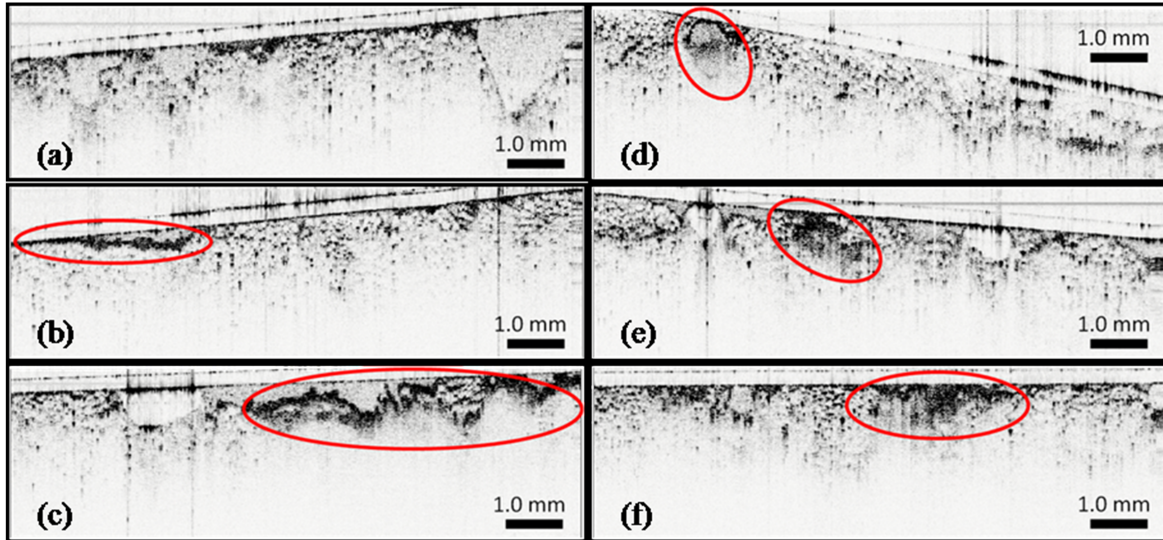


Figure 2.2: Representative OCT images of surgical margins from lumpectomy specimens acquired for the training set. Images of normal tissue (a) were identified by the homogenous pattern of large adipose cells. Readily identified surgical artifacts included blood (b), which appeared as a thin film of scatterers, and cauterized tissue (c), which had a patch-like appearance. Image of a potential duct (d) with a mixed distribution of low and high scattering areas. Images of positive margins (e & f) containing tumor cells and tissue represented by a highly scattering area that was more heterogeneous and disruptive compared to the surrounding tissue architecture.

2.7 Study Data Set

OCT images with histological correlations from an additional 20 patients were used for the study set. A total of 210 OCT images were acquired from 20 lumpectomy specimens with an average of 10 OCT images per specimen. Specimen margins were classified either as positive or as negative using the criteria established in the training set. A margin was considered positive if there was evidence of tumor cells or tissue either at the immediate surface, or within the imaging depth of OCT (1-2 mm). Eleven tissue margins were identified as positive and 9 as negative with OCT analysis. Analysis of the corresponding H&E-stained histological sections yielded 9 true positives, 9 true negatives, 2 false positives, and 0 false negatives, giving a sensitivity of 100% and specificity of 82% (Table 2.1). Overall accuracy of OCT was 90% with a positive predictive value and a negative predictive value of 82% and 100%, respectively. Three representative cases from the study set are presented in Figure 2.3 and Figure 2.4. The first patient (female, age 66) was diagnosed with DCIS via ultrasound-guided core-needle biopsy with a 3.0 cm primary tumor. This case (Figure 2.3) demonstrates OCT assessment of a negative tumor margin, which consists primarily of large lipid-filled adipocytes with interweaving microvasculature. The small dark highly scattering point-like regions in the OCT image correspond to individual nuclei of adipocytes. Histological evaluation indicated that tumor cells were located more than 3 mm from the surface, confirming the OCT findings of a negative margin.

A second patient (female, age 60), diagnosed with invasive papillary carcinoma via ultrasound-guided core-needle biopsy, had a 0.8 cm primary tumor removed by lumpectomy. A third patient (female, age 51) was diagnosed with poorly differentiated infiltrating ductal carcinoma and high-grade ductal carcinoma *in situ* with a 2.3 cm primary tumor.

Intraoperative OCT imaging of the margins (Figure 2.4) revealed suspicious regions with increased and heterogeneous scattering within 1 mm of the inked surface (Figure 2.4a, female, age 60, patient #2) and within 0.5 to 1.25 mm of the surface (Figure 2.4c, female, age 51, patient #3). The matching H&E stained histology sections for the OCT images shown in Figure 2.4a and Figure 2.4c are provided in Figure 2.4b and Figure 2.4d, respectively, and confirmed the diagnostic features observed. These sections contained small and highly scattering cells, which contributed to the increased contrast when compared to adjacent adipocytes. The increased scattering is from strong reflections from tightly packed cells, which provides the contrast observed in OCT. These results demonstrate distinct structural features identified with real-time intraoperative OCT on unstained tissue specimens that can be used to identify positive and negative margins without compromising the structural integrity of the specimens.

Table 2.1: Intraoperative Tumor Margin Assessment (OCT vs. Histopathology).

	Histology (Positive)	Histology (Negative)	Total	
OCT (Positive)	9 (TP)	2 (FP)	11	PPV = 82%
OCT (Negative)	0 (FN)	9 (TN)	9	NPV = 100%
Total	9	11	20	

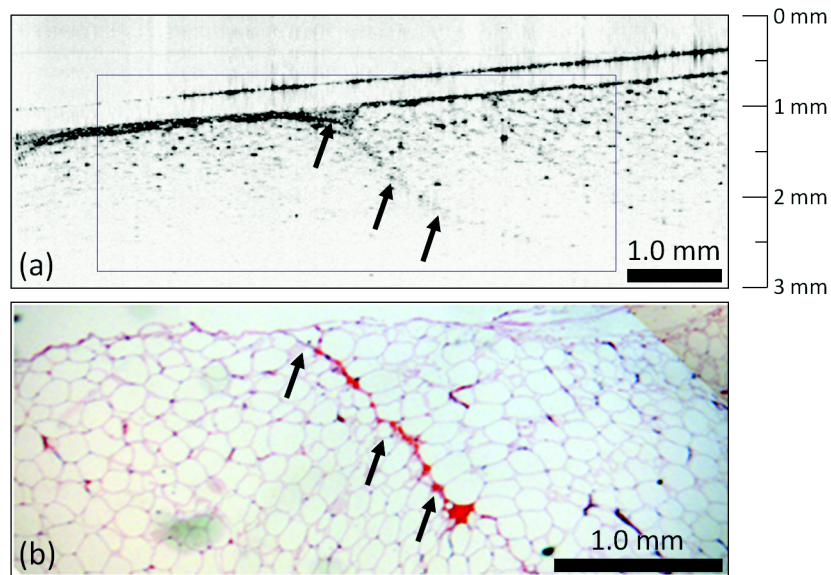


Figure 2.3: Negative tumor margin. OCT (a) and corresponding H&E-stained histology (b) of normal breast tissue near the surface of a lumpectomy specimen. The large adipose cells with point-like scattering nuclei predominate in the OCT image, which also contains a region of microvasculature (arrows). Features found in the real-time intraoperative OCT image correspond well to those identified in the post-surgical paraffin-embedded histology section.

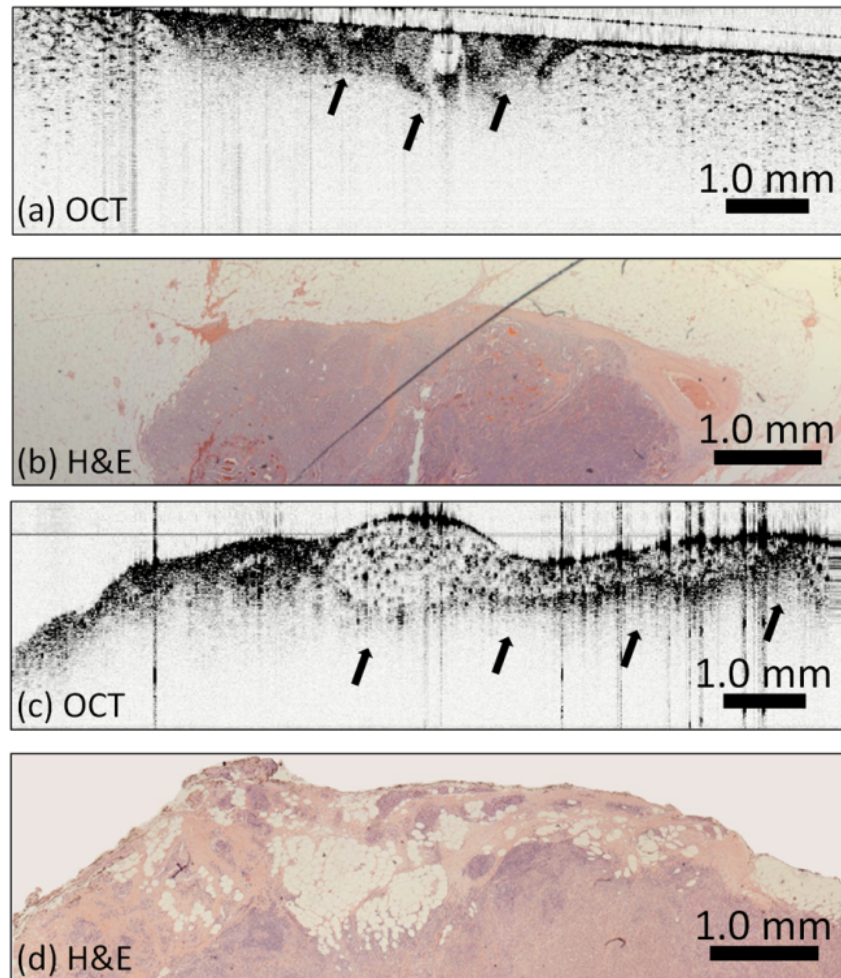


Figure 2.4: Positive tumor margins. OCT images (a, c) show a distinct heterogeneously scattering region (arrows) with small, highly scattering foci indicative of collections of tumor cells. These features clearly extend to both the surface (the surgical margin) in (a) and the left side (c) of the specimen, but also are evident below adipose tissue in (c). The OCT image in (a) was acquired with a coverslip over the surface to reduce back reflection artifacts, which appear as vertical lines in (c). Corresponding H&E-stained histology (b, d) images show corresponding features, confirming the presence of these positive margins.

This study presents the first intraoperative demonstration of OCT as a real-time, high resolution imaging technique for the microscopic assessment of breast tumor margins. By providing subsurface imaging capabilities 1-2 mm deep with micron-scale resolution, OCT provides surgeons with the ability to assess margin status in real-time, complement current gross visual examination, potentially reduce the number of positive / close margins discovered post-operatively, and thereby reduce the need for additional surgical procedures. In the current standard of care, pathologists perform microscopic margin assessment within 2 mm range of the tissue surface using FSA or PSA to determine the need for additional tissue removal.

OCT identified areas of homogeneous adipocytes, suspicious regions with highly scattering and tightly packed cells, and heterogeneous scattering patterns as some of the key features used to classify margins as negative or positive, as verified by histopathology. The large relative cell size difference easily separates the identification of adipocytes from tumor cells and stromal tissue. Increased nuclear density and changes in chromatin texture are believed to be responsible for high levels of scattering observed from cancer cells [26, 27]. At later tumor stages, observed characteristics change from open to filled ducts and lobules, and to heterogeneous tumor masses. Focal regions of scatterers embedded in adipose tissue, as identified under OCT, indicated smaller clusters of tumor cells. More advanced stages of cancer were identified by areas of highly scattering tissue with irregular and heterogeneous patterns. Due to the increased sampling rate of tumor margins offered by OCT, we expect to identify an increased number of positive surgical margins not otherwise grossly identifiable and likely missed due to limited sampling of standard histopathological analysis.

Surgical artifacts such as cauterized tissue and superficial blood are identified in OCT images as a contiguous layer of dark scatterers. These artifacts appear homogeneous in nature and are limited to the cut surface of the surgical margin rather than extending deep into the tissue. A relatively large pool of blood or cauterized tissue can limit the penetration depth of OCT due to high scattering. The imaging penetration depth with a bloody surface (Figure 2.4b) is slightly diminished, compared to a cauterized surface (Figure 2.2c) where penetration depth drops off sharply with little to no features observed beyond the cauterized tissue. Intravascular blood in small vessels and capillaries makes up a relatively small percentage of the tissue volume and has a minimal impact on the OCT penetration depth. In cases with residual surface blood, saline has been used to rapidly irrigate the surface to regain OCT imaging depth. OCT has been demonstrated for *in vivo* intravascular applications in humans, where an OCT imaging catheter is fully immersed in blood and imaging is performed following a saline flush [28]. These surgical artifacts can be differentiated from intrinsic tissue properties, and can be quickly addressed without interfering with the ability of OCT to assess the margin. The presence of dyes such as methylene blue or lymphazurin, which are used to map lymph drainage for sentinel and axillary lymph node dissections, absorb in the spectral region below 700 nm (Figure 2.5). Therefore, the presence of these dyes does not affect OCT imaging since our system operates in the spectral region around 1300 nm.

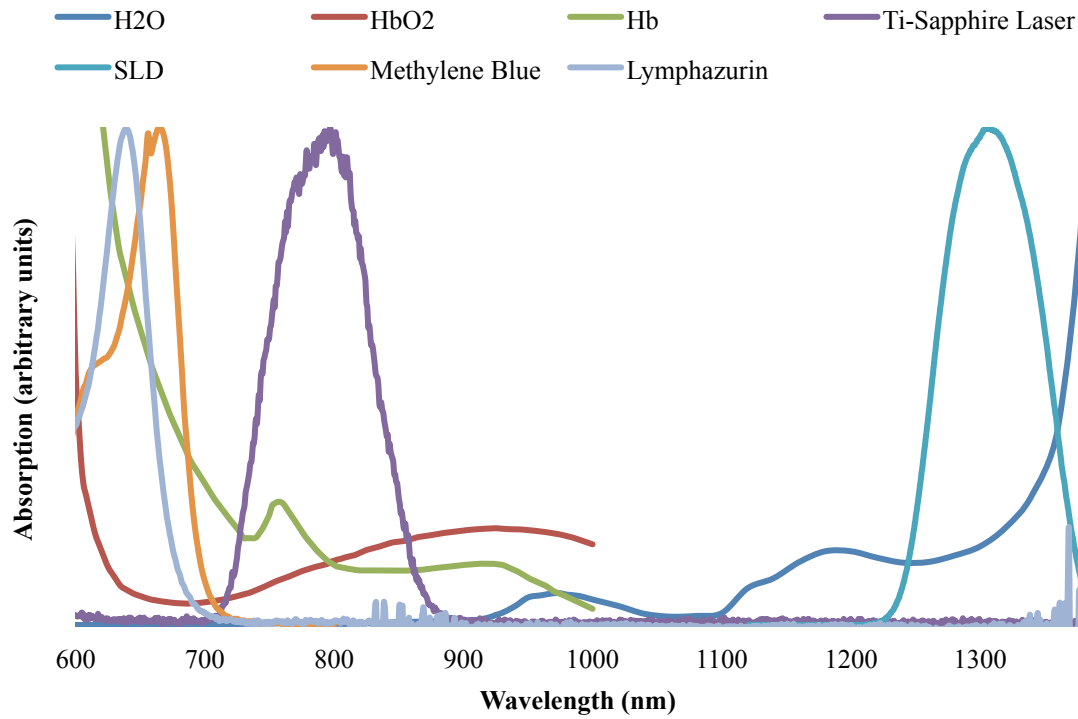


Figure 2.5: Absorption spectra from water (H₂O) [29], oxyhemoglobin (HbO₂) [30], hemoglobin (Hb) [30], Ti:Sapphire Laser (800 nm lab bench-based OCT systems), SLD (1300 nm portable clinical OCT system), Methylene Blue [31], and Lymphazurin.

Recent advances in OCT technology have increased data acquisition speeds to 200,000 axial scans per second or greater [32]. This could permit acquisition of 400 frames per second for a scan range of 10 mm and a lateral resolution of 35 μm . For a 1 cm^2 area, imaging could be achieved in a few seconds while maintaining the full lateral resolution in both x and y directions. Novel computational algorithms such as Interferometric Synthetic Aperture Microscopy (ISAM) are being implemented for real-time OCT imaging, yielding spatially-invariant lateral resolution equivalent to that achieved at the focus of the beam [33]. These combined advances offer the potential to vastly increase data acquisition rates and resolution without sacrificing the large scan area and real-time capabilities of OCT. The significant increase in data volume and limited time to analyze and interpret image sets will increase the need for automated classification algorithms [34, 35].

The differentiation of malignant (carcinoma) from benign (fibroadenoma) tumors is an ongoing research effort, as with many other biomedical imaging techniques. Stromal tissue, which makes up a larger percentage of breast tissue in younger patients, is primarily composed of connective tissue and favorably, is generally less scattering compared to tumor tissue [36]. Studies have shown that the optical refractive index does not differ greatly between stromal and tumor tissue [37]. Preliminary results from our laboratory have identified a promising combined method for distinguishing between the two tissue types by examining the power attenuation in the signal, the periodicity of the scattering profile, and the extracted refractive index information to aid in automated classification of OCT signals [35, 37, 38]. Differentiation between benign fibrocystic changes versus malignant lesions will be important in further clinical studies. Cysts are expected to be readily distinguished due to their relatively large size, thin membranes, and low amount of scatterers within the cyst. Early morphological

changes such as ductal hyperplasia or dysplasia, characterized by increased cell density and nuclear-to-cytoplasm ratio, are likely to exhibit increased scattering. Ongoing work to improve resolution and to extract distinct image features may be necessary for distinguishing these early changes.

2.8 Conclusions

This study demonstrates the potential of real-time intraoperative OCT for margin assessment from resected breast lumpectomy specimens. OCT acquires images in the same physical range as that used in histological analysis to classify surgical margins as positive, close (< 2mm), or negative. The development of faster scanning handheld probes for OCT will allow surgeons to rapidly scan the *in situ* tumor cavity wall in addition to the lumpectomy specimen margin, providing surgeons guidance on tissue removal. *In situ* OCT imaging would effectively double the sampling depth by evaluating depths up to 2 mm on the specimen and on the cavity wall. Further studies with even higher resolution, comprehensive volumetric imaging, and automated tissue type classification are expected to reveal additional unique features that can be used to further improve the identification of positive and negative margins intraoperatively with OCT. Intraoperative identification of positive margins will decrease the need for additional surgical procedures and potentially the rate of local recurrence in breast cancer patients.

2.9 References

1. Taghian A, Mohiuddin M, Jagsi R, Goldberg S, Ceilley E, Powell S. Current perceptions regarding surgical margin status after breast-conserving therapy: Results of a survey. *Ann Surg*, 2005. 241 (4): p. 629-39.
2. Dillon MF, Hill AD, Quinn CM, Mcdermott EW, O'higgins N. A pathologic assessment of adequate margin status in breast-conserving therapy. *Ann Surg Oncol*, 2006. 13 (3): p. 333-9.
3. Luini A, Rososchansky J, Gatti G, Zurrada S, Caldarella P, Viale G, Rosali Dos Santos G, Frasson A. The surgical margin status after breast-conserving surgery: Discussion of an open issue. *Breast Cancer Res Treat*, 2009. 113 (2): p. 397-402.
4. Aziz D, Rawlinson E, Narod SA, Sun P, Lickley HL, Mccready DR, Holloway CM. The role of reexcision for positive margins in optimizing local disease control after breast-conserving surgery for cancer. *Breast J*, 2006. 12 (4): p. 331-7.
5. Cefaro GA, Genovesi D, Marchese R, Ursini LA, Cianchetti E, Ballone E, Di Nicola M. Predictors of local recurrence after conservative surgery and whole-breast irradiation. *Breast Cancer Res Treat*, 2006. 98 (3): p. 329-35.
6. Cellini C, Hollenbeck ST, Christos P, Martins D, Carson J, Kemper S, Lavigne E, Chan E, Simmons R. Factors associated with residual breast cancer after re-excision for close or positive margins. *Ann Surg Oncol*, 2004. 11 (10): p. 915-20.
7. Connolly JL, Boyages J, Nixon AJ, Peiro G, Gage I, Silver B, Recht A, Harris JR, Schnitt SJ. Predictors of breast recurrence after conservative surgery and radiation therapy for invasive breast cancer. *Mod Pathol*, 1998. 11 (2): p. 134-9.

8. Dillon MF, Mc Dermott EW, O'doherty A, Quinn CM, Hill AD, O'higgins N. Factors affecting successful breast conservation for ductal carcinoma *in situ*. *Ann Surg Oncol*, 2007. 14 (5): p. 1618-28.
9. Huston TL, Pigalarga R, Osborne MP, Tousimis E. The influence of additional surgical margins on the total specimen volume excised and the reoperative rate after breast-conserving surgery. *Am J Surg*, 2006. 192 (4): p. 509-12.
10. McIntosh A, Freedman G, Eisenberg D, Anderson P. Recurrence rates and analysis of close or positive margins in patients treated without re-excision before radiation for breast cancer. *Am J Clin Oncol*, 2007. 30 (2): p. 146-51.
11. Schouten Van Der Velden AP, Van De Vrande SL, Boetes C, Bult P, Wobbes T. Residual disease after re-excision for tumour-positive surgical margins in both ductal carcinoma *in situ* and invasive carcinoma of the breast: The effect of time. *J Surg Oncol*, 2007. 96 (7): p. 569-74.
12. Scopa CD, Aroukatos P, Tsamandas AC, Aletra C. Evaluation of margin status in lumpectomy specimens and residual breast carcinoma. *Breast J*, 2006. 12 (2): p. 150-3.
13. Smitt MC, Nowels KW, Zdeblick MJ, Jeffrey S, Carlson RW, Stockdale FE, Goffinet DR. The importance of the lumpectomy surgical margin status in long-term results of breast conservation. *Cancer*, 1995. 76 (2): p. 259-67.
14. Swanson GP, Ryneerson K, Symmonds R. Significance of margins of excision on breast cancer recurrence. *Am J Clin Oncol*, 2002. 25 (5): p. 438-41.
15. Zavagno G, Goldin E, Mencarelli R, Capitanio G, Del Bianco P, Marconato R, Mocellin S, Marconato G, Belardinelli V, Marcon F, Nitti D. Role of resection

- margins in patients treated with breast conservation surgery. *Cancer*, 2008. 112 (9): p. 1923-31.
16. Cefaro GA, Genovesi D, Marchese R, Di Tommaso M, Di Febo F, Ballone E, Di Nicola M. The effect of delaying adjuvant radiation treatment after conservative surgery for early breast cancer. *Breast J*, 2007. 13 (6): p. 575-80.
 17. Van Der Velden AP, Peeters PH, Koot VC, Hennipman A. Local recurrences after conservative treatment of ductal carcinoma-*in-situ* of the breast without radiotherapy: The effect of age. *Ann Surg Oncol*, 2006.
 18. Olson TP, Harter J, Munoz A, Mahvi DM, Breslin T. Frozen section analysis for intraoperative margin assessment during breast-conserving surgery results in low rates of re-excision and local recurrence. *Ann Surg Oncol*, 2007. 14 (10): p. 2953-60.
 19. Mclaughlin SA, Ochoa-Frongia LM, Patil SM, Cody HS, 3rd, Sclafani LM. Influence of frozen-section analysis of sentinel lymph node and lumpectomy margin status on reoperation rates in patients undergoing breast-conservation therapy. *J Am Coll Surg*, 2008. 206 (1): p. 76-82.
 20. Valdes EK, Boolbol SK, Cohen JM, Feldman SM. Intra-operative touch preparation cytology; does it have a role in re-excision lumpectomy? *Ann Surg Oncol*, 2007. 14 (3): p. 1045-50.
 21. Goldfeder S, Davis D, Cullinan J. Breast specimen radiography: Can it predict margin status of excised breast carcinoma? *Academic Radiology*, 2006. 13 (12): p. 1453-9.
 22. Erguvan-Dogan B, Whitman GJ, Nguyen VA, Dryden MJ, Stafford RJ, Hazle J, McAlee KR, Phelps MJ, Ice MF, Kuerer HM, Middleton LP. Specimen radiography in

- confirmation of mri-guided needle localization and surgical excision of breast lesions. *AJR Am J Roentgenol*, 2006. 187 (2): p. 339-44.
23. Karni T, Pappo I, Sandbank J, Lavon O, Kent V, Spector R, Morgenstern S, Lelcuk S. A device for real-time, intraoperative margin assessment in breast-conservation surgery. *Am J Surg*, 2007. 194 (4): p. 467-73.
 24. Haka AS, Volynskaya Z, Gardecki JA, Nazemi J, Lyons J, Hicks D, Fitzmaurice M, Dasari RR, Crowe JP, Feld MS. *In vivo* margin assessment during partial mastectomy breast surgery using raman spectroscopy. *Cancer Res*, 2006. 66 (6): p. 3317-22.
 25. Nguyen FT, Zysk AM, Kotynek JG, Bellafiore FJ, Rowland KM, Johnson PA, Chaney EJ, Boppart SA. Portable real-time optical coherence tomography system for intraoperative imaging and staging of breast cancer. in *SPIE - Photonics West BiOS - Advanced Biomedical and Clinical Diagnostic Systems V*. 2007. San Jose, CA.
 26. Arifler D, Guillaud M, Carraro A, Malpica A, Follen M, Richards-Kortum R. Light scattering from normal and dysplastic cervical cells at different epithelial depths: Finite-difference time-domain modeling with a perfectly matched layer boundary condition. *J Biomed Opt*, 2003. 8 (3): p. 484-94.
 27. Drezek R, Guillaud M, Collier T, Boiko I, Malpica A, Macaulay C, Follen M, Richards-Kortum R. Light scattering from cervical cells throughout neoplastic progression: Influence of nuclear morphology, DNA content, and chromatin texture. *J Biomed Opt*, 2003. 8 (1): p. 7-16.
 28. Bouma BE, Tearney GJ, Yabushita H, Shishkov M, Kauffman CR, DeJoseph Gauthier D, Macneill BD, Houser SL, Aretz HT, Halpern EF, Jang IK. Evaluation of

- intracoronary stenting by intravascular optical coherence tomography. *Heart*, 2003. 89 (3): p. 317-20.
29. Hale GM, Querry MR. Optical constants of water in the 200-nm to 200-microm wavelength region. *Appl Opt*, 1973. 12 (3): p. 555-63.
 30. Prahl S, Gratzner WB, Kollias N (1998). Tabulated molar extinction coefficient for hemoglobin in water. Retrieved from <http://omlc.org/spectra/hemoglobin/summary.html>.
 31. Prahl S (1998). Tabulated molar extinction coefficient for methylene blue in water. Retrieved from <http://omlc.org/spectra/mb/mb-water.html>.
 32. Huber R, Adler DC, Fujimoto JG. Buffered fourier domain mode locking: Unidirectional swept laser sources for optical coherence tomography imaging at 370,000 lines/s. *Opt Lett*, 2006. 31 (20): p. 2975-7.
 33. Ralston TS, Marks DL, Scott Carney PS, Boppart SA. Interferometric synthetic aperture microscopy. *Nat Phys*, 2007. 3 (2): p. 129-134.
 34. Goldberg BD, Iftimia NV, Bressner JE, Pitman MB, Halpern E, Bouma BE, Tearney GJ. Automated algorithm for differentiation of human breast tissue using low coherence interferometry for fine needle aspiration biopsy guidance. *J Biomed Opt*, 2008. 13 (1): p. 014014.
 35. Zysk AM, Boppart SA. Computational methods for analysis of human breast tumor tissue in optical coherence tomography images. *J Biomed Opt*, 2006. 11 (5): p. 054015.
 36. Abramson RG, Mavi A, Cermik T, Basu S, Wehrli NE, Houseni M, Mishra S, Udupa J, Lakhani P, Maidment AD, Torigian DA, Alavi A. Age-related structural and

functional changes in the breast: Multimodality correlation with digital mammography, computed tomography, magnetic resonance imaging, and positron emission tomography. *Semin Nucl Med*, 2007. 37 (3): p. 146-53.

37. Zysk AM, Chaney EJ, Boppart SA. Refractive index of carcinogen-induced rat mammary tumours. *Phys Med Biol*, 2006. 51 (9): p. 2165-77.

38. Zysk AM, Adie SG, Armstrong JJ, Leigh MS, Paduch A, Sampson DD, Nguyen FT, Boppart SA. Needle-based refractive index measurement using low-coherence interferometry. *Opt Lett*, 2007. 32 (4): p. 385-7.

CHAPTER 3

OPTICAL COHERENCE TOMOGRAPHY IN LYMPH NODE ASSESSMENT

3.1 Introduction

3.1.1 Clinical Importance of Lymph Node Assessment

Lymph nodes serve as the primary site for filtering, sequestering, and degrading foreign particles that travel through the lymphatic system. Lymph nodes are typically classified as normal, reactive, or metastatic. A reactive node and a metastatic node are both relatively enlarged in size as lymphocytes and macrophages are recruited to the node in response to the presence of foreign particles or abnormal cells. However, in a metastatic node, there is an increased presence and involvement of cancer cells in addition to the inflammatory response. When the lymphatic system becomes impaired due to the disruption of the lymphatic network, lymphatic obstruction develops, leading to the accumulation of lymph fluid or lymphedema. Currently, nearly 20% of the patients that undergo axillary lymph node dissection (ALND) suffer from these types of edema [1, 2]. In addition, a recent study reported that the presence of micrometastases in the axillary lymph nodes contributed to a decrease in the five-year survival rates for women with early breast cancer [3].

3.1.2 Mapping of Lymph Nodes

In lymph node mapping, a radioactive tracer (technetium-99) and/or a dye (methylene blue) is injected near the site of the primary tumor prior to the surgery. The tracer and/or dye are allowed to circulate for several hours, after which the sentinel node(s) are located and resected during the lumpectomy or mastectomy procedure [4]. Other lymphatic mapping methods include standard X-ray and computed tomography (CT) in conjunction with contrast

agents, or fluorescence techniques using near-infrared (NIR) quantum dots [5, 6] or indocyanine green (ICG) dye [7], which provide better localization of the lymph node. Lymph nodes are typically only removed in order to stage disease progression using histopathological analysis. A positive sentinel node status will prompt surgeons to consider patients for axillary lymph node dissections, further node sampling via biopsies, or whole-body imaging to determine the extent of the metastatic spread of cancer.

3.1.3 Current and Experimental Nodal Assessment Techniques

The current standard of care for lymph node assessment is paraffin section histopathological analysis. No real-time intraoperative microscopic technique is currently being widely used for the assessment of lymph nodes. The use of frozen section histopathology of lymph nodes is also an accepted nodal assessment method, but often takes 20-30 minutes to perform, lengthening the time the patient is under general anesthesia [8, 9]. Several other intraoperative techniques are currently under investigation including touch imprint cytology [10, 11], molecular marker assays [12], frozen section analysis [8, 9], and Fourier transform infrared micro-spectroscopy [13]. All of these techniques require the physical sectioning of the lymph node, leading to the physical destruction of the nodal structural integrity and cellular architecture in order to perform the molecular assay, staining, or probing protocols. The use of wide-field NIR fluorescence imaging has also been developed to better visualize the dynamics of the lymphatic system [14, 15]. Preliminary studies using a laboratory based OCT system centered at 800 nm on lymph nodes resected from a rat animal model and from a human head and neck lymph node demonstrated the ability for OCT to image the capsule and sub-capsular features of the lymph nodes [16].

3.2 Portable Clinical Spectral-Domain Optical Coherence Tomography System

A clinical spectral-domain OCT (SD-OCT) system [31], previously described in Chapters 1 and 2, was used to assess sentinel lymph nodes for this feasibility imaging study. The OCT system uses an SLD centered at 1310 nm with a bandwidth of 92 nm. The system has a transverse resolution of 35.0 μm with a confocal parameter of 1.47 mm. The broad bandwidth of the optical light source resulted in an axial resolution of 8.2 μm in air or 5.9 μm in tissue. The penetration depth of OCT imaging in human axillary lymph nodes was 1-2 mm. A commercial OCT system (Biotigen, Inc., Research Triangle Park, NC) with similar instrument specifications and performance parameters as the custom built system described previously was also used for this study. Both systems used light sources centered at 1310 nm with a bandwidth of 90-100 nm, used the same detection system, and had similar optical elements in the sample arm yielding comparable axial and transverse resolutions. The main difference between the two systems was the beam scanning mechanism, which enabled the custom-built system to scan over longer lateral distances (10 mm) to produce two-dimensional images, while the commercial system was able to scan over a 5x5 mm region to produce three-dimensional volumetric images. The acquisition times were \sim 25 seconds for a single two-dimensional image (10 mm) for the custom-built system and \sim 25 seconds for a full three-dimensional volumetric block of images (5 mm x 5 mm) for the commercial OCT system.

3.3 Clinical Study

The patients identified and recruited for this study had primary breast tumors (invasive and/or *in situ* carcinoma) in need of surgical resection, and/or in need of sentinel lymph node dissection, as determined by their physicians at Carle Foundation Hospital and Carle Clinic Association, Urbana, Illinois, based on previous radiological films, biopsy results, and other relevant diagnostic information. Patients were consented prior to each surgery based on the approved protocols from the institutional review boards (IRB) at the University of Illinois at Urbana-Champaign and Carle Foundation Hospital. After resection of the sentinel and/or axillary lymph node(s) by the surgeon, and prior to microscopic assessment by the pathologist, the lymph node was imaged in the operating room using the clinical OCT system. Of the lymph nodes resected during each procedure, one sentinel lymph node, as determined by the surgeon, was imaged per patient for this feasibility study. In cases with multiple sentinel lymph nodes, only the first resected sentinel node was chosen and imaged. No additional nodes were imaged, due to time constraints, and no other criteria were used in determining which lymph node would be imaged. In cases where the sentinel lymph node could not be clearly distinguished from other resected lymph nodes, the first axillary lymph node excised was imaged. The intact outer capsule of the sentinel lymph node was exposed for imaging without affecting the structural integrity of the tissue specimen. The OCT beam was laterally scanned across the node over a 10 mm distance to produce a two-dimensional cross-sectional OCT image. Subsequently, multiple parallel OCT images (spaced 1 mm apart) were acquired orthogonal to the long axis of the node. In cases where the commercial OCT system was used, 5x5 mm blocks of images were acquired covering the entire node. Upon completion of the imaging session, the sentinel node was returned to the surgical staff for

standard specimen processing, and transported to the pathology department for sectioning, staining, and histopathological analysis.

3.3.1 Specimen Information

A total of 30 sentinel lymph nodes and an additional 106 axillary lymph nodes were surgically resected from 17 patients as determined by the surgeons as part of the standard of care. A subset (16 sentinel, 1 axillary) of the lymph nodes (1 per patient) chosen, based on the order they were resected, were imaged with OCT intraoperatively. Of all the nodes resected, 11 (8%) were metastatic and even fewer, 2 (1%), were reactive, resulting in 91% of all nodes resected being classified as normal. When considering only the sentinel lymph nodes as labeled by the surgeons, 4/30 (13%) sentinel lymph nodes and 1/30 (3%) were classified as metastatic and reactive, respectively, by histopathological analysis, resulting in 84% of the sentinel nodes being reported as normal.

OCT images of 17 lymph nodes from 17 patients were used to identify unique image features that could potentially be used to classify lymph nodes as normal, reactive, or metastatic. OCT images were acquired from 16 of the 30 sentinel lymph nodes from 16 patients, and 1 axillary lymph node from the 17th patient, where identification of the sentinel node was not possible by the surgeon. Of the 17 nodes imaged with OCT, histopathological analysis classified 3 nodes as metastatic, 1 node as reactive, and the remaining 13 nodes as normal. OCT images from two of the three metastatic nodes were excluded from the study because they could not be adequately interpreted due to poor exposure of the node capsule from the surrounding fatty tissue, which placed the nodal architectural features beyond the imaging depth of OCT. The third metastatic node was imaged using a commercial OCT system.

3.4 OCT Image Processing & Evaluation Protocol

OCT images were standardized by subtracting the background power spectrum from the raw data, resampling the data using the cubic spline interpolation technique, and displaying the images on the same intensity scale to account for day-to-day system variations. The background power spectrum was determined by acquiring an image with the sample arm blocked and recording the power spectrum of the light reflected in the reference arm. This process removes image artifacts that are inherent to the OCT system at the time of imaging. Fifteen patients were enrolled as part of this study to evaluate the potential of OCT imaging for real-time intraoperative assessment of lymph nodes using the custom-built system. An additional two patients were enrolled to evaluate the commercial OCT system and the advantages of three-dimensional volumetric data acquisition. OCT images were evaluated by a single interpreter intraoperatively, allowing for consistent identification of suspicious areas based on the level and distribution of scattering intensity in the outer layers and cortex of the nodes, and the ability to distinguish the boundary between the capsule and cortex of the nodes. Since nodal status is not currently determined intraoperatively by surgeons but rather post-operatively by pathologists, no information about the nodes was transmitted between the surgeons or surgical staff, and the researcher imaging and evaluating the OCT images. Using these image features, a single researcher in a single setting evaluated and classified OCT images into normal and abnormal categories where both metastatic and reactive nodes were considered abnormal nodes.

3.5 Histopathological Image Evaluation Protocol

According to the standard of care, the sentinel lymph node was bisected, paraffin embedded, and sectioned for histopathological analysis in the pathology department. The tissue sections were H&E stained and in some cases also stained immunohistochemically for cytokeratin 7 (CK7) to further confirm the presence of and characterize the cancer cells in the sentinel node originated from the breast. The histology slides were digitized using a light microscope (BH-2, Olympus, Inc., Center Valley, PA) at 4X magnification and autostitched together (Adobe Photoshop CS3) to provide a single montage for viewing and comparison purposes. The H&E stained histology slides were reviewed by board-certified pathologists at Carle Foundation Hospital (Urbana, IL) and classified as normal, reactive, or metastatic. The histopathological processing and analysis were performed as part of the standard of care and reported by the pathology department at Carle Foundation Hospital (Urbana, IL).

3.6 OCT Images of Normal, Reactive, and Metastatic Lymph Nodes

Representative intraoperative images from normal (Figure 3.1 and Figure 3.3), reactive (Figure 3.2), and metastatic (Figure 3.4) axillary lymph nodes are shown. In the normal lymph nodes (Figure 3.1 and Figure 3.3), there is a distinct highly scattering capsule present, in comparison to the lower scattering cortex. The transverse sinuses separating the lymphoid follicles of the lymph node can be observed by OCT in Figure 3.3. The corresponding H&E stained histological slides show normal nodes with expected architecture that are either largely lipid filled (Figure 3.1) or contain more eosinophilic (pink) structures indicative of the presence of intracellular and extracellular proteins (Figure 3.3). The sub-

capsular sinus separates the capsule from the cortex, and is organized into discrete lymphoid nodules with germinal centers observable in normal lymph nodes. The distinct boundary between the capsule and the cortex is no longer visible in reactive (Figure 3.2) and metastatic (Figure 3.4) nodes where the entire node becomes more highly scattering, matching the scattering intensity level from the capsule, forming a single homogeneous scattering layer.

The corresponding H&E histology slides presented in Figure 3.2 and Figure 3.4 have more basophilic structures as exhibited by darker blue staining specific to nucleic acids found in ribosomes, chromatin in the nucleus, and RNA in the cytoplasm. The metastatic lymph node shows a loss of normal tissue architecture as there is an obvious lymphoid depletion characterized by a decrease in the number and size of follicles with some or no germinal centers. At the same time, the decrease of sinus spaces and increased density of cells observed is due to the high level of cancer cell proliferation.

Three-dimensional OCT reconstructions are presented in Figure 3.3 and Figure 3.4, demonstrating the added level of details available through the reconstructions. These renderings identify the same features as those found in the two-dimensional images but further allows for the arbitrary optical sectioning of the tissue along planes that are not necessarily the same as the OCT imaging acquisition planes. These intraoperative findings from human lymph nodes extend our observations from previously reported OCT image data of lymph nodes from a rat mammary model [16]. The normal rat lymph node exhibited a highly scattering layer that correspond to the capsule, compared to the low scattering areas which are more representative of the lymph node cortex [16]. In the same report, OCT images from a necrotic metastatic lymph node exhibited a high level of scattering intensity and capsule disruption.

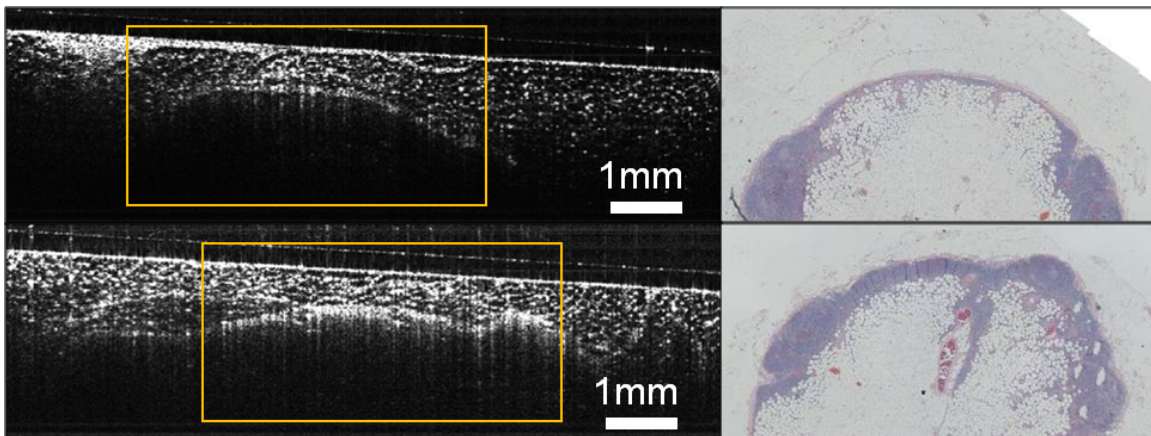


Figure 3.1: Normal Lymph Node. OCT images from a normal sentinel lymph node (left) with corresponding H&E histology (right) demonstrate an intact capsule structure that is easily distinguishable from the cortex of the lymph node. The OCT images are highlighted (orange boxes) with the regions that correlate with the histology images.

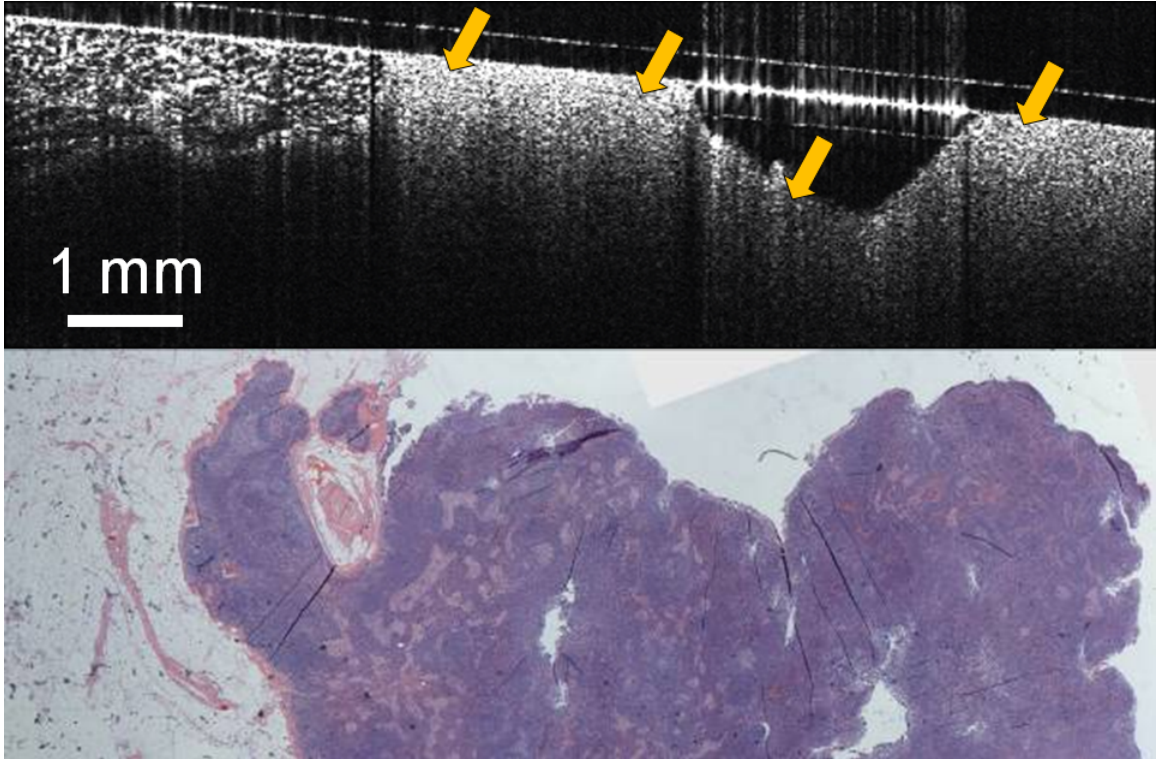


Figure 3.2: Reactive Lymph Node. OCT image from a reactive axillary lymph node (top) with corresponding H&E histology (bottom). In this case, increased cellular density in the cortex, representative of a reactive lymph node, contributed to an increased scattering signal observed under OCT. The change in scattering intensity in the cortex begins to match the scattering intensity of the capsule, decreasing the ability to distinguish the capsule from the cortex under the OCT images (arrows).

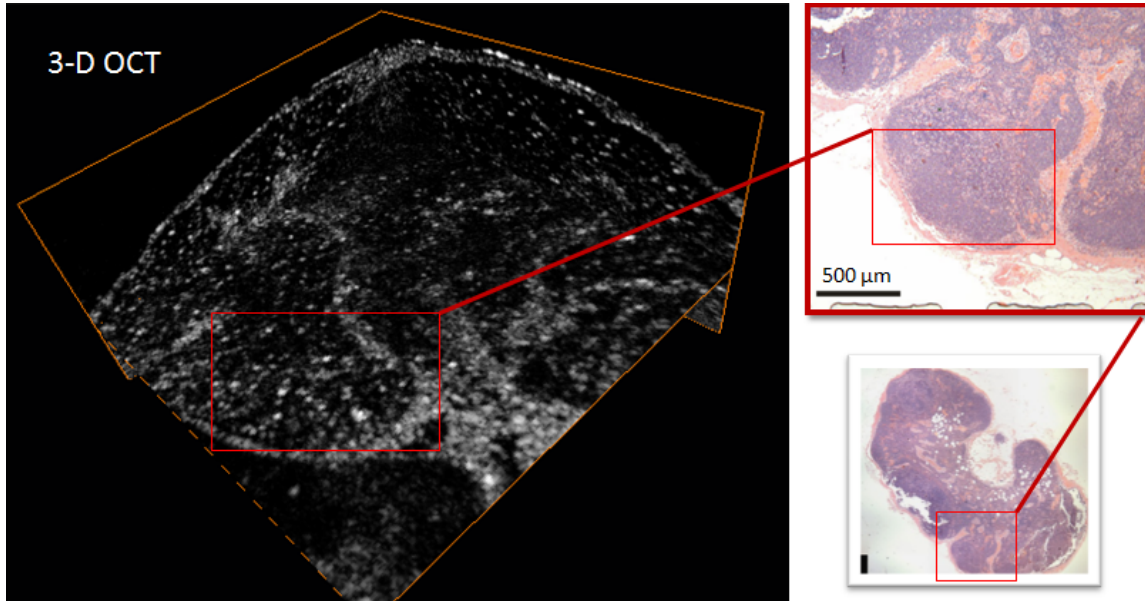


Figure 3.3: Three-dimensional rendering of a normal lymph node. OCT image volume acquired from a normal sentinel lymph node (left) is shown with the corresponding H&E histology (right). The normal lymph node presents a clear capsule that is easily differentiated from the low-scattering cortex. The OCT images correlate to regions in the histology sections that are highlighted by red boxes. The OCT image block measures 5 x 5 x 1.7 mm.

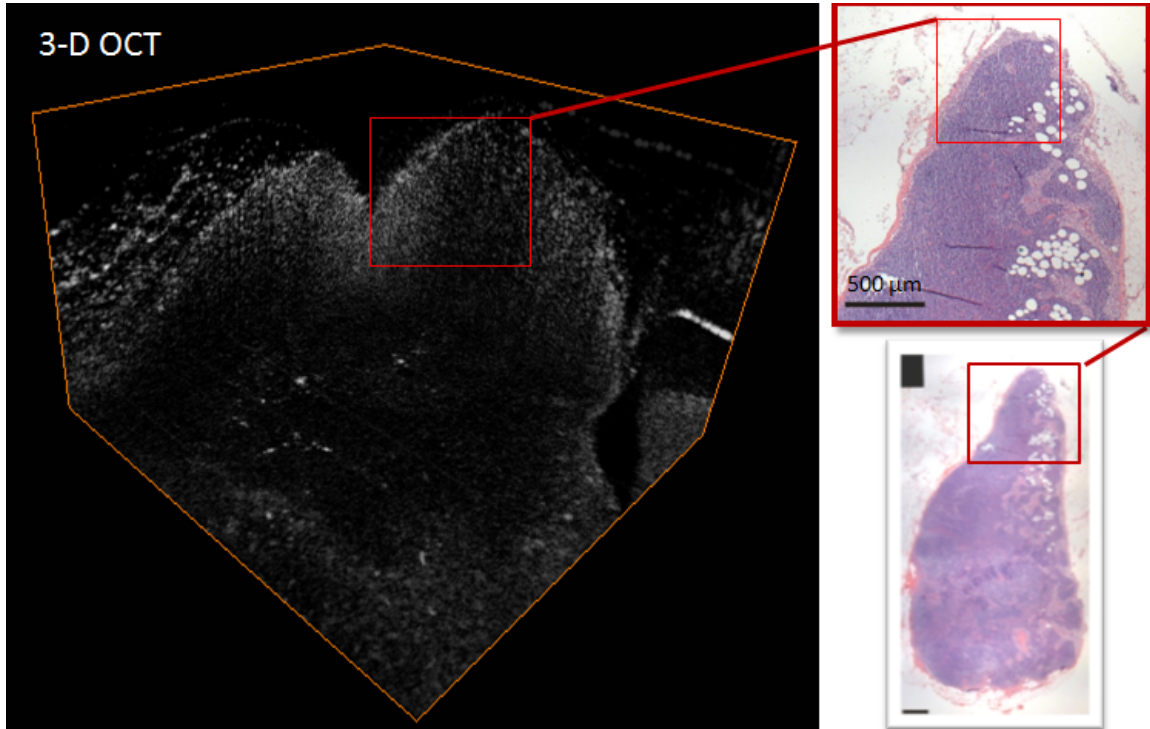


Figure 3.4: Three-dimensional rendering of a metastatic lymph node. OCT image volume acquired from a metastatic axillary lymph node (left) in a single session is shown with the corresponding H&E histology (right). As with reactive lymph nodes, increased scattering from the node is observed in the OCT data, and the ability to differentiate distinct boundaries between the node capsule and cortex has been lost. The OCT images correlate to regions in the histology sections that are highlighted by red boxes. The OCT image block measures 5 x 5 x 1.7 mm.

The relatively high percentage of normal nodes resected during lymph node dissection procedures, as was evidenced in the patients enrolled in this study, points to the significant need for a real-time intraoperative microscopic nodal assessment technology. OCT has the potential to fill this crucial role by providing real-time intraoperative information through the identification of unique architectural features observed in the capsule and outer cortex of the lymph node. These features correspond to known morphological changes in reactive and metastatic lymph nodes, and all are accessible within the penetration depth of OCT.

3.6.1 Identification of Normal Nodes from Reactive and Metastatic Lymph Nodes

When cancer cells metastasize through the lymphatic system, the nodes serve as the primary line of defense to sequester the cancer cells and initiate a tumor-specific immunological response. This process will initially cause an enlargement of the lymph node as part of the reactive inflammatory response, but this enlargement can also be attributed to the replication of cancer cells in the nodes. The presence of inflammation in the node, however, does not sufficiently indicate the presence of cancer cells. Hypercellularity of the lymph node, either due to the inflammatory response or the replication and expansion of cancer cells, not only increases the relative size of the node but also increases the cellular density within the node. These changes typically correspond to an increase in scattering observed in OCT, and match the scattering levels observed in the capsule. As the scattering intensity in the capsule and cortex areas become similar, the differentiation of the capsule from the cortex becomes less distinct. Increased changes in scattering observed in the cortex of reactive and metastatic nodes are more likely due to increased cellular density, but could also be attributed to an increased number of cancer cells which have a higher N/C ratio. These

changes are more predominant in the cortex region where the germinal centers and follicles, the primary sites of lymphocyte recruitment and aggregation, are located.

3.6.2 Potential Clinical Impact

A large majority of the lymph nodes resected for breast cancer staging are negative normal lymph nodes. In addition, the major purpose for resecting the lymph nodes has been largely for the staging of the disease and not the management or treatment of the disease. In addition, the primary surgical risk factors for lymphedema are nodal dissection of the axillary lymph nodes, as well as associated scarring from surgical intervention. Therefore, reducing the number or eliminating the need to resect normal nodes during surgery may not only reduce the number of lymph nodes resected, but also decrease the risk of developing lymphedema. With a 1-2 mm imaging penetration depth, OCT is a suitable modality for visualizing the microscopic lymph node architecture, including the capsule and the outer cortex containing the follicles and germinal centers. In normal nodes, OCT is capable of clearly defining the boundary between the capsule and the cortex based on scattering intensities; this boundary is lost in abnormal lymph nodes. While there is currently no suitable real-time intraoperative method to assess the lymph node prior to its surgical resection, OCT would fill this niche by providing high-resolution microscopic images in real time. Histopathological analysis from paraffin sections, the current standard of care, is unable to provide surgeons with real-time information on the nodal status that could be used to guide the surgical resection of lymph nodes. OCT is capable of providing this information intraoperatively in real time, with the potential for *in vivo* or *in situ* imaging, thereby potentially eliminating the need for further lymph node resections and reducing the number of resulting complications.

3.7 Conclusions

The intraoperative OCT imaging data from the lymph nodes in this feasibility study demonstrate promising results. Distinct morphological differences were observed in OCT images between defined classifications of lymph nodes, and they correlated strongly with corresponding histopathological findings within the penetration depth of the OCT imaging system. These initial studies demonstrate that the relevant diagnostic information needed to classify lymph nodes is accessible by OCT from outside the lymph node capsule, leaving the lymph node structurally intact. Trans-capsule imaging by OCT, along with the implementation of a fast scanning handheld probe [17], will allow rapid *in situ* imaging of lymph nodes. Needle-based OCT imaging probes would allow further minimally-invasive probing of nodes that are not fully exposed or easily accessible, particularly for transcutaneous needle-biopsy procedures of lymph nodes [18-20].

Future *in vivo* studies will further determine the clinical impact of OCT on reducing the number of normal lymph nodes removed and the subsequent rate of morbid complications associated with lymph node dissections and breast cancer surgeries. The implementation of recent technological advances to further increase the resolution of OCT [21] and data acquisition speed [22], and to computationally classify tissue types [18, 23], will improve the usability and effectiveness of OCT in the intraoperative assessment of lymph nodes by enhancing the capability to examine the underlying lymph node micro-architecture, by rendering three-dimensional OCT data sets for multi-sectional assessment, and by rapidly classifying features and tissue types using computer-aided detection.

3.8 References

1. Bumpers HL, Best IM, Norman D, Weaver WL. Debilitating lymphedema of the upper extremity after treatment of breast cancer. *Am J Clin Oncol*, 2002. 25 (4): p. 365-7.
2. Langer I, Guller U, Berclaz G, Koechli OR, Schaer G, Fehr MK, Hess T, Oertli D, Bronz L, Schnarwyler B, Wight E, Uehlinger U, Infanger E, Burger D, Zuber M. Morbidity of sentinel lymph node biopsy (sln) alone versus sln and completion axillary lymph node dissection after breast cancer surgery: A prospective swiss multicenter study on 659 patients. *Ann Surg*, 2007. 245 (3): p. 452-61.
3. De Boer M, Van Deurzen CH, Van Dijck JA, Borm GF, Van Diest PJ, Adang EM, Nortier JW, Rutgers EJ, Seynaeve C, Menke-Pluymers MB, Bult P, Tjan-Heijnen VC. Micrometastases or isolated tumor cells and the outcome of breast cancer. *N Engl J Med*, 2009. 361 (7): p. 653-63.
4. Krag D, Weaver D, Ashikaga T, Moffat F, Klimberg VS, Shriver C, Feldman S, Kusminsky R, Gadd M, Kuhn J, Harlow S, Beitsch P. The sentinel node in breast cancer--a multicenter validation study. *N Engl J Med*, 1998. 339 (14): p. 941-6.
5. Frangioni JV, Kim SW, Ohnishi S, Kim S, Bawendi MG. Sentinel lymph node mapping with type-ii quantum dots. *Methods Mol Biol*, 2007. 374: p. 147-59.
6. Kim S, Lim YT, Soltesz EG, De Grand AM, Lee J, Nakayama A, Parker JA, Mihaljevic T, Laurence RG, Dor DM, Cohn LH, Bawendi MG, Frangioni JV. Near-infrared fluorescent type ii quantum dots for sentinel lymph node mapping. *Nat Biotechnol*, 2004. 22 (1): p. 93-7.

7. Nimura H, Narimiya N, Mitsumori N, Yamazaki Y, Yanaga K, Urashima M. Infrared ray electronic endoscopy combined with indocyanine green injection for detection of sentinel nodes of patients with gastric cancer. *Br J Surg*, 2004. 91 (5): p. 575-9.
8. Ali R, Hanly AM, Naughton P, Castineira CF, Landers R, Cahill RA, Watson RG. Intraoperative frozen section assessment of sentinel lymph nodes in the operative management of women with symptomatic breast cancer. *World J Surg Oncol*, 2008. 6: p. 69.
9. Mclaughlin SA, Ochoa-Frongia LM, Patil SM, Cody HS, 3rd, Sciafani LM. Influence of frozen-section analysis of sentinel lymph node and lumpectomy margin status on reoperation rates in patients undergoing breast-conservation therapy. *J Am Coll Surg*, 2008. 206 (1): p. 76-82.
10. Creager AJ, Geisinger KR, Shiver SA, Perrier ND, Shen P, Ann Shaw J, Young PR, Levine EA. Intraoperative evaluation of sentinel lymph nodes for metastatic breast carcinoma by imprint cytology. *Mod Pathol*, 2002. 15 (11): p. 1140-7.
11. Motomura K, Nagumo S, Komoike Y, Koyama H, Inaji H. Accuracy of imprint cytology for intraoperative diagnosis of sentinel node metastases in breast cancer. *Ann Surg*, 2008. 247 (5): p. 839-42.
12. Julian TB, Blumencranz P, Deck K, Whitworth P, Berry DA, Berry SM, Rosenberg A, Chagpar AB, Reintgen D, Beitsch P, Simmons R, Saha S, Mamounas EP, Giuliano A. Novel intraoperative molecular test for sentinel lymph node metastases in patients with early-stage breast cancer. *J Clin Oncol*, 2008. 26 (20): p. 3338-45.

13. Bird B, Miljkovic M, Romeo MJ, Smith J, Stone N, George MW, Diem M. Infrared micro-spectral imaging: Distinction of tissue types in axillary lymph node histology. *BMC Clin Pathol*, 2008. 8: p. 8.
14. Sevick-Muraca EM, Sharma R, Rasmussen JC, Marshall MV, Wendt JA, Pham HQ, Bonefas E, Houston JP, Sampath L, Adams KE, Blanchard DK, Fisher RE, Chiang SB, Elledge R, Mawad ME. Imaging of lymph flow in breast cancer patients after microdose administration of a near-infrared fluorophore: Feasibility study. *Radiology*, 2008. 246 (3): p. 734-41.
15. Sharma R, Wendt JA, Rasmussen JC, Adams KE, Marshall MV, Sevick-Muraca EM. New horizons for imaging lymphatic function. *Ann N Y Acad Sci*, 2008. 1131: p. 13-36.
16. Luo W, Nguyen FT, Zysk AM, Ralston TLS, Brockenbrough J, Marks DL, Oldenburg AL, Boppart SA. Optical biopsy of lymph node morphology using optical coherence tomography. *Technology in Cancer Research & Treatment*, 2005. 4 (5): p. 539-547.
17. Liu X, Cobb MJ, Chen Y, Kimmey MB, Li X. Rapid-scanning forward-imaging miniature endoscope for real-time optical coherence tomography. *Opt Lett*, 2004. 29 (15): p. 1763-5.
18. Goldberg BD, Iftimia NV, Bressner JE, Pitman MB, Halpern E, Bouma BE, Tearney GJ. Automated algorithm for differentiation of human breast tissue using low coherence interferometry for fine needle aspiration biopsy guidance. *J Biomed Opt*, 2008. 13 (1): p. 014014.

19. Zysk AM, Adie SG, Armstrong JJ, Leigh MS, Paduch A, Sampson DD, Nguyen FT, Boppart SA. Needle-based refractive index measurement using low-coherence interferometry. *Opt Lett*, 2007. 32 (4): p. 385-7.
20. Zysk AM, Chaney EJ, Boppart SA. Refractive index of carcinogen-induced rat mammary tumours. *Phys Med Biol*, 2006. 51 (9): p. 2165-77.
21. Zawadzki RJ, Cense B, Zhang Y, Choi SS, Miller DT, Werner JS. Ultrahigh-resolution optical coherence tomography with monochromatic and chromatic aberration correction. *Opt Express*, 2008. 16 (11): p. 8126-43.
22. Huber R, Adler DC, Srinivasan VJ, Fujimoto JG. Fourier domain mode locking at 1050 nm for ultra-high-speed optical coherence tomography of the human retina at 236,000 axial scans per second. *Opt Lett*, 2007. 32 (14): p. 2049-51.
23. Zysk AM, Boppart SA. Computational methods for analysis of human breast tumor tissue in optical coherence tomography images. *J Biomed Opt*, 2006. 11 (5): p. 054015.

CHAPTER 4

PROTEIN MICROSPHERES

4.1 Introduction

Optical coherence tomography has been shown to have great potential as an optical imaging technique for assessing cancer [1-5]. It has also been well studied for cardiovascular applications and is currently being widely used as part of a standard of care in the field of ophthalmology [6]. OCT provides micron-scale resolution images at depths of 1-3 mm beneath the sample surface for highly scattering tissues. However, OCT is largely limited by only providing structural information about the sample. In the detection and diagnosis of diseases, the earlier that disease can be detected, the earlier it can be treated, and the higher the success rate for treatment and recovery. To further increase the utility of OCT in biomedical applications, it would be beneficial to extend or compliment structural OCT with the development of functional modalities of OCT, the development of contrast agents, or integrating OCT as part of a multi-modal imaging system to detect changes in the tissue before morphological changes become readily apparent under structural OCT.

Various functional modalities of OCT have been developed over the last several years including spectroscopic OCT (S-OCT) [7-12], pump-probe OCT [13-16], polarization-sensitive OCT (PS-OCT) [17-28], and magnetomotive OCT (MM-OCT) [29-35] to move OCT into the molecular imaging domain. The utility of these techniques is greatly enhanced when combined with exogenous contrast agents compared to relying only on the tissues' endogenous contrast. In addition, the use of contrast agents can also provide either nonspecific or targeted contrast to the sample. Research in biomedical

imaging is transitioning from the development of individual imaging modalities as the technology matures to more emphasis on the development of complimentary contrast agents or the development of multi-modal imaging systems combining the strengths of multiple techniques.

The utility of OCT can be extended through the addition of targeted contrast agents by visualizing structures or molecular changes not readily visible under structural OCT. Contrast agents have been widely developed to complement the capabilities of imaging modalities by providing nonspecific contrast to images or by providing targeted contrast to better highlight areas of interest. The exogenous contrast can be overlaid on top of the endogenous contrast from OCT and combines the molecular sensitivity of targeted contrast agents with the micron-scale resolution structural imaging of OCT.

In the field of biomedical optics, there is a great need to combine wide field imaging modalities with microscopic imaging modalities. A limitation of optical techniques such as OCT, Raman spectroscopy, fluorescence spectroscopy, or reflectance techniques is the relatively limited field of view. A compromise must be made to balance the advantages of high resolution microscopic imaging made possible by optical imaging methods and the practical need to sample over large fields of view in a clinical setting. This balance is more critical at earlier disease stages when lesions are not physically palpable or visible to the human eye. To overcome this balancing act, different imaging modalities can be combined to better guide microscopic imaging and to increase the overall detection sensitivity and specificity of the disease. In this scenario, the use of multi-modal contrast agents detectable by both wide field (magnetic resonance imaging, ultrasound imaging, or fluorescence imaging) and microscopic imaging modalities (OCT,

MM-OCT, fluorescence microscopy) are highly beneficial for targeted localization of sites of interest and allow improved co-registration of the imaging data across imaging modalities.

Contrast agents for OCT can be categorized by various design strategies. The simplest design strategy is to directly increase the backscattering in the tissue by introducing strongly scattering particles. The presence of these particles should change the effective refractive index of the targeted local microenvironment compared to the neighboring non-targeted areas. The inability to differentiate between exogenous scattering of the contrast agents and endogenous scattering of the tissue specimen is a limitation of this method especially in applications where taking an OCT image prior to the introduction of contrast agents may not be possible. This strategy is most advantageous for the non-specific increase in the contrast of low scattering tissues and samples. When using targeted scattering contrast agents, the endogenous contrast should be well characterized to study the increased contrast from the scattering agents.

The ideal strategy for designing a contrast agent begins with a particle that can serve as the construct or vehicle. The particle can then be modified with different nanoparticles that are individually optimized for each imaging modality of interest. This flexible framework for designing a multi-modal contrast agent by incorporating nanoparticles that are specific to each imaging modality is more advantageous than the development of a single nanoparticle that could be detected under multiple imaging modalities. In this thesis, protein microspheres serve as a novel vehicle that couples a diverse array of nanoparticle-based contrast agents for multiple imaging modalities.

Various nanoparticles that provide scattering, fluorescent, and/or magnetic contrast can be encapsulated into the inner core of the microspheres or embedded in the protein shell.

The utility of the microsphere design as an encapsulation vehicle can be extended beyond contrast agents to function as a targeted therapeutic delivery method. The surface of the protein microspheres can be functionalized using a layer-by-layer (LBL) adhesion method described in this chapter and in more detail in Chapter 5. Surface-functionalized microspheres encapsulated with hydrophobic drugs such as paclitaxel could provide a targeted cellular method for killing single cells, by which therapeutic agents could be released into the cell cytoplasm upon cellular uptake of the microsphere. Furthermore, the microspheres could be externally controlled by magnetic fields or ultrasound waves to trigger their potential rupture or controlled release of their contents into the local vasculature or extracellular matrix of the targeted area. Lastly, the surface-functionalized microspheres could be encapsulated with heat-absorbing particles to induce targeted hyperthermia. Through these potential therapeutic strategies, protein microspheres could fill a critical need for the targeted treatment of diseases.

4.2 Protein Microspheres

The modified oil-filled protein microspheres presented in this thesis were initially developed in Prof. Suslick lab at the University of Illinois at Urbana-Champaign [36, 37]. These microspheres are sonochemically synthesized using high-frequency ultrasound. The sonication process creates a fluid mixing state during the emulsification process, forming a protein shell that encapsulates the oil and hydrophobic nanoparticles. Traditionally, these microspheres are-filled with air or perfluorocarbon for use as

ultrasound contrast agents. Replacing the inner core with vegetable oil instead of a gas renders these microspheres much more stable, less likely to rupture, and extending their lifetimes from several days to several months when compared to their gas-filled counterparts [36, 38].

The size of the microspheres can vary from 200 nm to 15 μm in diameter [36]. According to previous reports, the most important factor in determining the size of the microsphere is the surface tension between the oil and protein layers at the time of synthesis [38-40]. The use of surfactants were previously reported to alter the surface tension between these layers and produce microspheres as small as 200-400 nm [38, 39]. In addition to surfactants, the concentration of bovine serum albumin (BSA) used to synthesize the microspheres can be increased to reduce the size of the microspheres [38]. Increasing the concentration of BSA increased the formation of partially cross-linked BSA aggregates in solution. Increasing both the sonication frequency and the acoustic power also had a large effect in increasing the resulting yield of microspheres, but had little impact on the resulting size distribution of the protein microspheres [38].

In previously reported studies, protein microspheres were initially modified to provide added contrast for OCT by incorporating scattering nanoparticles. These earlier experiments demonstrated that the effective refractive index of the protein microspheres can be altered by modifying the inner core or shell with nanoparticles that have refractive indices that are different (e.g. gold, RI = 0.18, or carbon, RI = 3.08) compared to tissue (RI = 1.48) [36, 38]. This differential in refractive index provides an increased backscattering of light from the sample and thus increases the ability to see more structures where the microspheres are located. These same microspheres have been

synthesized to encapsulate the iron oxide in the inner core providing contrast for magnetic resonance imaging (MRI) and magnetomotive optical coherence tomography (MM-OCT) [33, 38-40]. Encapsulation of various dyes, which absorb / emit in the visible and near infrared regions, has also been used for fluorescence applications [38, 39].

The protein microspheres presented in this thesis were designed and optimized primarily to provide enhanced contrast under wide-field fluorescence imaging, magnetic resonance imaging, MM-OCT, and fluorescence microscopy with the goal of *in vivo* targeting of these microspheres to tumors. The protein microspheres encapsulated iron oxide, Nile Red dye, and DiR dye. In designing the protein microspheres as a contrast agent for MM-OCT and OCT, the microspheres were initially tested to ensure that they could provide sufficient added contrast above the endogenous OCT contrast [33]. Although strong scatterers are advantageous for detection by OCT, a sample that is too strongly scattering will severely limit the OCT penetration depth, as was apparent in imaging strongly scattering tissues such as tumors. The design and development of protein microspheres as a contrast agent will be described in greater detail in Chapter 5. This chapter focuses on the synthesis of protein microspheres and encapsulation of contrast particles, the visual characterization of the microspheres through scanning electron microscopy and transmission electron microscopy, and the effects of the encapsulating particles on the size distribution of the protein microspheres.

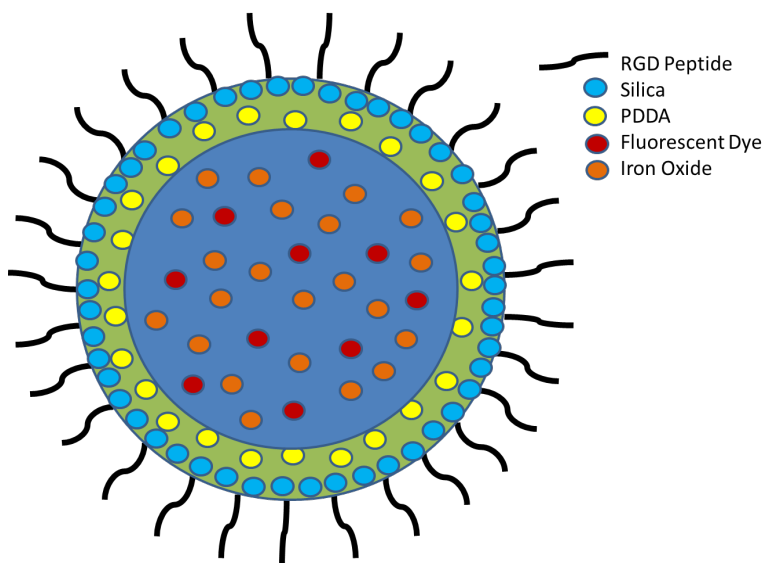


Figure 4.1: Representation of the protein microsphere as a targeted multi-modal contrast agent. The inner oil core (blue) contains the hydrophobic contrast agents such as fluorescent dyes (Nile Red or DiR) and magnetic particles (iron oxide). The boundary between the blue and green layers represents the BSA protein shell. The PDDA (yellow dots) is layered to reverse the surface charge of the microspheres. The silica is layered (blue dots) on top of the PDDA layer. The RGD poly-lysine sequence is layered (black lines) on top of the silica layer with the poly-lysine sequence end adhering to the silica and the exposed RGD sequence end to the surroundings to target the protein microsphere to the integrin receptor.

4.3 Protein Microsphere Synthesis

The structure of the protein microsphere is composed of three main compartments: the inner hydrophobic core, the outer hydrophilic protein shell, and the surface of the shell. Each of these components can incorporate a varying number of particles to provide contrast or add functionality to the protein microspheres. The versatility of the protein microsphere to incorporate a wide variety of dyes, nanoparticles, and ligands makes it an ideal construct for biomedical applications. By being able to combine multiple contrast mechanisms into a single vehicle, the protein microsphere can provide simultaneous contrast under a wide field imaging modality (such as magnetic resonance imaging, ultrasound, or fluorescence imaging) and a microscopic imaging modality (such as optical coherence tomography, or other spectroscopic techniques). Particles that are more hydrophilic or not as easily miscible into the oil can be suspended into the BSA protein layer and become embedded into the protein shell. Lastly, the microspheres can be targeted with ligands on the shell surface using the layer-by-layer adhesion method. In addition to *in vivo* targeting of the microspheres, cellular binding of the microspheres via these ligands can be used to probe cell mechanics and dynamics.

In order to modify the content of the inner oil core, the particles must be miscible in vegetable oil. Typically particles are first suspended in a solvent prior to being placed into the oil suspension. For example, iron oxide and Nile Red are initially dissolved in hexane, while DiR is dissolved in 100% ethanol (200 proof) and bubbled with nitrogen. Similarly, to modify the composition of the outer protein shell, the particles of interest must be hydrophilic and thoroughly suspended into the 5% BSA protein solution. The outer protein shell measures approximately 50 nm in thickness [36], and when compared

to the volume of the inner core, the loading capacity of particles into the shell is relatively much lower than the encapsulated particles in the oil core. Although this has not yet been well studied, it is conceivable that having too many particles incorporated into the protein shell could have several effects on the characteristics and stability of the synthesized microspheres. The type, concentration, and size of particles used, as well as the ability for the BSA protein to form shells and crosslink, could hinder microsphere synthesis by decreasing the overall stability of the protein microspheres. The addition of these particles and/or solvents into either the oil or protein solution could alter the surface tension between the two layers. The change in surface tension could alter the resulting size distribution of the protein microspheres.

The synthesis of protein microspheres depends on three primary concepts: the emulsification process, the aggregation of protein at the oil / water interface, and the chemical crosslinking of protein. In the case of BSA protein, crosslinking occurs via the formation of disulfide bonds through inter-protein cysteine oxidation. The detailed methods for synthesizing protein microspheres with encapsulated iron oxide nanoparticles, Nile Red fluorescent dye, or DiR fluorescent dye in an oil core will be described. For the studies presented in this thesis, the outer protein shell was not altered and only consisted of BSA. Lastly, the microsphere surface was functionalized by adding layers of polydimethyl diallyl chloride (PDDA), followed by silica, and then followed by an Arginine-Glycine-Aspartic Acid peptide sequence attached to a poly-lysine sequence (linear sequence of amino acids, RGDKKKKK) using the layer-by-layer method.

4.3.1 Encapsulation of Particles in the Oil Core of the Protein Microspheres

Many different types of particles have been previously encapsulated into the oil core of protein microspheres. Lee, et. al., were successful at synthesizing scattering microspheres that encapsulated melanin, gold, or carbon [36]. Toublan demonstrated the encapsulation of bodipy dye, Nile Red dye, heptamethylcyanine NIR dye, and iron oxide nanoparticles [38]. The feasibility of incorporating a wide variety of materials into the oil core makes protein microspheres an ideal vehicle that could serve not only as a contrast agent but also as a therapeutic agent. The main challenge for incorporating particles into the inner core of the microspheres is the ability to dissolve them into the vegetable oil.

To synthesize the protein microcapsules, iron oxide (Sigma Aldrich, 544884-25G) was initially dissolved into hexane at a concentration of 250 mg of iron oxide / 2 mL of hexane. The iron oxide must be well dissolved into the hexane prior to mixing with vegetable oil. Additional hexane may be added or the solution may be placed in a sonicator for at least 15 mins to expedite this process. Once well dissolved, the solution was resuspended into the vegetable oil at a concentration of 50 mg of iron oxide to 1 mL of vegetable oil. Studies presented in this thesis will demonstrate that there was an upper limit to the amount of iron oxide that could be encapsulated into the protein microspheres. The solution was sonicated for an additional 30 mins or until it was well dissolved.

The Nile Red dye oil solution was prepared in a similar fashion to the iron oxide oil solution. It was dissolved into hexane at a concentration of 2.5 mg of Nile Red / 1 mL of hexane. After sonication for at least 15 mins, the Nile Red solution was resuspended into the oil solution at a concentration of 0.5 mg of Nile Red to 1 mL of vegetable oil.

The solution was sonicated for an additional 30 mins or until the solution was well dissolved.

The DiR dye (AAT Bioquest, 22070) was dissolved into 100% or 200 proof ethanol at a concentration of 25 mg (1 vial) to 5 mL of ethanol. It is important to note that the DiR solution should not be placed into the sonicator, exposed to heat, or exposed to light. The DiR dye in its pure form is highly sensitive to heat and light and was stored at -80°C in the dark. Once dissolved into 100% ethanol, the DiR solution was immediately mixed into the vegetable oil at a concentration of 5 mg of DiR to 1 mL of vegetable oil. The solution was quickly vortexed to ensure that it was well mixed.

Synthesis of the oil solutions was prepared in amber-colored glass vials to protect the fluorophores from exposure to light. Glass vials were used instead of plastic conical vials because the oil solutions were later placed into a water bath to evaporate the solvents that initially suspended the nanoparticles. Depending on the temperatures used, the plastic conical vials could melt or react with the oil solution itself.

For solutions containing iron oxide and/or Nile Red, the oil solutions were placed in a water bath set to 80-100°C in a chemical fume hood in order to evaporate hexane. For solutions containing DiR dye, the water bath temperature was set at no higher than 55°C in a chemical fume hood in order to evaporate ethanol. The fluorescent properties of DiR can quickly deteriorate at temperatures higher than 55°C, and this was evidenced by a color change from a bright green to a yellow-orange solution. In addition to the requirement for a lower water bath temperature, nitrogen gas must be bubbled through the DiR oil solution during the evaporation of ethanol. This also helped preserve the fluorescent properties of the DiR dye. It takes 1-2 hrs for the hexane to evaporate from

the iron oxide or Nile Red oil stock solutions and 30 mins for the ethanol to evaporate from the DiR oil stock solution. Once the solvents (hexane or ethanol) were evaporated, the oil stock solutions could be kept for extended periods (months) on a rotisserie rotator in the fridge at 0°C. The DiR oil stock solution was kept frozen at -20°C.

4.3.2 Embedding Particles in the Protein Shell of the Microspheres

The protein shell of the microspheres was comprised of bovine serum albumin (BSA). A 5% (by weight) BSA solution was made using BSA (Sigma, A7030-50G) and nanopure water. A pH level of the solution around 7.4 was necessary for successful layer-by-layer adhesion on the microsphere surface. In order to embed particles into the outer protein shell of microspheres, the particles can first be suspended in a solvent or polymer that makes it more miscible into the hydrophilic BSA solution. Toublan, et. al., used this method to embed colloids of gold nanoparticles into the protein shell because encapsulating the gold nanoparticles into the oil core was too challenging [38].

4.3.3 Emulsification of the Protein Microspheres

Once all of the solutions were prepared, 4 mL of the BSA solution was aliquoted into the bottom of the Suslick reaction vessel (Figure 4.2). The Suslick reaction vessel was mounted into the collar around the ultrasonic horn. The tip of the ultrasonic horn was slightly submerged in the BSA layer. One milliliter of any particular oil solution containing the desired particles for encapsulation was added to the reaction vessel through one of the three inlets, forming a continuous layer of oil solution on top of the BSA layer. Deviations from an 80:20 ratio of protein to oil can be used as long as the final level of the oil-protein interface was at the tip of the ultrasonic horn.

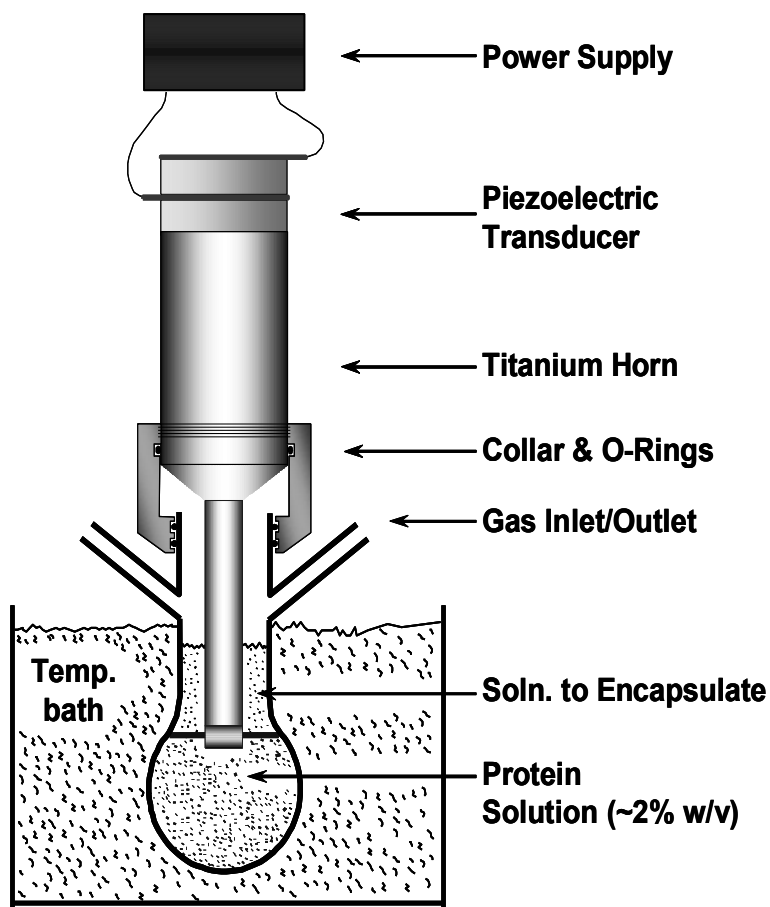


Figure 4.2: Setup for the sonochemical synthesis of microspheres. The Suslick reaction vessel containing an emulsion of the oil layer (top layer) and the protein layer (bottom layer) was mounted into a collar around an ultrasonic titanium horn oriented upright to the reaction vessel. The tip of the ultrasonic horn was optimally placed at the oil-protein interface [38-40]. (Courtesy of Prof. Kenneth Suslick's group)

The reaction vessel was lowered into a 45°C water bath. This temperature was previously reported to provide the maximum energy for the radical formation without reaching a temperature above 60°C during the sonochemical process [39]. Since proteins denature at temperatures above 65°C, it was critical to monitor the temperature. The solution was emulsified using an ultrasonic horn with a tip size of 1 cm at a frequency of 20 KHz and an acoustic power of 35 Watts/cm² (amplitude set at 70%) for three mins.

4.3.4 Protein Microsphere Washing and Purification

The resulting solution was resuspended in cold phosphate buffered saline (PBS, pH 7.0) to a volume of 12 mL in a 15 mL conical vial. A 500 mL solution of PBS was prepared with 500 mL of nanopure water, 2.98 g of NaCl, and 6.85 g KH₂PO₄. The pH of the PBS was adjusted to a pH of 7 using KOH pellets (~15-16 pellets). The microsphere solution at this stage were filtered based on size to remove particles greater than 5 µm, although this was generally not necessary because the microspheres synthesized using this particular protocol were already under 5 µm according to size distribution measurements. The microsphere solutions were equally divided into twelve 1.5 mL Eppendorf tubes and centrifuged at 0°C for 6 mins at 3500 RPM. Once centrifuged, the microspheres separated into a top layer while the aqueous solution was on the bottom. The microsphere layer was pierced using a glass pipette, and the bottom layer was removed. At this point, the twelve Eppendorf tubes of microspheres were consolidated into no less than three Eppendorf tubes. The microspheres were washed using ice cold PBS and resuspended using plastic transfer pipettes. Plastic transfer pipettes were used because microspheres had a tendency to stick to the sides of glass pipettes, resulting in a higher loss of sample. Care was taken to avoid agitating microsphere solutions by

vortexing or pipetting up and down, as these techniques increased aggregation of microspheres. Once resuspended in PBS, the microspheres were centrifuged for 5 mins at 6000 RPM. These centrifugal washes were repeated until the bottom aqueous layer became clear. Once the microspheres were washed, they could be stored for several months in a 4°C refrigerator. Microspheres should not be kept constantly rotating on a rotisserie rotator or shaken long term once the LBL procedure has been completed. This constant motion and force exerted as the microspheres swing from one end of the Eppendorf tube to the other end decreases their stability and can cause them to leak or rupture over longer periods of time of weeks and months.

4.3.5 Surface Functionalization of Protein Microspheres using Layer-By-Layer Adhesion

Microspheres were centrifugally washed and resuspended in 200 µL of cold PBS (pH 7.0). 1mL of cold 1 mg/mL PDDA solution (50 µL PDDA/10 mL PBS) was added to the microsphere solution. The solution was mixed and placed on a rotating rotisserie shaker for 30 mins in the 4°C refrigerator. The PDDA layer reversed the charge of the surface and thereby facilitated the coating of silica nanoparticles. In cases where the silica layer was not needed, the RGD was layered directly onto the bare microsphere.

Microspheres were centrifugally washed at 6000 RPM for 5 mins. The aqueous layer was removed and the microspheres were resuspended into 200 µL of cold PBS. One milliliter of a 1% silica solution (300 µL of 34% silica/10 mL of PBS) was added to the microsphere solution. The solution was lightly mixed and placed on a rotisserie shaker for 30 mins in the refrigerator at 4°C. Microspheres layered with silica sank to the bottom of the solution during centrifugation. Microspheres still floating in the upper layer likely were not successfully layered with PDDA and silica.

Next, the microspheres were centrifugally washed at 6000 RPM for 5 mins. The aqueous layer was removed, and the microspheres were resuspended into 200 μ L cold PBS. 1 mL of a 1 mg/mL RGD solution (1 mg RGDKKKKKK peptide/1 mL PBS) was added to the microsphere solution. The RGDKKKKKK peptide sequence was synthesized by the Protein Sciences Facility at the Roy J. Carver Biotechnology Center at the University of Illinois at Urbana-Champaign. The placement of the arginine-glycine-aspartic acid residues at the amino terminus of the RGDKKKKKK sequence was previously reported to be the most optimal linear peptide sequence for targeting the microspheres to integrins using the RGD motif [41].

4.4 Scanning Electron Microscopy of Protein Microspheres

Modified protein microspheres were washed with PBS (pH 7.4) 10-15 times to purify the sample by removing the excess material. Approximately 15×10^6 microspheres were suspended into 850 μ L of PBS and 500 μ L of the 14% glutaraldehyde solution. The solution was vortexed and fixed at room temperature for 2 hrs on the rotating rotisserie shaker. The microspheres were washed three times in a 0.1 M Na-Cacodylate buffer (pH 7.4) solution for 10 mins each on a shaker.

The microsphere layer was isolated after being centrifuged at 6000 RPM for a period of 5 mins. The microspheres were stained for 2 hrs with 1% osmium tetroxide in a 0.1 M Na-Cacodylate buffer (pH 7.4) solution on the rotisserie shaker. The microspheres were washed three times in a 0.1 M Na-Cacodylate Buffer (pH 7.4) solution for a period of 10 mins each on a shaker.

The microspheres were gradually dehydrated from 10% ethanol to 25%, 50%, 75%, 95%, and finally to 100% ethanol (twice) each in 5 mins incubations. The microspheres were resuspended in a 1:1 solution of 100% ethanol and hexamethyldisilazane (HMDS). Two more washes of the microspheres were performed with 100% HMDS.

The microspheres were resuspended in HMDS and allowed to air dry onto nitrocellulose membrane filters (0.22 μm pore size, 13 mm diameter) under the chemical fume hood. This method of depositing and drying the microspheres proved to be much better than critical point drying of the microspheres. The latter process resulted in a filmy layer from the dried alcohol or other solvents on top of the microspheres hindering the ability to visualize the finer structures on the microsphere surface. After the HMDS evaporated, the membrane filters were secured to SEM chucks with black carbon tape.

Samples were made conductive for SEM imaging by sputter coating for 90 s to achieve a ~ 20 nm layer of gold/palladium coating using a turbo-pumped sputter coater (Denton Vacuum – Model # Desk-1 TSC). The thicker coating permitted the use of higher beam intensity and longer imaging times, which enabled higher resolution and sharper images. If the coating was too thin, the microspheres easily collapsed under the high power beam intensities or under long acquisition time periods of the electron beam. The sides of metal chucks were coated with silver paint to provide a continuous conducting surface between the gold/palladium coating and the metal chuck.

Samples were imaged using a scanning electron microscope (SEM) (FEI Company – Phillips 30 ESEM-FEG) in the Imaging Technology Group's Microscopy Suite at the Beckman Institute for Advanced Science and Technology at the University of

Illinois at Urbana-Champaign. Samples were imaged with an electron beam intensity of 5.0 kV, a working distance of 3.2 mm, a spot size setting of 2 nm, and magnifications ranging from 6,000X to 120,000X.

SEM images of bare protein microspheres, PDDA-coated microspheres, PDDA/Silica-coated microspheres, PDDA/Silica/RGD-coated microspheres, and RGD-coated microspheres are shown in Figures 4.3-4.8. The microspheres were 1-5 μm in size, which is in agreement with the dynamic light scattering (DLS) results described later in this chapter. Differences in the texture of the surface of microspheres can be visualized with each added layer. Small (2-5 microspheres) aggregates of protein microspheres were found for most of the coatings except for the PDDA-coated microspheres, where larger aggregates (50+ microspheres) formed. The layering of PDDA and silica provided a very homogeneous and continuous covering of the microsphere surface with the respective nanoparticle. Layering of the RGD peptide sequence onto the microsphere surface was not as homogeneous or as complete compared to the other layers, which could affect the binding affinity of RGD-coated microspheres to the integrin receptor. A quantitative estimate of RGD coverage cannot be easily determined with SEM since it is difficult to ascertain which particles are due to RGD alone, especially when it is layered on top of other layers. In addition, the assumption is that the RGD is evenly layered across the entire microsphere surface. For future studies, other sequences attached to the RGD should be explored for maximizing the covering of the protein microsphere with the RGD increasing the number of exposed RGD ligands capable of binding integrin receptors.

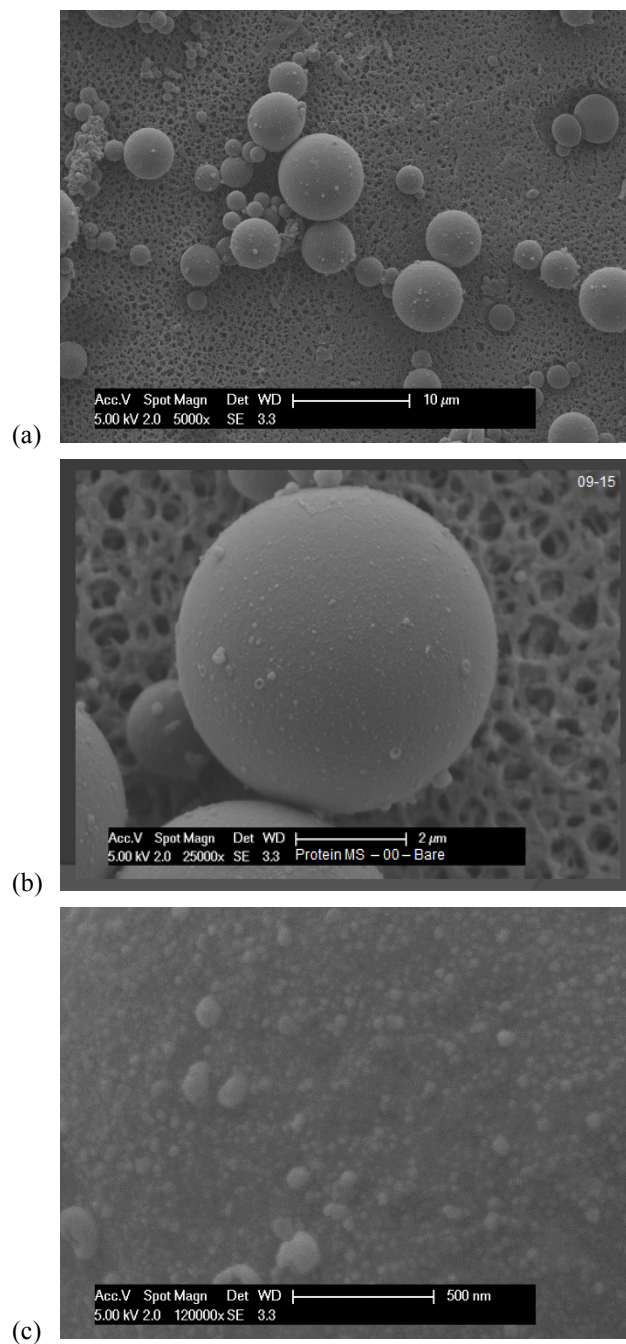


Figure 4.3: Scanning electron microscope images of bare microspheres without any additional layers at (a) 5,000X, (b) 25,000X, and (c) 120,000X. The surface of the bovine serum albumin protein shell is shown at a higher resolution in the bottom image of the sequence.

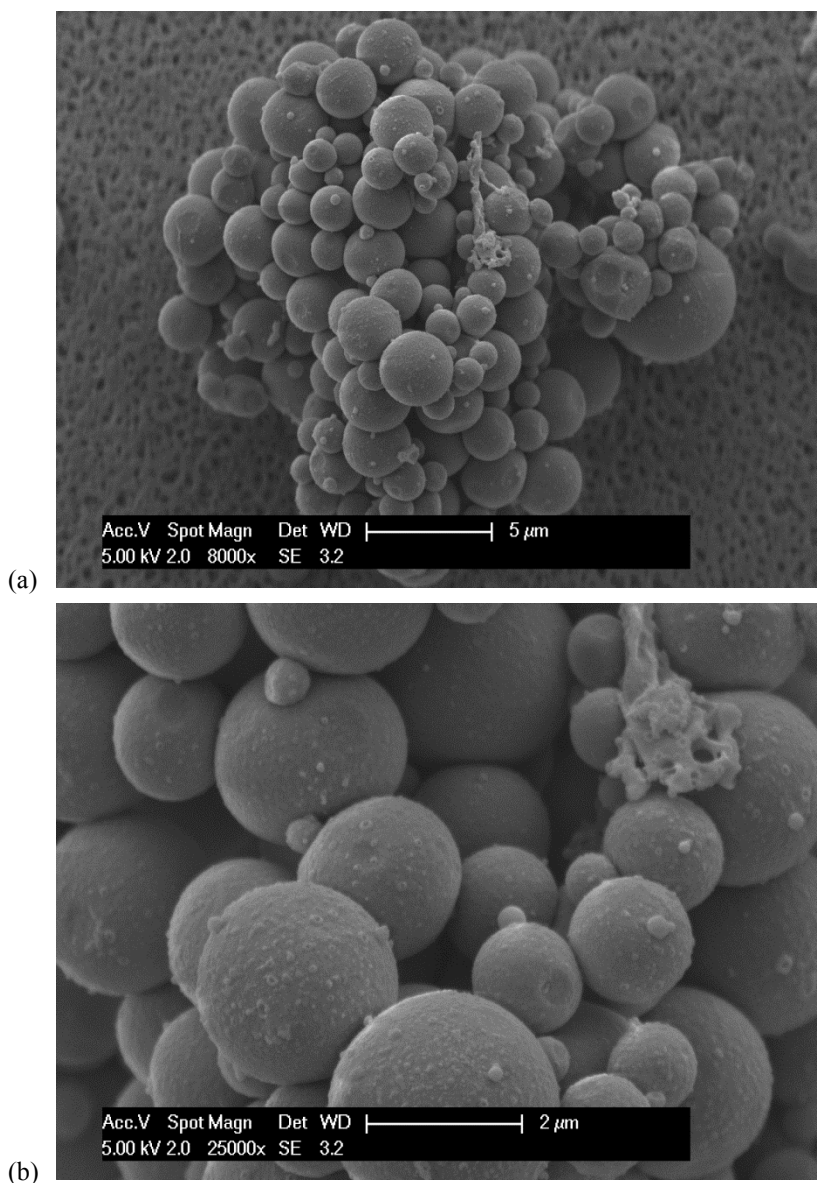


Figure 4.4: Scanning electron microscope images of microspheres that have been coated with PDDA using the layer-by-layer adhesion method at (a) 8,000X and (b) 25,000X. This coating reversed the charge on the outer shell of the microsphere in order to allow for the layering of silica. Due to this change in the charge, these particular microspheres were more likely to aggregate during the SEM processing of these microspheres and shown in the resulting SEM images above. Compared to bare microspheres, more texture is present on the surface of the microspheres.

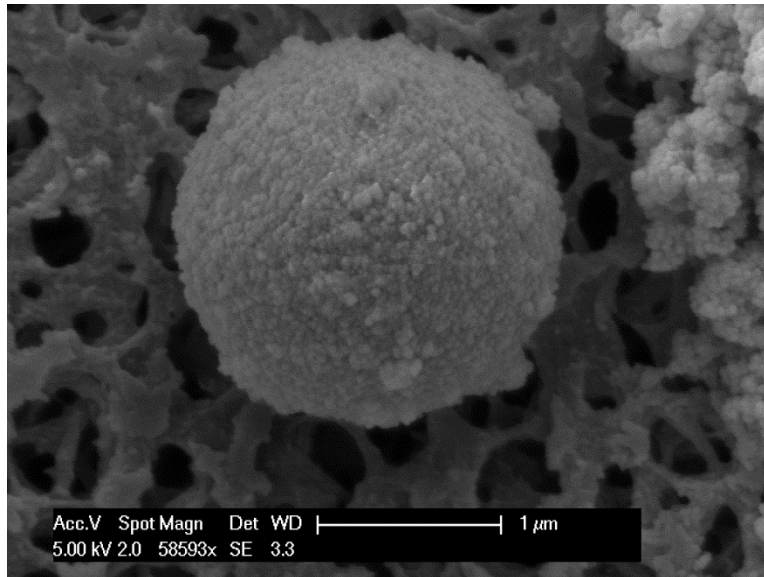


Figure 4.5: Scanning electron microscope (58593X magnification) images of a microsphere that has been coated with a PDDA layer and silica layer using the layer-by-layer adhesion method. Compared to the PDDA microspheres, the surface of the microspheres was completely covered with silica nanoparticles. Microspheres coated with silica precipitate to the bottom in solution, making them more suitable for *in vitro* studies where the cells are attached to the bottom of the culture dish.

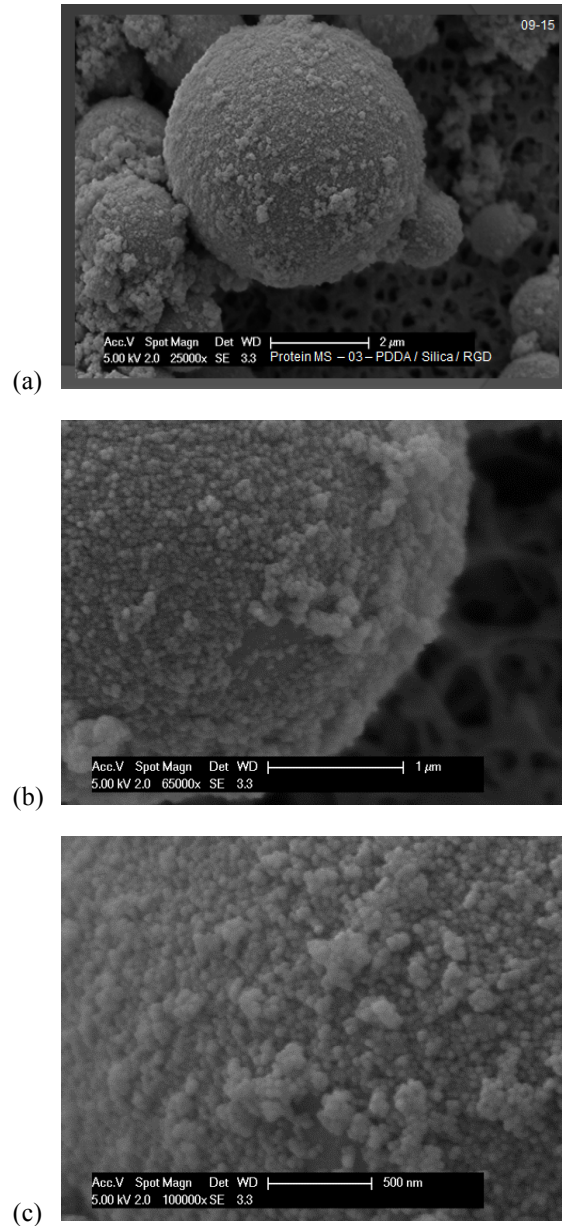


Figure 4.6: Representative scanning electron microscope images of microspheres coated with a PDDA layer, then a silica layer, and then a layer of RGD peptide (linear RGDKKKKKK) using layer-by-layer adhesion method at 25,000X (a), at 65,000X (b), and at 100,000X (c).

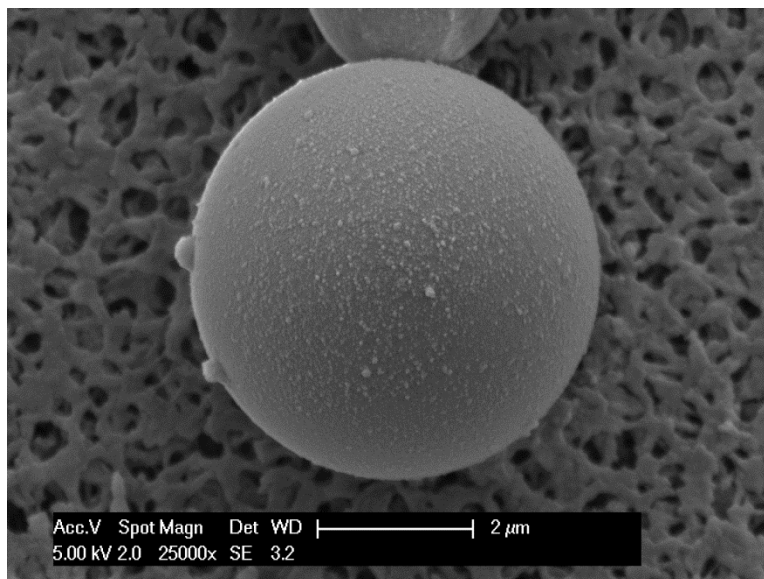


Figure 4.7: Scanning electron microscope images of microspheres coated with a layer of RGD peptide (linear RGDKKKKKK) using the layer-by-layer adhesion method. On the smooth surface of bare microspheres, the RGD layer appears textured. Similar to the PDDA/Silica/RGD-coated microspheres, the RGD layering does not appear to completely cover the microsphere surface.

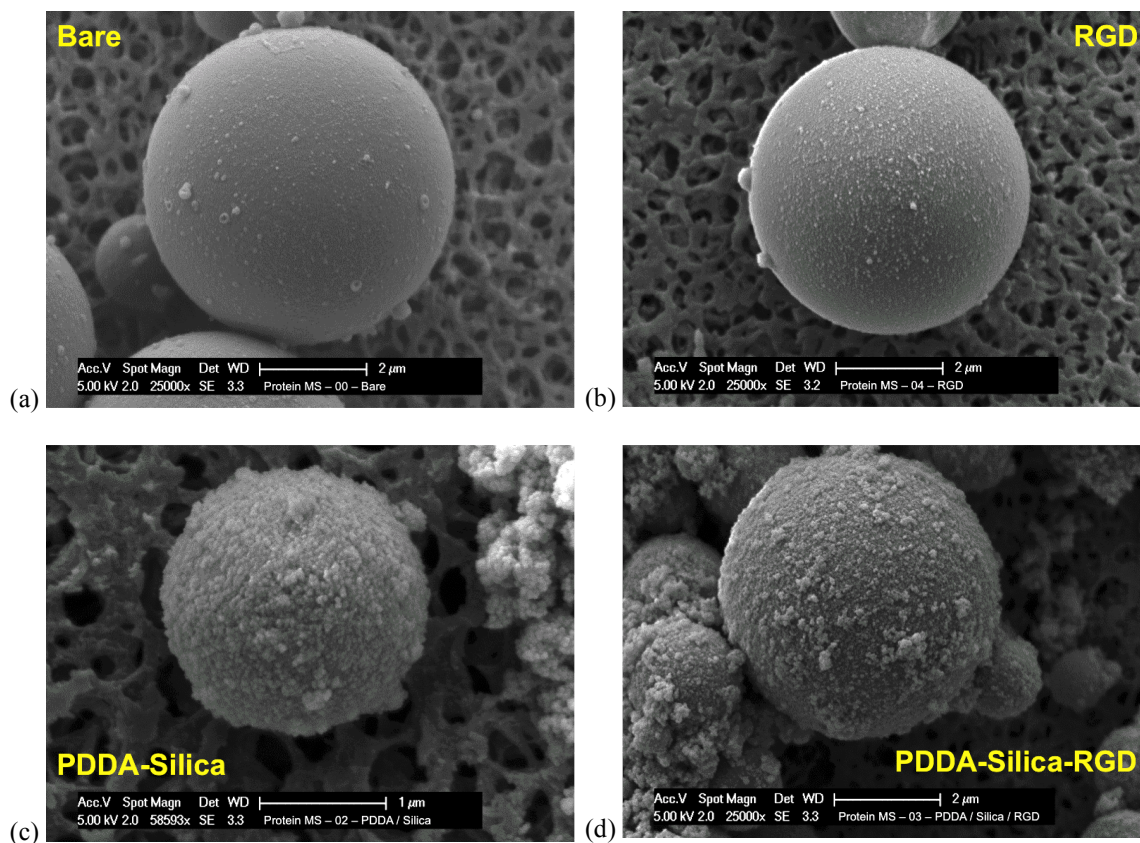


Figure 4.8: Summary of representative SEM images of protein microspheres [(a), (b), (d) at 25,000X; (c) at 58,593X magnifications] through each layering process via layer-by-layer electrostatic adhesion process. Bare microspheres before any layering (a); RGD layered directly onto the bare microspheres (b); bare microspheres first layered with PDDA and then with silica (c); bare microspheres first layered with a layer of PDDA followed by silica and followed by RGD (d).

4.5 Transmission Electron Microscopy of Protein Microspheres

The processing of microspheres for transmission electron microscopy (TEM) followed the same procedure as the SEM processing for the fixation, washing, staining, washing, and dehydration steps. Compared to SEM processing, the microspheres were left suspended in 100% Ethanol as the final step for TEM processing. In SEM processing, the microspheres were resuspended in HDMS as the final step.

The fixed microspheres were washed and infiltrated with an epoxy resin. They were first suspended in a 1:1 mixture of ethanol and acetonitrile for 10 mins. The microspheres were resuspended into a 100% solution of acetonitrile for an additional 10 mins. The epoxy resin was a solution of Embed 812 Mixture (Electron Microscopy Sciences) with DMP-30, an epoxy accelerator. The microspheres were suspended into a 1:1 mixture of acetonitrile and the Embed 812 with DMP-30 epoxy resin solution for 10 mins. They were then suspended into a 100% epoxy resin solution and allowed to fully infiltrate overnight at room temperature. The microspheres were embedded into the epoxy resin and cured in a vacuum-sealed oven at 60°C for 3 days. The cured samples were cooled to room temperature and sectioned using a diamond knife in 100 nm slices on an ultramicrotome (Leica Ultracut UCT). The sections were placed on copper mesh grids (Electron Microscopy Sciences, 200 Mesh Copper Gilder Grids, G200-Cu) and imaged with a transmission electron microscope (Philips CM200) at a voltage of 120 kV.

Representative TEM images of each layer are presented in Figure 4.9. Due to differences in the staining penetration of the osmium tetroxide of the layered particles, distinct layers could not always be observed. Distinct structural differences and particle distribution can be seen with each added layer along with the encapsulated iron oxide.

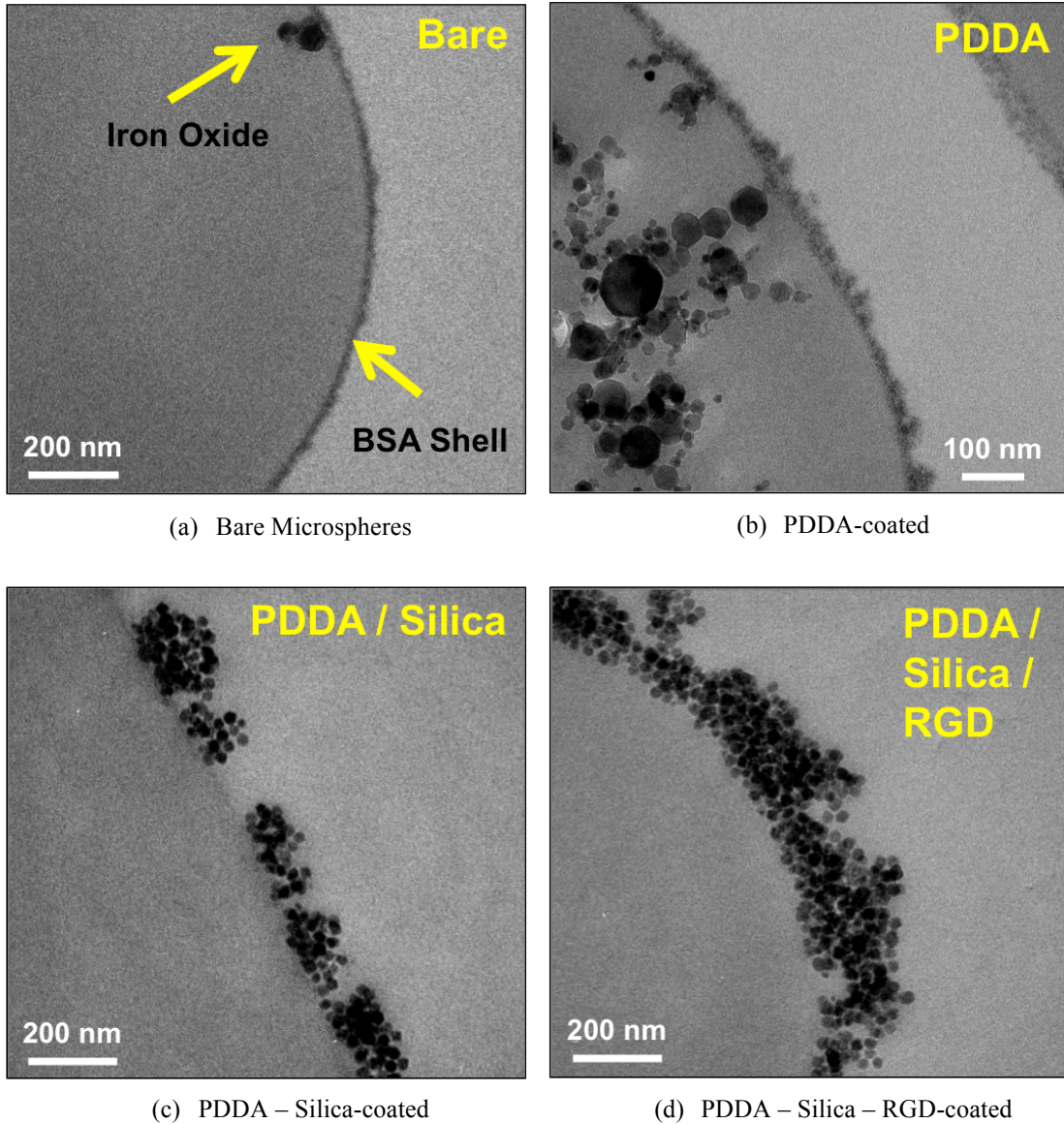


Figure 4.9: TEM images of protein microspheres through each layering process via layer-by-layer electrostatic adhesion process. TEM images of (a) bare microspheres before any layering; (b) bare microspheres layered with PDDA; (c) bare microspheres layered with PDDA and silica; (d) bare microspheres layered with PDDA, Silica, and RGD. Iron oxide particles can be seen in the oil core of the microspheres (a, b).

4.6 Size Distribution of Protein Microspheres

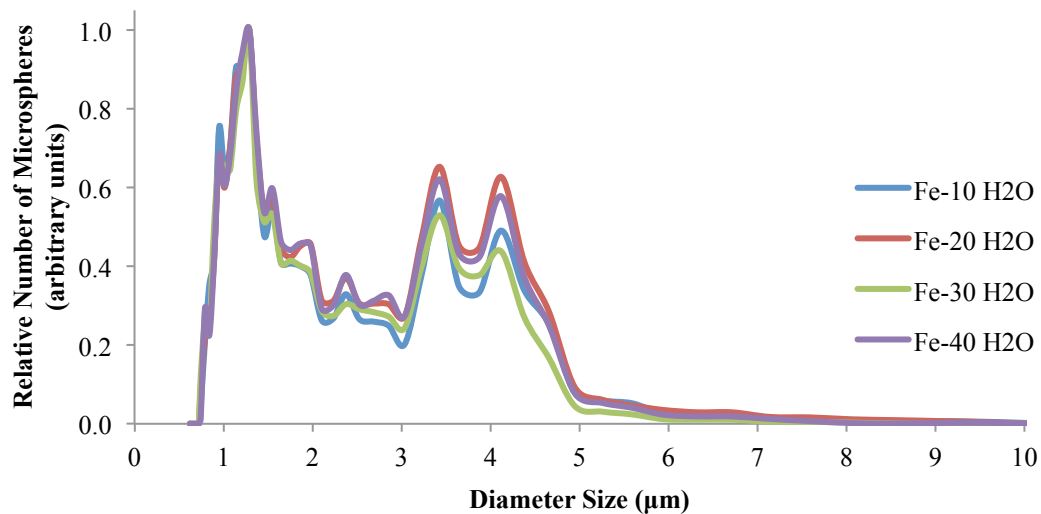
The size distribution of protein microspheres using this synthesis method was previously reported by Prof. Suslick's research group as 1-3 μm [38, 39]. The size distribution of protein microspheres was found to be largely dependent on the surface tension between the oil phase and the BSA protein phase during the emulsification process of the sonochemical synthesis of microspheres [38, 39]. Other factors such as the ultrasonic power intensity and acoustic frequency affected the yield of microspheres but not their size. The size distribution is an important parameter to control because it influences the *in vivo* circulation pattern and lifetime of the protein microspheres.

While determining the loading capacity of protein microspheres to encapsulate various magnetic and fluorescent nanoparticles of interest, I studied the effects of increasing the concentrations of encapsulated Nile Red dye, DiR dye, and iron oxide on the microsphere size distribution. In order to maximize the contrast under magnetic imaging modalities (MM-OCT and MRI) and fluorescence imaging modalities, the microspheres should encapsulate the maximum amount of dye or iron oxide into the inner core. The size distribution of these microspheres was measured to determine the effects of increased nanoparticles in the inner core on the final microsphere size distribution.

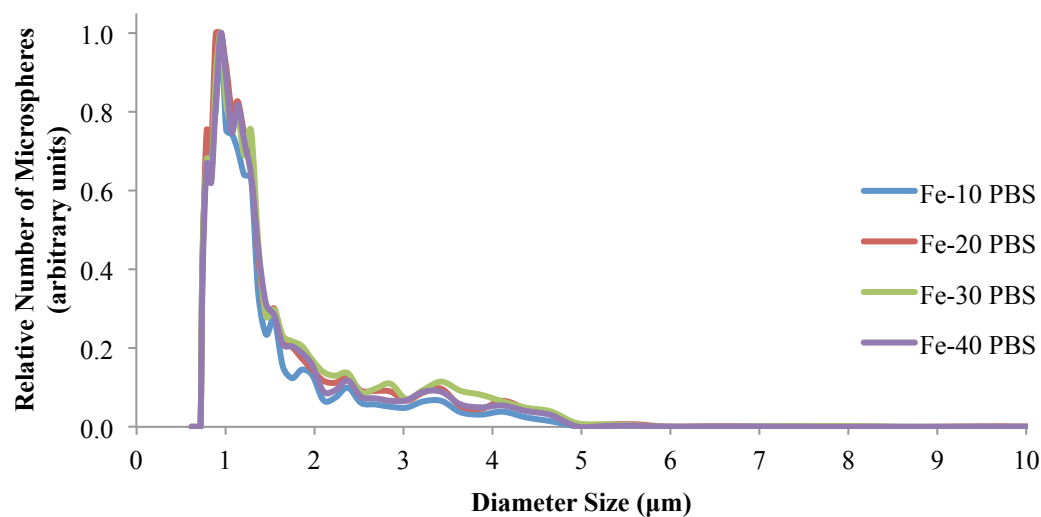
A DLS instrument (Accusizer FX Particle Sizer) located in the Microscopy Suite of the Imaging Technology Group of the Beckman Institute for Advanced Science and Technology at the University of Illinois at Urbana-Champaign measured the size distribution and quantified the concentration of microspheres. The instrument uses a flow system to pass the particles through the detection channel. This method provided more reproducible measurements of the size distribution of the particles and quantifying the

particle concentration compared to the cuvette-based DLS instrument due to the properties of the synthesized microspheres. Microspheres will precipitate over time to the bottom of the vial during the DLS imaging studies. When the microspheres are initially suspended in hydrophilic solutions, they easily separated into a top layer, moving out of the imaging volume of the cuvette cell over the course of the DLS imaging session over time. This effect contributed to large variations in the measured size distribution using the cuvette-based DLS instrument compared to the flow-based DLS instrument. It was also found that the solvent used to re-suspend the microspheres could lead to the aggregation of the microspheres such as the case when comparing between H₂O and PBS (Figure 4.10). The presence of a second peak was attributed to the aggregation of microspheres that occurred when the microspheres were resuspended in water as opposed to PBS. This peak decreased in size but did not completely disappear when the sample was sonicated for a period of several hours just prior to the DLS imaging session.

The results of the DLS measurements from the iron oxide-filled microspheres (Figure 4.11), the Nile Red-filled microspheres (Figure 4.12), and the DiR-filled microspheres (Figure 4.13) showed little changes in the size distribution of the microspheres. The size distributions reported here are similar to those previously synthesized and reported by Prof. Suslick's research group using similar synthesis protocol [38, 39]. Using a Coulter counter, the size distribution of microspheres was primarily between 1-3 μm with the right tail of the distribution ending DLS light scattering and the Coulter counter are acceptable methods for measuring the size distribution of microspheres.

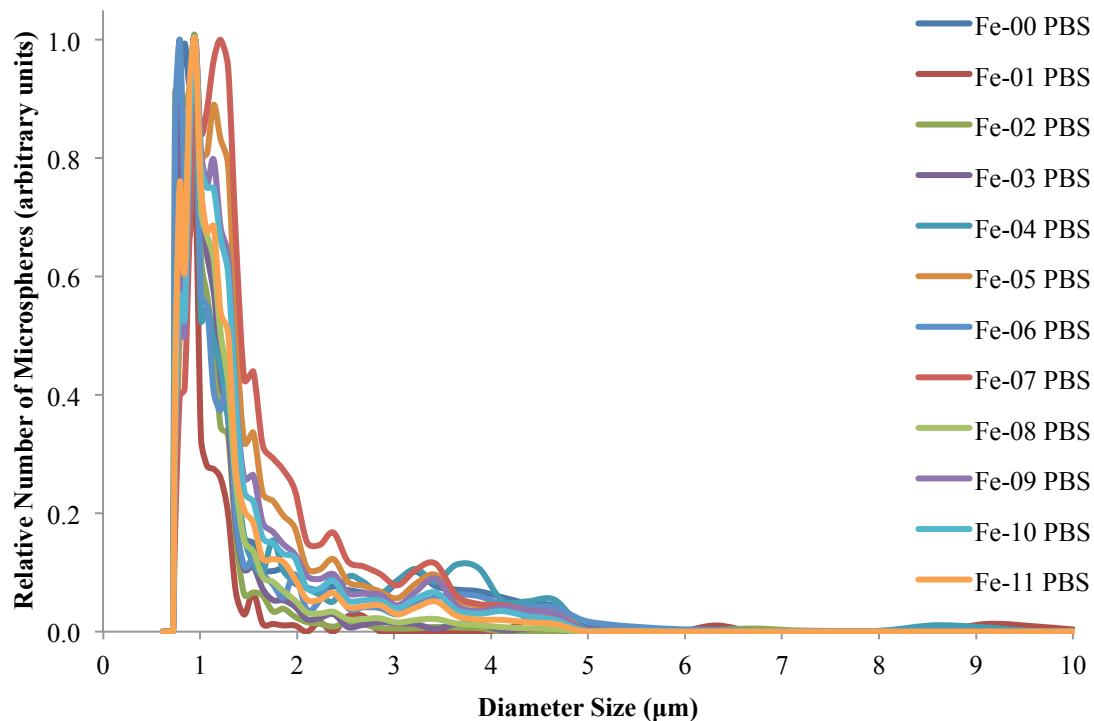


(a)



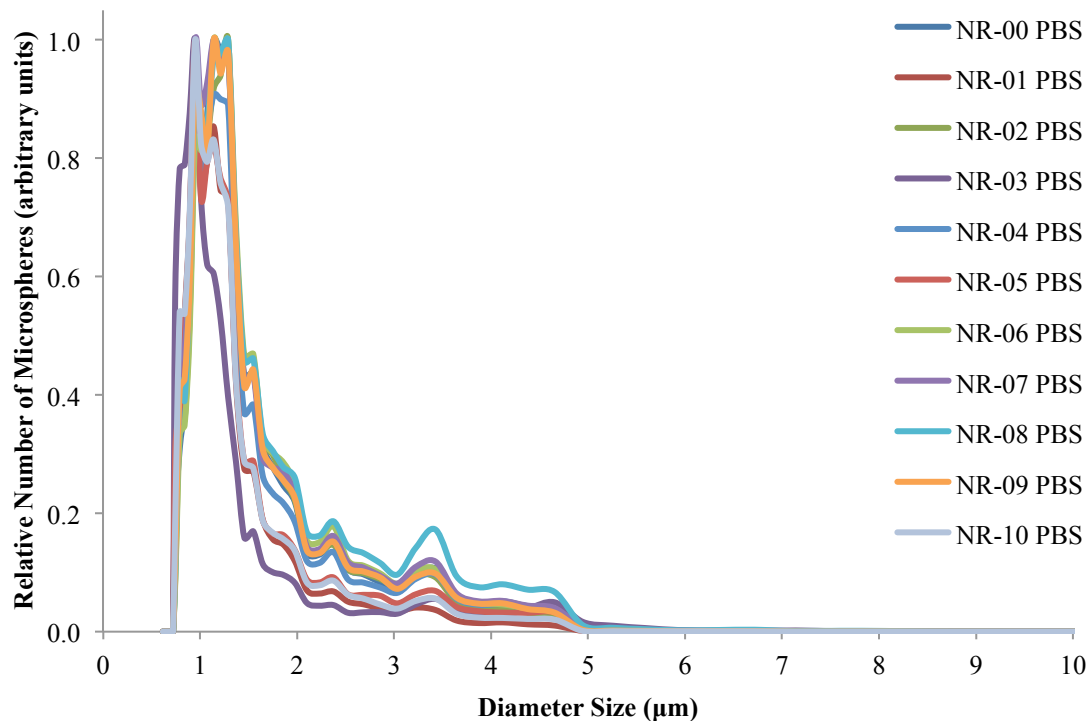
(b)

Figure 4.10: DLS size measurements of the same four batches of iron oxide-filled microspheres that were re-suspended into water (H₂O) (a) or into PBS (b). The solvent used to suspend the microspheres contributes to the aggregation of microspheres as observed by the larger size distribution and extra peak between 3-5 μm. The second largest peak at ~3.4 μm was largely attributed to the aggregation of 2-3 microspheres. Disrupting the aggregates via sonication can also reduce this peak



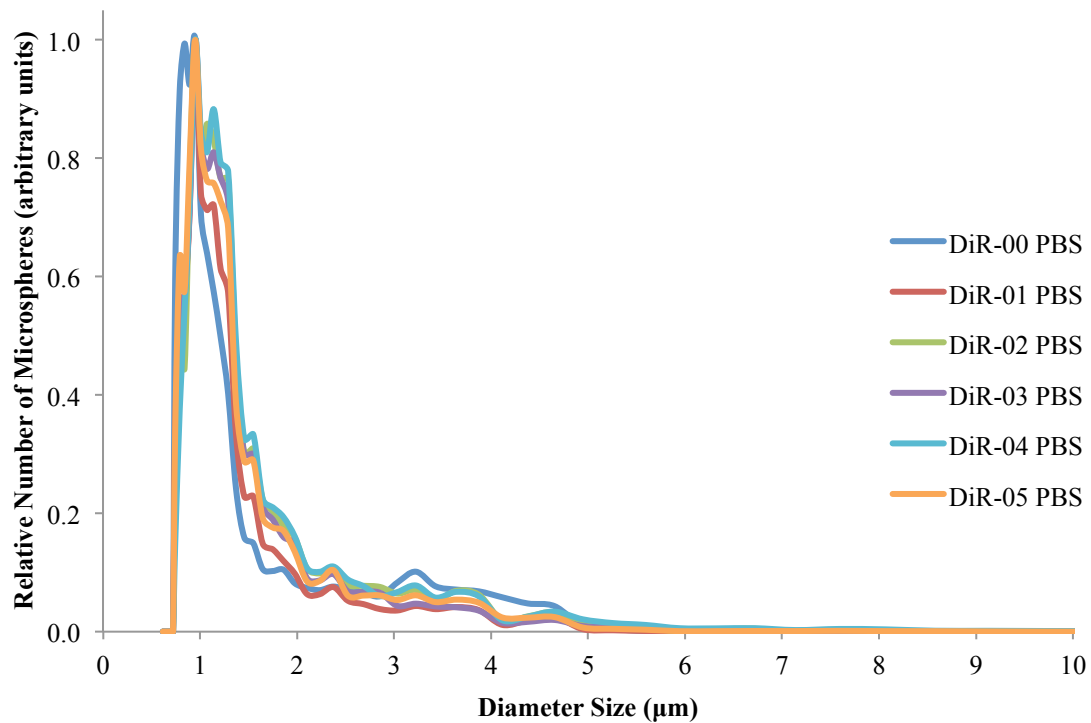
	Iron Oxide (Fe ₂ O ₃) Concentration of Oil Stock Solution		Iron Oxide (Fe ₂ O ₃) Concentration of Oil Stock Solution
Fe-00	0.0 mg/mL	Fe-07	15 mg/mL
Fe-01	0.5 mg/mL	Fe-08	20 mg/mL
Fe-02	0.2 mg/mL	Fe-09	40 mg/mL
Fe-03	1.0 mg/mL	Fe-10	60 mg/mL
Fe-04	2.0 mg/mL	Fe-11	80 mg/mL
Fe-05	5.0 mg/mL	Fe-12	100 mg/mL
Fe-06	10 mg/mL		

Figure 4.11: Size distribution of protein microspheres with increasing concentration of encapsulated iron oxide nanoparticles. As the concentration of iron oxide is increased, there is very little change in the size distribution. The main peak of the protein microspheres is located at ~1.3 μm.



	Nile Red Dye Concentration of Oil Stock Solution		Nile Red Dye Concentration of Oil Stock Solution
NR-00	0.0 mg/mL	NR-06	0.6 mg/mL
NR-01	0.1 mg/mL	NR-07	0.7 mg/mL
NR-02	0.2 mg/mL	NR-08	0.8 mg/mL
NR-03	0.3 mg/mL	NR-09	0.9 mg/mL
NR-04	0.4 mg/mL	NR-10	1.0 mg/mL
NR-05	0.5 mg/mL		

Figure 4.12: Size distribution of protein microspheres with increasing concentration of encapsulated Nile Red dye molecules. As the concentration of Nile Red is increased, there was very little change in the size distribution.



	DiR Dye Concentration of Oil Stock Solution		DiR Dye Concentration of Oil Stock Solution
DiR-00	0.0 mg/mL	DiR-03	3.0 mg/mL
DiR-01	1.0 mg/mL	DiR-04	4.0 mg/mL
DiR-02	2.0 mg/mL	DiR-05	5.0 mg/mL

Figure 4.13: Size distribution of protein microspheres with increasing concentration of encapsulated DiR dye molecules. As the concentration of DiR is increased, there was very little change in the size distribution.

4.7 Conclusions

Protein microspheres were successfully synthesized using a modified protocol from Prof. Suslick's laboratory. They were successfully encapsulated with commercially available iron oxide nanoparticles, Nile Red dye, and DiR dye for use in MM-OCT, MRI, wide field fluorescence imaging system, and fluorescence microscopy. Protein microspheres layered with PDDA, silica, and RGD peptide were visualized using scanning electron microscopy and transmission electron microscopy. The size distribution and concentration of the protein microspheres was characterized using a flow-based DLS instrument. The type and concentration of encapsulated particles did not have any effect on the overall size distribution or synthesis yield of the protein microspheres. The DLS measurements indicated that the measurement variability within the sample and across samples of the same microsphere type to be minimal. DLS was identified as a suitable method to rapidly quantify the concentration and characterize the size distribution of microspheres. The size distribution reported from the DLS measurements indicated that the majority of the protein microspheres were 1-2 μm in size with a smaller distribution in the 2-5 μm , which is consistent with the sizes observed under SEM reported in Figures 4.3-4.8. The size distribution was also consistent with previously reported measurements via the Coulter counter. This characterization was necessary to ensure minimal intersample variability when scaling up the synthesis of microspheres for *in vivo* or *ex vivo* animal experiments.

4.8 References

1. Nguyen FT, Zysk AM, Chaney EJ, Kotynek JG, Oliphant UJ, Bellafiore FJ, Rowland KM, Johnson PA, Boppart SA. Intraoperative evaluation of breast tumor margins with optical coherence tomography. *Cancer Research*, 2009. 69 (22): p. 8790-8796.
2. Nguyen FT, Zysk AM, Chaney EJ, Adie SG, Kotynek JG, Oliphant UJ, Bellafiore FJ, Rowland KM, Johnson PA, Boppart SA. Optical coherence tomography: The intraoperative assessment of lymph nodes in breast cancer. *IEEE Eng Med Biol Mag*, 2010. 29 (2): p. 63-70.
3. Nguyen FT, Zysk AM, Kotynek JG, Bellafiore FJ, Rowland KM, Johnson PA, Chaney EJ, Boppart SA. Portable real-time optical coherence tomography system for intraoperative imaging and staging of breast cancer. in *SPIE - Photonics West BiOS - Advanced Biomedical and Clinical Diagnostic Systems V*. 2007. San Jose, CA.
4. Zysk AM, Nguyen FT, Chaney EJ, Kotynek JG, Oliphant UJ, Bellafiore FJ, Johnson PA, Rowland KM, Boppart SA. Clinical feasibility of microscopically-guided breast needle biopsy using a fiber-optic probe with computer-aided detection. *Technology in Cancer Research & Treatment*, 2009. 8 (5): p. 315-321.
5. Zysk AM, Chaney EJ, Boppart SA. Refractive index of carcinogen-induced rat mammary tumours. *Phys Med Biol*, 2006. 51 (9): p. 2165-77.
6. Zysk AM, Nguyen FT, Oldenburg AL, Marks DL, Boppart SA. Optical coherence tomography: A review of clinical development from bench to bedside. *Journal of Biomedical Optics*, 2007. 12 (5).

7. Oldenburg AL, Hansen MN, Ralston TS, Wei A, Boppart SA. Imaging gold nanorods in excised human breast carcinoma by spectroscopic optical coherence tomography. *J Mater Chem*, 2009. 19: p. 6407-6411.
8. Graf RN, Wax A. Temporal coherence and time-frequency distributions in spectroscopic optical coherence tomography. *J Opt Soc Am A Opt Image Sci Vis*, 2007. 24 (8): p. 2186-95.
9. Xu C, Carney PS, Boppart SA. Wavelength-dependent scattering in spectroscopic optical coherence tomography. *Opt Express*, 2005. 13 (14): p. 5450-62.
10. Xu C, Ye J, Marks DL, Boppart SA. Near-infrared dyes as contrast-enhancing agents for spectroscopic optical coherence tomography. *Opt Lett*, 2004. 29 (14): p. 1647-9.
11. Adler DC, Ko TH, Herz PR, Fujimoto JG. Optical coherence tomography contrast enhancement using spectroscopic analysis with spectral autocorrelation. *Opt Express*, 2004. 12 (22): p. 5487-501.
12. Morgner U, Drexler W, Kartner FX, Li XD, Pitris C, Ippen EP, Fujimoto JG. Spectroscopic optical coherence tomography. *Opt Lett*, 2000. 25 (2): p. 111-3.
13. Jacob D, Shelton RL, Applegate BE. Fourier domain pump-probe optical coherence tomography imaging of melanin. *Opt Express*, 2010. 18 (12): p. 12399-410.
14. Yaqoob Z, McDowell E, Wu J, Heng X, Fingler J, Yang C. Molecular contrast optical coherence tomography: A pump-probe scheme using indocyanine green as a contrast agent. *J Biomed Opt*, 2006. 11 (5): p. 054017.

15. Applegate BE, Izatt JA. Molecular imaging of endogenous and exogenous chromophores using ground state recovery pump-probe optical coherence tomography. *Opt Express*, 2006. 14 (20): p. 9142-55.
16. Rao KD, Choma MA, Yazdanfar S, Rollins AM, Izatt JA. Molecular contrast in optical coherence tomography by use of a pump-probe technique. *Opt Lett*, 2003. 28 (5): p. 340-2.
17. Lee SW, Yoo JY, Kang JH, Kang MS, Jung SH, Chong Y, Cha DS, Han KH, Kim BM. Optical diagnosis of cervical intraepithelial neoplasm (cin) using polarization-sensitive optical coherence tomography. *Opt Express*, 2008. 16 (4): p. 2709-19.
18. Kuo WC, Hsiung MW, Shyu JJ, Chou NK, Yang PN. Assessment of arterial characteristics in human atherosclerosis by extracting optical properties from polarization-sensitive optical coherence tomography. *Opt Express*, 2008. 16 (11): p. 8117-25.
19. Wu CC, Wang YM, Lu LS, Sun CW, Lu CW, Tsai MT, Yang CC. Tissue birefringence of hypercholesterolemic rat liver measured with polarization-sensitive optical coherence tomography. *J Biomed Opt*, 2007. 12 (6): p. 064022.
20. Moneron G, Boccara AC, Dubois A. Polarization-sensitive full-field optical coherence tomography. *Opt Lett*, 2007. 32 (14): p. 2058-60.
21. Kuo WC, Chou NK, Chou C, Lai CM, Huang HJ, Wang SS, Shyu JJ. Polarization-sensitive optical coherence tomography for imaging human atherosclerosis. *Appl Opt*, 2007. 46 (13): p. 2520-7.

22. Makita S, Yasuno Y, Endo T, Itoh M, Yatagai T. Polarization contrast imaging of biological tissues by polarization-sensitive fourier-domain optical coherence tomography. *Appl Opt*, 2006. 45 (6): p. 1142-7.
23. Giattina SD, Courtney BK, Herz PR, Harman M, Shortkroff S, Stamper DL, Liu B, Fujimoto JG, Brezinski ME. Assessment of coronary plaque collagen with polarization sensitive optical coherence tomography (ps-oct). *Int J Cardiol*, 2006. 107 (3): p. 400-9.
24. Strasswimmer J, Pierce MC, Park BH, Neel V, De Boer JF. Polarization-sensitive optical coherence tomography of invasive basal cell carcinoma. *J Biomed Opt*, 2004. 9 (2): p. 292-8.
25. Kuo WC, Shyu JJ, Chou NK, Lai CM, Huang HC, Chou C, Jan GJ. Imaging of human aortic atherosclerotic plaques by polarization-sensitive optical coherence tomography. *Conf Proc IEEE Eng Med Biol Soc*, 2004. 2: p. 1222-4.
26. De Boer JF, Milner TE. Review of polarization sensitive optical coherence tomography and stokes vector determination. *J Biomed Opt*, 2002. 7 (3): p. 359-71.
27. Roth JE, Kozak JA, Yazdanfar S, Rollins AM, Izatt JA. Simplified method for polarization-sensitive optical coherence tomography. *Opt Lett*, 2001. 26 (14): p. 1069-71.
28. De Boer JF, Milner TE, Van Gemert MJ, Nelson JS. Two-dimensional birefringence imaging in biological tissue by polarization-sensitive optical coherence tomography. *Opt Lett*, 1997. 22 (12): p. 934-6.

29. John R, Nguyen FT, Kolbeck KJ, Chaney EJ, Marjanovic M, Suslick KS, Boppart SA. Targeted multifunctional multimodal protein-shell microspheres as cancer imaging contrast agents. *Mol Imaging Biol*, 2012. 14 (1): p. 17-24.
30. Wang J, Wang MR, Jiang H, Shen M, Cui L, Bhattacharya SK. Detection of magnetic particles in live dba/2j mouse eyes using magnetomotive optical coherence tomography. *Eye Contact Lens*, 2010. 36 (6): p. 346-51.
31. Oldenburg AL, Gallippi CM, Tsui F, Nichols TC, Beicker KN, Chhetri RK, Spivak D, Richardson A, Fischer TH. Magnetic and contrast properties of labeled platelets for magnetomotive optical coherence tomography. *Biophys J*, 2010. 99 (7): p. 2374-83.
32. John R, Rezaeipoor R, Adie SG, Chaney EJ, Oldenburg AL, Marjanovic M, Haldar JP, Sutton BP, Boppart SA. *In vivo* magnetomotive optical molecular imaging using targeted magnetic nanoprobe. *Proc Natl Acad Sci U S A*, 2010. 107 (18): p. 8085-90.
33. Nguyen FT, Dibbern EM, Chaney EJ, Oldenburg AL, Suslick KS, Boppart SA. Magnetic protein microspheres as dynamic contrast agents for magnetomotive optical coherence tomography. in *SPIE Photonics West BIOS: Molecular Probes for Biomedical Applications II*. 2008. San Jose, CA.
34. Oldenburg AL, Gunther JR, Boppart SA. Imaging magnetically labeled cells with magnetomotive optical coherence tomography. *Opt Lett*, 2005. 30 (7): p. 747-9.
35. Oldenburg AL, Toublan FJ, Suslick KS, Wei A, Boppart SA. Magnetomotive contrast for *in vivo* optical coherence tomography. *Opt Express*, 2005. 13 (17): p. 6597-614.

36. Lee TM, Oldenburg AL, Sitafalwalla S, Marks DL, Luo W, Toublan FJ, Suslick KS, Boppart SA. Engineered microsphere contrast agents for optical coherence tomography. *Opt Lett*, 2003. 28 (17): p. 1546-8.
37. Toublan FJ, Suslick KS, Boppart SA, Lee TM, Oldenburg AL. Modification of protein microspheres for biomedical application. *Polymer Preprints*, 2003. 44: p. 185.
38. Toublan FJ. *Methods to tailor protein microspheres for biomedical applications* [dissertation]. Urbana, IL: University of Illinois at Urbana-Champaign; 2005.
39. Dibbern EM. *Core-shell microspheres for biomedical applications* [dissertation]. Urbana, IL: University of Illinois at Urbana-Champaign; 2007.
40. Kolbeck KJ. *The biomedical applications of protein microspheres* [dissertation]. Urbana, IL: University of Illinois at Urbana-Champaign; 1999.
41. Toublan FJ, Boppart SA, Suslick KS. Tumor targeting by surface-modified protein microspheres. *J Am Chem Soc*, 2006. 128 (11): p. 3472-3.

CHAPTER 5 PROTEIN MICROSPHERES AS CONTRAST AGENTS

5.1 Introduction

Modified protein microspheres have great potential as novel multi-modal contrast agents. This chapter will focus on the development and evaluation of protein microspheres as magnetic contrast agents for MM-OCT [1] and MRI. The encapsulation capacity of iron oxide into the microspheres was increased to maximize the magnetic contrast. The fluorescence properties of these microspheres were evaluated with wide-field fluorescence imaging and fluorescence microscopy. These imaging modalities will be evaluated for their potential to detect and quantify the concentration of iron oxide-filled microspheres and fluorescent dye filled microspheres in samples. Being able to quantify the concentration of microspheres in a sample would provide information about the binding specificity and relative bio-distribution of the microspheres when examined in an *in vivo* animal experiment. Lastly, the effects of combining both the iron oxide and the dyes into a single multi-modal protein microsphere will be explored.

5.1.1 Previous Uses of Protein Microspheres as Imaging Agents

Protein microspheres have been previously reported for use as imaging agents in a number of different biomedical applications. Iron oxide colloids were first embedded into the shell of protein microspheres by Kolbeck [2] and encapsulated into the oil core of protein microspheres by Toublan [3]. Iron oxide protein microspheres were first developed as contrast agents for histopathological analysis [2] as the iron oxide could be stained with Prussian Blue. Gadolinium and perfluoronane filled protein microspheres were explored as magnetic contrast

agents for MRI applications [2]. Air-filled and oil-filled microspheres have been widely explored for contrast and drug delivery applications in ultrasound [2, 4]. Fluorescent microspheres were developed for fluorescence microscopy and spectroscopic OCT [2, 3, 5]. Protein microspheres, modified with carbon, gold, or melanin, have also been studied as scattering contrast agents for OCT [3, 6]. The diversity of microsphere types developed over the years for different imaging modalities reinforces the high level of customization and flexibility available with protein microspheres. Most of the studies to date using protein microspheres as contrast agents have focused on single imaging applications. The work presented in this thesis reveals the first in-depth efforts for the development and optimization of protein microspheres as multi-modal contrast agents that can bridge imaging modalities that respectively image on different scale sizes.

5.2 Protein Microspheres as Magnetic Contrast Agents

One main application for the modified microspheres described in this thesis would be to serve as magnetic contrast agents in MM-OCT [1]. As previously described, MM-OCT provides additional functional contrast to structural OCT images by modulating a magnetic field off and on during OCT imaging. The magnetomotive contrast is dependent on the physical displacement of scatterers caused by the movement of magnetic particles when the field is turned on. As part of the multi-modal design of this microsphere, magnetic nanoparticles encapsulated by the microsphere should also be detectable under MRI, a wide-field biomedical imaging modality.

In the following studies, the protein microspheres were synthesized using an oil stock solution with a concentration of 50 mg of iron oxide/mL of vegetable oil. The protein

microspheres were washed and purified as previously described in Chapter 4 and characterized using a flow-based DLS instrument. Different samples (1% low melting agarose gel) were made with different concentrations of microspheres. The final gel volume at the same final 1% concentration of agarose gel should correlate to similar overall stiffness across the different samples (Table 5.1). The assumption made was that the amount of microspheres in the final gel samples would not significantly contribute to the overall gel stiffness. Since the MM-OCT signal is dependent on the physical displacement of scatterers by magnetic particles, the stiffness of the sample plays a significant role in the displacement magnitude of the scatterers. The sample stiffness was inversely correlated with the distance the magnetic particles were able to displace the surrounding scatterers.

Table 5.1: Increasing concentrations of microspheres suspended in 1% low melting agarose gel. The resulting approximate microsphere concentrations ranged from $\sim 5.3 \times 10^6$ to 2.6×10^7 microspheres/mL of agarose gel.

Name	Microsphere Stock Volume	PBS Volume	1% Low Melting Agarose Volume	Total Volume	Microsphere Conc. (# of Microspheres/mL of solution)
Sample 1	000 uL	200 uL	7.0 mL	7.2 mL	0/mL
Sample 2	040 uL	160 uL	7.0 mL	7.2 mL	5.3×10^6 /mL
Sample 3	080 uL	120 uL	7.0 mL	7.2 mL	1.1×10^7 /mL
Sample 4	120 uL	080 uL	7.0 mL	7.2 mL	1.6×10^7 /mL
Sample 5	160 uL	040 uL	7.0 mL	7.2 mL	2.1×10^7 /mL
Sample 6	200 uL	000 uL	7.0 mL	7.2 mL	2.6×10^7 /mL

5.2.1 Iron Oxide-filled Microspheres under MM-OCT

The MM-OCT images (Figure 5.1) demonstrate that these microspheres can provide MM-OCT contrast at concentrations between 5.3×10^6 and 1.6×10^7 microspheres/mL in the 1% low melting temperature agarose gel. The MM-OCT signal intensity pixel values were averaged over the entire image and plotted as a function of the microsphere concentration in Figure 5.2. This plot shows that MM-OCT can quantitatively measure the microsphere concentration derived from the average magnetomotive intensity signals for samples at concentrations less than 1.1×10^7 microspheres/mL of gel (with iron oxide concentration of 50 mg/mL in the inner core). At concentrations greater than 1.1×10^7 microspheres/mL, the MM-OCT signal reached a plateau around an MM-OCT signal of 4.5-5.5 dB. The plateau occurs when the amplitude of the displacement of the scatterer, as the magnetic field is modulated, is large enough that the optical phase changes by more than π [7]. When this occurs, it is not possible to properly unwrap the optical phase.

MM-OCT can also be used to quantify the number of microspheres with known concentration of encapsulated iron oxide. Oil stock solutions were prepared with increasing iron oxide concentrations from 0 to 100 mg/mL as described in Table 5.2. The microspheres were synthesized using these initial stock solutions and embedded into 1% low melting temperature agarose gels at concentrations of 1.0×10^7 microspheres/mL in 35 mm x 10 mm petri dishes. The average MM-OCT intensity signals are plotted as a function of the concentration of iron oxide encapsulated in the protein microspheres in Figure 5.4.

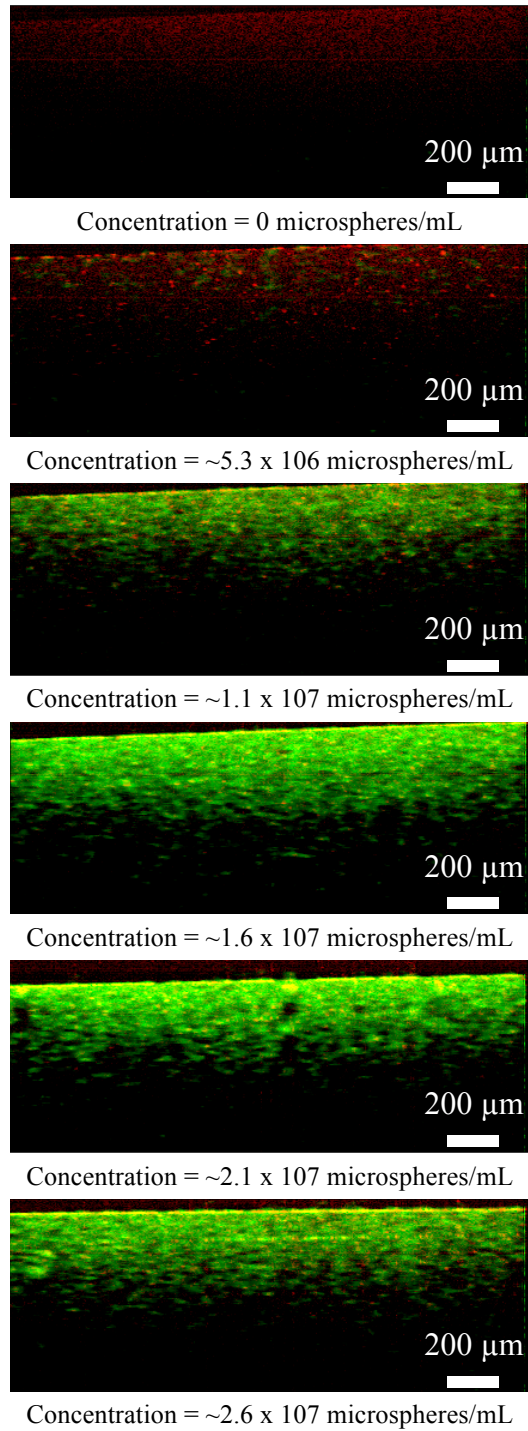


Figure 5.1: MM-OCT images of 1% agarose gels with increasing microsphere concentration

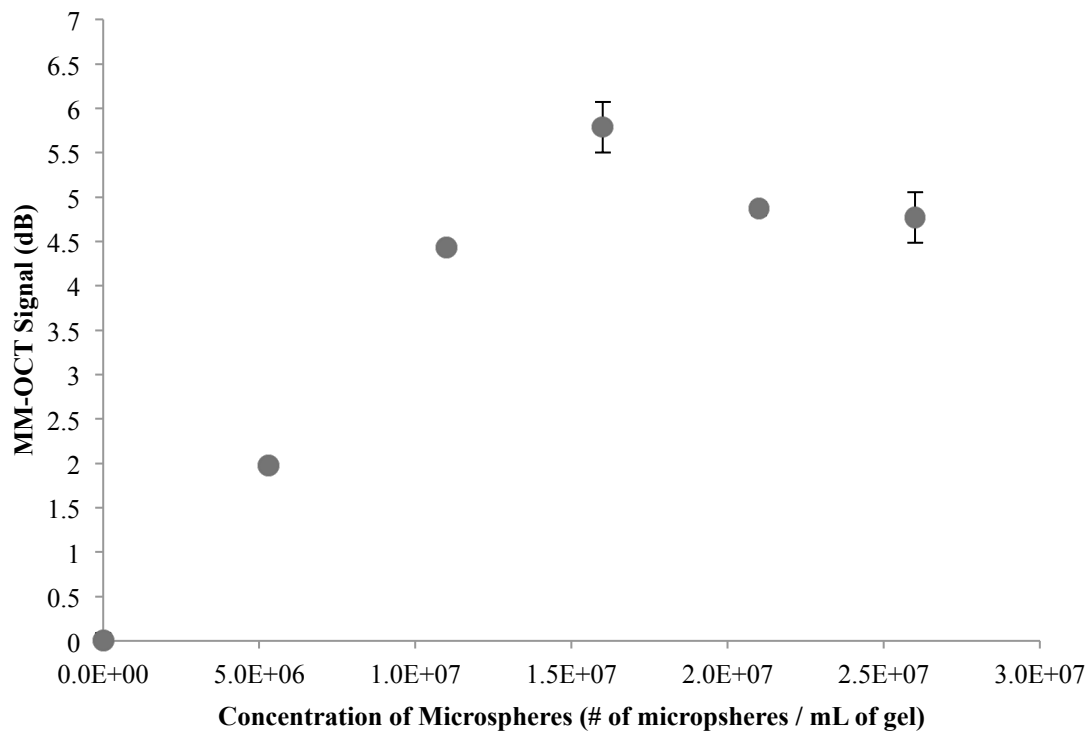


Figure 5.2: MM-OCT signal as a function of increasing microsphere concentration with a constant iron oxide concentration per microsphere. Average MM-OCT signal was calculated by averaging the MM-OCT signal across all the pixels in the image.

According to the MM-OCT images (Figure 5.3) and plot of MM-OCT signal intensity as a function of iron oxide/microsphere synthesis concentration (Figure 5.4), the MM-OCT signal increased linearly with increasing encapsulated iron oxide concentrations up until about 40 mg of iron oxide/mL of oil of the stock solution at the time of synthesis. At higher concentrations, the average magnetomotive signal began to plateau suggestive of a maximum amount of iron oxide that could be encapsulated into these particular protein microspheres. This trend was also observed experimentally during the protein microsphere synthesis. As the iron oxide concentration of the oil stock solutions was increased, increasing amounts of excess iron oxide pelleted to the bottom during centrifugal washing of the protein microspheres. This resulted in an increasing number of washes needed to achieve a clear aqueous layer. This trend was also observed with MRI data used to quantify the iron oxide encapsulated inside the microsphere presented later in this chapter. The last data point shows an increase above the initial plateau, which may be unreliable due to the phase wrapping issues previously described. When looking at the corresponding MM-OCT image in Figure 5.3 (Fe-11), the MM-OCT image is saturated in various areas, individual scatterers cannot be easily distinguished from one another compared to the other images in Figure 5.3.

Table 5.2: Microspheres encapsulated with increasing concentrations of iron oxide in 1% low melting agarose gels.

Label	Iron Oxide Conc.	Microsphere Volume	PBS Volume	Agarose Gel Volume	Total Volume
Fe-00	0.0 mg/mL	75 μ L	125 μ L	7.0 mL	7.2 mL
Fe-01	0.5 mg/mL	75 μ L	125 μ L	7.0 mL	7.2 mL
Fe-02	1.0 mg/mL	75 μ L	125 μ L	7.0 mL	7.2 mL
Fe-03	2.0 mg/mL	75 μ L	125 μ L	7.0 mL	7.2 mL
Fe-04	5.0 mg/mL	75 μ L	125 μ L	7.0 mL	7.2 mL
Fe-05	10.0 mg/mL	75 μ L	125 μ L	7.0 mL	7.2 mL
Fe-06	15.0 mg/mL	75 μ L	125 μ L	7.0 mL	7.2 mL
Fe-07	20.0 mg/mL	75 μ L	125 μ L	7.0 mL	7.2 mL
Fe-08	40.0 mg/mL	75 μ L	125 μ L	7.0 mL	7.2 mL
Fe-09	60.0 mg/mL	75 μ L	125 μ L	7.0 mL	7.2 mL
Fe-10	80.0 mg/mL	75 μ L	125 μ L	7.0 mL	7.2 mL
Fe-11	100.0 mg/mL	75 μ L	125 μ L	7.0 mL	7.2 mL

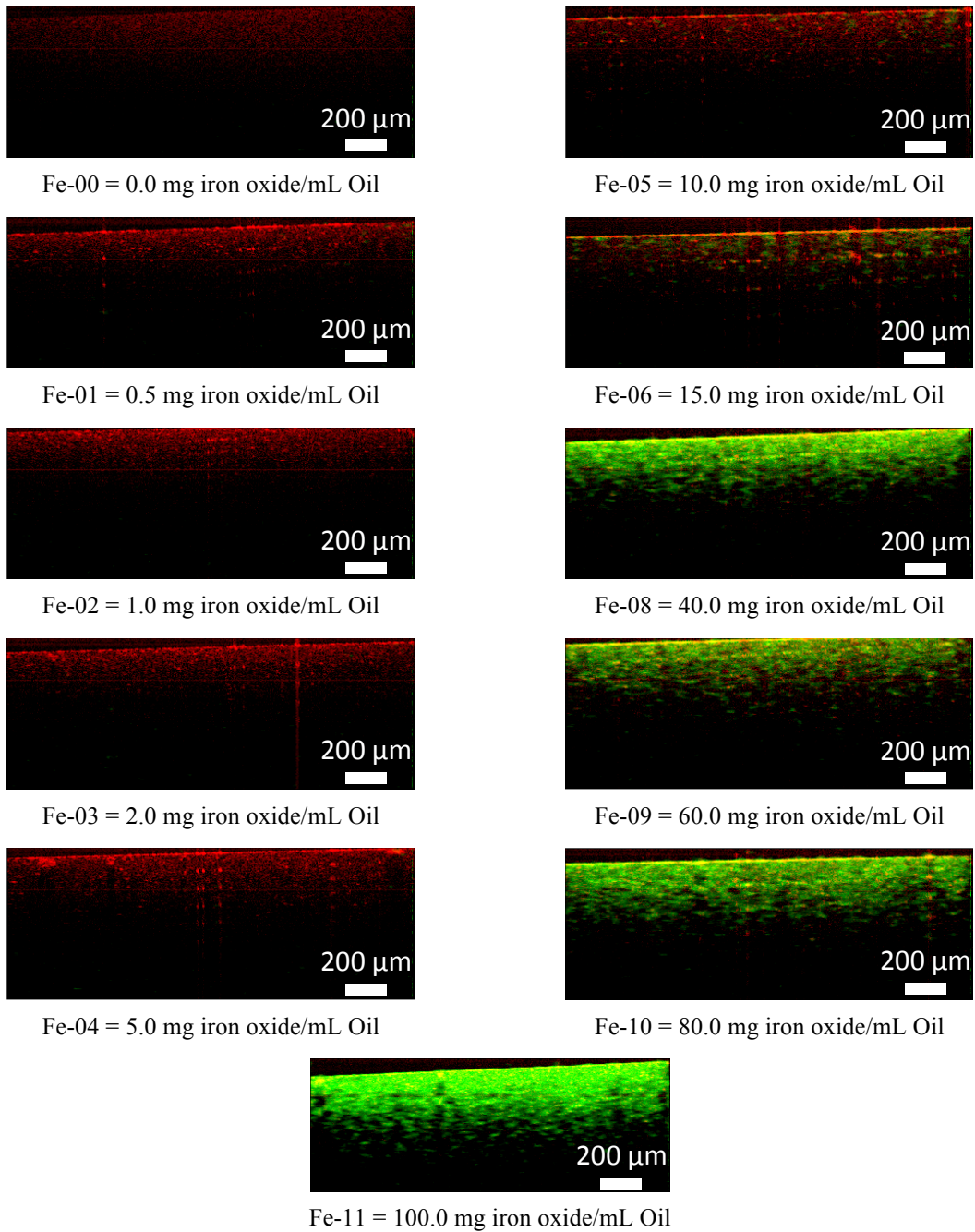
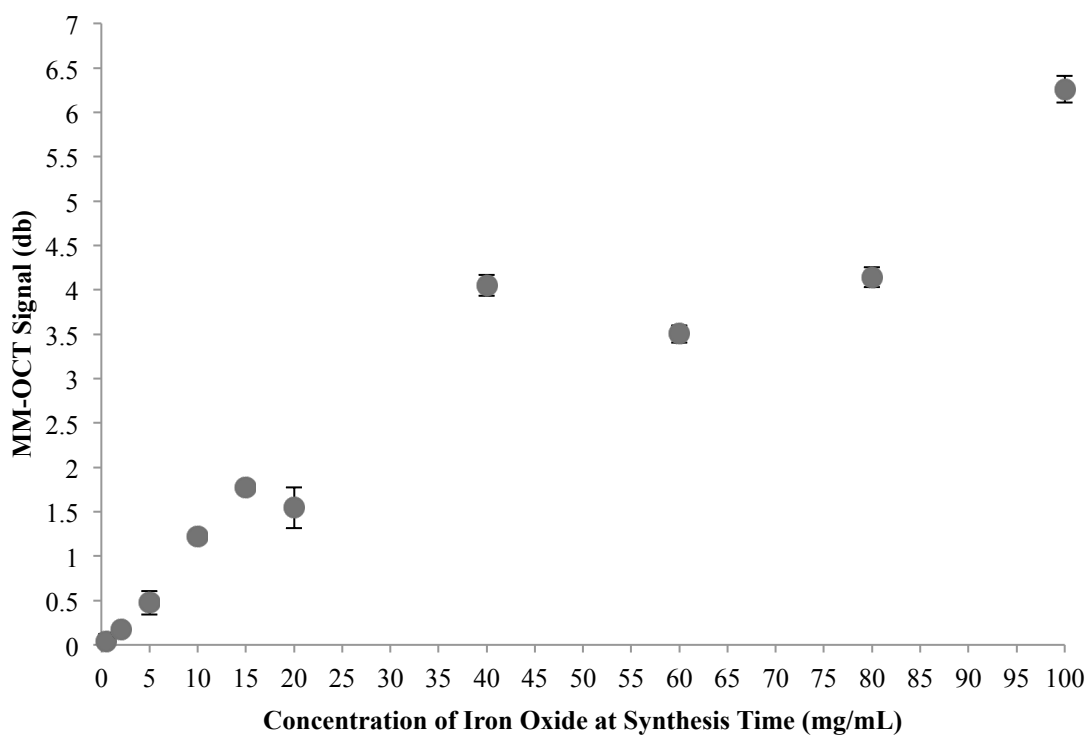


Figure 5.3: Representative MM-OCT images of agarose gels of protein microspheres with increasing concentration of encapsulated iron oxide. The microspheres were suspended into 1% agarose gels at a concentration of $\sim 1.0 \times 10^7$ microspheres/mL.



Sample Name	Concentration of Iron Oxide in Oil Stock Solution	Sample Name	Concentration of Iron Oxide in Oil Stock Solution
Fe-00	0.0 mg/mL	Fe-06	15.0 mg/mL
Fe-01	0.5 mg/mL	Fe-07	20.0 mg/mL
Fe-02	1.0 mg/mL	Fe-08	40.0 mg/mL
Fe-03	2.0 mg/mL	Fe-09	60.0 mg/mL
Fe-04	5.0 mg/mL	Fe-10	80.0 mg/mL
Fe-05	10.0 mg/mL	Fe-11	100.0 mg/mL

Figure 5.4: MM-OCT signal as a function of increasing inner core iron oxide concentration inside the microsphere with a constant concentration of microspheres per volume of agarose gel. Microspheres were embedded into a 1% agarose gel at a concentration of 10^6 / mL of gel.

5.2.2 Quantification of Encapsulated Iron Oxide using MRI

The saturation of the MM-OCT signal observed in Figure 5.4 could be due to a couple of reasons including the saturation limits of the imaging system or reaching the maximum encapsulation concentration of iron oxide in the protein microsphere. To determine the cause of the saturation, it was necessary to identify a method to quantify the amount of iron oxide encapsulated in the microsphere. Several methods were explored to quantify the amount of iron oxide to determine if the maximum encapsulation capacity of iron oxide had been reached. Methods for accurately measuring the amount of iron oxide concentration include magnetic relaxometry and Prussian blue staining [8, 9]. Prussian blue staining can penetrate the protein shell and stain the encapsulated iron oxide when allowed to stain for a period of at least 25-30 minutes. To quantify the iron concentration using Prussian blue staining, absorption spectra of the stained microspheres was measured using a Beckman DU-640 spectrophotometer over the range of 190-1100 nm. The main absorption peak for Prussian blue is at 650 nm. Although the Prussian blue clearly stained the iron oxide particles inside the microspheres on visual inspection when compared to microspheres without iron oxide, the broad and strong absorption of the microsphere interfered with the detection of the Prussian blue absorption peak.

MRI was another potential method for quantifying the iron oxide concentration in microspheres. Superparamagnetic iron oxide (SPIO) nanoparticles have been extensively studied as MRI contrast agents both *in vitro* and *in vivo* for cancer applications [9-31]. The 14.1 Tesla Varian system with a bore magnet 89 mm in size and a 600 MHz Varian Unity / Inova NMR spectrometer from the Biomedical Imaging Center of the Beckman Institute for Advanced Science and Technology at the University of Illinois at Urbana-Champaign was

used. From the MRI studies presented in Figures 5.5-5.10, the iron oxide nanoparticles in oil or the iron oxide-filled protein microspheres were suspended in 1% low melting agarose gels. The gels were allowed to solidify in capillary tubes. To reduce the formation of air bubbles and the potential settling of microspheres that would contribute to sample inhomogeneities, the capillary tubes were vortexed and placed into a water bath at room temperature to facilitate a rapid and uniform solidification process. The MRI measurements were taken at four different echo times of 3.3 ms, 5.0 ms, 7.0 ms, and 9.0 ms. Nineteen MRI slices were taken throughout the full volume of the gel in the capillary tubes.

A standard curve was created using the MRI measurements from agarose gels with increasing concentrations of iron oxide nanoparticles between 10-25 μg of iron oxide/mL of agarose gel. The mean MRI signals as a function of the echo times are plotted in Figure 5.5. From this data, the relaxation times ($T2^*$) were extracted using a Matlab script code and the relative volume distribution plotted as a function of the $T2^*$ values. The relaxation rates ($R2^*$) were calculated from the $T2^*$ values and plotted against the concentration of iron oxide (mM) demonstrating a linear correlation as shown in Figure 5.6. The relaxivity per iron oxide particle was determined by fitting a linear regression line to the plot in Figure 5.6. The relaxivity was found to be $621.0 \text{ mM}^{-1}\text{s}^{-1}$ per iron oxide (Fe_2O_3) particle or $310.5 \text{ mM}^{-1}\text{s}^{-1}$ per iron particle using a 14.1 T field, which is on the same order of magnitude to previously published reports of 500-550 $\text{mM}^{-1}\text{s}^{-1}$ for Fe_2O_3 using a 4.7 T field [11], 134 $\text{mM}^{-1}\text{s}^{-1}$ for Fe_2O_3 using a 1.5 T field [13], and 61.16-505 $\text{mM}^{-1}\text{s}^{-1}$ per Fe of iron oxide particles [12]. The variability in relaxivity depends on several factors including the core size of the iron oxide and the ligands that are complexed with the iron oxide [11-13, 22, 23].

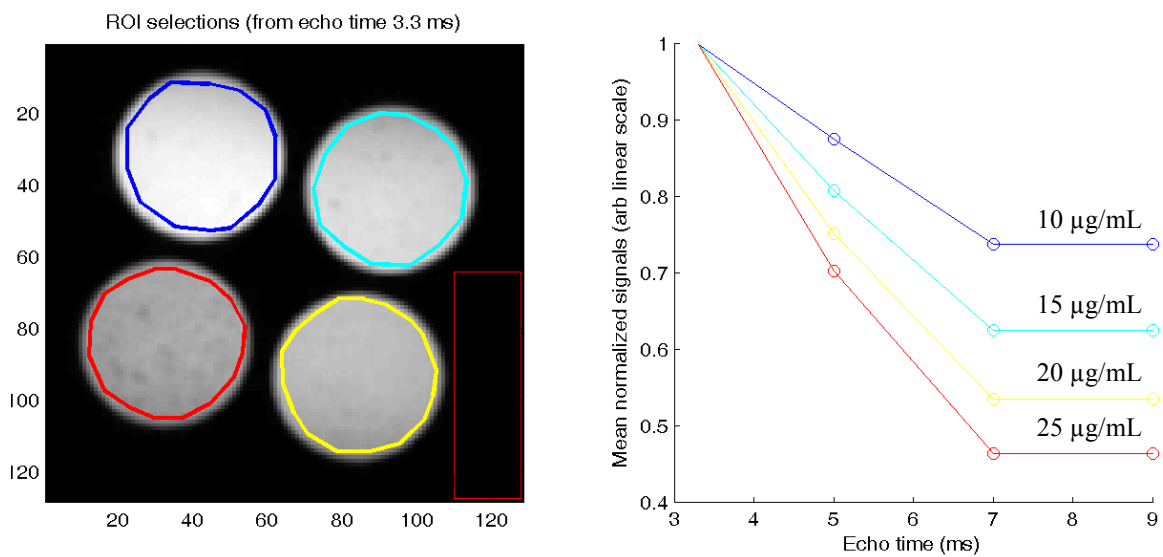


Figure 5.5: MRI measurements of agarose gels with increasing concentrations of iron oxide. On the left side is a representative MRI slice from a volume of 19 images taken. The graph on the right plots the mean normalized MRI signal from the 19 images against the echo time.

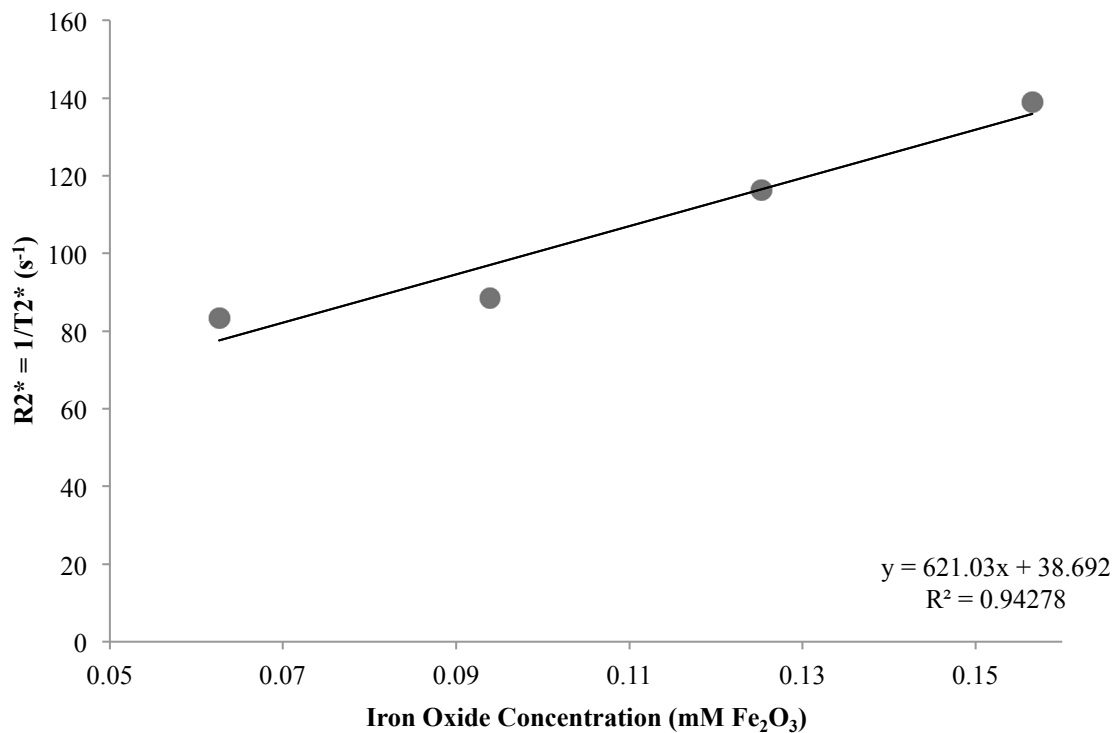


Figure 5.6: Plot of relaxation rate [$R2^*$ or $1/T2^*$ (s^{-1})] as a function of the non-encapsulated iron oxide concentration of the gel phantoms. The relaxivity, r_2 , calculated from the slope of the plot was determined to be $621.0 \text{ mM}^{-1}\text{s}^{-1}$.

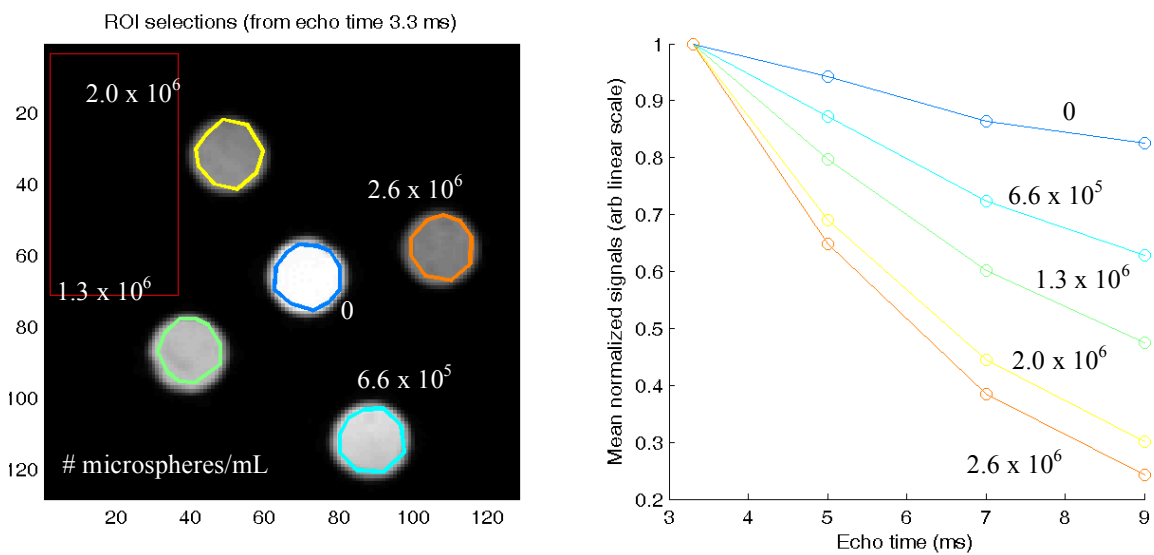


Figure 5.7: MRI measurements of agarose gels with increasing concentration of microspheres with constant inner iron oxide concentration (oil stock solution iron oxide concentration = 15.0 mg/mL). On the left side is a representative MRI slice from a volume of 19 images taken. The graph on the right plots the mean normalized MRI signal from the 19 images against the echo time.

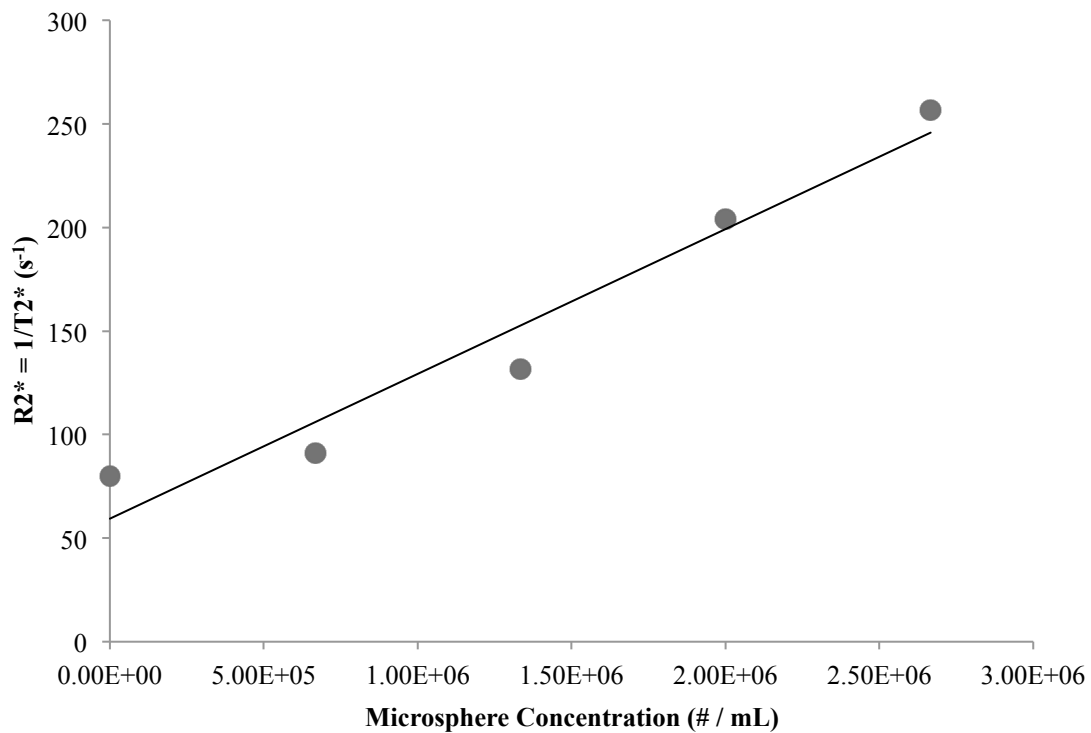


Figure 5.8: Plot of relaxation rate [$R2^*$ or $1/T2^*$ (s^{-1})] as a function of the microsphere concentration ($\# / \text{mL}$). The iron oxide concentration of the oil stock solution used for the microsphere synthesis was constant at 15.0 mg/mL.

A similar experiment using increasing concentrations of iron oxide-filled microspheres was performed to determine the upper limit for quantifying the microsphere concentration using the MRI system. Agarose gels with increasing concentrations of microspheres ranging from 6×10^5 to 2.6×10^6 microspheres/mL were imaged. The inner core iron oxide concentration per microsphere was kept constant with an oil stock iron oxide concentration of 15.0 mg/mL. The MRI data is presented in Figure 5.7. The relaxation rates ($R2^*$) were calculated from the $T2^*$ values and plotted against the microsphere concentration demonstrating a linear correlation (Figure 5.8).

A subset of the microspheres previously prepared for the MM-OCT iron quantification experiment presented in Table 5.2 and Figure 5.3 was used for the MRI iron quantification experiment in Table 5.3.

Table 5.3: Relative Iron Oxide Concentration of Iron Oxide-filled Protein Microspheres used for MRI Experiments.

Concentration of Iron Oxide at Synthesis Time	
Fe-00	0.0 mg/mL
Fe-02	1.0 mg/mL
Fe-04	5.0 mg/mL
Fe-06	15.0 mg/mL
Fe-07	20.0 mg/mL
Fe-08	40.0 mg/mL
Fe-09	60.0 mg/mL
Fe-10	80.0 mg/mL

The iron oxide-filled microspheres were suspended in 1% low melting agarose gels at a concentration of $\sim 2.0 \times 10^6$ microspheres/mL of gel and allowed to solidify inside the capillary tubes as previously described. The $T2^*$ values were extracted from the average MRI values over the volume of 19 MRI slices at the four echo times: 3.3 ms, 5.0 ms, 7.0 ms, and 9.0 ms.

Using the iron oxide concentration standard curve in Figure 5.6, the iron oxide concentrations were calculated from the $T2^*$ values. Using the concentration of microspheres measured from the DLS instrument, the iron oxide concentration per microsphere was calculated and plotted in Figure 5.11. A linear trend was observed at concentrations lower than 20 mg/mL of iron oxide in the oil stock solution (Figure 5.12). At oil stock concentrations of iron oxide greater than 20 mg/mL, the $T2^*$ values became constant (Figure 5.11). This trend indicated that the maximum encapsulated iron oxide/microsphere concentration had been reached. These findings agree with the MM-OCT results in Figure 5.3 and Figure 5.4, which found the maximum average magnetomotive OCT signal/microsphere reaching a plateau for microspheres made with iron oxide oil stock concentrations greater than 20-40 mg/mL. The MRI and MM-OCT both confirm the presence of an upper limit for encapsulating iron oxide nanoparticles into the protein microspheres. Based on these results, the average maximum effective amount of iron oxide encapsulated into a single microsphere was determined to be approximately ~ 14 ng. These calculations are made on the assumption that the encapsulation of iron oxide inside the microspheres does not change the relaxivity of iron oxide since the iron oxide was suspended in the oil in both samples. The microenvironment surrounding the iron oxide should be fairly similar between the non-encapsulated and encapsulated iron oxide.

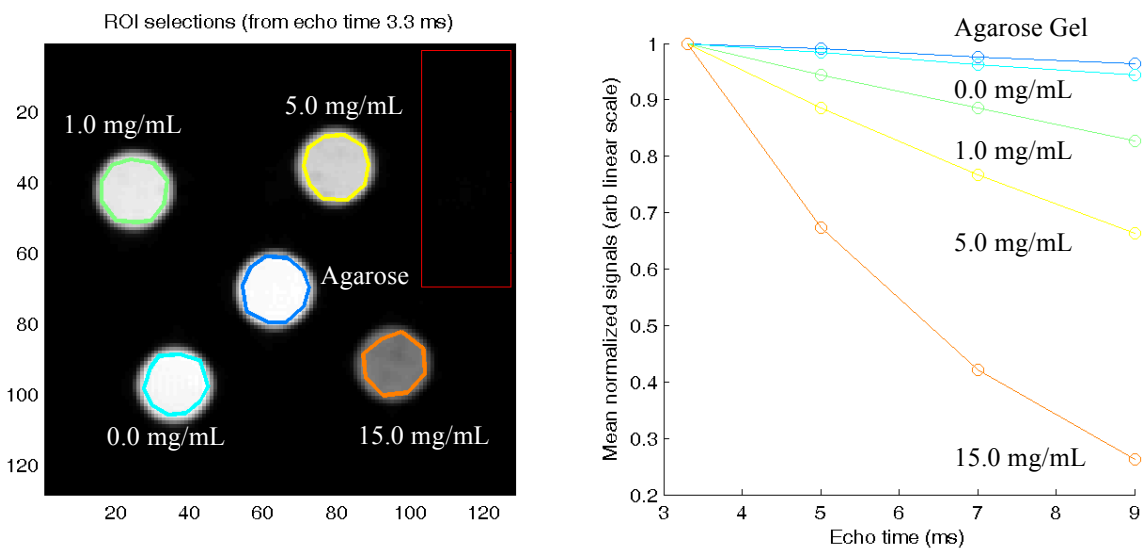


Figure 5.9: MRI measurements of agarose gels with microspheres of increasing inner core iron oxide concentration. On the left side is a representative MRI slice from a volume of 19 images taken. The graph on the right plots the mean normalized MRI signal against the echo time.

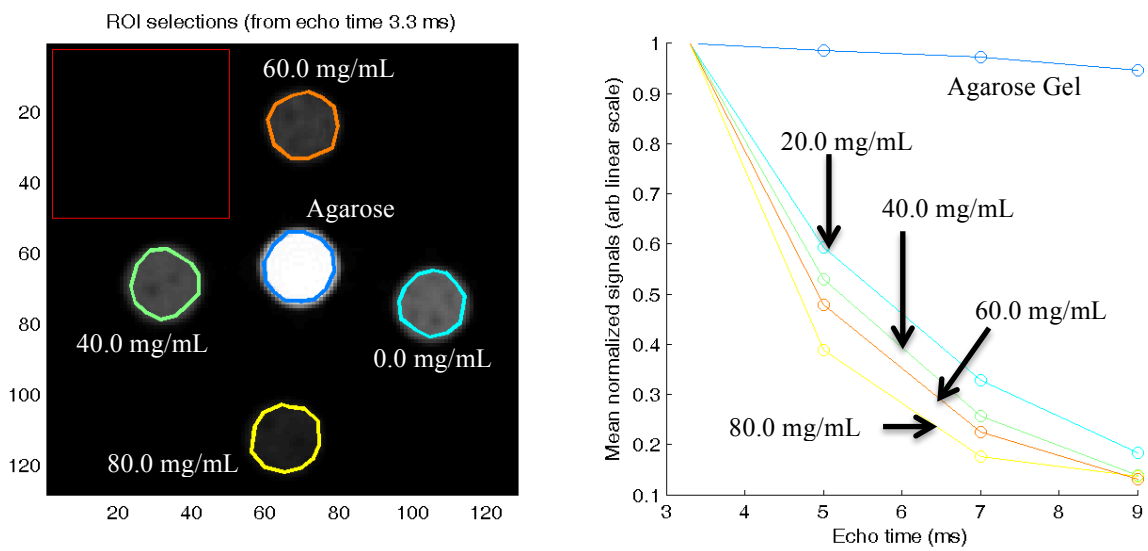
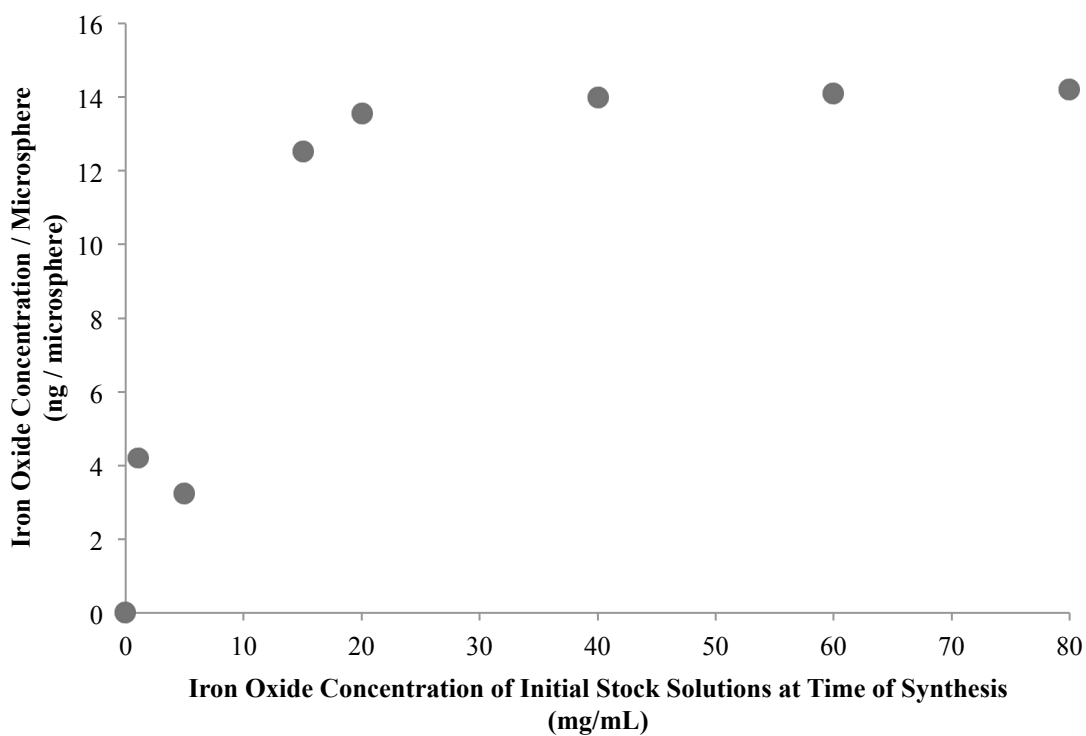


Figure 5.10: MRI measurements of agarose gels with microspheres of increasing inner core iron oxide concentration. On the left is a representative MRI slice from a volume of 19 images taken. The graph on the right plots the mean normalized MRI signal against the echo time.



	T2*	iron oxide concentration during synthesis - mg/mL	ng iron oxide / # of Microspheres
Agarose	N/A	0	0
Fe-00	N/A	0	0
Fe-02	11.7	1	4.2
Fe-04	12.6	5	3.2
Fe-06	4.5	15	12.5
Fe-07	3.4	20	13.6
Fe-08	3	40	14.0
Fe-09	2.9	60	14.1
Fe-10	2.8	80	14.2

Figure 5.11: The iron oxide / microsphere concentration calculated from the measured T2* value and plotted against the initial concentration of iron oxide in the oil stock solution used to synthesize the protein microspheres.

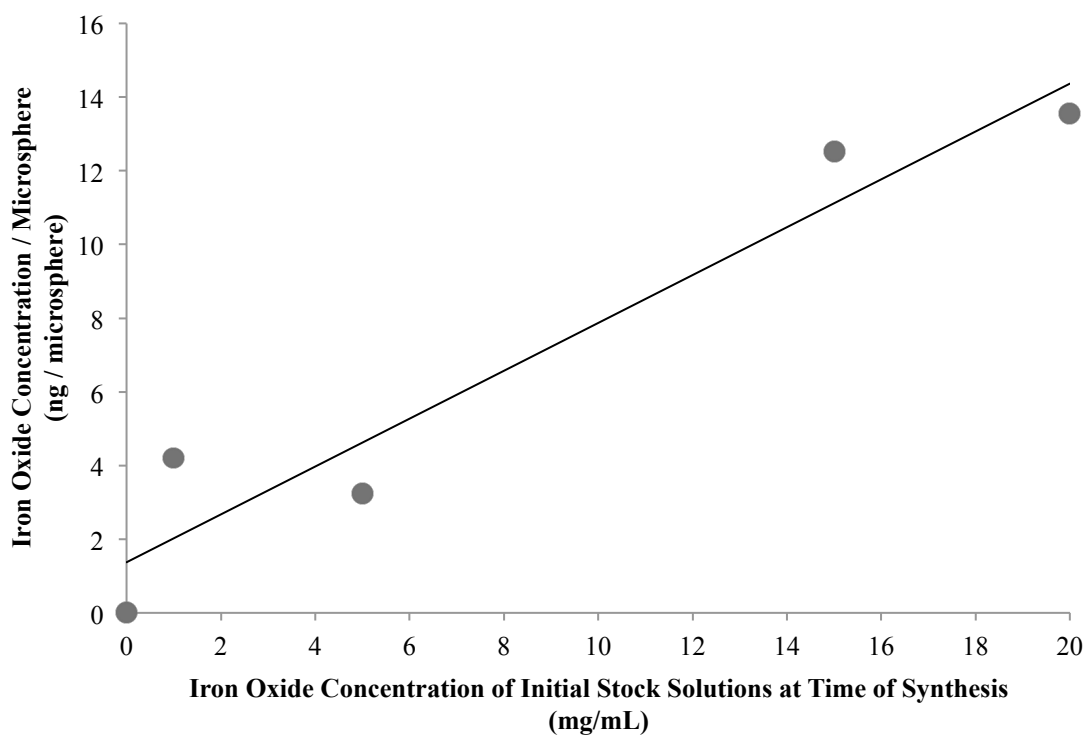


Figure 5.12: Zoomed in graph of Figure 5.11 demonstrating the linear relationship of iron oxide / microsphere concentration as a function of the initial concentration of iron oxide in the oil stock solution used to synthesize the protein microspheres.

5.3 Protein Microspheres as Fluorescent Contrast Agents

Fluorescent dyes such as FITC, Bodipy, Nile Red, and Heptamethylcyanine NIR dye have previously been encapsulated into protein microspheres [1-3]. The use of NIR dyes is most advantageous in the field of biomedical optical imaging due to the deeper penetration depth possible with NIR light. In this region of the spectrum, the fluorescence peak of the encapsulated dye should have minimal overlap with the strong tissue autofluorescence found in the visible region of the spectrum. The NIR dye previously encapsulated by Toublan was reported to be unstable, resulting in a loss of the fluorescence properties within 24 hours of synthesis [3]. In addition, the peak absorption for this particular NIR dye is at 800 nm, which is above the current maximum excitation wavelength (760 nm) of the wide-field fluorescence imaging system (CRi Maestro) in our laboratory. This section focuses on the encapsulation of DiR iodide [1,1-dioctadecyl-3,3,3,3-tetramethylindotricarbocyanine iodide], a NIR fluorescent dye, optimizing the protein microspheres for the wide-field fluorescence imaging system, and studying the effects of encapsulating both magnetic and fluorescent agents into a single microsphere on its fluorescence properties.

Nile Red [5H-benzo-phenoxa-5-one-9-diethylamine] filled microspheres have previously been synthesized and characterized by Prof. Suslick's research group [3, 5]. The Nile Red-filled microspheres were previously reported to have an emission peak at approximately 580 nm when excited between 450 nm and 550 nm [3, 5]. The encapsulation efficiency of Nile Red into the microspheres was reported to be at 68% for Nile Red-filled BSA microspheres [5]. The Nile Red-filled microspheres can be used in both the wide-field fluorescence imaging system for small animal *in vivo* imaging and on a standard fluorescence

or confocal microscope for histopathological analysis. The latter application may be useful for confirming the localization of microspheres or their contents in tissue.

DiR is part of a group of lipophilic dyes commonly used to stain lipids such as membranes for cellular applications. DiR has a reported excitation maximum at 750 nm and a maximum emission at 780 nm. DiR was initially suspended in hexane and dissolved into the oil stock solution. The hexane was evaporated in a protocol similar to the Nile Red and iron oxide oil suspensions. Although the dye appeared to be well dissolved in the oil and assumed to be encapsulated into the microspheres, the fluorescence properties of the DiR were vastly diminished during this process. The 80°C water bath used to evaporate the hexane was too high, causing a large loss in the fluorescence properties of DiR and a shift in the fluorescence excitation and emission. Other solvents were explored to make the DiR more miscible in oil while conserving the absorption and fluorescence properties of DiR. Methanol, ethanol, dichloromethane [32], and hexane were used to dissolve the DiR into the oil suspension. The solvents were evaporated by placing them in a water bath at temperatures listed in Table 5.4 and by bubbling nitrogen gas through the oil solution during the evaporation.

Table 5.4: Solvents Used to Dissolve DiR into Vegetable Oil.

Solvent	Boiling Point	Temperature Used for Evaporation
Ethanol	78°C	55°C
Methanol	65°C	55°C
Dichloromethane	40°C	55°C
Hexane	69°C	55°C

Microspheres were synthesized from each of these resulting oil stock solutions and embedded into 1% agarose gel phantoms at equal microsphere concentrations. The gel samples were imaged using the wide-field imaging system with an excitation window between 670 nm and 710 nm, and an emission detection window greater than 750 nm. The results in Figure 5.13 indicated that the use of ethanol, nitrogen bubbling, and the lower water bath temperature proved to be the most successful in preserving the fluorescence properties of the dye during the microsphere synthesis process.

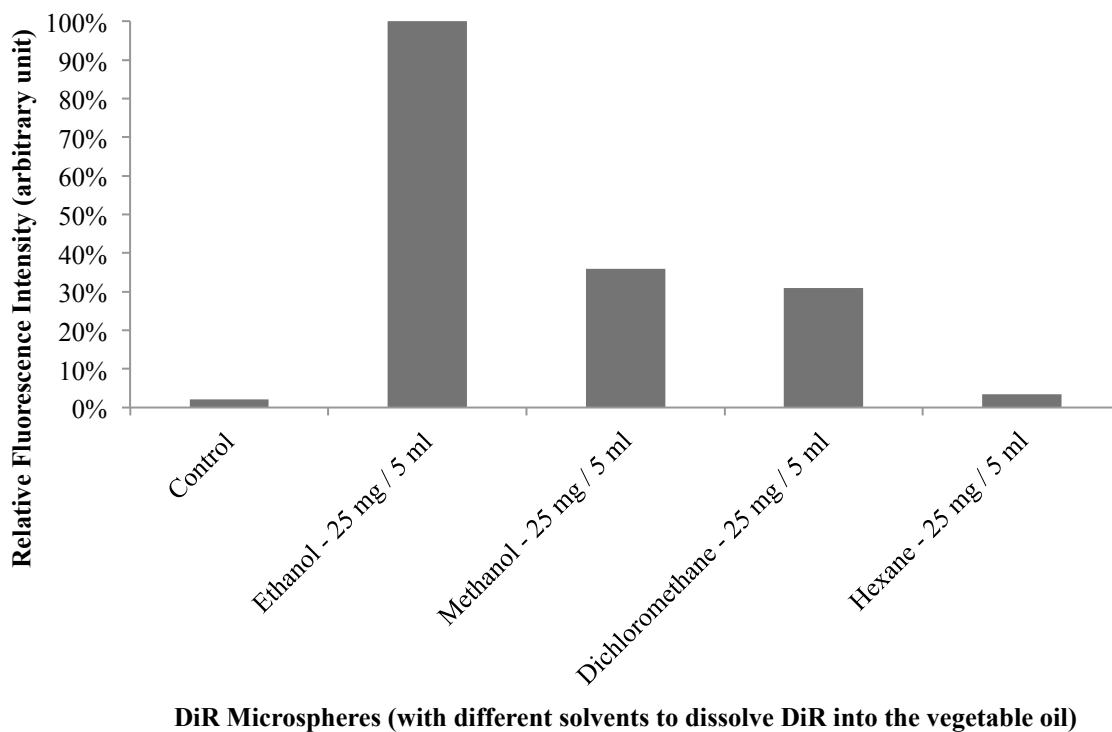
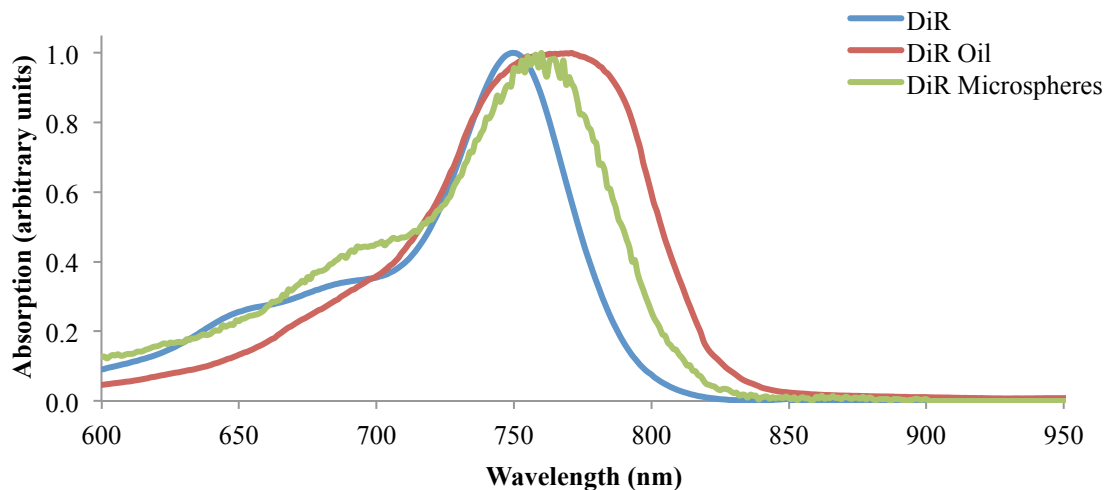


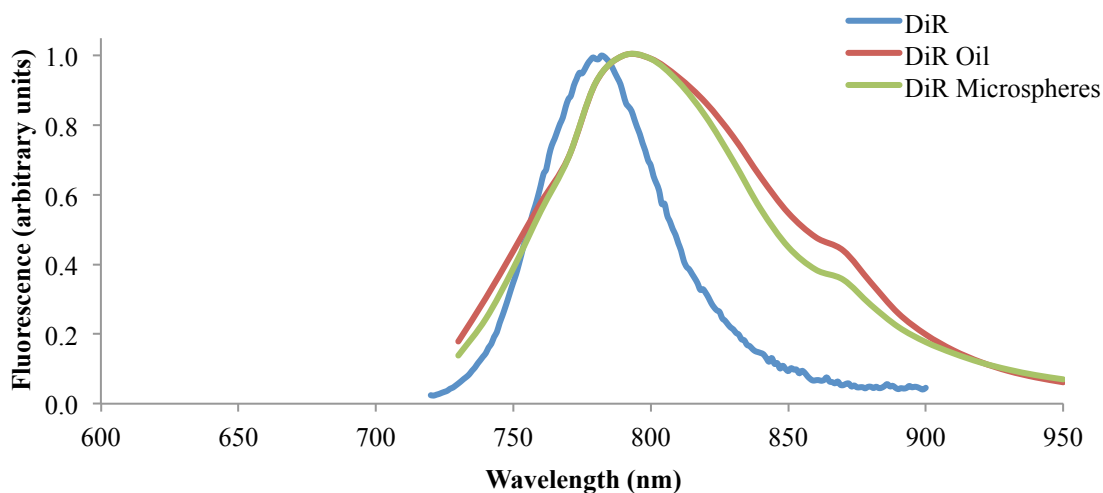
Figure 5.13: Relative fluorescence intensity of DiR encapsulated microspheres prepared using different solvents to dissolve the DiR into the oil.

Given the sensitivity of DiR to elevated temperatures and light exposure, additional studies examined the stability of the absorption and fluorescence properties of the DiR through each major step of the microsphere synthesis. The absorption spectra of DiR in oil, and of the synthesized DiR-filled microspheres were measured on a UV-VIS spectrophotometer (Synergy H1 Multi-Mode Reader). The fluorescence spectra were acquired on the wide-field fluorescence imaging system (CRi Maestro) using an excitation light source at 670-710 nm. The main regions of interest for DiR are 600-900 nm for the excitation peak and 700-950 nm for the emission peak. The results, presented in Figure 5.14, show a slight red shift in both the absorption and emission peaks of DiR once dissolved into vegetable oil with little to no significant changes to the spectral shape of the DiR absorption and emission peaks.

Similarly, the absorption and fluorescence properties of the Nile Red dye was also measured through each step of the Nile Red-filled protein microsphere synthesis. The absorption spectra of Nile Red in oil, and of the synthesized Nile Red-filled protein microspheres were measured on a UV-VIS spectrophotometer (Synergy H1 Multi-Mode Reader). The fluorescence spectra were measured on the wide-field fluorescence imaging system (CRi Maestro) using an excitation light source at 503-555 nm. Compared to the DiR, there was a blue shift in both the absorption and fluorescence spectra for the Nile Red once it was dissolved into the oil and encapsulated inside the microsphere (Figure 5.15). Based on these spectra, the encapsulation process had minimal effect on the absorption and fluorescence spectral shape and location.



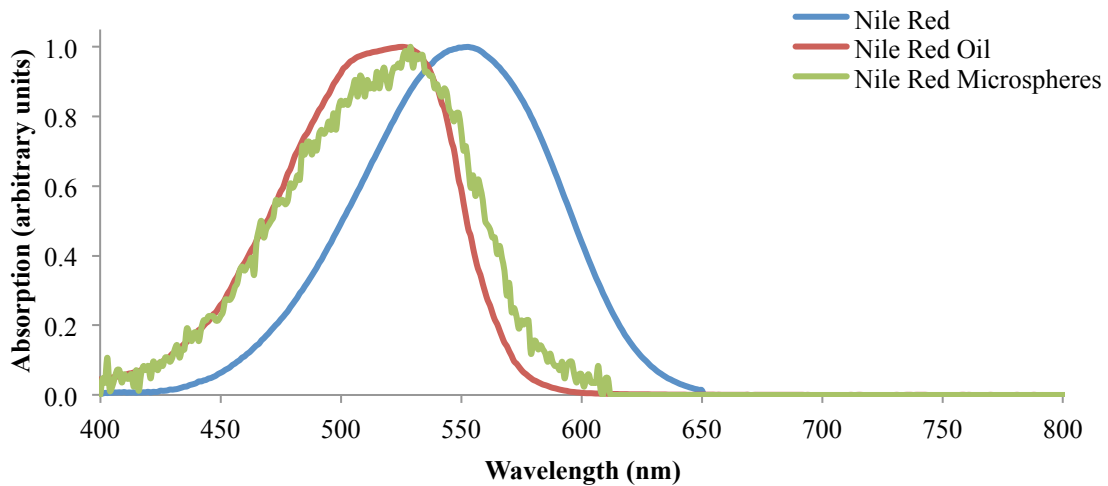
(a)



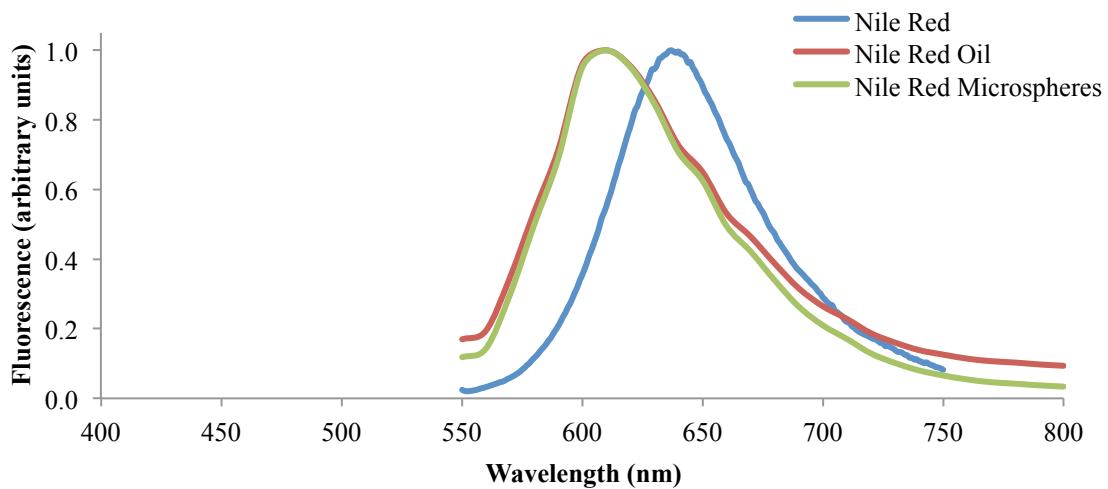
(b)

	Peak Excitation Wavelength	Peak Emission Wavelength
DiR	750 nm	779 nm
DiR in Oil	770 nm	790 nm
DiR in Microspheres	760 nm	790 nm
Fluorescence Imaging System	670-710 nm	> 750 nm

Figure 5.14: Absorption (a) and fluorescence (b) properties of DiR through each major step of microsphere synthesis. *Absorption and fluorescence data from manufacturer (Life Technologies). ** Fluorescence data was acquired using excitation at 670-710 nm.



(a)



(b)

	Excitation Wavelength	Emission Wavelength
Nile Red*	553 nm	637 nm
Nile Red in Oil**	525 nm	610 nm
Nile Red in Microspheres**	528 nm	610 nm
Fluorescence Imaging System	503-555 nm	> 580 nm

Figure 5.15: Absorption (a) and fluorescence (b) properties of Nile Red through each major step of the microsphere synthesis. * Absorption and fluorescence data from manufacturer (Life Technologies). ** Fluorescence data was acquired using excitation at 503-555 nm.

5.3.1 Protein Microspheres under the Wide-field Fluorescence Imaging System

The wide-field fluorescence imaging system was used to detect and to quantify the microspheres in gels using the measured fluorescence signal. The optimum concentration of microsphere for detection by the fluorescence imaging system was assessed. In addition, since there was not necessarily a high overlap between the bandpass filter windows provided by the instrument and the excitation peaks of the fluorophores (DiR and Nile Red), it was necessary to ensure that there was adequate overlap to excite and detect the fluorophores.

Two batches of microspheres were synthesized to examine two different spectral regions. The DiR-filled microspheres were synthesized using an oil stock solution with a concentration of 50 mg/mL of iron oxide and 10 mg/mL of DiR. The average fluorescence intensity per pixel in the region of interest increased linearly with the concentration of microspheres. The Nile Red-filled microspheres were made using an oil stock solution with a concentration of 50 mg/mL of iron oxide and 1 mg/mL of Nile Red dye. Similar to the DiR-filled microspheres, a linear trend was observed with increasing microsphere concentrations (Figure 5.17 and Figure 5.18). At microsphere concentrations greater than 3.7×10^6 /mL, the fluorescence signal saturated the detection system.

Each fluorescent dye has its advantages and disadvantages. A disadvantage of Nile Red-filled microspheres is the strong overlap with tissue autofluorescence within the visible range, making it potentially difficult to spectrally resolve during *in vivo* targeting experiments in rats. The advantage of using the spectral range of DiR is the deeper tissue penetration with NIR light. There is also less spectral overlap between the emission spectrum of DiR and tissue autofluorescence. In contrast, the primary advantage of Nile Red-filled microspheres is that they have higher fluorescence intensities compared to DiR-filled microspheres due to both the

higher degree of overlap between the absorption peak and the imaging system's bandpass filter window and the higher quantum efficiency of the Nile Red dye relative to the DiR dye. The quantum yield for Nile Red is 0.7 [33, 34] compared to 0.25 for DiR [32]. However, equally important to the quantum yield would be the fluorescence lifetime, or the time in which the fluorophore spends in the excited state before the detected photon is emitted. The fluorescence lifetime of Nile Red has been reported to be 4.50 ns [33] and the fluorescence lifetime of DiR was 1.1 ns [32].

To further investigate the viability of these dye and iron oxide filled microspheres for long-term imaging for future *in vivo* experiments, the Nile Red and iron oxide filled-microspheres and DiR and iron oxide-filled microspheres were embedded into a 1% agarose gel and imaged under the wide-field fluorescence imaging system (CRi Maestro). The imaging was done over a period of 2 hrs using continuous light source exposure (503-555 nm for Nile Red; 670-710 nm for DiR) and fluorescence measurement acquisition every 60 s. Over that time period, the Nile Red and iron oxide-filled microspheres showed a 57% decrease in fluorescence intensity as the Nile Red dye (Figure 5.19). However, over that same period of time, the DiR and iron oxide-filled microspheres, the fluorescence intensity increased by 39% (Figure 5.19). These results indicate that although Nile Red-filled microspheres with a higher quantum yield are able to produce higher intensity fluorescent images (~40-50x fluorescence intensity difference in the experiments above), compared to DiR-filled microspheres; over longer continuous imaging periods, the fluorescence lifetime of DiR becomes the more dominant factor allowing for better long-term imaging and decreased rates of photobleaching with DiR compared to Nile Red.

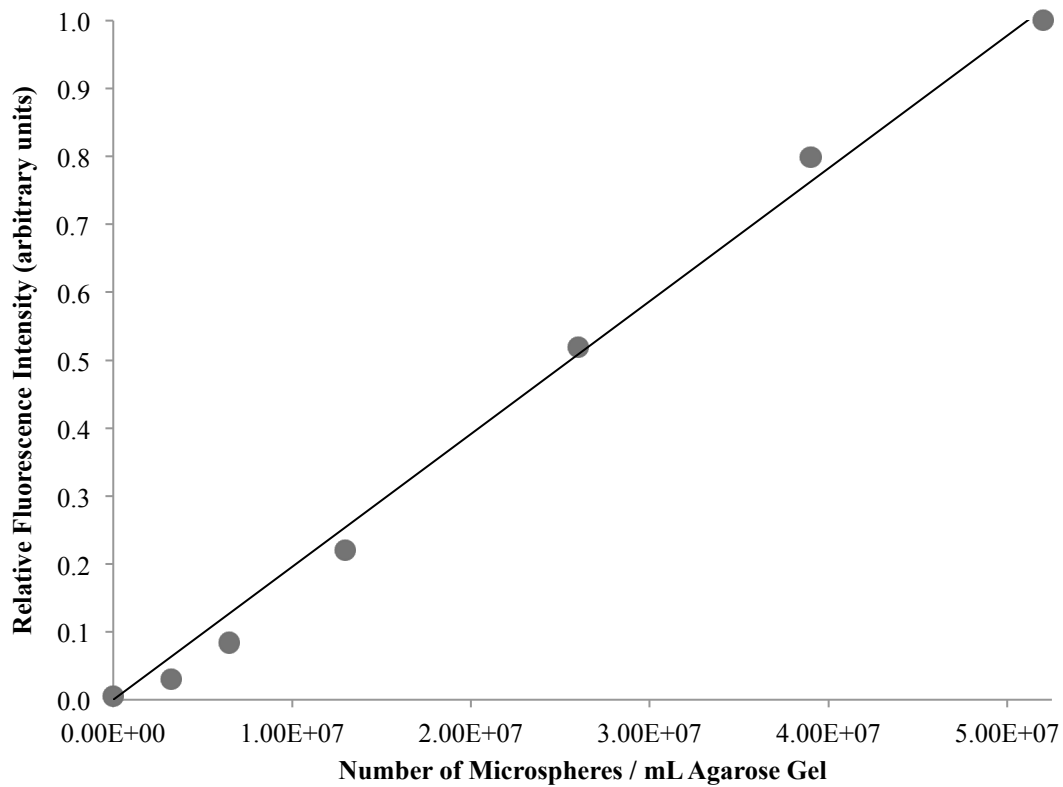


Figure 5.16: Effect of DiR-filled microspheres concentration on fluorescence intensity. Microspheres were made with an oil stock solution of 50 mg/mL iron oxide and 10 mg/mL DiR dye. Agarose gels with increasing concentration of DiR-filled fluorescence microspheres were measured using the wide-field fluorescence imaging system. The results show a linear trend and indicate that the fluorescence signals do not saturate the detection system.

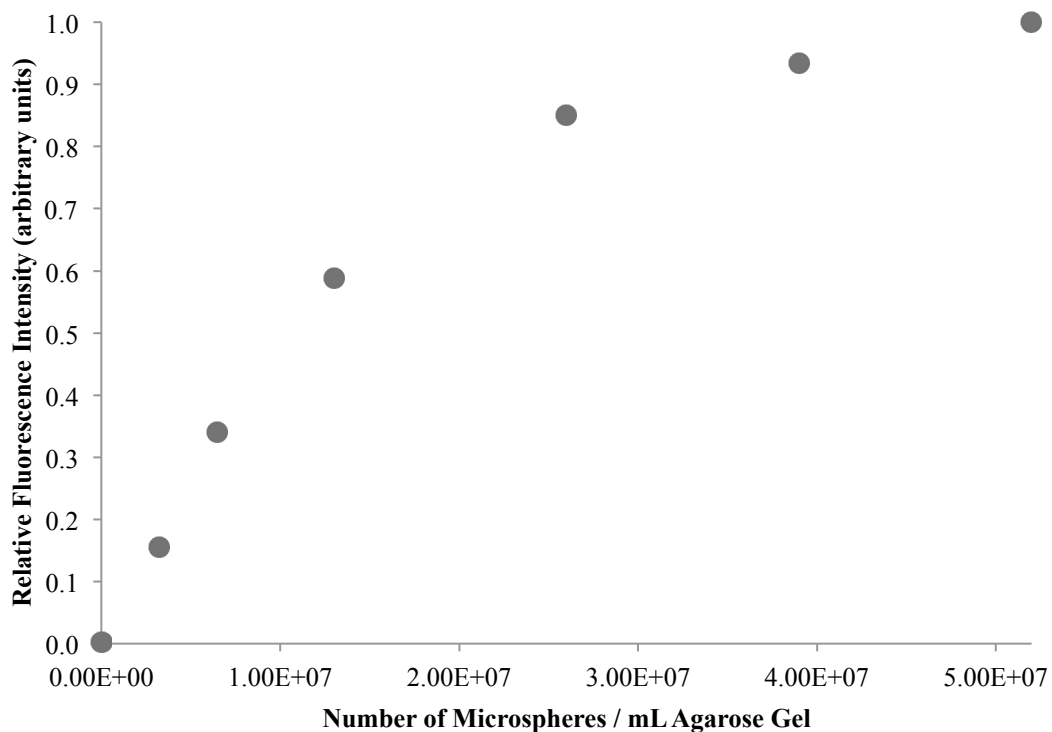


Figure 5.17: Effect of Nile Red microspheres concentration on fluorescence intensity. Microspheres were made with an oil stock solution of 50 mg/mL iron oxide and 1 mg/mL Nile Red dye. Agarose gels with increasing concentration of Nile Red-filled microspheres were measured using the wide-field fluorescence imaging system. The results show a linear trend followed by a plateau where the Nile Red-filled microspheres saturate the detection system.

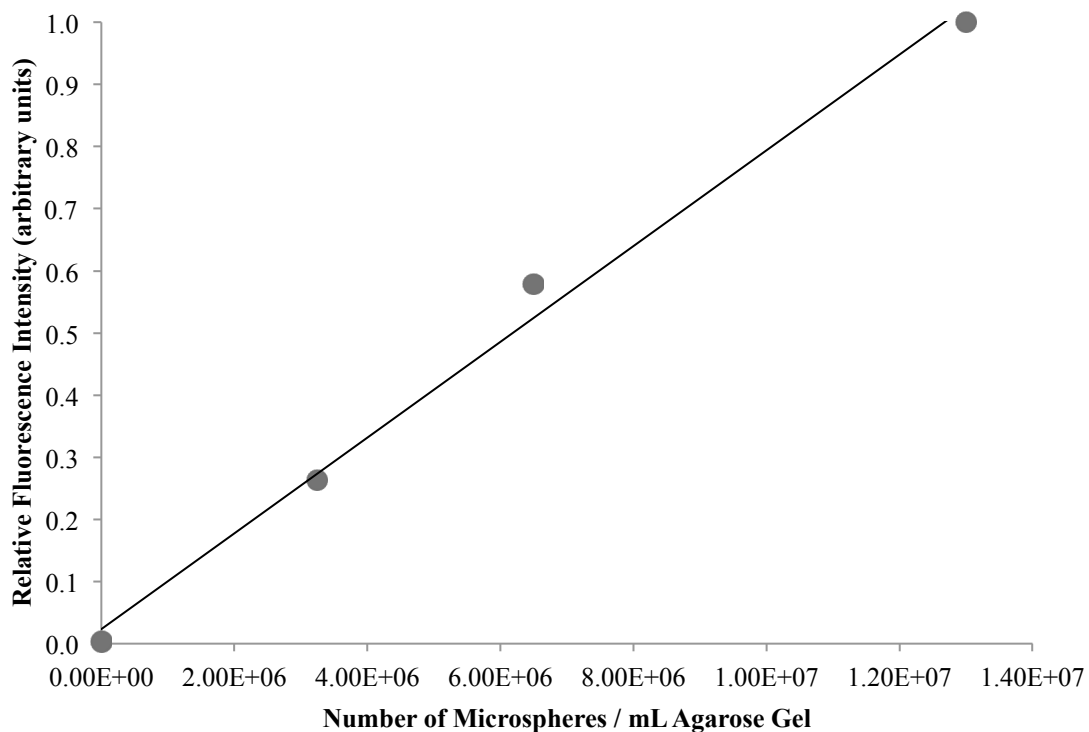


Figure 5.18: Figure 5.17 zoomed in on the range of 0-1.4 x 10⁷ microspheres to better depict the linear correlation between concentration of Nile Red-filled microspheres and the measured fluorescence intensity. Microspheres were made with an oil stock solution of 50 mg/mL iron oxide and 1 mg/mL Nile Red dye.

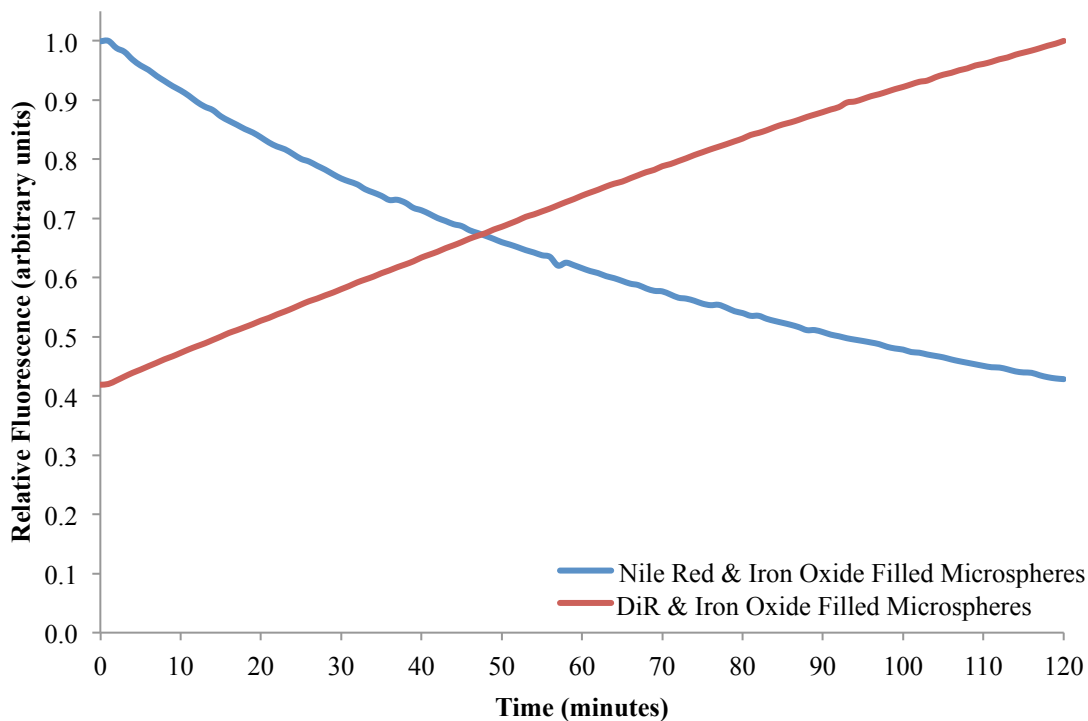


Figure 5.19: Nile Red and iron oxide filled microspheres (blue line) and DiR and iron oxide filled microspheres (red line) were embedded into a 1% agarose gel. The gels were imaged under the wide-field fluorescence imaging system (CRi Maestro) over a period of 2 hours using continuous light source exposure (503-555 nm for Nile Red; 670-710 nm for DiR) and fluorescence measurement acquisition every 60 seconds.

5.3.2 Loading Capacity of Iron Oxide and Dye

In order to achieve the ultimate goal of designing a multi-modal contrast agent, the needs for high magnetic contrast and high fluorescence contrast must be balanced. Given that there was a maximum amount of iron oxide that could be encapsulated into the inner core of the protein microspheres as previously described, it is conceivable that the loading of iron oxide could potentially displace or affect the loading of dyes into the core of the microspheres. Batches of microspheres were synthesized using a constant concentration of fluorescent dye (Nile Red or DiR) and increasing concentrations of iron oxide. The first batch of microspheres had a constant concentration of 0.5 mg of Nile Red dye/mL of oil and increasing concentrations from 0.0 to 50.0 mg/mL of iron oxide in oil.

The second batch of microspheres had a constant concentration of 5.0 mg/mL DiR dye/mL of oil and increasing concentrations from 0.0 to 50.0 mg/mL of iron oxide in oil. The protein microspheres were resuspended into a 1% low melting temperature gel agarose at a concentration of $\sim 3.8 \times 10^5$ microspheres/mL and allowed to solidify in the lid of 35 mm Petri dishes. The samples were imaged using the wide-field fluorescence imaging system using the same exposure time for all the samples in each batch of microspheres. The Nile Red and iron oxide-filled microspheres were excited by a white light source passing through a 503-555 nm bandpass filter. The emitted fluorescence from the Nile Red-filled microspheres was filtered through a 580 nm long pass filter. The DiR and iron oxide-filled microspheres were excited by a white light source passing through a 710-760 nm bandpass filter. The emitted fluorescence from DiR-filled microspheres was filtered through an 800 nm long pass filter.

The presence of iron oxide affected the effective fluorescence signal of the Nile Red and DiR differently. In the case of Nile Red-filled microspheres, the measured fluorescence

decreased as the concentration of encapsulated iron oxide was increased (Figure 5.20 and Figure 5.21). This trend was also observed with the oil stock solution with Nile Red and iron oxide, which indicates that the encapsulation into a microsphere likely has little effect on this observed trend. One report cited that the increased presence of magnetite in solution with Nile Red would change the hydrophobicity of the solution and allow for increased aggregation of the particles [35]. This aggregation and decreased hydrophobicity was previously reported to be the primary mechanism of the quenching of the Nile Red fluorescence [34, 36, 37]. When looking at the absorption spectrum of Nile Red (alone) and Nile Red with iron oxide, the Nile Red absorption peak at 525 nm is broadened and relatively lower in intensity above iron oxide absorption spectrum (Figure 5.24). Another potential but unlikely cause could be the physical displacement of Nile Red by the iron oxide nanoparticles during the microsphere synthesis process. However, the same trend of decreasing fluorescence with increased iron oxide concentration was also observed the original oil stock solutions prior to encapsulation.

In the case of the DiR-filled microspheres, the measured fluorescence increased as the iron oxide concentration was increased (Figure 5.22 and Figure 5.23). The original oil stock solutions used to synthesize the DiR-filled microspheres were also imaged using wide-field fluorescence imaging system. The trend of increasing iron oxide concentration correlated to increased fluorescence intensities was present for both DiR and iron oxide-filled microspheres as well as the original DiR and iron oxide oil stock solution, indicating that this behavior is due to the interaction between DiR and the iron oxide. For a constant concentration of DiR, the measured fluorescence increased linearly with the concentration of iron oxide. There are few reports that have identified dyes complexed with iron oxide that lead to enhanced fluorescence and even fewer that describe potential mechanisms. However,

superparamagnetic Fe_2O_3 and Fe_3O_4 nanoparticles have been complexed with 2-(4-fluorophenyl)-1-phenyl-1H-phenanthro [9,10-d] imidazole (FPPI) [38]. The authors reported the enhanced fluorescence occurred via photo-induced electron transfer (PET), where the binding of the dye to the iron oxide nanoparticles lowered the energy levels of the highest occupied molecular orbital (HOMO) and lowest unoccupied molecular orbital (LUMO) [38]. When compared to the absorption spectrum of Nile Red with iron oxide, the absorption spectrum of DiR with iron oxide more closely approximates the shape the sum of the DiR absorption spectrum and the iron oxide absorption spectrum. There is also a higher overall absorption across the entire spectrum (area under the curve) in the DiR with iron oxide absorption spectrum (Figure 5.25). Further fluorescence lifetime experiments need to be performed to determine the effects of iron oxide binding to DiR has on the fluorescence lifetime and decay rates of DiR.

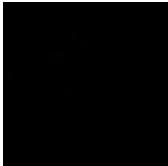
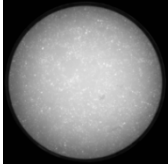
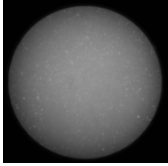
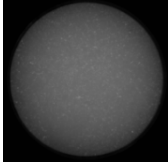
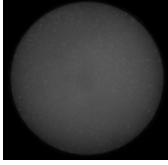
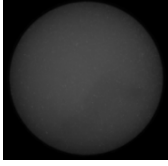
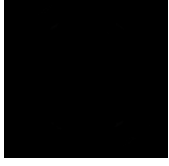
	mg of Nile Red/mL of oil	mg of iron oxide/mL of oil	Fluorescence Image
Agarose Gel with Protein Microspheres	0.0	0.0	
Agarose Gel with Protein Microspheres	0.5	0.0	
Agarose Gel with Protein Microspheres	0.5	12.5	
Agarose Gel with Protein Microspheres	0.5	25.0	
Agarose Gel with Protein Microspheres	0.5	37.5	
Agarose Gel with Protein Microspheres	0.5	50.0	
Agarose Gel without Protein Microspheres	N/A	N/A	

Figure 5.20: Protein microspheres synthesized with the same concentration of Nile Red dye and increasing concentrations of iron oxide nanoparticles at the time of synthesis.

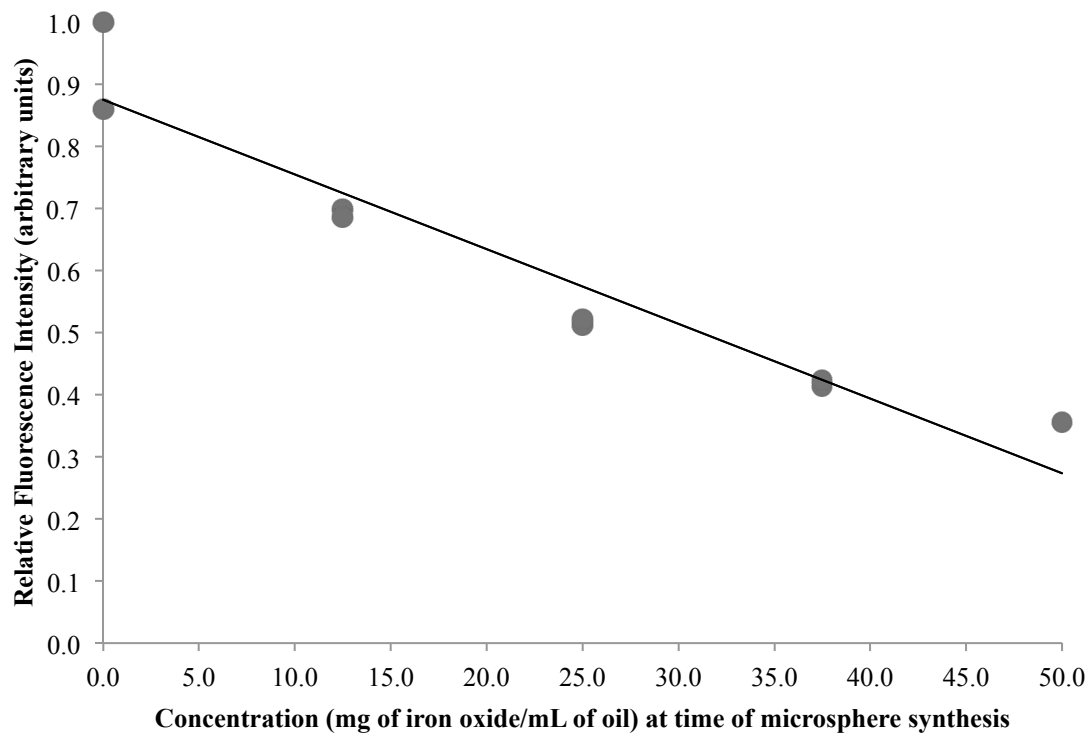


Figure 5.21: Relative fluorescence intensities of agarose gel phantoms of a series of protein microspheres with increasing concentration of encapsulated iron oxide nanoparticles and constant concentration of Nile Red dye.


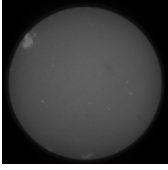
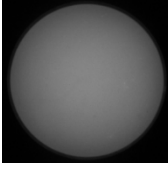
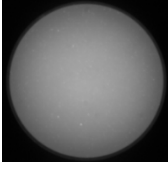
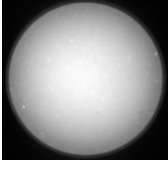
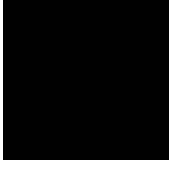
	mg of DiR/mL of oil	mg of iron oxide/mL of oil	Fluorescence Image
Agarose Gel with Protein Microspheres	0.0	0.0	
Agarose Gel with Protein Microspheres	5.0	0.0	
Agarose Gel with Protein Microspheres	5.0	12.5	
Agarose Gel with Protein Microspheres	5.0	25.0	
Agarose Gel with Protein Microspheres	5.0	50.0	
Agarose Gel without Protein Microspheres	N/A	N/A	

Figure 5.22: Protein microspheres synthesized with the same concentration of DiR dye and increasing concentrations of iron oxide nanoparticles at the time of synthesis.

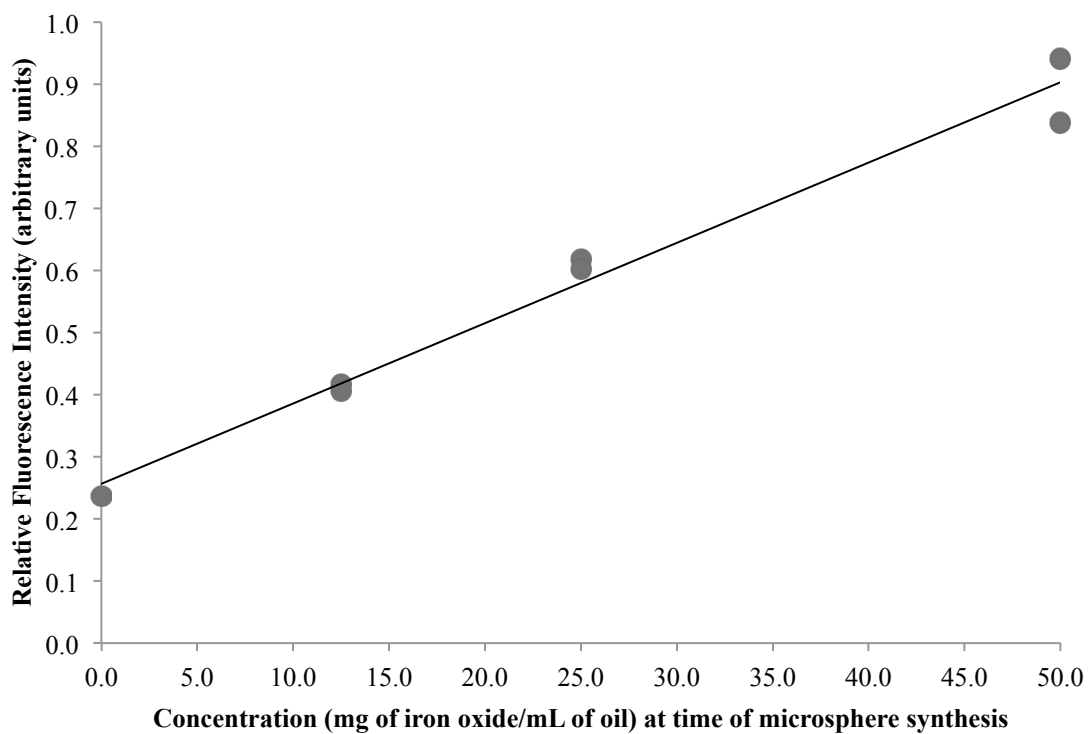


Figure 5.23: Relative fluorescence intensities of agarose gel phantoms of a series of protein microspheres with increasing concentration of encapsulated iron oxide nanoparticles and constant concentration of DiR dye.

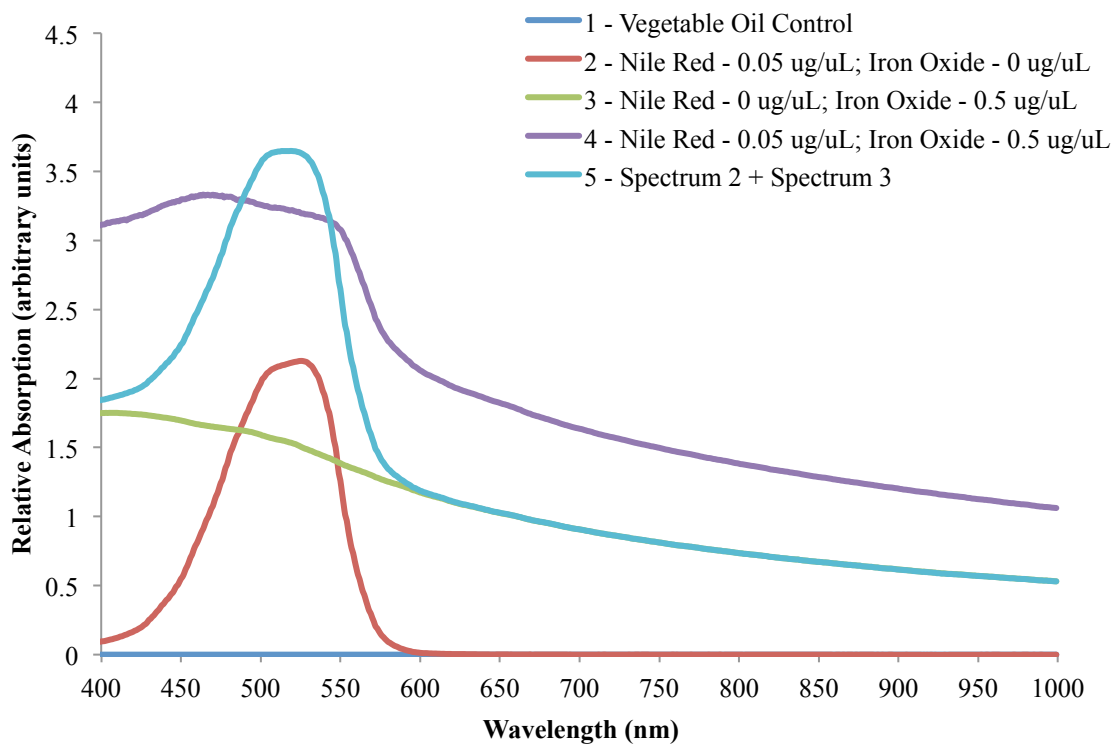


Figure 5.24: Absorption spectra of the vegetable oil (1), Nile Red mixed in the oil (2), iron oxide mixed in the oil (3), and Nile Red and iron oxide mixed together in the oil (4). Spectra 2 and 3 were added together to reflect the theoretical absorption spectrum of a mixed solution of Nile Red and iron oxide since absorption is normally an additive process.

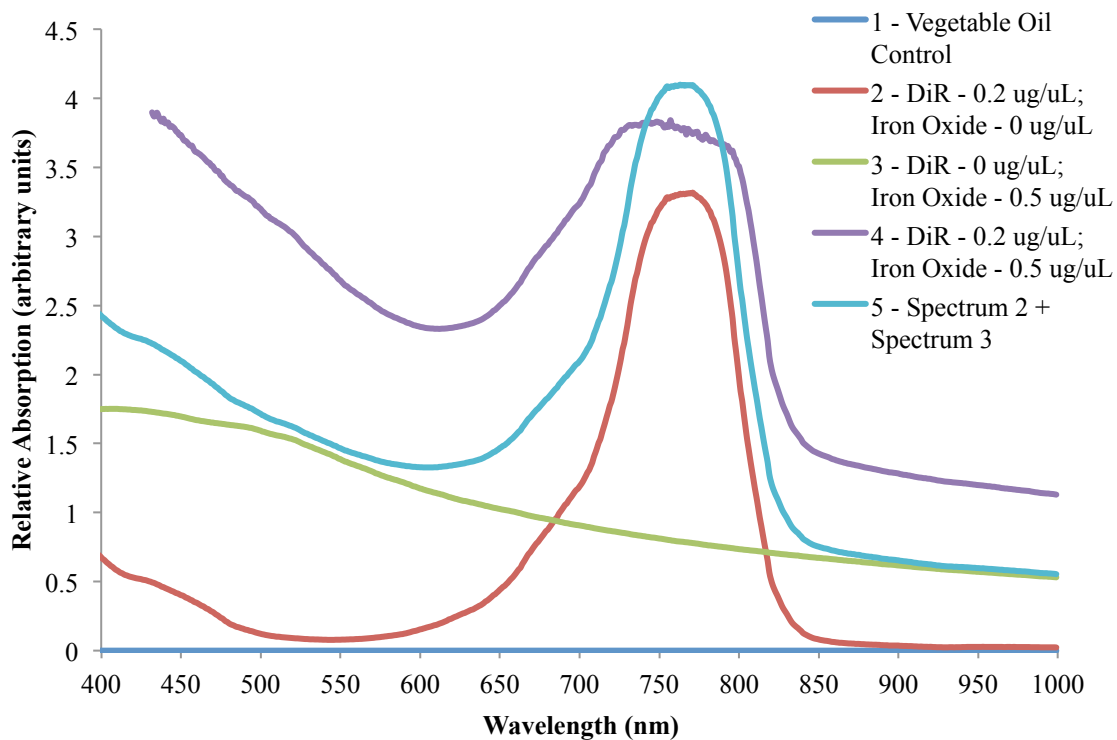


Figure 5.25: Absorption spectra of the vegetable oil (1), DiR mixed in the oil (2), iron oxide mixed in the oil (3), and DiR and iron oxide mixed together in the oil (4). Spectra 2 and 3 were added together to reflect the theoretical absorption spectrum of a mixed solution of DiR and iron oxide since absorption is normally an additive process.

5.4 Conclusions

The magnetic properties of iron oxide-filled protein microspheres were characterized using MM-OCT and MRI. The results from each modality are in agreement with each other. Both methods are able to quantify the concentration of iron oxide-filled protein microspheres. The fluorescence properties of DiR-filled microspheres and Nile Red-filled microspheres were characterized and quantified using the wide-field fluorescence imaging system. The integrity of the optical properties of the DiR and Nile Red dyes through the microsphere synthesis process was assessed by monitoring changes to both the excitation and emission peaks of DiR and Nile Red. By making modifications to the encapsulation protocol of DiR such as the solvent used to initially dissolve the DiR, and the temperature at which the solvent was evaporated, the fluorescence properties of DiR were maintained (Figure 5.13). The microspheres could be detected and quantified under MM-OCT, MRI, and wide-field fluorescence imaging in gel samples. The maximum loading capacity of iron oxide into the inner core of microspheres was determined using MRI data. However, the assumption was made that encapsulation of the iron oxide with oil would have minimal effect on the relaxivity of the iron oxide since in both cases the iron oxide was still suspended in the oil and was not shown to heavily aggregate (Figure 4.9) under TEM images. The presence of iron oxide appears to have quenched the Nile Red fluorescence likely due to Nile Red's sensitivity to changes in the hydrophobicity and polarity of the microenvironment. The enhanced fluorescence of DiR by iron oxide is a phenomenon that needs to be studied further mechanistically though others have reported enhanced fluorescence with iron oxide nanoparticles due to photo-induced energy transfer.

5.5 References

1. Nguyen FT, Dibbern EM, Chaney EJ, Oldenburg AL, Suslick KS, Boppart SA. Magnetic protein microspheres as dynamic contrast agents for magnetomotive optical coherence tomography. in *SPIE Photonics West BIOS: Molecular Probes for Biomedical Applications II*. 2008. San Jose, CA.
2. Kolbeck KJ. *The biomedical applications of protein microspheres* [dissertation]. Urbana, IL: University of Illinois at Urbana-Champaign; 1999.
3. Toublan FJ. *Methods to tailor protein microspheres for biomedical applications* [dissertation]. Urbana, IL: University of Illinois at Urbana-Champaign; 2005.
4. John R, Nguyen FT, Kolbeck KJ, Chaney EJ, Marjanovic M, Suslick KS, Boppart SA. Targeted multifunctional multimodal protein-shell microspheres as cancer imaging contrast agents. *Mol Imaging Biol*, 2012. 14 (1): p. 17-24.
5. Dibbern EM. *Core-shell microspheres for biomedical applications* [dissertation]. Urbana, IL: University of Illinois at Urbana-Champaign; 2007.
6. Lee TM, Oldenburg AL, Sitafalwalla S, Marks DL, Luo W, Toublan FJ, Suslick KS, Boppart SA. Engineered microsphere contrast agents for optical coherence tomography. *Opt Lett*, 2003. 28 (17): p. 1546-8.
7. Oldenburg AL, Crecea V, Rinne SA, Boppart SA. Phase-resolved magnetomotive OCT for imaging nanomolar concentrations of magnetic nanoparticles in tissues. *Opt Express*, 2008. 16 (15): p. 11525-39.
8. Boutry S, Forge D, Burtea C, Mahieu I, Murariu O, Laurent S, Vander Elst L, Muller RN. How to quantify iron in an aqueous or biological matrix: A technical note. *Contrast Media Mol Imaging*, 2009. 4 (6): p. 299-304.

9. Raynal I, Prigent P, Peyramaure S, Najid A, Rebuzzi C, Corot C. Macrophage endocytosis of superparamagnetic iron oxide nanoparticles: Mechanisms and comparison of ferumoxides and ferumoxtran-10. *Invest Radiol*, 2004. 39 (1): p. 56-63.
10. Peng XH, Qian X, Mao H, Wang AY, Chen ZG, Nie S, Shin DM. Targeted magnetic iron oxide nanoparticles for tumor imaging and therapy. *Int J Nanomedicine*, 2008. 3 (3): p. 311-21.
11. Horáka D, Babiča M, Jendelovác P, Herynekd V, Trchováa M, Likavčanovác K, Kapcalovác M, Hájekb M, Sykovác E. Effect of different magnetic nanoparticle coatings on the efficiency of stem cell labeling. *J Magn Magn Mater*, 2009. 321 (10): p. 1539–1547.
12. Li L, Jiang W, Luo K, Song H, Lan F, Wu Y, Gu Z. Superparamagnetic iron oxide nanoparticles as mri contrast agents for non-invasive stem cell labeling and tracking. *Theranostics*, 2013. 3 (8): p. 595-615.
13. Zhang C, Jugold M, Woenne EC, Lammers T, Morgenstern B, Mueller MM, Zentgraf H, Bock M, Eisenhut M, Semmler W, Kiessling F. Specific targeting of tumor angiogenesis by rgd-conjugated ultrasmall superparamagnetic iron oxide particles using a clinical 1.5-t magnetic resonance scanner. *Cancer Res*, 2007. 67 (4): p. 1555-62.
14. Basti H, Ben Tahar L, Smiri LS, Herbst F, Vaulay MJ, Chau F, Ammar S, Benderbous S. Catechol derivatives-coated fe₃o₄ and gamma-fe₂o₃ nanoparticles as potential mri contrast agents. *J Colloid Interface Sci*, 2010. 341 (2): p. 248-54.
15. Na HB, Song IC, Hyeon T. Inorganic nanoparticles for mri contrast agents. *Advanced Materials*, 2009. 21 (21): p. 2133-2148.

16. Sun C, Fang C, Stephen Z, Veiseh O, Hansen S, Lee D, Ellenbogen RG, Olson J, Zhang M. Tumor-targeted drug delivery and mri contrast enhancement by chlorotoxin-conjugated iron oxide nanoparticles. *Nanomedicine (Lond)*, 2008. 3 (4): p. 495-505.
17. Wu W, He Q, Jiang C. Magnetic iron oxide nanoparticles: Synthesis and surface functionalization strategies. *Nanoscale Res Lett*, 2008. 3 (11): p. 397-415.
18. Park JH, Von Maltzahn G, Zhang L, Schwartz MP, Ruoslahti E, Bhatia SN, Sailor MJ. Magnetic iron oxide nanoworms for tumor targeting and imaging. *Adv Mater*, 2008. 20 (9): p. 1630-1635.
19. Bulte JW, Kraitchman DL. Iron oxide mr contrast agents for molecular and cellular imaging. *NMR Biomed*, 2004. 17 (7): p. 484-99.
20. Laurent S, Forge D, Port M, Roch A, Robic C, Vander Elst L, Muller RN. Magnetic iron oxide nanoparticles: Synthesis, stabilization, vectorization, physicochemical characterizations, and biological applications. *Chem Rev*, 2008. 108 (6): p. 2064-110.
21. Weissleder R, Elizondo G, Wittenberg J, Rabito CA, Bengele HH, Josephson L. Ultrasmall superparamagnetic iron oxide: Characterization of a new class of contrast agents for mr imaging. *Radiology*, 1990. 175 (2): p. 489-93.
22. Tong S, Hou S, Zheng Z, Zhou J, Bao G. Coating optimization of superparamagnetic iron oxide nanoparticles for high t2 relaxivity. *Nano Lett*, 2010. 10 (11): p. 4607-13.
23. Laconte LE, Nitin N, Zurkiya O, Caruntu D, O'connor CJ, Hu X, Bao G. Coating thickness of magnetic iron oxide nanoparticles affects r2 relaxivity. *J Magn Reson Imaging*, 2007. 26 (6): p. 1634-41.

24. Laurent S, Boutry S, Mahieu I, Vander Elst L, Muller RN. Iron oxide based mr contrast agents: From chemistry to cell labeling. *Curr Med Chem*, 2009. 16 (35): p. 4712-27.
25. Laurent S, Bridot JL, Elst LV, Muller RN. Magnetic iron oxide nanoparticles for biomedical applications. *Future Med Chem*, 2010. 2 (3): p. 427-49.
26. Nitin N, Laconte LE, Zurkiya O, Hu X, Bao G. Functionalization and peptide-based delivery of magnetic nanoparticles as an intracellular mri contrast agent. *J Biol Inorg Chem*, 2004. 9 (6): p. 706-12.
27. Tassa C, Shaw SY, Weissleder R. Dextran-coated iron oxide nanoparticles: A versatile platform for targeted molecular imaging, molecular diagnostics, and therapy. *Acc Chem Res*, 2011. 44 (10): p. 842-52.
28. Babic M, Horak D, Jendelova P, Herynek V, Proks V, Vanecek V, Lesny P, Sykova E. The use of dopamine-hyaluronate associate-coated maghemite nanoparticles to label cells. *Int J Nanomedicine*, 2012. 7: p. 1461-74.
29. Thorek DL, Tsourkas A. Size, charge and concentration dependent uptake of iron oxide particles by non-phagocytic cells. *Biomaterials*, 2008. 29 (26): p. 3583-90.
30. Sangeetha J, Thomas S, Arutchelvi J, Doble M, Philip J. Functionalization of iron oxide nanoparticles with biosurfactants and biocompatibility studies. *J Biomed Nanotechnol*, 2013. 9 (5): p. 751-64.
31. Mou Y, Hou Y, Chen B, Hua Z, Zhang Y, Xie H, Xia G, Wang Z, Huang X, Han W, Ni Y, Hu Q. *In vivo* migration of dendritic cells labeled with synthetic superparamagnetic iron oxide. *Int J Nanomedicine*, 2011. 6: p. 2633-40.

32. Texier I, Goutayer M, Da Silva A, Guyon L, Djaker N, Josserand V, Neumann E, Bibette J, Vinet F. Cyanine-loaded lipid nanoparticles for improved *in vivo* fluorescence imaging. *J Biomed Opt*, 2009. 14 (5): p. 054005.
33. Cser A, Nagy K, Biczók L. Fluorescence lifetime of nile red as a probe for the hydrogen bonding strength with its microenvironment. *Chemical Physics Letters*, 2002. 360 (5-6): p. 473-478.
34. Sackett DL, Wolff J. Nile red as a polarity-sensitive fluorescent probe of hydrophobic protein surfaces. *Anal Biochem*, 1987. 167 (2): p. 228–234.
35. Balasubramaniam S, Pothayee N, Lin Y, House M, Woodward RC, Pierre TGS, Davis RM, Riffle JS. Poly(n-isopropylacrylamide)-coated superparamagnetic iron oxide nanoparticles: Relaxometric and fluorescence behavior correlate to temperature-dependent aggregation. *Chemistry of Materials*, 2011. 23 (14): p. 3348-3356.
36. Dutta AK, Kamada K, Ohta K. Spectroscopic studies of nile red in organic solvents and polymers. *Journal of Photochemistry and Photobiology A: Chemistry*, 1996. 93 (1): p. 57–64.
37. Tajallia H, Gilania AG, Zakerhamidia MS, Tajallia P. The photophysical properties of nile red and nile blue in ordered anisotropic media. *Dyes and Pigments*, 2008. 78 (1): p. 15-24.
38. Karunakaran C, Jayabharathi J, Sathishkumar R, Jayamoorthy K. Interaction of fluorescent sensor with superparamagnetic iron oxide nanoparticles. *Spectrochim Acta A Mol Biomol Spectrosc*, 2013. 110: p. 151-6.

CHAPTER 6

IN VITRO TARGETING OF PROTEIN MICROSPHERES IN CANCER

6.1 Introduction

Layer-by-layer (LBL) assembly is a versatile technique for depositing or layering of thin films on particles or surfaces for a wide variety of applications including biosensing, drug delivery, and tissue engineering. The focus in this chapter will be on the use of the LBL technique to target the protein microsphere to the $\alpha_v\beta_3$ integrin receptor using the RGD motif. The use of core-shell particles and capsules such as liposomes, protein microspheres, polymer micelles, and dendrimers is advantageous for targeted drug delivery applications [1-8]. These core-shell particles can potentially encapsulate large therapeutic payloads while providing a protective shell increasing their circulation time and bypassing the normal clearance of the drugs by the body. These particles are also capable of encapsulating not just a single drug but also multiple drugs similar to how we are encapsulating multiple contrast agents into a single protein microsphere. This type of research would help further advance the research field for targeted multi-drug therapy.

The targeting of core-shell particles and capsules ranging in size from 20 nm to 3 μ m can be accomplished using LBL assembly to functionalize the outer surface with ligands such as RGD peptides or specific antibodies [8-18]. It was recently demonstrated that 800 nm-sized capsules made of poly (N-vinyl pyrrolidone) could be functionalized with azide-functionalized antibodies using LBL and successfully targeted [19]. The protein microspheres described in this thesis have also been functionalized with RGD peptide sequences using LBL for targeting HT-29 tumor cells [20]. In Chapter 4, the LBL assembly method was used to

layer PDDA, silica, and RGD on to the protein microspheres surface for *in vitro* and *in vivo* applications. More recently, a targeted nanoparticle was developed using LBL assembly where the outer layer would be degraded once it reached the target site [16]. In this particular report, the PEG layer was shed based on the acidity of the tumor microenvironment [16]. With the recent research advances using the LBL assembly, there are many opportunities to further customize the contrast, therapeutic, and targeting properties of the protein microsphere. In addition to encapsulating contrast agents in the inner core as previously described in Chapter 4, layers of contrast agents can be deposited on the microsphere surface using LBL. The functionality of the microsphere can also be altered through the addition of different particles such as the addition to silica to precipitate the microspheres for *in vitro* experiments, or adding a PEG coating to increase the *in vivo* circulation of microspheres.

The LBL assembly method previously described in Chapter 4 depends on the adsorption of alternating charged particles. For example, in the case of the protein microspheres described in this thesis, the surface of the BSA protein shell provides a negatively charged surface. The PDDA or the RGD poly-lysine peptide sequence can both be individually layered directly onto the bare surface of the protein microspheres since both have large positively charged domains. To layer negatively charged silica on top of the protein microspheres, the protein microspheres must first be coated by a positively charged layer such as PDDA to reverse the charge on the surface from negative to positive. Due to the electrostatic interactions, the layering of the particles is fairly uniform in distribution, forming thin films across the surface of the core-shell particle.

6.1.1 Previous Studies on Layering of Protein Microspheres using RGD sequence

The RGD peptide was previously layered to the surface of protein microspheres using the LBL assembly method [20]. Since RGD is not highly positively charged, a poly-lysine sequence was attached to the RGD sequence in order to take advantage of the LBL method to layer the RGD sequence onto the surface of protein microspheres. The effect of placing the RGD sequence at different locations of the poly-lysine sequence was investigated to determine which sequence provided the greatest binding to HT-29 cells [20]. The RGD sequence was placed on the amino terminus (RGDKKKKKK), in the middle (KKKRGDKKK), and on the carboxyl terminus (KKKKKKRGD). The sequence that best secured the RGD-coated microsphere to the cell surface was when the RGD was placed on the amino terminus [20]. These initial findings allowed us to use this construct as the basis to further study the binding specificity and cellular uptake of the RGD-coated protein microspheres to the $\alpha_v\beta_3$ integrin receptor, which is often overexpressed in metastatic cancer cells and tumor angiogenesis.

6.1.2 Initial Studies using RGD-coated Protein Microspheres

Preliminary experiments were repeated to confirm the successful synthesis of RGD-coated protein microspheres. The RGD-coated and non-coated microspheres were incubated with HT-29 cancer cells for two hours and washed with PBS to remove any excess unbound microspheres. The HT-29 cell line is a colon cancer cell line that is known to have an overexpression of the integrin receptors [21-23]. After the 2 hrs incubation, the cells were washed with phosphate buffer saline three times and imaged using a light microscope. The light microscopy images shown in Figure 6.1 confirmed the results previously reported by Toublan [20]. The higher binding affinity of the HT-29 cells to the RGD-coated protein

microspheres can be clearly seen when compared to the non-coated protein microspheres. Although the RGD-coated microspheres attached and remained bound to the HT-29 cells, little was known about the binding mechanism and the cellular uptake of microspheres. This chapter will examine the correlation between the binding specificity of RGD-coated protein microspheres to various cancer cell lines and the $\alpha_v\beta_3$ integrin receptor expression level of the cells. Time-lapse fluorescence microscopy studies will also be discussed to gain insights on the cellular uptake mechanism of targeted and non-targeted protein microspheres.

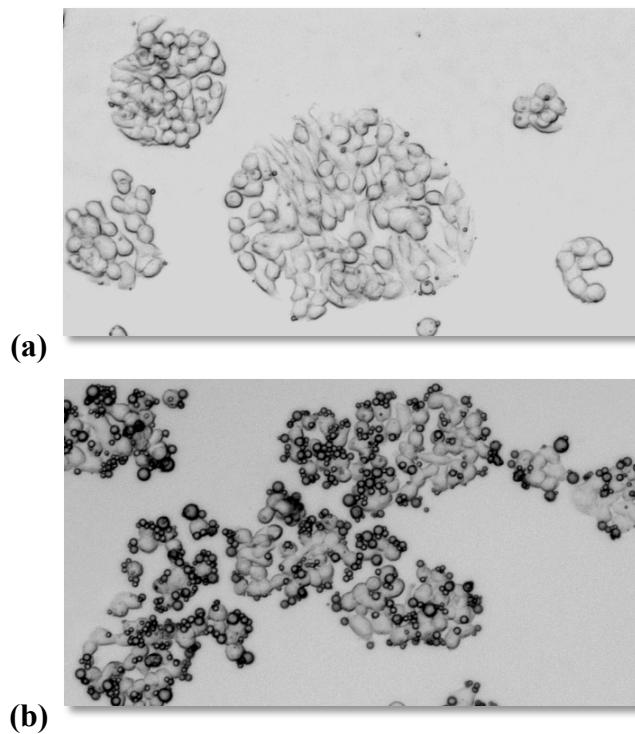


Figure 6.1: Brightfield images of HT-29 cells at 10X after they have been incubated for two hours with non-targeted (a) and targeted (b) protein microspheres.

6.2 Quantifying the Expression of $\alpha_v\beta_3$ Integrin Receptors on Cells using Indirect Immunofluorescence Staining and Flow Cytometry

To gain a better understanding about the targeting specificity of the RGD-coated protein microspheres to $\alpha_v\beta_3$ integrin receptors expressed on cancer cell lines, a panel of cancer cell lines with differing levels of receptor expression were examined. Absolute quantification of $\alpha_v\beta_3$ integrin receptors expressed on the cell surface can be measured by flow cytometric analysis of cells labeled with fluorochrome-coupled monoclonal antibodies specific to the alpha and beta subunits of the integrin receptor. However, this method is not without limitations when used to evaluate binding of the protein microspheres to these receptors, and it may be more relevant to compare relative trends between different cell lines rather than absolute numbers. Specifically, SEM characterization of the RGD-coated protein microspheres revealed that the microspheres do not appear to be uniformly and completely coated with RGD peptides (Figures 4.3-4.8). If the coverage of the microsphere surface by RGD peptides is not uniform or not completely covered, the orientation of the microsphere relative to the binding site now becomes an issue. In addition, the overall size of microspheres (1-3 μm) is relatively large compared to monoclonal antibodies (~5-10 nm) and the average cell sizes of 10-15 μm . This size difference may physically constrain access for additional microspheres but not the antibodies to bind nearby integrin receptors exposed on the cell surface. Lastly, compared to fluorescence microscopy, which examines cells that are attached to the bottom of Petri dishes, the entire cell surface is exposed during flow cytometry. This is important because significant populations of integrin receptors, which mediate cell-substrate adhesion, are likely present at the junction between the cells and the bottom of the culture dish rather than exposed on the apical side of the cells, exposed to the overlying culture medium.

Given all of these factors, it is more important to measure the relative expression of the integrin receptors on the cell surface or the binding of the receptor by the microsphere between different cell lines.

For the flow cytometric study of $\alpha_v\beta_3$ integrin receptor expression on various cancer cell lines listed in Figure 6.4 and Figure 6.5, confluent monolayers of cells were cultured in Petri dishes. The cells were washed with warm (37°C) sterile PBS three times to ensure the complete removal of cell culture medium. The cells were trypsinized with 1X trypsin (0.05% Trypsin + 0.2 g / L EDTA 0.85 g / L NaCl). After about 10-15 minutes, the cells detached from the bottom of the cell culture dishes. The cells were diluted in their respective culture medium to rapidly deactivate the trypsin. The cells were centrifuged at 1500 RPM for 5 mins and resuspended in culture medium. The cells were spun down once more to remove any residual trypsin. The cells were resuspended in sterile PBS and counted using a hemocytometer. Four aliquots of 1×10^6 cells (one negative staining control and three positive controls) for each cell line were prepared into 1.5 mL Eppendorf tubes. Throughout the procedure, it was important to keep the cells on ice in order to maintain their viability.

The cells were washed twice by resuspension in cold PBS buffer solution (1X PBS, 1% BSA, 0.5 mM EDTA) and centrifugation at 6000 RPM for 5 mins. The primary $\alpha_v\beta_3$ antibody (mouse monoclonal IgG1, GeneTex cat. #GTX4013) was added to each of three cell aliquots marked for positive staining at a concentration of $1 \mu\text{g} / 1 \times 10^6$ cells. This step labels exposed $\alpha_v\beta_3$ integrin receptors on the cell surface. The cells were incubated in this solution at 4°C on an orbital shaker set at ~200 RPM for 30 minutes.

Cells were washed twice with cold buffer solution, as previously described. At this point, all overhead lights were turned off to prevent photobleaching of the light-sensitive

fluorescence tags. The secondary antibody (anti-mouse conjugated with FITC) was added to all four aliquots of cells at a concentration of $1 \mu\text{g} / 1 \times 10^6$ cells. The samples were covered with foil and placed on an orbital shaker at ~ 200 RPM and incubated at 4°C for 30 minutes. The cells were washed twice with cold buffer solution and then resuspended in $300 \mu\text{L}$ of the cold buffer solution. The cells were maintained on ice and covered with foil until they could be analyzed by flow cytometry.

The flow cytometry facilities at the Roy J. Carver Biotechnology Center at the University of Illinois at Urbana-Champaign were used for these experiments. The flow cytometer was a BD Biosciences LSR II system. Before each experiment, passing a bleach solution through the flow channel cleaned the instrument. The first step involved taking measurements of FITC fluorescent bead standards (Bang Laboratories, #555A, Quantum FITC-5 MESF). There were five different standards in this particular kit of five populations of $7\text{-}9 \mu\text{m}$ beads, each with different levels of FITC fluorescence intensities per bead. Comparison of stained samples to the standards allowed quantification of fluorescent particles per scattering particle (the cell) through the flow channel.

A standard curve (Figure 6.3) was generated by plotting the channel number at which the fluorescence intensity peaked against the known values measured and calibrated by Bangs Laboratories. Next, the stained cell samples were measured using the flow cytometer. Ten thousand scattering events (or cells) were collected for each aliquot (triplicate positive staining controls and one negative control). The data were analyzed using FCS Express software (DeNovo Software). Each data set was initially gated in a plot of the forward scattering against the side scattering signal in order to exclude non-cellular particles. A second gating was made to isolate live cells versus dead cells by plotting the forward

scattering width against the forward scattering amplitude. The resulting FITC intensity fluorescence peak was identified using the median channel value. These channel values were converted to MESF/ABC values using the standard curve previously established. The MESF/ABC corresponds to the measured fluorescence intensity per cell. The MESF/ABC values for the positively stained cells were subtracted by the MESF/ABC values of the negative controls. The resulting values were averaged across triplicate samples for each cell line. These values are reported as the number of $\alpha_v\beta_3$ integrin molecules per each cell (Figures 6.5-6.6). The flow cytometry data were also re-analyzed to examine the ratio of specific binding (positively stained minus negatively stained) to non-specific binding (negatively stained) to more easily compare the expression results from flow cytometry to the fluorescence microscopy data of the targeting of the RGD-coated protein microspheres *in vitro*.

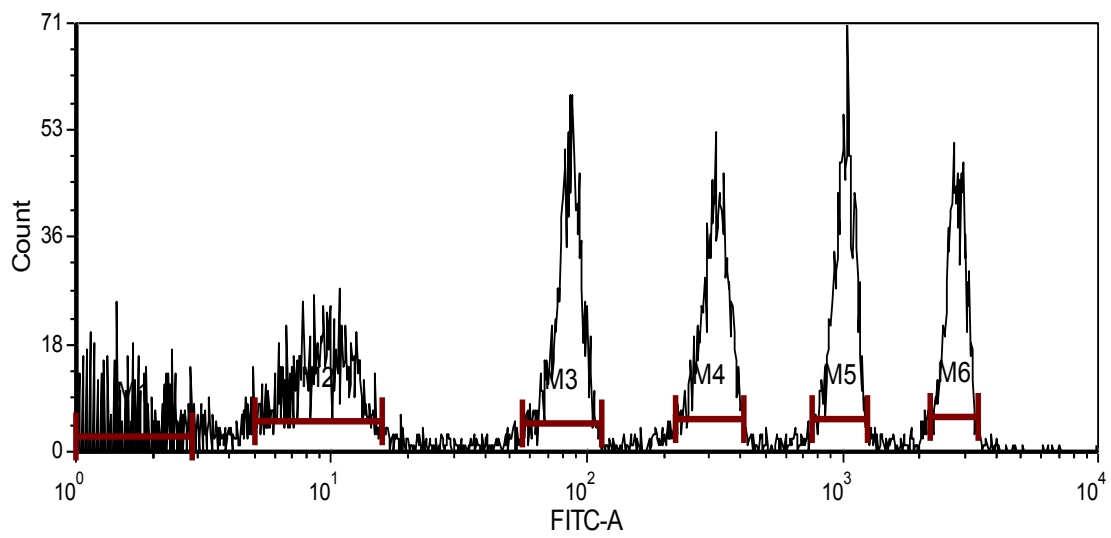


Figure 6.2: Flow cytometry measurements of the FITC intensities from five standard beads used to correlate the measured FITC fluorescence intensities to the absolute number of fluorophores.

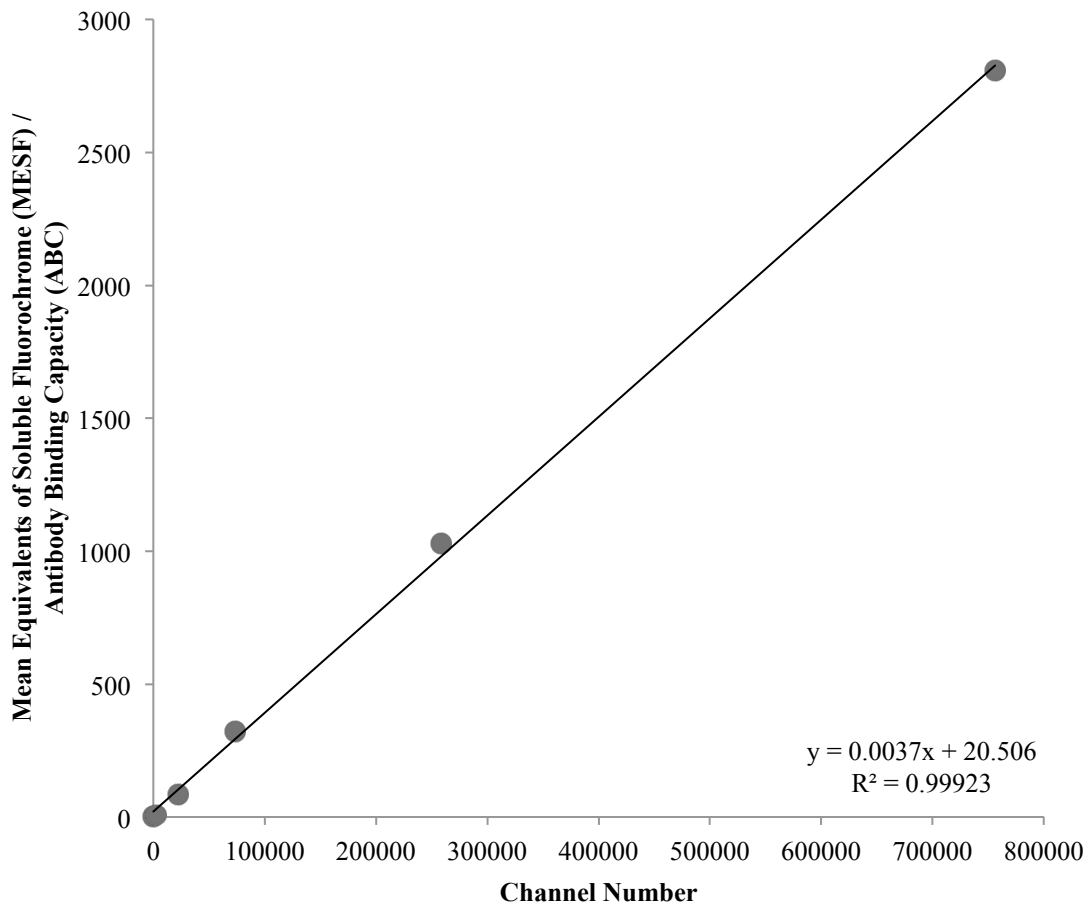


Figure 6.3: Standard curve of FITC fluorescent bead standards used to calibrate fluorescence intensity measurements from the flow cytometer. The mean equivalent of soluble fluorochrome (MESF) per antibody binding capacity (ABC) is plotted against the fluorescence intensity channel.

Cell Line	ATCC #	Description
MAT III 13762	CRL-1666	Rat – Mammary Gland – Adenocarcinoma – Epithelial
HT-29	HTB-38	Human – Colon – Colorectal Adenocarcinoma – Epithelial
SK-BR-3	HTB-30	Human – Mammary Gland – Breast – Adenocarcinoma – Epithelial
MCF-7	HTB-22	Human – Mammary Gland – Breast – Adenocarcinoma – Epithelial
hTERT-HME1	CRL-4010	Human – Mammary Gland – Breast – Immortalized – Epithelial
HCC38	CRL-2314	Human – Mammary Gland – Breast – Primary Ductal Carcinoma – Epithelial
ZR-75-1	CRL-1500	Human – Mammary Gland – Breast – Ductal Carcinoma – Epithelial

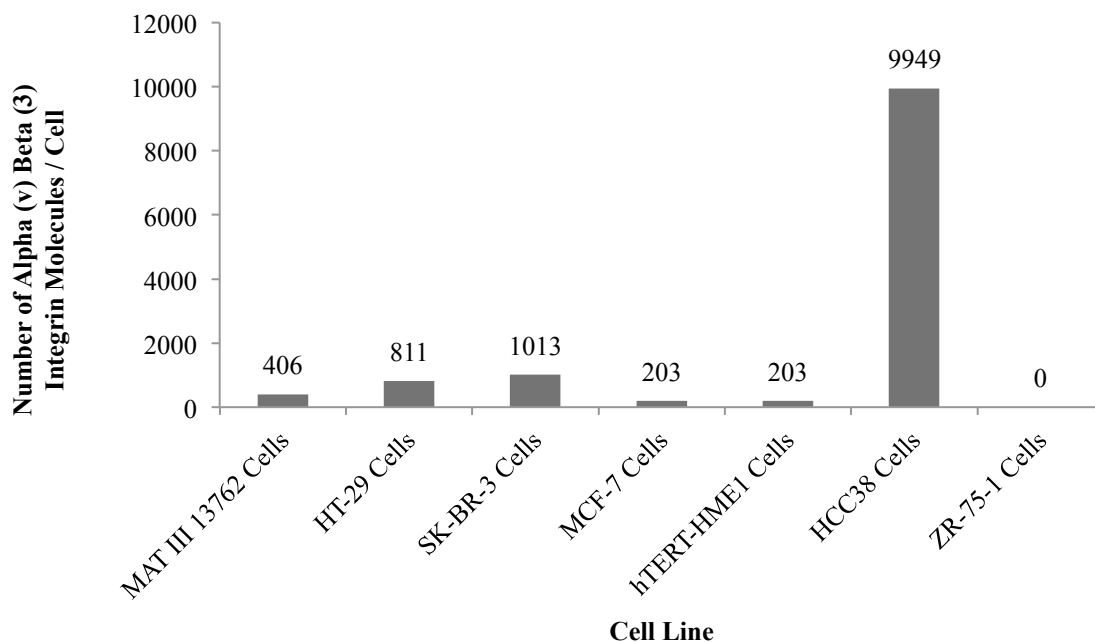


Figure 6.4: Flow cytometric analysis quantified the $\alpha_v\beta_3$ integrin receptor expression on a panel of cancer cell lines available in Prof. Boppart’s laboratory. These results demonstrate that aside from the HCC38 cell line, the majority of the cell lines had relatively little active expression of the $\alpha_v\beta_3$ integrin receptor at the time the studies were performed.

The results suggest that flow cytometry is a suitable method for quantifying $\alpha_v\beta_3$ integrin receptor expression on cells. Between two sets of measurements taken approximately six months apart, the trends are fairly similar aside from one cell line (HCC38). Although as much as possible was done to ensure that the same conditions and protocols were used, many factors could alter expression levels of the integrin receptors. These factors include: the confluence levels of the cells, the passage number of the cells, the day to day variations of the flow cytometer, and other factors that may affect the health of the cell and the integrity of the receptor.

After the first set of results (Figure 6.4) was analyzed, two new breast cancer cell lines (MDA-MB-231 and MDA-MB-435S) were acquired. These particular cell lines are well characterized as highly metastatic and have also been used effectively by others for the study of cancer metastasis in mice models [24-26]. As shown in Figure 6.5, the expression levels of these two cell lines are several times higher than those of the other cell lines available in Prof. Boppart's laboratory.

Currently, our laboratory uses two main animal tumor models. The first is an N-nitroso-N-methylurea (NMU) carcinogen induced tumor animal model that produces spontaneous tumors 8-10 weeks after injecting NMU carcinogen into the animal. The second model is induced by injecting MAT III 13762 cell lines sub-cutaneously to form primary tumors. The quantification of the integrin receptor expression of the cell lines could help dictate which cell lines would be most effective in a xenograft tumor model to test the *in vivo* targeting of protein microspheres (Figures 6.5-6.6).

Cell Line	ATCC #	Description
HT-29	HTB-38	Human – Colon – Colorectal Adenocarcinoma – Epithelial
SK-BR-3	HTB-30	Human – Mammary Gland – Breast – Adenocarcinoma – Epithelial
MCF-7	HTB-22	Human – Mammary Gland – Breast – Adenocarcinoma – Epithelial
hTERT-HME1	CRL-4010	Human – Mammary Gland – Breast – Immortalized – Epithelial
HCC38	CRL-2314	Human – Mammary Gland – Breast – Primary Ductal Carcinoma – Epithelial
ZR-75-1	CRL-1500	Human – Mammary Gland – Breast – Ductal Carcinoma – Epithelial
MDA-MB-231	HTB-26	Human – Mammary Gland – Breast – Adenocarcinoma – Epithelial
MDA-MB-435S	HTB-129	Human – Mammary Gland – Breast – Ductal Carcinoma – spindle shaped

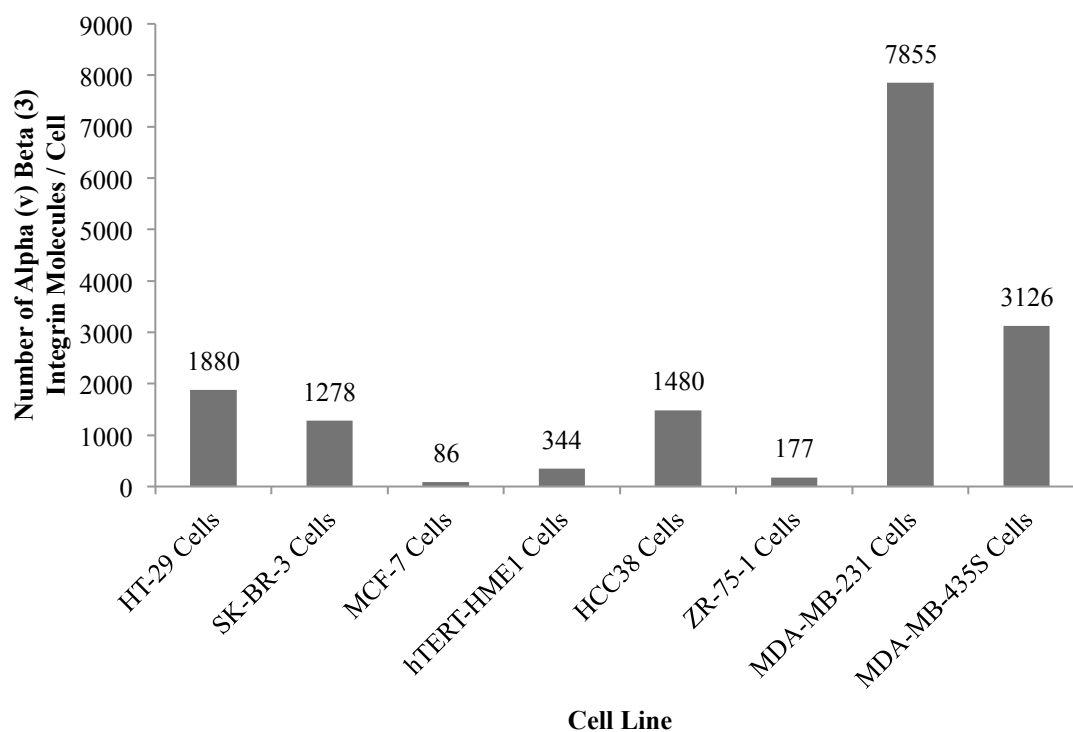


Figure 6.5: Flow cytometry results of $\alpha_v\beta_3$ integrin expression on the cancer cell lines from Figure 6.4 and two highly metastatic cell lines, MDA-MB-231 and MDA-MB-435S. High expression levels of $\alpha_v\beta_3$ integrin receptors closely corresponded with the cell metastatic behavior [27-31].

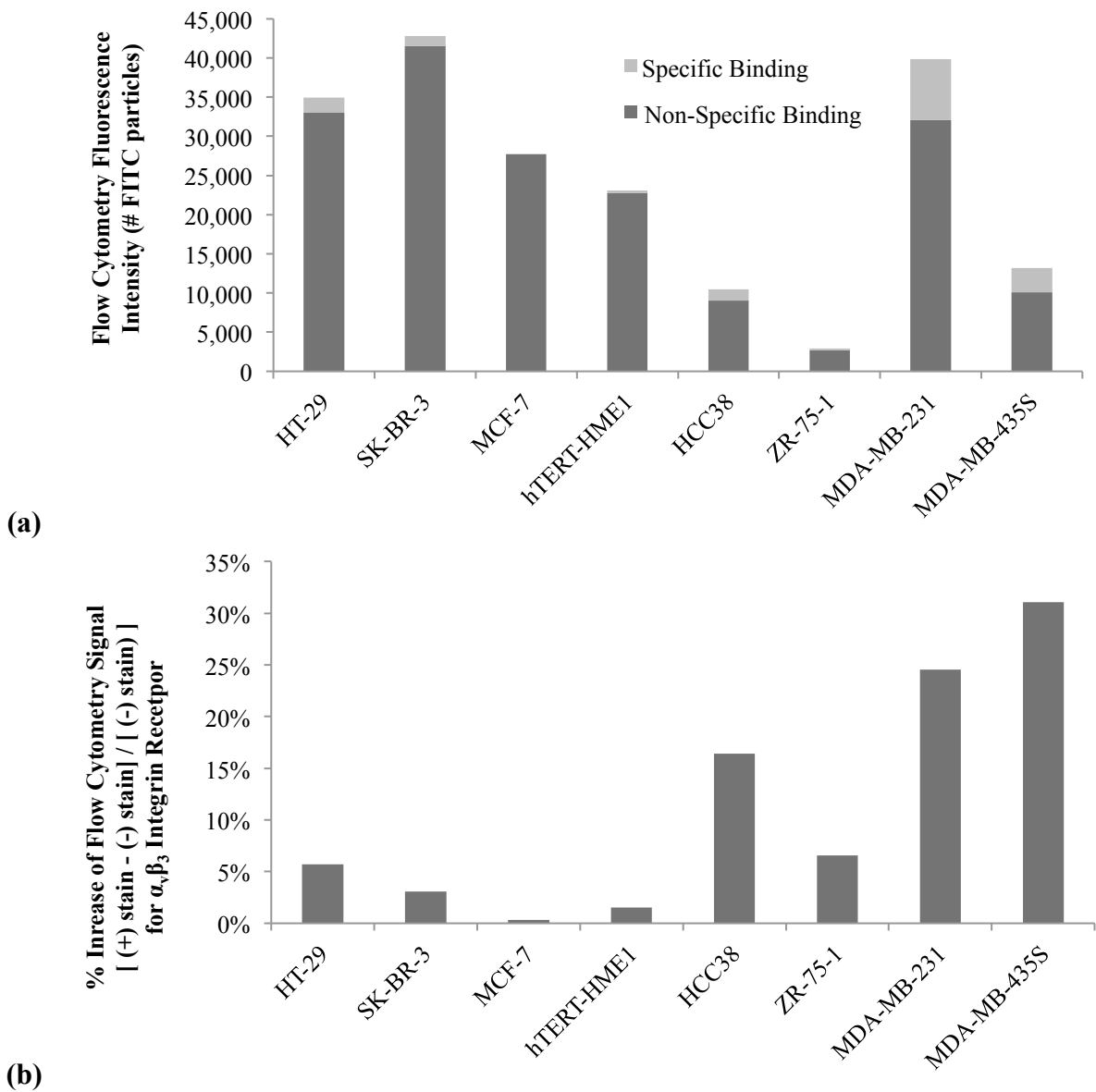


Figure 6.6: Flow cytometry results expressed as an absolute values (a) and as a ratio of specific binding [(+) stain – (-) stain] to non-specific binding [(-) stain] (b). Representing the data in this format allows a more direct comparison to the fluorescence microscopy data that will be presented later in this chapter. Compared to Figure 6.5, there is a lower level of non-specific binding in the MDA-MB-435S cell line compared to the MDA-MB-231 cell line.

6.3 Targeting of the RGD-coated Microspheres to the $\alpha_v\beta_3$ Integrin Receptor *In Vitro*

Protein microspheres with encapsulated Nile Red dye were used for fluorescence imaging experiments to assess the targeting of the microspheres to $\alpha_v\beta_3$ integrin receptors expressed on various cell lines. Using the LBL adhesion method, microspheres were coated with a layer of PDDA followed by a layer of silica. One batch of microspheres was additionally coated with a layer of RGDKKKKKK, and a second batch of microspheres remained uncoated at the silica layer. Approximately 100,000 cells from each cancer cell line (HT-29, SK-BR 3, MCF-7, hTERT-HME1, ZR-75-1, MDA-MB-231, MDA-MB-435S) were seeded into each well of a 4-well chamber slide. The HT-29 cell line, a colon cancer cell line, was chosen to correlate results with previous data from Prof. Suslick's laboratory [7, 20]. The MCF-7 cell line was chosen as a negative control since it has a low to no expression of the $\alpha_v\beta_3$ integrin receptor [32]. The MDA-MB-231 and MDA-MB-435S cell lines are highly metastatic breast cancer cell lines overexpressing the $\alpha_v\beta_3$ receptor [32]. The remaining breast cancer cell lines were chosen to provide a spectrum of $\alpha_v\beta_3$ receptor expression levels.

The expression of this receptor has been highly associated with more aggressive and metastatic cancers different organ systems [33]. With increased expression of $\alpha_v\beta_3$ receptor, the cell is more likely to migrate, invade into nearby tissue by adhesion into the extracellular matrix, and as a promoter for angiogenesis [32-35]. As the vascular requirements of the cancer cell or tumor increases, so does the expression of $\alpha_v\beta_3$ receptor [34]. When contrasting *in vitro* versus *in vivo* expression of the $\alpha_v\beta_3$ receptor, multiple variables will come into play including but not limited to: confluence or density of the cancer cells or mass, the cell's ability to adhere to a surface or another cell versus exposed to free air, the availability of nutrients, the cell cycle stage and associated metabolic demand of the cancer cell, etc. Hence,

it was important *in vitro* to ensure that cells were seeded in a high enough concentration and cultured into monolayers of cells to promote a greater expression of the $\alpha_v\beta_3$ receptor.

The seeding density of the cell cultures used was about 50% confluence to allow the cells to form a uniform monolayer of cells within 24 hours. By having this monolayer, the microspheres can interact directly with the cell surface decreasing the background signal due to microspheres adherent to the bottom of the Petri dish. Microspheres attached to the bottom of the dishes were very difficult to remove and required at least 5-10 PBS washes increasing the chances that the cells would also be washed off in the process. The cells were allowed to attach to the chamber slide for 24 hours. The cells were then washed three times with sterile PBS to remove any floating or dead cells. For each cell line, two of the four wells were incubated with RGD-coated Nile Red-filled microspheres. The other two wells were incubated with non-coated Nile Red-filled microspheres. The microspheres were first resuspended into culture medium at a concentration of $\sim 40,000$ microspheres / mL of media. Each well in the chamber slide was incubated with 1 mL of the microsphere solution for 1 hr. After the incubation period, cells were washed twice with sterile PBS to remove any excess or unbound microspheres. Cell cultures were resuspended with culture medium until the time of imaging. During fluorescence imaging, the cell medium was removed and PBS was added to reduce background fluorescence coming from the cell medium. Multidimensional acquisition of both fluorescence and brightfield images was taken using a 20X objective on a Zeiss Axiovert 200 inverted microscope. Images were acquired at ten different locations with similar densities of cells for each sample. Images in the fluorescence channel were taken using the auto-exposure setting to take advantage of the full dynamic range of the detection system and to reduce the chances of saturating the camera.

The fluorescence images were overlaid on top of their respective brightfield images to better visualize the localization of Nile Red dye that was initially encapsulated in the protein microspheres. The effective exposure time of the processed fluorescence images was normalized to allow for visual comparison of fluorescence intensities between RGD-coated or non-coated microspheres bound to different cell lines. The fluorescence intensity signals from the rescaled images were averaged over the entire image using ImageJ software (NIH, Version 1.45) and ten images were averaged for each cell type.

The percent increase in fluorescence was calculated by comparing average fluorescence intensities of RGD-coated vs. non-coated microspheres bound to each cell line $[(+) \text{ RGD-}\mu\text{spheres} - (-) \text{ RGD-}\mu\text{spheres}] / [(-) \text{ RGD-}\mu\text{spheres}]$ (Figure 6.14). This is the ratio of specific binding of the RGD-coated microspheres to the non-specific binding of the non-coated microspheres to the $\alpha_v\beta_3$ integrin receptors. The fluorescence data from the MCF-7 and hTERT-HEM1 cell lines were not included in Figure 6.14 as the difference between the average fluorescence intensities of the RGD-coated and non-coated microspheres fell within the error of the averages. The results of the fluorescence imaging experiments correlate well with the flow cytometry results. The two metastatic cell lines (MDA) that were the highest expressers of surface integrin receptors as measured by flow cytometry were also bound with the highest amount of RGD-coated microspheres as determined by fluorescence imaging. The fluorescence intensity values was calculated as the average fluorescence intensity across the entire image and does not make a distinction between the discrete bright spots corresponding to intact microspheres and diffuse areas of fluorescence corresponding to Nile Red in the cell cytoplasm after the microsphere has been internalized and ruptured by the cell. Hence, no conclusions can be made regarding the time course of the microsphere binding, uptake, and

rupture as separate entities with this particular data. Although the relative trends across the cell lines are in agreement, there are several reasons to be cautious in directly comparing the two. The flow cytometry data uses specific monoclonal antibodies targeted to the $\alpha_v\beta_3$ integrin receptor compared to the RGD on the microspheres, which generally target the $\alpha_v\beta_3$ integrin receptor but can also non-specifically bind to other cell surface receptors. The flow cytometry data also is able to assess the entire surface area of the cell, compared to the fluorescence microscopy data, where only the exposed cell surface not adhered to the bottom of the Petri dish is assessed. Cell-to-cell or cell-to-surface tension plays an important role in the expression of the integrin receptors and likely affect the physical distribution of the surface receptors [32, 33]. With an average cell size of approximately 15 μm , the surface area of the average cell is approximately 706.5 μm^2 . With an average microsphere size of 1-2 μm covering an area of 1-4 μm^2 , the maximum number of microspheres that could cover a cell would be between 175 – 700 microspheres per cell assuming that the availability of integrin receptors was not a limiting factor and that the microspheres could form a uniform layer.

For each cell line, the fluorescence images for the RGD-coated microspheres were higher in intensity compared to the non-coated microspheres. In most of the images, small, discrete, bright spots corresponded to intact microspheres (Figures 6.7-6.13). Diffuse fluorescence signals localized within cells suggested that microspheres were engulfed and broken down by the cell (Figures 6.7-6.13). Although no direct cell viability stains were done to assess the cells after being incubated with protein microspheres, it was noted that the cells were able to survive and continue replicating for at least 24 hours after incubation and upon prompt cell media replacement after the initial exposure to the microspheres. Further experiments were performed using a confocal microscope (Leica SP2 Visible Laser Confocal

Microscope) in the Beckman Institute for Advanced Science and Technology Microscopy Suite to confirm the location of the microspheres and the Nile Red dye. The cells were stained with DiO perchlorate (AAT Bioquest #22066), a lipophilic dye that stains the phospholipid cell membrane, and the cells reseeded at a high concentration into Petri dishes to quickly form a cell monolayer. The cells were kept in the incubator at 37°C for 4 hours to allow the cells to firmly adhere to the Petri dish surface and placed inside a foil wrap to prevent any potential photobleaching of the DiO dye. The microspheres used for these experiments contained Nile Red dye in the inner core. The microspheres were mixed in with the media, placed over cell monolayer, and confocal imaging was started immediately. After the first set of confocal images (~5 minutes) were taken, the cells were gently washed with PBS three times similar to the previous experiments, and imaged over a 30 min period. Using time lapsed imaging, the images demonstrate that the protein microspheres initially start as bright, discrete, and intact fluorescent spheres to eventually being diffused across the entire cell volume (Figure 6.15). In comparing the RGD-coated Nile Red-filled microspheres to the non-coated Nile Red-filled microspheres (Figure 6.16), the non-coated microspheres appear to stay attached to the cell surface as intact microspheres. Whereas in the case of RGD-coated microspheres, the fluorescence from the Nile Red can be seen in the cell cytoplasm at significantly higher intensities. This would be consistent with previous reports that RGD binding to the $\alpha_v\beta_3$ integrin receptor induces endocytosis of the attached ligands [35, 36]. Additional discussion on the uptake of microspheres by cells is in the next section. Confocal microscopy confirms the results observed under fluorescence microscopy: there is binding and uptake of protein microspheres by these cancer cells and there is preferential uptake of the RGD-coated protein microspheres over non-coated protein microspheres.

HT-29: Human – Colon – Colorectal Adenocarcinoma – Epithelial

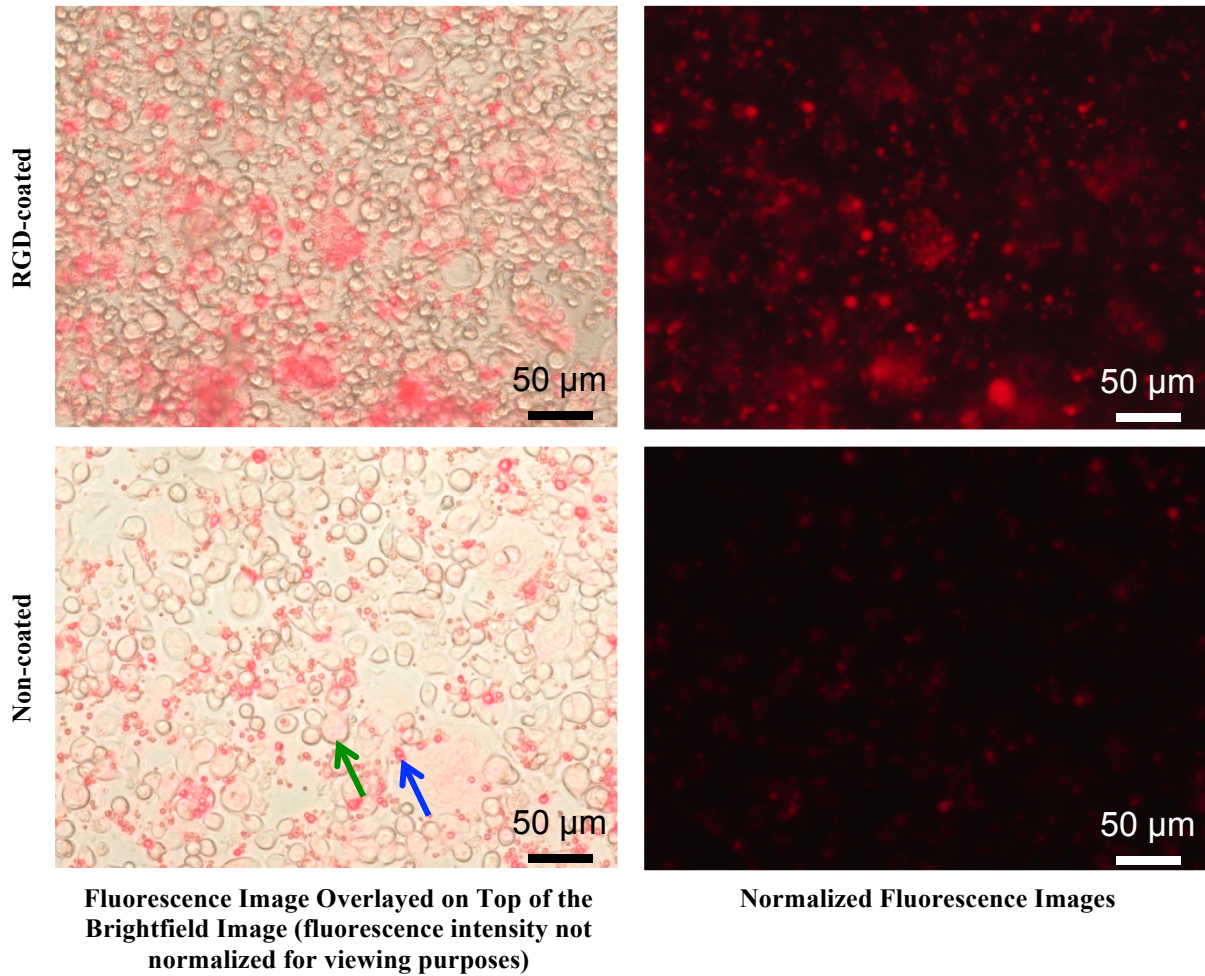


Figure 6.7: Fluorescence images of HT-29 cells incubated with RGD-coated and with non-coated Nile Red-filled microspheres after a 1 hr incubation period. The fluorescence images (right column) are normalized to the same effective exposure time. The fluorescence images overlayed on the brightfield images (left column) have not been normalized for viewing purposes. Bright discrete spots are intact protein microspheres (blue arrow). Diffuse fluorescence (green arrow) across the surface of the cell indicates binding, uptake, and degradation of the microsphere.

SK-BR-3: Human – Mammary Gland – Breast – Adenocarcinoma – Epithelial

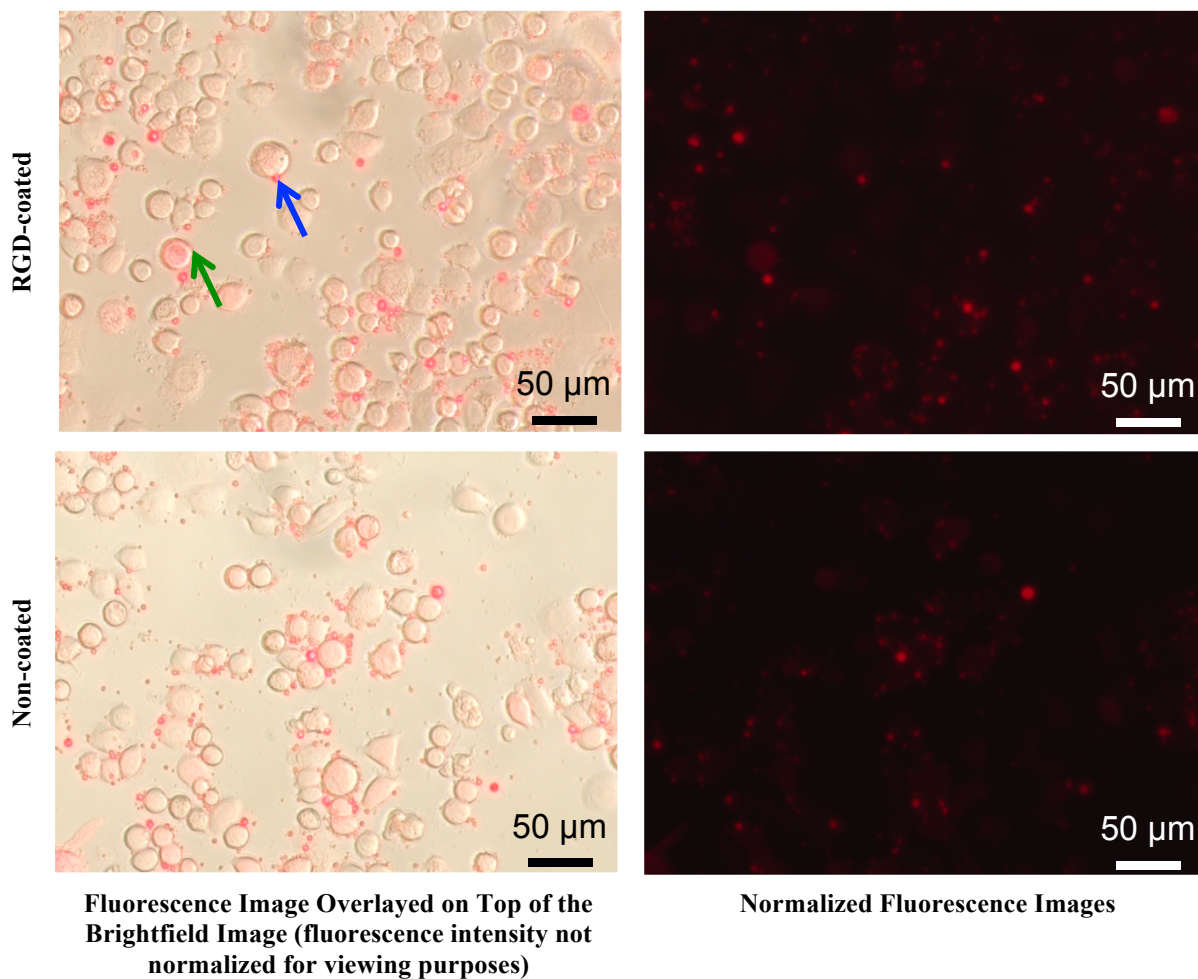


Figure 6.8: Fluorescence images of SK-BR-3 cells incubated with RGD-coated and with non-coated Nile Red-filled microspheres after a 1 hr incubation period. The fluorescence images (right column) are normalized to the same effective exposure time. The fluorescence images overlayed on the brightfield images (left column) have not been normalized for viewing purposes. Bright discrete spots are intact protein microspheres (blue arrow). Diffuse fluorescence (green arrow) across the surface of the cell indicates binding, uptake, and degradation of the microsphere.

MCF-7: Human – Mammary Gland – Breast – Adenocarcinoma – Epithelial

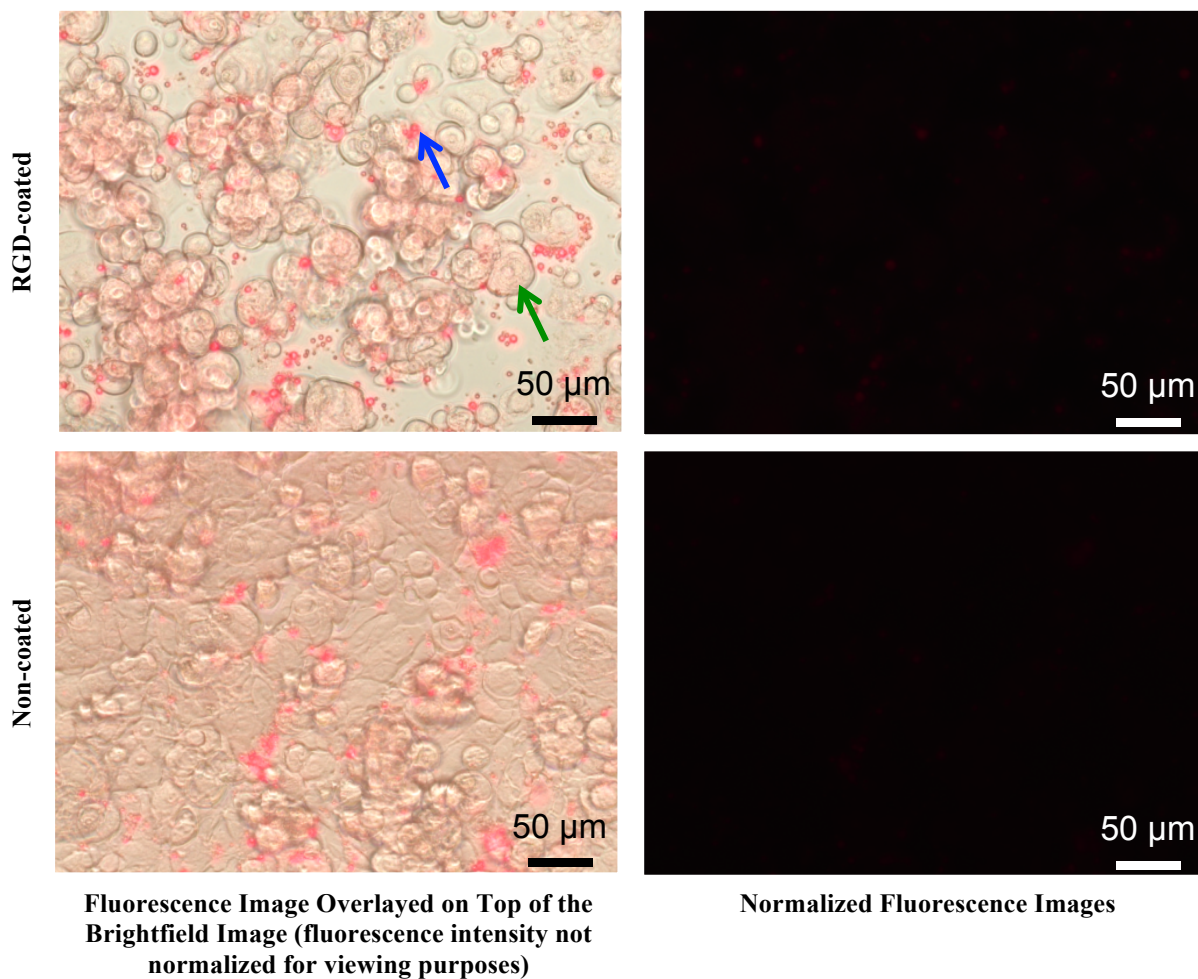


Figure 6.9: Fluorescence images of MCF-7 cells incubated with RGD-coated and with non-coated Nile Red-filled microspheres after a 1 hr incubation period. The fluorescence images (right column) are normalized to the same effective exposure time. The fluorescence images overlayed on the brightfield images (left column) have not been normalized for viewing purposes. Bright discrete spots are intact protein microspheres (blue arrow). Diffuse fluorescence (green arrow) across the surface of the cell indicates binding, uptake, and degradation of the microsphere.

hTERT – HME1: Human – Mammary Gland – Breast – Immortalized – Epithelial

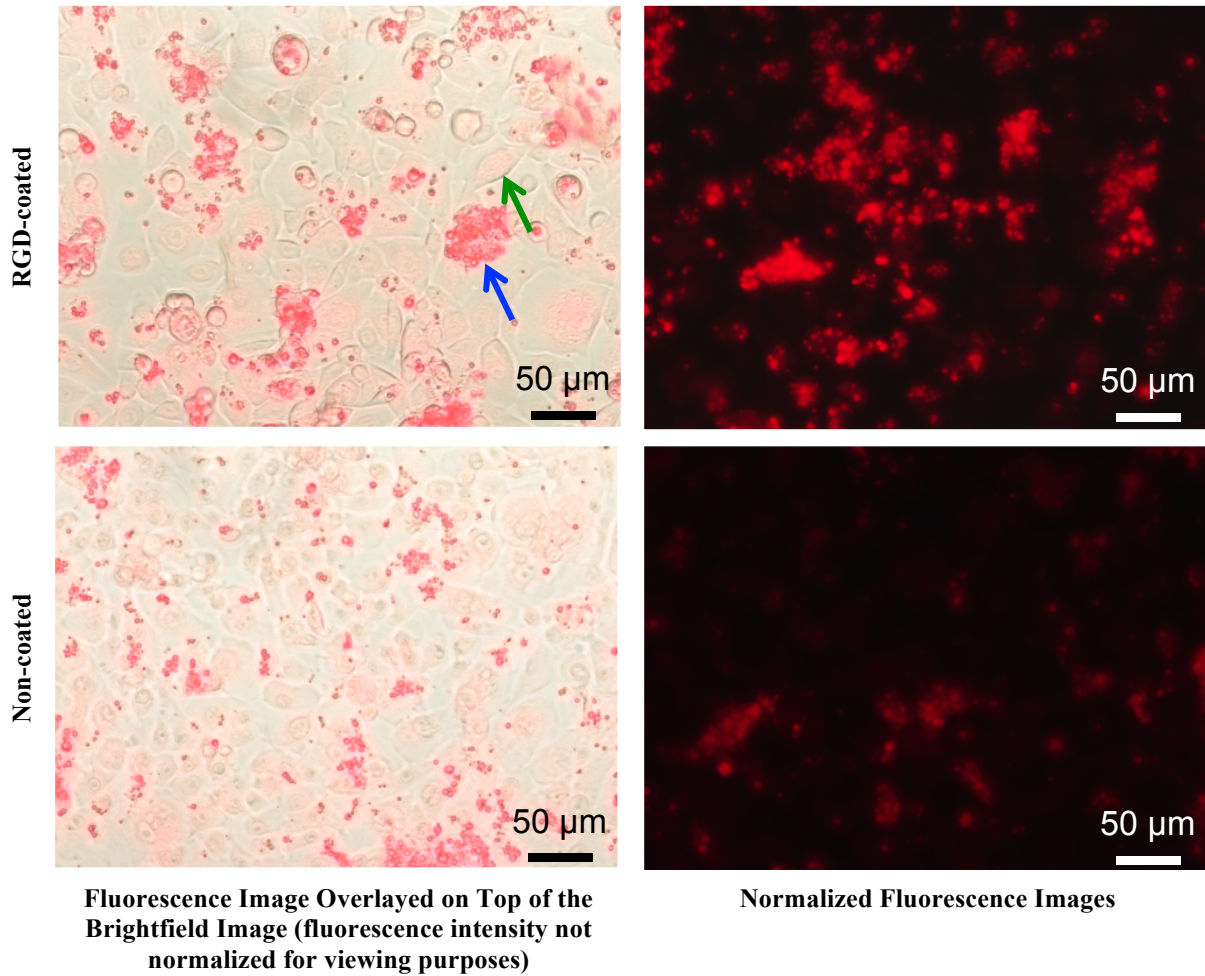


Figure 6.10: Fluorescence images of hTERT-HME1 cells incubated with RGD-coated and with non-coated Nile Red-filled microspheres after a 1 hr incubation period. The fluorescence images (right column) are normalized to the same effective exposure time. The fluorescence images overlayed on the brightfield images (left column) have not been normalized for viewing purposes. Bright discrete spots are intact protein microspheres (blue arrow). Diffuse fluorescence (green arrow) across the surface of the cell indicates binding, uptake, and degradation of the microsphere.

ZR-75-1: Human – Mammary Gland – Breast – Ductal Carcinoma – Epithelial

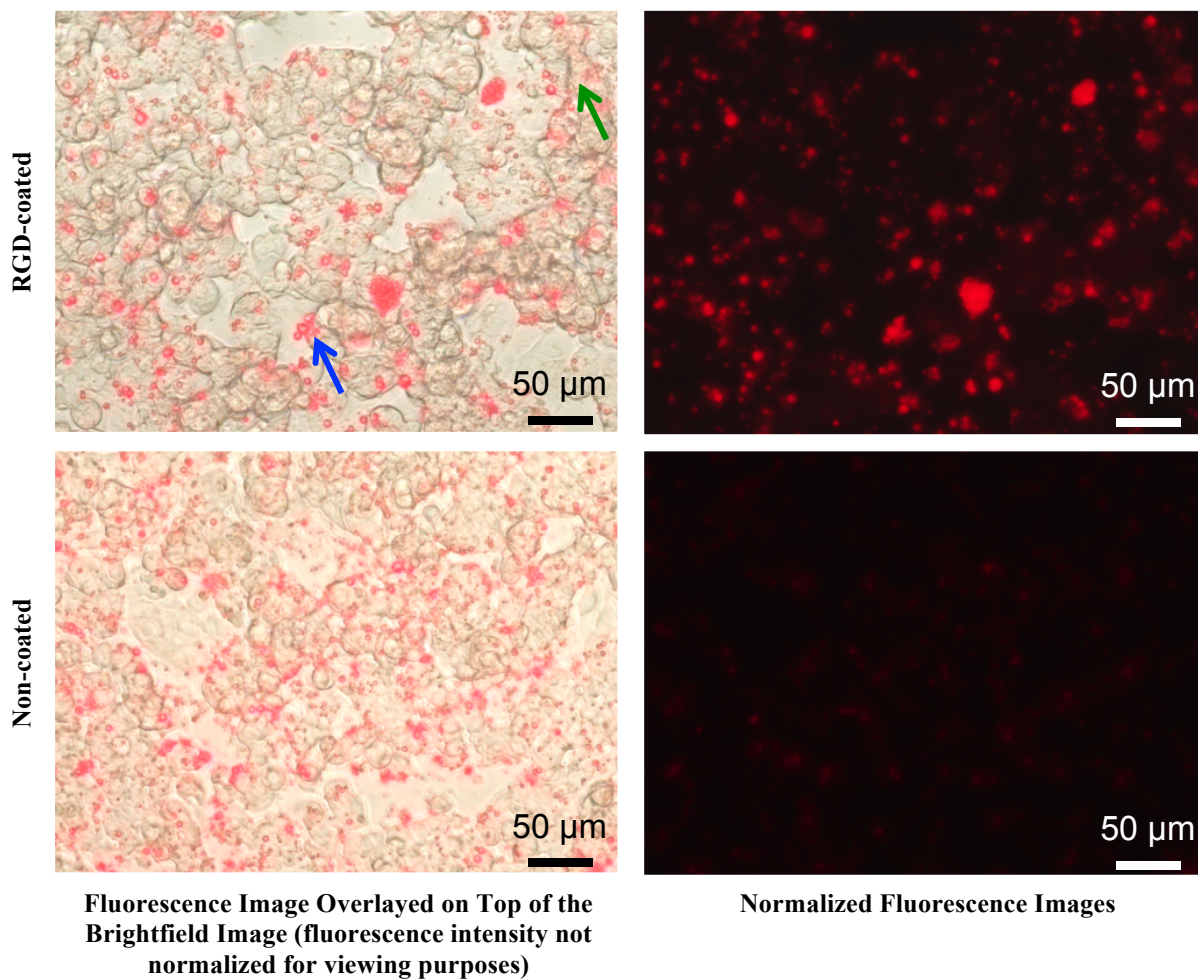


Figure 6.11: Fluorescence images of ZR-75-1 cells incubated with RGD-coated and with non-coated Nile Red-filled microspheres after a 1 hr incubation period. The fluorescence images (right column) are normalized to the same effective exposure time. The fluorescence images overlayed on the brightfield images (left column) have not been for viewing purposes. Bright discrete spots are intact protein microspheres (blue arrow). Diffuse fluorescence (green arrow) across the surface of the cell indicates binding, uptake, and degradation of the microsphere.

MDA-MB-231: Human – Mammary Gland – Breast – Adenocarcinoma – Epithelial

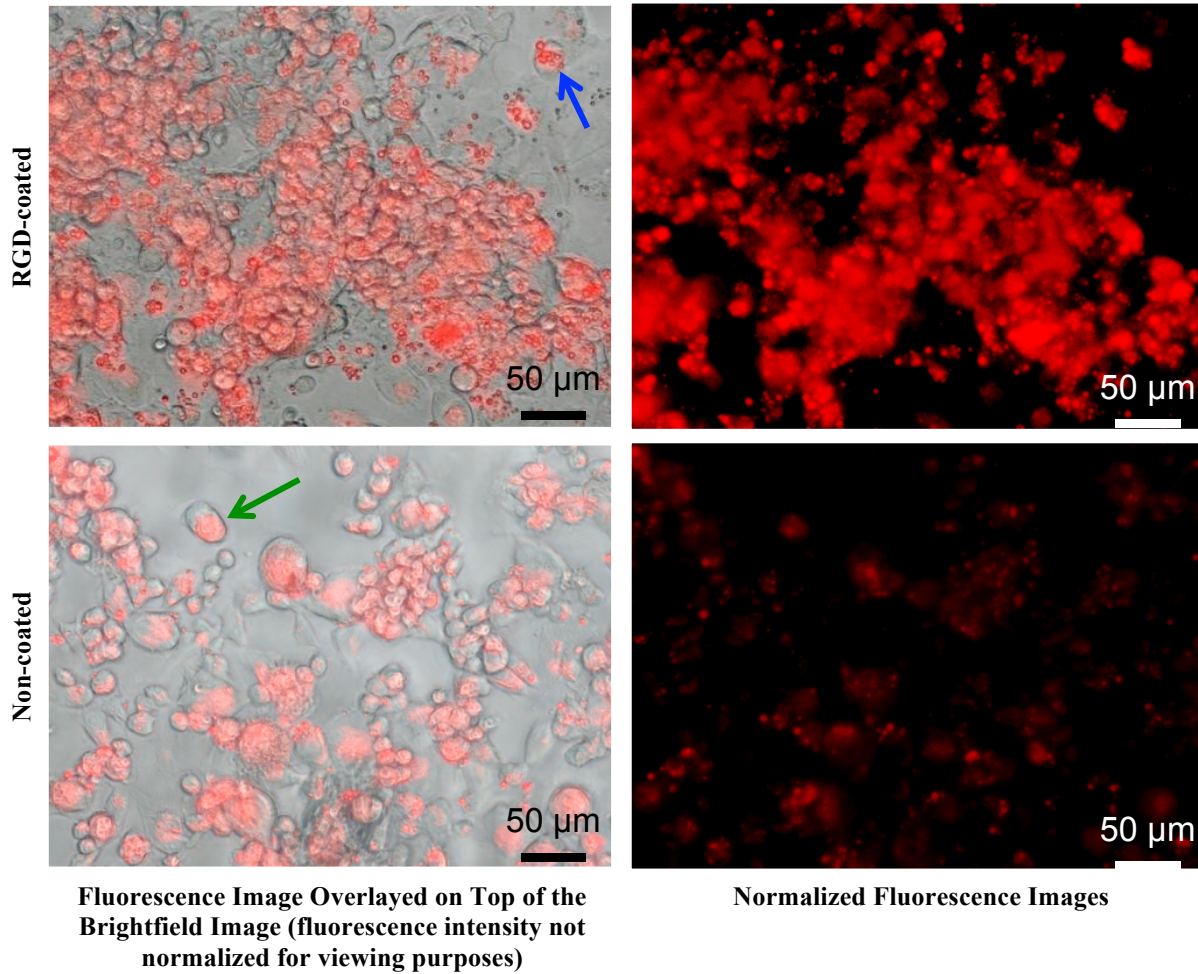


Figure 6.12: Fluorescence images of MDA-MB-231 cells incubated with RGD-coated and with non-coated Nile Red-filled microspheres after a 1 hr incubation period. The fluorescence images (right column) are normalized to the same effective exposure time. The fluorescence images overlayed on the brightfield images (left column) have not been normalized for viewing purposes. Bright discrete spots are intact protein microspheres (blue arrow). Diffuse fluorescence (green arrow) across the surface of the cell indicates binding, uptake, and degradation of the microsphere.

MDA-MB-435S: Human – Mammary Gland – Breast – Ductal Carcinoma – spindle shaped

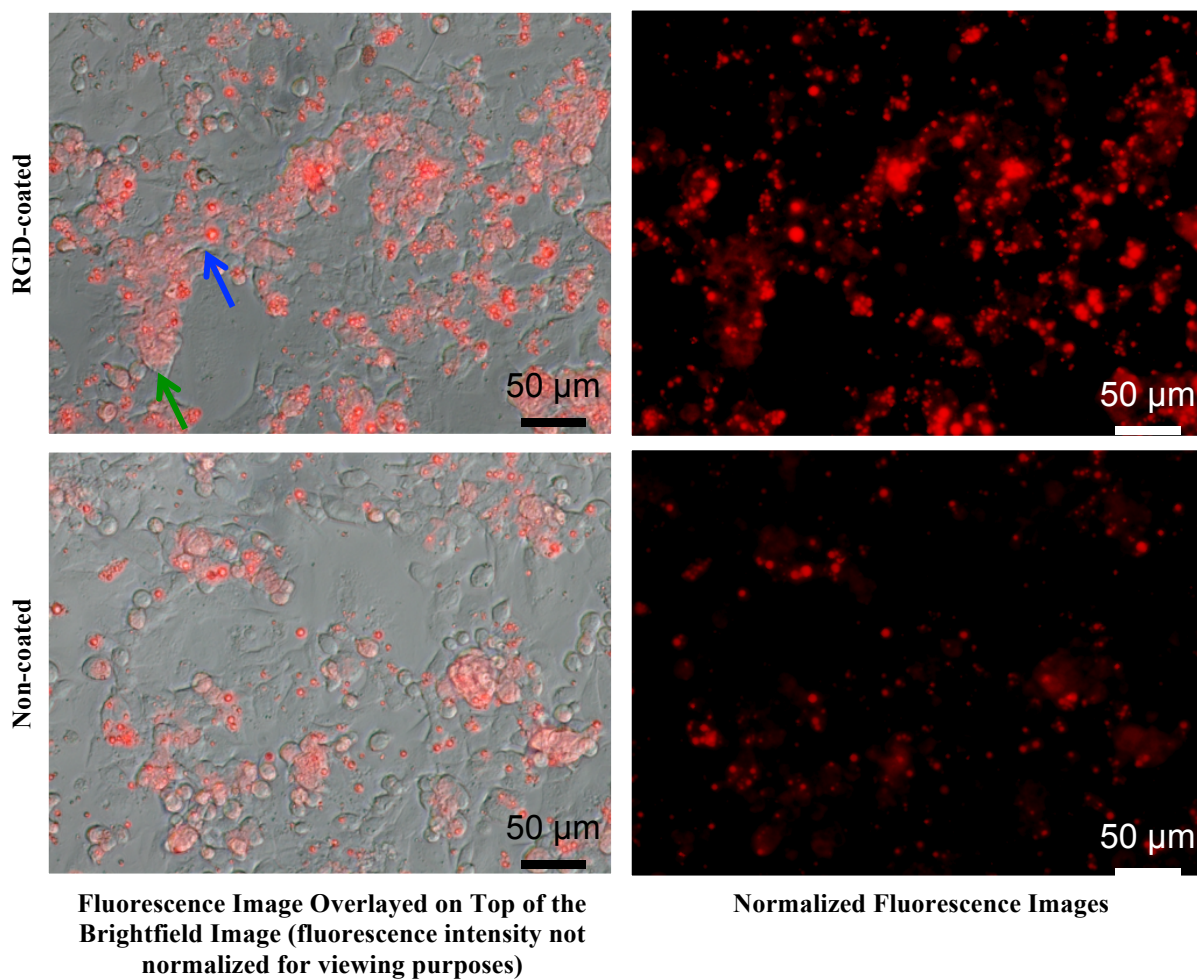
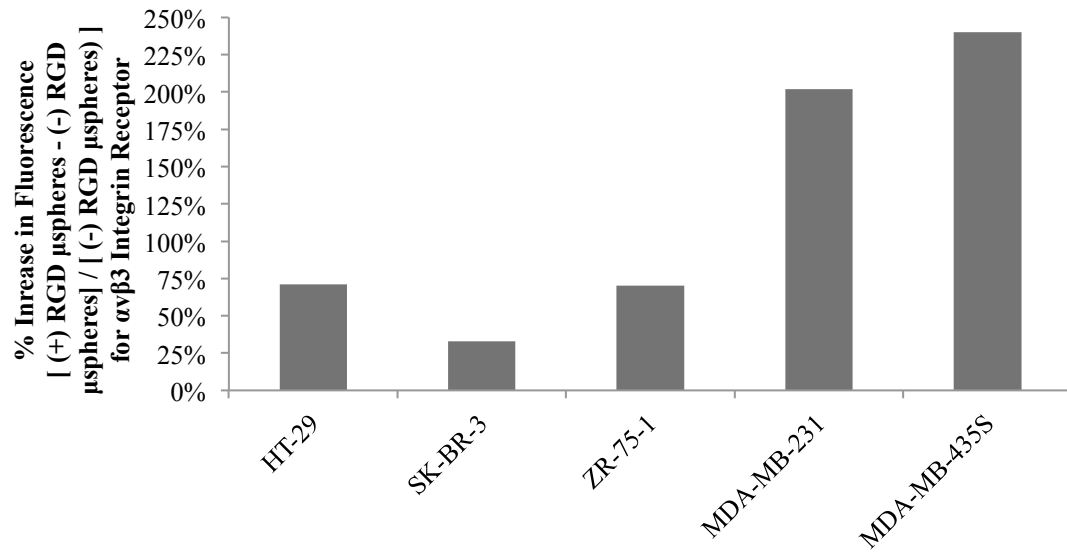
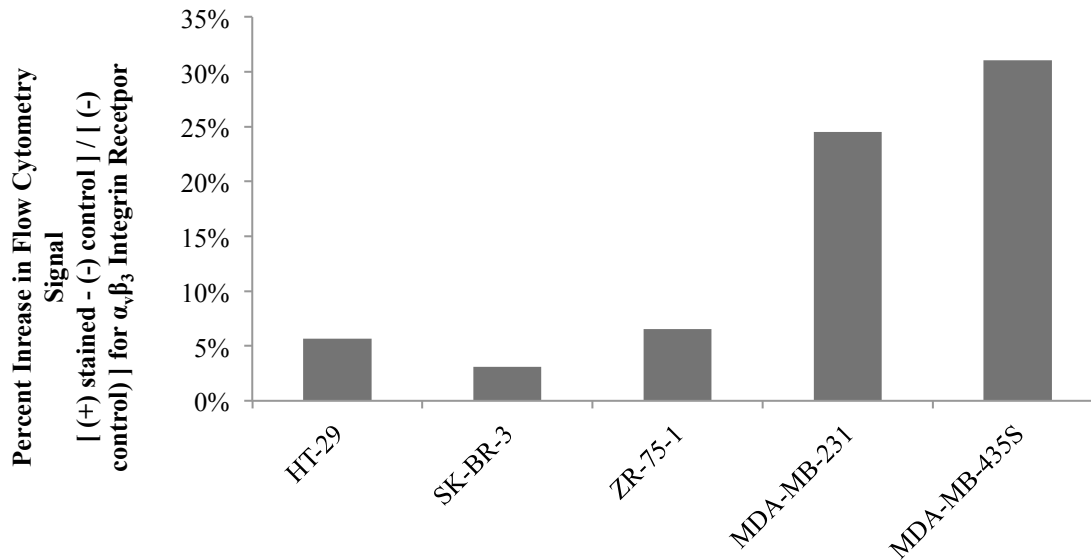


Figure 6.13: Fluorescence images of MDA-MB-435S cells incubated with RGD-coated and with non-coated Nile Red-filled microspheres after a 1 hr incubation period. The fluorescence images (right column) are normalized to the same effective exposure time. The fluorescence images overlayed on the brightfield images (left column) have not been normalized for viewing purposes. Bright discrete spots are intact protein microspheres (blue arrow). Diffuse fluorescence (green arrow) across the surface of the cell indicates binding, uptake, and degradation of the microsphere.



(a)



(b)

Figure 6.14: The percentage increase in the average fluorescence intensity of cells incubated with RGD-coated microspheres compared to cells incubated with non-coated microspheres [(+) RGD- μ spheres - (-) RGD- μ spheres] / [(-) RGD- μ spheres], as measured by fluorescence microscopy (a). Corresponding flow cytometry results of the integrin receptor expression levels shows a similar trend to the fluorescence imaging results (b).

MDA-MB-231 Cell Line w/ non-targeted Nile Red-filled microspheres

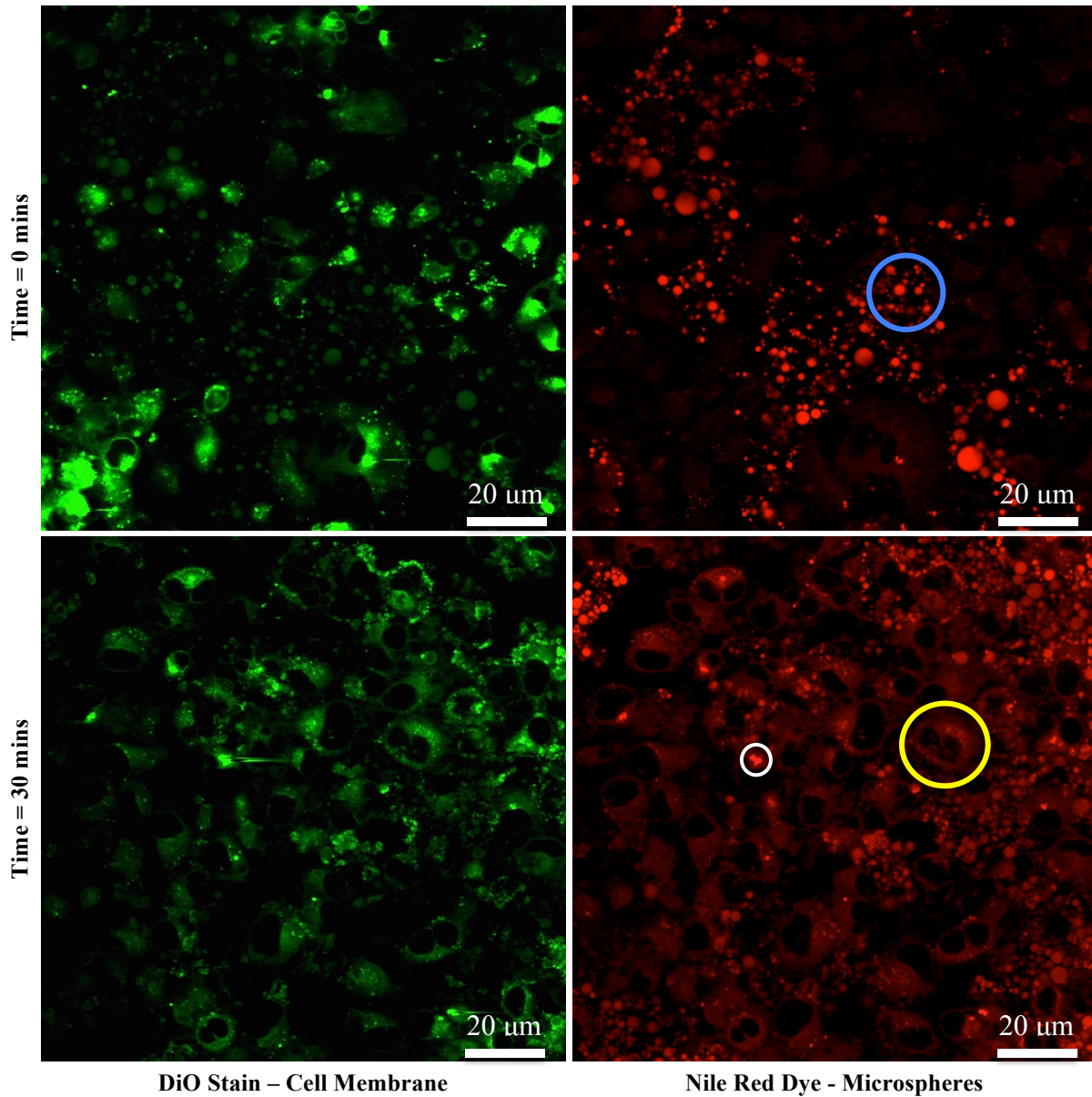


Figure 6.15: The MDA-MB-231 metastatic breast cancer cell line was incubated with non-targeted Nile Red-filled protein microspheres. There are initially distinct bright protein microspheres (blue) which progress to the diffuse staining of the entire cell cytoplasm (yellow) with smaller aggregates of Nile Red dye (white) seen after 30 minutes.

MDA-MB-435S Cell Line w/ non-targeted and targeted (RGD) Nile Red-filled microspheres

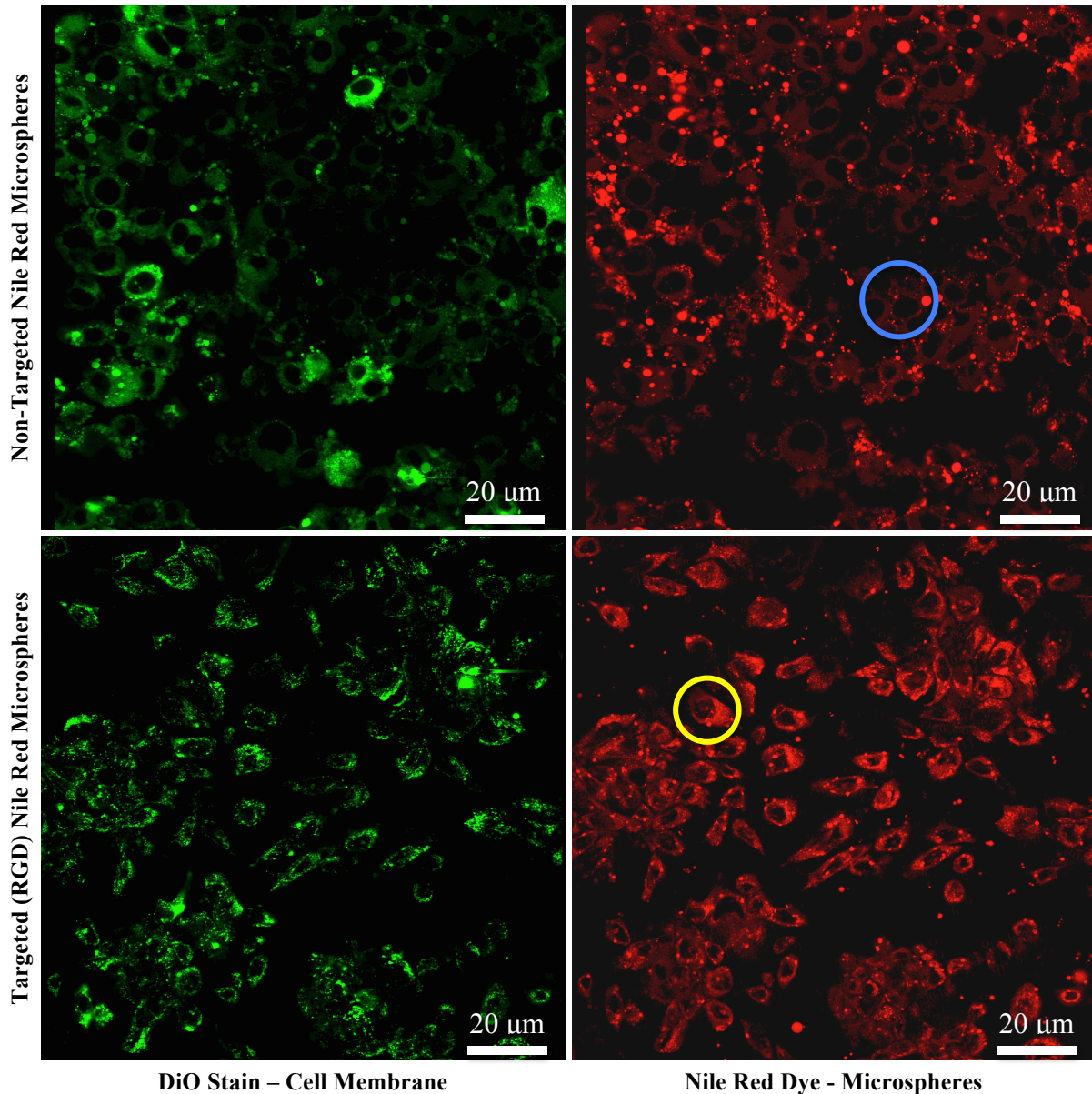


Figure 6.16: The MDA-MB-435S metastatic breast cancer cell line was incubated with non-targeted and targeted (RGD) Nile Red-filled protein microspheres for 30 mins. The non-targeted microspheres (blue: discrete bright intact spheres) remain largely adhered to the cell membrane compared to the targeted (RGD) microspheres have been internalized into the cell and stain the cell cytoplasm at much brighter intensities (yellow).

6.4 *In Vitro* Uptake of Microspheres by Cancer Cells

After the successful targeting of microspheres to the integrin receptor, the observation made in the previous study that microspheres could be engulfed by various cell lines raised interest in the cellular uptake mechanism of the microspheres. As described in the previous studies, intact microspheres were observed as discrete, bright spots; whereas, diffuse fluorescence signal throughout the entire surface area of cells suggested that the microspheres were engulfed and broken down by the cells. The relatively large size of the microspheres suggested that they would, be endocytosed if engulfed by cells. In addition, several published reports suggest that ligands bound to the $\alpha_v\beta_3$ integrin receptor itself may induce endocytosis of the attached ligand [35, 36]. Given that microspheres are an average of 1-3 μm in size, the most likely method of endocytosis is phagocytosis, which is used by cells to ingest the larger particulates. Phagocytosis can be undertaken by epithelial cells as previously reported in respiratory epithelial cells for microspheres that are 2-3 μm in size [37].

Initial studies of the cell uptake mechanism examined incubation of MCF-7 and MDA-MB-435S cells with RGD-coated and non-coated Nile Red-filled microspheres. The cells were examined at four different time points: 15, 30, 45, and 60 minutes. The cells were incubated for each of those time intervals, washed twice with PBS, and imaged with the fluorescence microscope, as previously described. The fluorescence data were similarly processed and are presented in Figures 6.17-6.20. In the first two figures (Figures 6.17-6.18), the fluorescence intensity averages were normalized to the 1 hr time point for each respective cell line. For the following two figures (Figures 6.19-6.20), the fluorescence intensity averages were normalized to the maximum value of both the RGD-coated and non-coated

cases. This would allow for the direct comparison of the binding and uptake of the RGD-coated and non-coated microspheres for each cell line.

The uptake dynamics of both RGD and non-coated microspheres appeared to follow the same time scale. At 30-45 minute incubation period, the binding and uptake of the microspheres by the cell was saturated as demonstrated in Figures 6.17-6.20. At later time points, no appreciative increase in the uptake of the microspheres by the cells is seen. The use of a one hour incubation time period was appropriately chosen for the previous study to look at the binding specificity of the microspheres by the cancer cells. From Figure 6.19 and Figure 6.20, the preferential binding and uptake of the RGD-coated microspheres over the non-coated microspheres is readily apparent with the MDA-MB-435S cells and is not noticeable with the MCF-7 cells. These results correlate with the previous flow cytometry results, which indicated that minimal expression of the $\alpha_v\beta_3$ in MCF-7 cells and a significant overexpression of the receptor in the MDA-MB-435S cells.

Fluorescence images of cells incubated with the microspheres revealed that the Nile Red dye is no longer confined to individual microspheres but stained the entire cell. The cancer cells are believed to uptake the microspheres by endocytosis and break down the microsphere releasing the encapsulated Nile Red. Further studies are needed to monitor in real time, without photobleaching the dyes, exactly how the cell internalizes the microspheres after binding and how the cell degrades the microspheres.

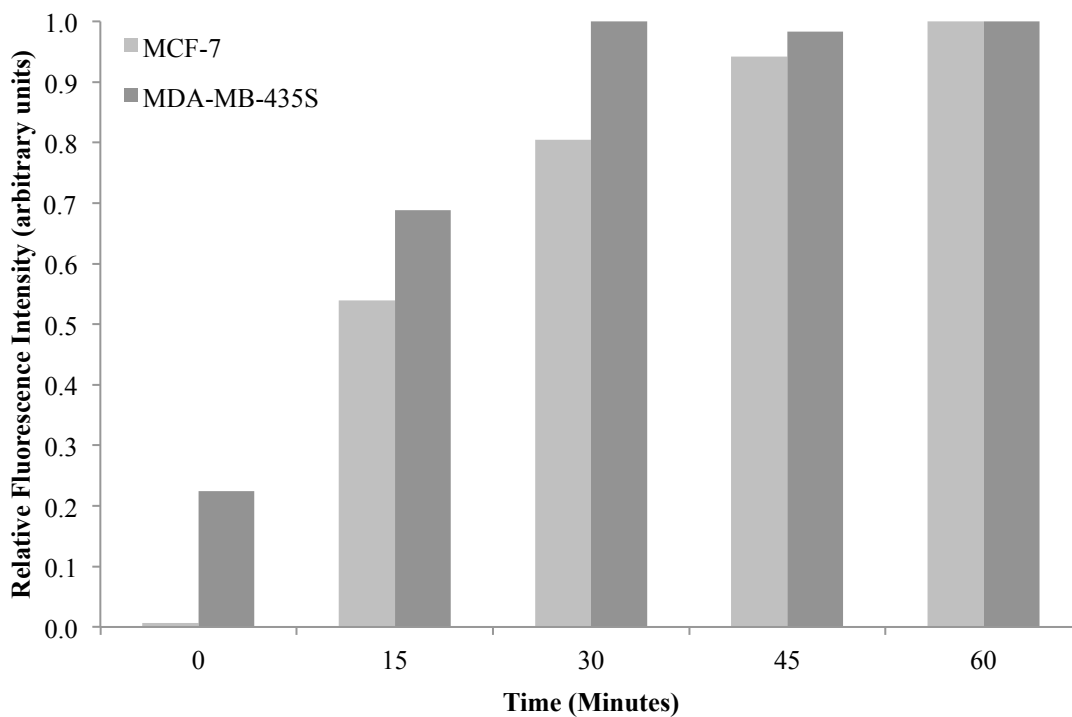


Figure 6.17: Time-lapse study of the binding and uptake of RGD-coated microspheres by the MCF-7 and MDA-MB-435S cells. Fluorescence signals were normalized to the 1 hr time point for each respective cell line. The maximum binding and uptake of the microspheres by the cells is reached at the 45 mins time point.

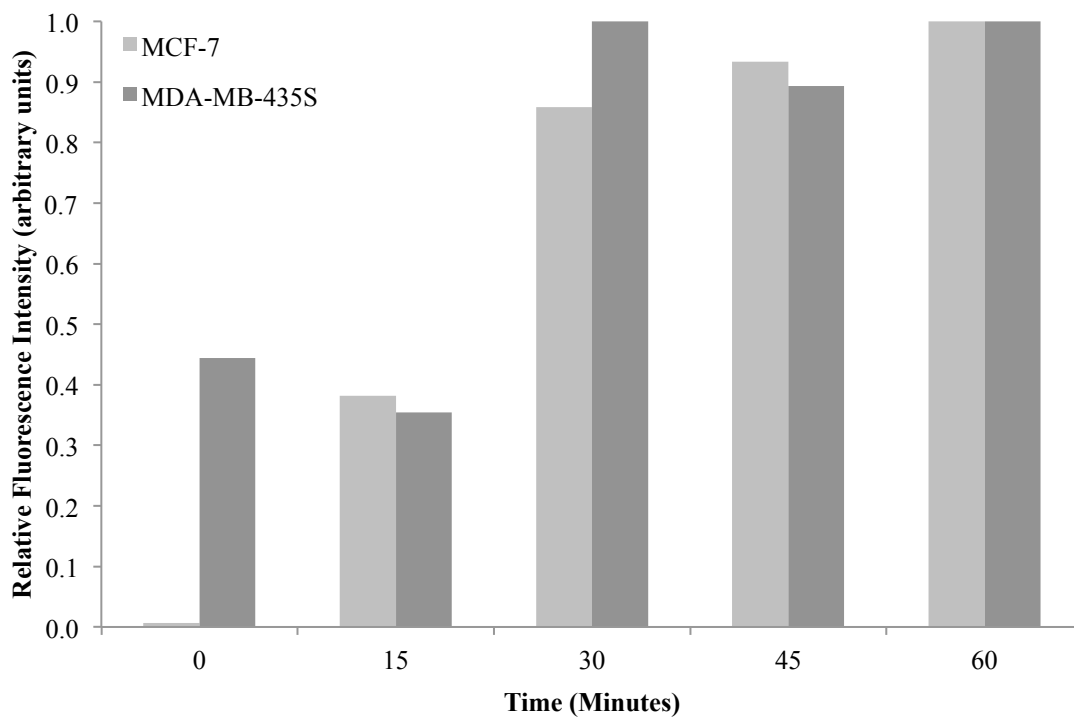


Figure 6.18: Time-lapse study of the binding and uptake of non-coated microspheres by the MCF-7 and MDA-MB-435S cells. Fluorescence signals were normalized to the 1 hr time point for each respective cell line. The maximum binding and uptake of the microspheres by the cells is reached at the 45 mins time point.

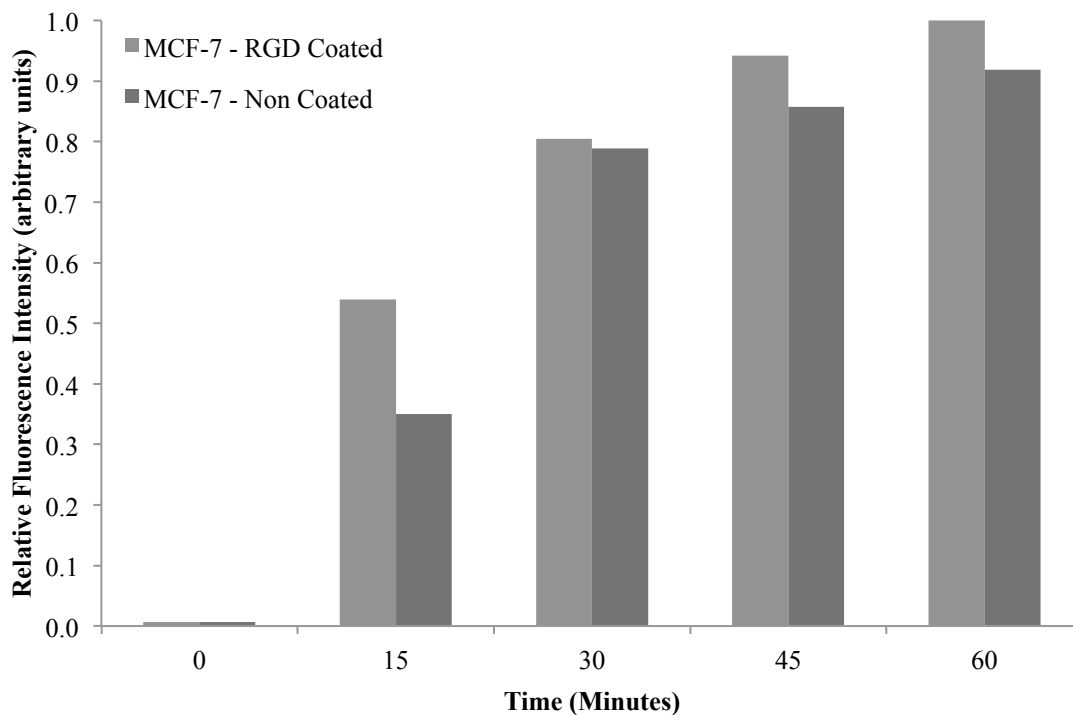


Figure 6.19: Time-lapse study of the binding and uptake of RGD and non-coated microspheres by MCF-7 cells. In the first 15 mins, the RGD-coated microspheres seem to preferentially bind to the MCF-7 cells. After 30 mins, there is little to no noticeable preferential binding of RGD-coated by the MCF-7 cells.

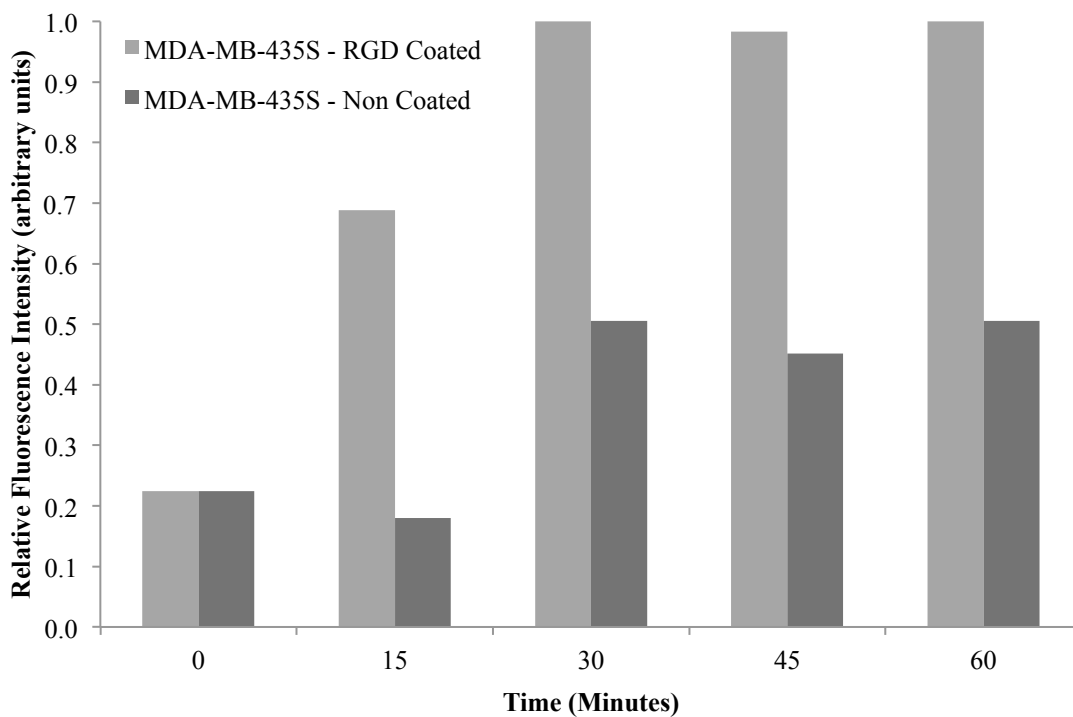


Figure 6.20: Time-lapse study of the binding and uptake of RGD-coated and non-coated microspheres by MDA-MB-435S cells. Throughout all four incubation time points, the results demonstrate that MDA-MB-435S cells have a stronger binding affinity for the RGD-coated microspheres over the non-coated microspheres.

6.5 Conclusions

The binding and cellular uptake of RGD-coated and non-coated Nile Red-filled protein microspheres by a panel of cancer cells was studied in this chapter. The expression of the $\alpha_v\beta_3$ integrin receptor for this panel of cancer cell lines was characterized and quantified using flow cytometry and indirect immunofluorescence staining of surface antigens. The RGD-coated and non-coated protein microspheres were incubated with cancer cell lines of varying expressions of the $\alpha_v\beta_3$ integrin receptor to study the binding specificity and affinity of the microsphere to the integrin receptor. Based on the flow cytometry results, two cell lines (MDA-MB-231, MDA-MB-435S) had the highest expression of the $\alpha_v\beta_3$ integrin receptor by at least one order of magnitude. These particular cell lines had been reported as being highly metastatic with overexpression of the $\alpha_v\beta_3$ integrin receptor [24-26]. The binding specificity of Nile Red-filled microspheres to the cancer cells was quantified using fluorescence microscopy. Based on the fluorescence microscopy data and the flow cytometry data, the use of RGD to target the microspheres to the $\alpha_v\beta_3$ integrin receptor correlated closely with the integrin receptor expression on the cell surface. The cellular uptake and degradation of protein microspheres by the cancer cells was demonstrated by the diffuse fluorescent dye across the surface area of the cell under both fluorescence microscopy and confocal fluorescence microscopy. Due to the size of the microsphere, the nonspecific staining of the entire cell by the Nile Red, and the binding of the microsphere by the cell via the $\alpha_v\beta_3$ integrin receptor, the most likely method of cellular uptake of the microsphere is endocytosis. Currently published studies of LBL particles up to several micrometers in size were also internalized by epithelial cells, monocytes, and dendritic cells via endocytosis [8].

6.6 References

1. Simone EA, Dziubla TD, Muzykantov VR. Polymeric carriers: Role of geometry in drug delivery. *Expert Opin Drug Deliv*, 2008. 5 (12): p. 1283-300.
2. Sahoo SK, Labhasetwar V. Nanotech approaches to drug delivery and imaging. *Drug Discov Today*, 2003. 8 (24): p. 1112-20.
3. Moghimi SM, Hunter AC, Murray JC. Nanomedicine: Current status and future prospects. *FASEB J*, 2005. 19 (3): p. 311-30.
4. Pisal DS, Kosloski MP, Balu-Iyer SV. Delivery of therapeutic proteins. *J Pharm Sci*, 2010. 99 (6): p. 2557-75.
5. Dibbern EM. *Core-shell microspheres for biomedical applications* [dissertation]. Urbana, IL: University of Illinois at Urbana-Champaign; 2007.
6. Kolbeck KJ. *The biomedical applications of protein microspheres* [dissertation]. Urbana, IL: University of Illinois at Urbana-Champaign; 1999.
7. Toublan FJ. *Methods to tailor protein microspheres for biomedical applications* [dissertation]. Urbana, IL: University of Illinois at Urbana-Champaign; 2005.
8. Yan Y, Such GK, Johnston AP, Lomas H, Caruso F. Toward therapeutic delivery with layer-by-layer engineered particles. *ACS Nano*, 2011. 5 (6): p. 4252-7.
9. Elbakry A, Zaky A, Liebl R, Rachel R, Goepferich A, Breunig M. Layer-by-layer assembled gold nanoparticles for sirna delivery. *Nano Lett*, 2009. 9 (5): p. 2059-64.
10. Schneider GF, Subr V, Ulbrich K, Decher G. Multifunctional cytotoxic stealth nanoparticles. A model approach with potential for cancer therapy. *Nano Lett*, 2009. 9 (2): p. 636-42.

11. Leung MK, Such GK, Johnston AP, Biswas DP, Zhu Z, Yan Y, Lutz JF, Caruso F. Assembly and degradation of low-fouling click-functionalized poly(ethylene glycol)-based multilayer films and capsules. *Small*, 2011. 7 (8): p. 1075-85.
12. Cavalieri F, Postma A, Lee L, Caruso F. Assembly and functionalization of DNA-polymer microcapsules. *ACS Nano*, 2009. 3 (1): p. 234-40.
13. Ochs CJ, Such GK, Yan Y, Van Koeverden MP, Caruso F. Biodegradable click capsules with engineered drug-loaded multilayers. *ACS Nano*, 2010. 4 (3): p. 1653-63.
14. Kinnane CR, Wark K, Such GK, Johnston AP, Caruso F. Peptide-functionalized, low-biofouling click multilayers for promoting cell adhesion and growth. *Small*, 2009. 5 (4): p. 444-8.
15. Shukla A, Fuller RC, Hammond PT. Design of multi-drug release coatings targeting infection and inflammation. *J Control Release*, 2011.
16. Poon Z, Chang D, Zhao X, Hammond PT. Layer-by-layer nanoparticles with a ph-sheddable layer for *in vivo* targeting of tumor hypoxia. *ACS Nano*, 2011. 5 (6): p. 4284-92.
17. Su X, Kim BS, Kim SR, Hammond PT, Irvine DJ. Layer-by-layer-assembled multilayer films for transcutaneous drug and vaccine delivery. *ACS Nano*, 2009. 3 (11): p. 3719-29.
18. Smith RC, Riollano M, Leung A, Hammond PT. Layer-by-layer platform technology for small-molecule delivery. *Angew Chem Int Ed Engl*, 2009. 48 (47): p. 8974-7.
19. Kamphuis MM, Johnston AP, Such GK, Dam HH, Evans RA, Scott AM, Nice EC, Heath JK, Caruso F. Targeting of cancer cells using click-functionalized polymer capsules. *J Am Chem Soc*, 2010. 132 (45): p. 15881-3.

20. Toublan FJ, Boppart SA, Suslick KS. Tumor targeting by surface-modified protein microspheres. *J Am Chem Soc*, 2006. 128 (11): p. 3472-3.
21. Reinmuth N, Liu W, Ahmad SA, Fan F, Stoeltzing O, Parikh AA, Bucana CD, Gallick GE, Nickols MA, Westlin WF, Ellis LM. Alpha v beta 3 integrin antagonist s247 decreases colon cancer metastasis and angiogenesis and improves survival in mice. *Cancer Res*, 2003. 63 (9): p. 2079-87.
22. Lee JW, Juliano RL. Alpha 5 beta 1 integrin protects intestinal epithelial cells from apoptosis through a phosphatidylinositol 3-kinase and protein kinase b-dependent pathway. *Mol Biol Cell*, 2000. 11 (6): p. 1973-87.
23. Laferriere J, Houle F, Huot J. Adhesion of ht-29 colon carcinoma cells to endothelial cells requires sequential events involving e-selectin and integrin beta4. *Clin Exp Metastasis*, 2004. 21 (3): p. 257-64.
24. Wetterwald A, Van Der Pluijm G, Que I, Sijmons B, Buijs J, Karperien M, Lowik CW, Gautschi E, Thalmann GN, Cecchini MG. Optical imaging of cancer metastasis to bone marrow: A mouse model of minimal residual disease. *Am J Pathol*, 2002. 160 (3): p. 1143-53.
25. Arap W, Pasqualini R, Ruoslahti E. Cancer treatment by targeted drug delivery to tumor vasculature in a mouse model. *Science*, 1998. 279 (5349): p. 377-80.
26. Wang CY, Chang YW. A model for osseous metastasis of human breast cancer established by intrafemur injection of the mda-mb-435 cells in nude mice. *Anticancer Research*, 1997. 17 (4A): p. 2471-4.

27. Brooks PC, Stromblad S, Klemke R, Visscher D, Sarkar FH, Cheresh DA. Antiintegrin alpha v beta 3 blocks human breast cancer growth and angiogenesis in human skin. *J Clin Invest*, 1995. 96 (4): p. 1815-22.
28. Cooper CR, Chay CH, Pienta KJ. The role of alpha(v)beta(3) in prostate cancer progression. *Neoplasia*, 2002. 4 (3): p. 191-4.
29. Liapis H, Flath A, Kitazawa S. Integrin alpha v beta 3 expression by bone-residing breast cancer metastases. *Diagn Mol Pathol*, 1996. 5 (2): p. 127-35.
30. Hanahan D, Weinberg RA. Hallmarks of cancer: The next generation. *Cell*, 2011. 144 (5): p. 646-74.
31. Hanahan D, Weinberg RA. The hallmarks of cancer. *Cell*, 2000. 100 (1): p. 57-70.
32. Taherian A, Li X, Liu Y, Haas TA. Differences in integrin expression and signaling within human breast cancer cells. *BMC Cancer*, 2011. 11: p. 293.
33. Desgrosellier JS, Cheresh DA. Integrins in cancer: Biological implications and therapeutic opportunities. *Nat Rev Cancer*, 2010. 10 (1): p. 9-22.
34. Brooks PC, Clark RA, Cheresh DA. Requirement of vascular integrin alpha v beta 3 for angiogenesis. *Science*, 1994. 264 (5158): p. 569-71.
35. Danhier F, Le Breton A, Preat V. Rgd-based strategies to target alpha(v) beta(3) integrin in cancer therapy and diagnosis. *Mol Pharm*, 2012. 9 (11): p. 2961-73.
36. Sancey L, Garanger E, Foillard S, Schoehn G, Hurbin A, Albiges-Rizo C, Boturyn D, Souchier C, Grichine A, Dumy P, Coll JL. Clustering and internalization of integrin alphavbeta3 with a tetrameric rgd-synthetic peptide. *Mol Ther*, 2009. 17 (5): p. 837-43.

37. Foster KA, Yazdanian M, Audus KL. Microparticulate uptake mechanisms of *in vitro* cell culture models of the respiratory epithelium. *J Pharm Pharmacol*, 2001. 53 (1): p. 57-66.

CHAPTER 7 FUTURE DIRECTIONS AND CONCLUSIONS

7.1 Optical Coherence Tomography in Breast Cancer

The initial studies presented in this thesis reveal that OCT is a very promising technology for the field of oncology, in particular breast cancer. I have shown that OCT provides real-time intraoperative feedback about the status of tumor margins and lymph nodes, and has the potential to be an invaluable aid for the diagnosis as well as surgical resection of malignant tissue. These initial studies could be further expanded as we develop OCT technology for translation into the clinic. This section will focus largely on the potential future directions of structural OCT in cancer detection, diagnosis, and treatment.

The first direction is the development and assessment of automated methods for classifying the OCT data. Preliminary research in different types of tissues (tumor, adipose, stromal) suggests promising methods for automating the classification of OCT images, which include power attenuation of the OCT signal and the spatial frequency of scatterers along a single axial scan [1-4]. A potential limitation of these two methods is the assumption that the tissue is homogeneous along the depth of an axial scan. Further studies should determine the effects of tissue heterogeneity on the ability to classify different regions as tumor, stromal, or fat tissue. Recent advances in the acquisition speeds of OCT systems, the move to three-dimensional imaging, and increases in resolution will enable the development of crucial algorithms that can initially and rapidly identify suspicious areas for the physician or trained OCT user.

The second direction is to extend the scope of the studies presented in this thesis into larger clinical studies. There are several other factors that would provide additional value to the development of OCT for the assessment of breast cancer. It would be important to determine how demographic information such as patient age or past surgical history affects the interpretation of OCT images.

The average age of patients enrolled in the study reported in this thesis was 64. Younger patients are expected to have less fat tissue and more stromal tissue in the breast than older patients. Previous reports indicate that the bulk refractive index of stromal tissue is similar to the refractive index of tumor tissue; hence, an increasing challenge for the development of OCT technology will be the ability to differentiate abnormal tissue from healthy surrounding tissue, particularly in younger patients. With a larger pool of patients, the potential to image and assess smaller specimens and smaller lesions will increase.

Prior surgical procedures on breast tissue that lead to the introduction of scarred tissue could affect OCT-based detection of cancerous tissue. A large scale clinical study of the intraoperative use of OCT in the assessment of breast cancer tumor margins and axillary lymph nodes would be necessary for investigating and addressing the following factors: system-to-system variability, user-to-user variability during acquisition, and user-to-user variability in data interpretation. With this study, the rates at which re-operation occurs to remove additional breast tissue to close or positive margins would be an important short-term outcomes assessment since additional surgeries exposes the patient to additional surgical risks such as infections and lymphadenopathy. Once OCT is validated in larger clinical trials, the impact of intraoperative OCT imaging can be evaluated through outcomes-based studies. One study could determine the effects of OCT intervention in the assessment of tumor margins and

the rate of local recurrence and metastatic spread of the cancer. A second study would determine the effects of OCT intervention in lymph node resection and the development of complications such as lymphedema.

In addition to the intraoperative application of OCT for breast cancer surgeries, this technology could be valuable in the field of pathology by guiding the sectioning of tissue specimens submitted for histopathological analysis. In the current standard of care, tissue specimens are vastly undersampled, and they are guided inefficiently and subjectively, most often by visual inspection and manual palpation. Usually no more than a series of ten to twenty histology sections are taken from tissue specimens with average sizes of 5 x 5 x 5 cm, or 125 cm³. The high scanning speeds currently available with OCT could enable rapid imaging of tissue specimens and could identify suspicious regions for further histopathological analysis.

7.2 Protein Microspheres

The methodologies for synthesizing and customizing protein microspheres have been studied in depth for the last two decades. Protein microspheres are demonstrated as a versatile and durable vehicle for encapsulating particles into the inner core, embedding particles into the protein shell, and layering thin films onto the microsphere surface using the layer-by-layer assembly method.

The development of protein microspheres as a multi-modal contrast agent largely depends on the clinical application and stage of research (i.e. basic science, *in vitro*, animal, or human studies). For example, this thesis focused primarily on the development of a protein microsphere that could provide magnetic and fluorescence contrast. The aim of the research

was to bridge a wide-field fluorescence imaging system, commonly used to study drug delivery in small animals, with microscopic imaging using magnetomotive OCT. Fluorescence microscopy or confocal microscopy can be used to confirm the localization of the protein microspheres in tissues during histological analysis.

Once the stage of research moves from a small animal model to larger animals and eventually to humans, the use of a fluorescence imaging system for *in vivo* monitoring of the circulation and localization of microspheres will no longer be useful. At these scale ranges, the penetration depth for fluorescence imaging will be severely diminished. This issue was already observed when using rats instead of mice to study *in vivo* targeting of the RGD-coated protein microspheres discussed in Chapter 6. In such cases, other wide field imaging modalities with deeper penetration depths such as MRI or ultrasound imaging should be explored.

The modifications made to target protein microspheres primarily focused on the use of a linear RGD peptide. The flow cytometry and fluorescence imaging data demonstrated that linear RGD-coated microspheres effectively bound to cancer cells expressing high levels of the $\alpha_v\beta_3$ integrin receptor. Fluorescence imaging data still revealed levels of non-specific binding of the RGD-coated protein microspheres to the cells. In order to improve the targeting capabilities of the protein microspheres, additional research will need to be performed to increase the level of specific binding of the protein microspheres to the $\alpha_v\beta_3$ integrin receptor. Several other modifications could be explored for increasing the binding specificity to $\alpha_v\beta_3$ integrin receptors. The first would be a quantitative determination of the coverage of RGDKKKKKK layered on the surface of protein microspheres. SEM results suggested that the RGD sequence was not uniformly layered and did not fully cover the surface of the

microspheres. However, it is not clear whether any of the procedures used to process the microspheres for SEM and TEM analysis had any impact on the RGD peptide layer. Once the amount of RGD coating on microspheres is quantified, methods for increasing the coverage of the linear RGD peptide can be investigated. Questions that may be important to test include: whether the length of the poly-lysine residues contained in the RGD sequence alters binding to the protein microspheres, and whether there is difference in the layering of linear RGD vs. cyclic RGD onto the microspheres. Many studies suggest that cyclic RGD has a higher binding specificity and affinity to the $\alpha_v\beta_3$ integrin receptor than linear RGD [5-8]. The circulation lifetime of cyclic RGD was found to be higher than that of linear RGD; cyclic RGD was not as quickly degraded and cleared from the body as linear RGD [5-8].

The RGD peptide sequence is known to bind to a family of integrin receptors, which supports non-specific binding of RGD-coated protein microspheres to other receptors aside from $\alpha_v\beta_3$ integrins. The use of monoclonal antibodies targeted against both the alpha and beta subunits of the integrin receptor could help increase binding specificity and decrease non-specific binding of the protein microspheres to cells. Based on published reports, it is possible to use click chemistry for doing covalent LBL assembly instead of depending solely on electrostatic or hydrogen bonding interactions employed by traditional LBL assembly [9]. This method was used to couple monoclonal antibodies functionalized with an azide group to a capsule surface containing alkynes [9, 10].

In addition to the contrast and targeting properties of the protein microspheres described in this thesis, further applications of protein microspheres were mentioned in Chapter 4, ranging from the encapsulation of hydrophobic drugs to the encapsulation of heat absorbing particles to induce hyperthermia. Before any major studies are undertaken to

explore the use of protein microspheres as therapeutic agents, further *in vitro* and *in vivo* work should be performed to study the mechanisms and consequences of the cellular uptake of the protein microspheres. $\alpha_v\beta_3$ integrins can mediate endocytosis of the ligands bound to this receptor [11-13], suggesting a role of integrins in the cellular uptake of microspheres observed in studies described in this thesis. Cellular uptake and degradation of microspheres enabling the release of encapsulated therapeutic agents would be desired in applications where diseased cells are targeted; however, for imaging purposes in which the microspheres serve as contrast agents, destruction of the microspheres would render this application useless. Studying the mechanisms of cellular uptake will provide insights in the design of the protein microsphere as targeted therapeutic agents.

7.3 *In Vitro* Targeting of Protein Microspheres

RGD-coated protein microspheres were used for *in vitro* studies targeting $\alpha_v\beta_3$ integrin receptors expressed on the cell surface of a variety of cancer cell lines. The previous discussion focused on increasing the binding specificity of the protein microspheres to the $\alpha_v\beta_3$ integrin receptor by identifying methods for increasing the RGD coating of microspheres. The *in vitro* studies reported in this thesis used single cell monolayers to quantify and compare microsphere binding to integrin receptors exposed on the cell surface. In this configuration, the basal sides of the cells were not exposed to protein microspheres. Since integrins mediate cell-substrate adhesion, it is conceivable that a significant portion of the integrin receptors may be located at the junction between the cell and the Petri dish rather than being exposed at the apical side of the cells. Other methods should be explored for studying the dynamics of binding between free floating protein microspheres and cancer cells

to better mimic the physiological environment in which protein microspheres would bind to circulating tumor cells located in the vasculature or lymphatic system.

In order to extend initial findings that suggested that protein microspheres were readily engulfed by cancer cells via endocytosis and degraded by the cells, studies should be performed to identify the timescale of microsphere binding and destruction by cells. Based on the studies presented in Chapter 6, the encapsulated Nile Red from the microspheres was found localized to the cell. Performing confocal fluorescence microscopy would provide better information about whether the dye localizes to the cell membrane or to the cell cytoplasm.

An increased understanding about the interactions between microspheres and cells would guide the development of microcapsules for cellular therapeutic delivery. This would be the first step towards the molecular targeting of therapeutics using protein microspheres. If cells readily uptake the protein microspheres, then the development of external methods to rupture the microspheres or induce hyperthermia using the microspheres may not be necessary. Further, toxicity studies of the protein microspheres and encapsulated particles should be carried out to determine the effects of non-specific binding of these protein microspheres.

7.4 *Ex Vivo* and *In Vivo* Targeting of Protein Microspheres in Cancer Animal Models

Previous studies using protein microspheres in animals were largely focused at the bio-distribution of non-targeted protein microspheres *in vivo* or on demonstrating increased non-specific contrast in organs [14-16]. In earlier studies, I looked at whether iron oxide-filled protein microspheres could be detected by MM-OCT under a number of different

microenvironments: microspheres in an agarose gel, microspheres inside of macrophages in an agarose gel, and microspheres injected into tumor tissue. The results, in Figure 7.1, indicated the ability to see individual or small aggregates of iron oxide-filled protein microspheres under both low-scattering and high-scattering microenvironments.

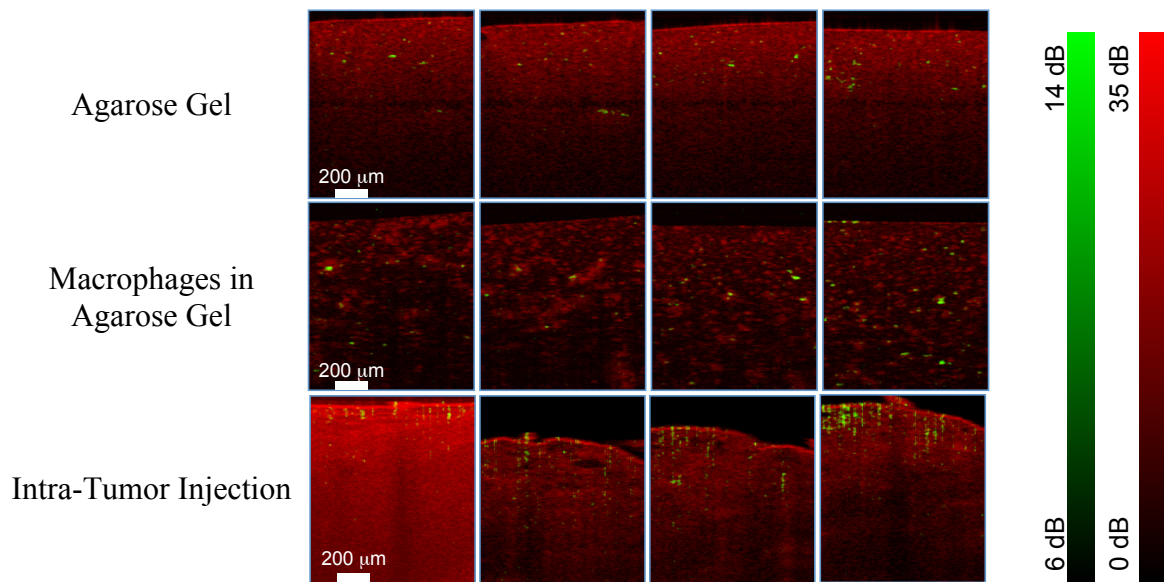


Figure 7.1: Iron oxide-filled protein microspheres embedded in agarose gel (top row). Iron oxide-filled protein microspheres uptaken by macrophages subsequently embedded in an agarose gel (middle row). Iron oxide-filled protein microspheres that were injected into a tumor sample from an NMU carcinogen induced rat.

The studies presented in this thesis are the first attempts at using targeted protein microspheres *in vitro* for cancer applications. A wide-field fluorescence imaging system was

initially identified for its ease of use and its potential for *in vivo* tracking of fluorescent microspheres. In a preliminary animal model experiment with the NMU carcinogen induced rat animal model, RGD-coated Nile Red-filled protein microspheres were injected via the tail vein as a bolus injection. This initial experiment showed some very promising results where the RGD-coated protein microspheres traveled to and aggregated to the locations of the tumors and lymph nodes (Figure 7.2). At the end of this time period, the rat was euthanized and dissected. The tumors and surrounding tissue were imaged with the wide-field fluorescence imaging system which identified the protein microspheres not only at the tumor site but clearly delineating the extensive vascular and lymphatic system that surrounded the tumor (Figure 7.3). Upon further dissection, it was also observed that the protein microspheres had traveled to and localized to the abdominal lymph nodes (Figure 7.3).

Studies are still ongoing to test the *in vivo* targeting of RGD-coated protein microspheres in an animal cancer model. As further studies were undertaken to further investigate the preliminary results above, several issues were identified that should be addressed in future *in vivo* targeting animal studies. As described in Chapters 4 and 5 of this thesis, the microspheres designed for this system were imaged in gel phantoms. Despite characterization and systematic optimization of the fluorescent protein microspheres for this system, the microspheres were not readily visible during *in vivo* administration in rats. The main reasons were attributed to the use of an inappropriate animal cancer model. The larger size of a rat interfered with the ability to monitor the *in vivo* circulation of the protein microspheres. Furthermore, although the rat hair was shaved off, the thick rat skin largely interfered with the ability to visualize fluorescent microspheres deeper in the rat tissue. Future studies of the *in vivo* targeting of protein microspheres could be done with nude mice.

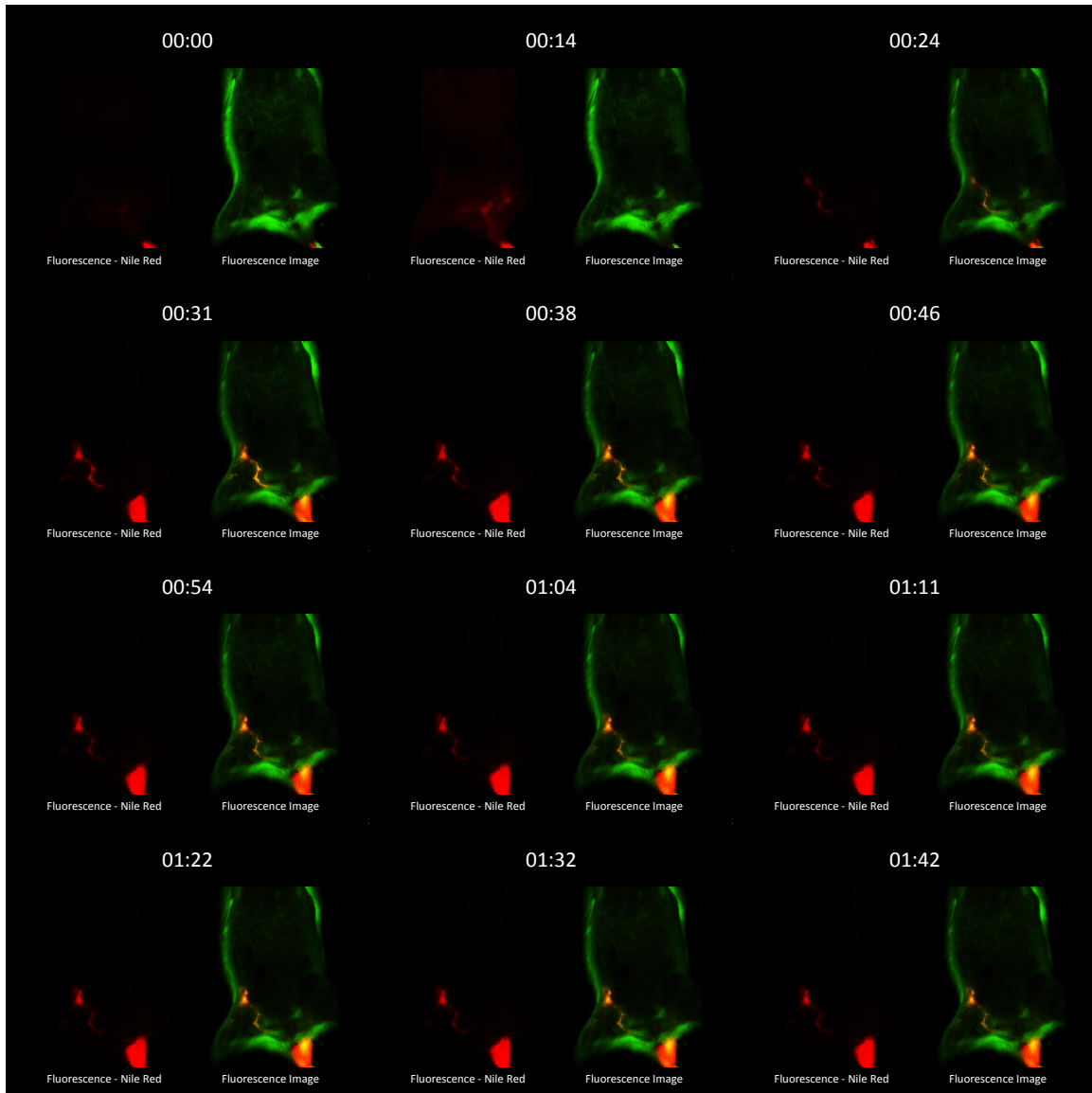


Figure 7.2: Wide-field fluorescence imaging of a NMU carcinogen induced rat animal in real time. The RGD-coated Nile Red-filled protein microspheres were injected at time 0. The time scale shown above is at 0 hrs 0 mins on the first image to 1 hrs 42 mins on the last image.

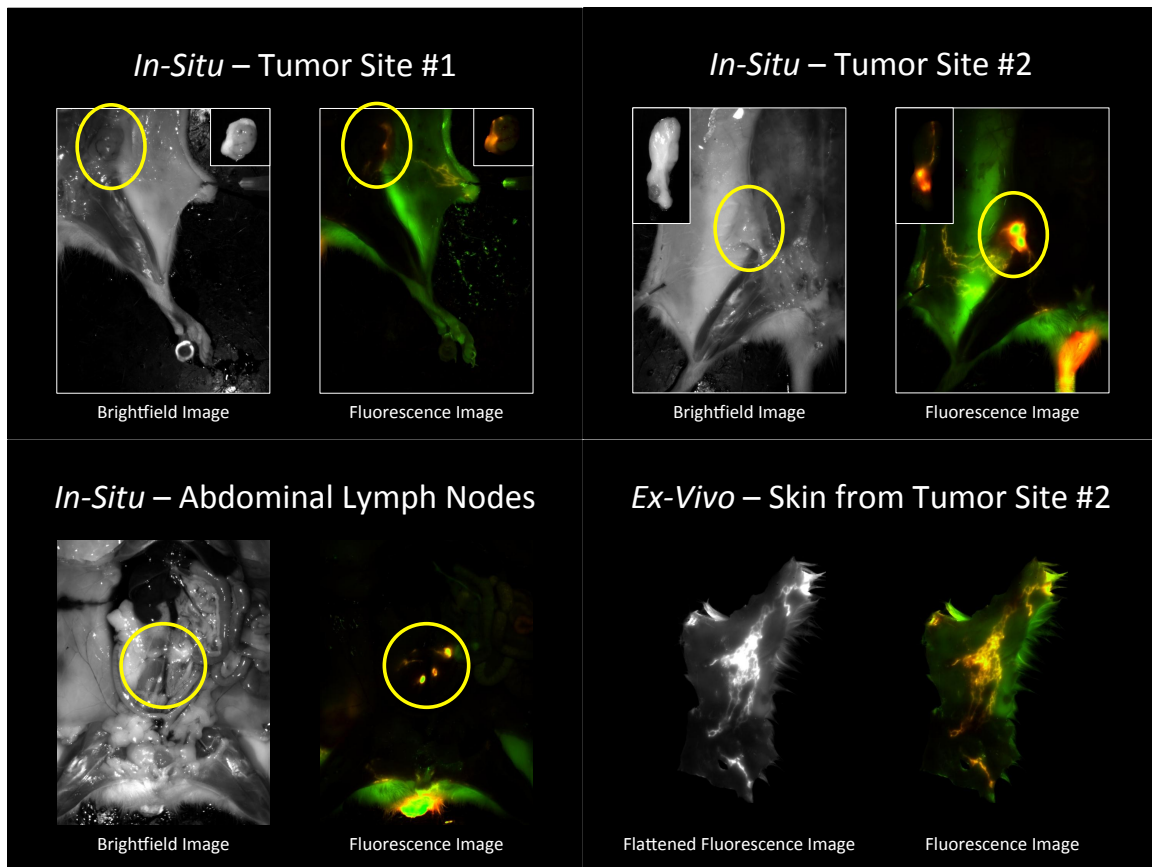


Figure 7.3: Wide-field fluorescence imaging of the two tumor sites, the abdominal lymph nodes, and the skin from the site of the 2nd tumor in the NMU carcinogen induced rat animal. The skin sample showed that the microspheres were present in vast extensive network of blood vessels and lymph vessels surrounding the tumor.

A more appropriate mouse tumor model should be developed and characterized for testing the *in vivo* targeting of microspheres. The RGD-coated microspheres were designed to target the vasculature with high levels of expression of the $\alpha_v\beta_3$ integrin receptor since their large size precludes them from migrating from the lumen of the vasculature into the extracellular matrix to reach the cancer cells. During tumor angiogenesis, it is known that the tumor vasculature has elevated expression of the $\alpha_v\beta_3$ integrin receptors as the tumor tries to recruit the development of new blood vessels. Tumor angiogenesis occurs once the tumor is larger than a few millimeters and can no longer support itself from the passive diffusion of nutrients.

Preliminary results for a NMU-carcinogen induced rat tumor model, a spontaneous tumor model indicated that the maximum expression of the integrin receptor occurred at tumor sizes between 0.5 cm and 1.0 cm. This rat tumor model has been shown to most closely mimic the natural development and progression of human breast tumors notably ductal carcinoma in situ. Although the NMU carcinogen induced mammary tumors in normal rats, the injection of the NMU carcinogen in nude rats and mice did not form any tumors.

Another tumor model available in Prof. Boppart's laboratory is a xenograft model in which MAT III 13762 cells (a rat mammary cancer cell line) are injected sub-cutaneously or intraperitoneally into the rat. This model successfully forms tumors within 2-3 weeks of injection. However, as characterized by *in vitro* work in Chapter 6, the MAT III 13762 cell line does not highly express the $\alpha_v\beta_3$ integrin receptor *in vitro*. Similar to the quantification of the $\alpha_v\beta_3$ integrin receptor *in vitro*, the receptor expression should be quantified for the tumors and vasculature in various animal models. A more suitable animal model may be the xenograft model using the two metastatic cell lines MDA-MB-231 or MDA-MB-435S, which

demonstrated high expression levels of $\alpha_v\beta_3$ integrins *in vitro*. However, it is unclear the expression of the $\alpha_v\beta_3$ integrin receptors on cancer cells is correlated to the integrin receptor expression in the neighboring vasculature.

Studying the pharmacokinetics and pharmacodynamics of the protein microspheres in more detail will be instrumental for successfully monitoring the circulation and localization of targeted protein microspheres. In current animal experiments, protein microspheres were introduced into the tail vein using a syringe pump at a constant rate over 1 hr. However, since little is known about the rate of clearance of the microspheres from the circulation, it is difficult to determine an appropriate method and rate of injection. Available methods include the administration of microspheres in a single bolus injection, a bolus injection followed by a maintenance dose, or a continuous injection for an extended period of time. Because previous reports identified aggregation of protein microspheres at the site of injection or within the circulation, the continuous injection method was initially chosen over bolus injections to decrease the chances of aggregation. Although there appeared to be decreased fluorescence signals at the site of injection with continuous injections during, there were difficulties being able to reliably localize and quantify the fluorescence signal from the microspheres at the major organs. The results were also not reliably reproducible from one animal to another animal. Other methods of introducing the microspheres into the vasculature should be examined, including alternative injection sites.

7.5 *Ex Vivo* and *In Vivo* Targeting of Protein Microspheres in Atherosclerosis

As previously discussed in Chapter 1, the potential of the research presented in this thesis can also be applicable to the field of atherosclerosis. Since the targeting of the protein

microspheres is via the $\alpha_v\beta_3$ integrin receptor, any disease processes that involves inflammation, the activation of angiogenesis, and the proliferation of new blood vessels will also likely benefit from the results presented in this thesis. In atherosclerosis, the primary cell of interest is now the macrophage, which plays an integral role in the development and eventual rupture of atherosclerotic lesions and plaques. Macrophages embedded in an agarose gel and macrophages, previously incubated with iron oxide-filled protein microspheres, also embedded in an agarose gel were imaged under MM-OCT (Figure 7.4). Under the structural OCT image (red), the main scatterers observed correspond to individual macrophages. In the bottom row of images, the iron oxide-filled protein microspheres (green) can be seen under MM-OCT and can be seen localized inside the scattering macrophages (red).

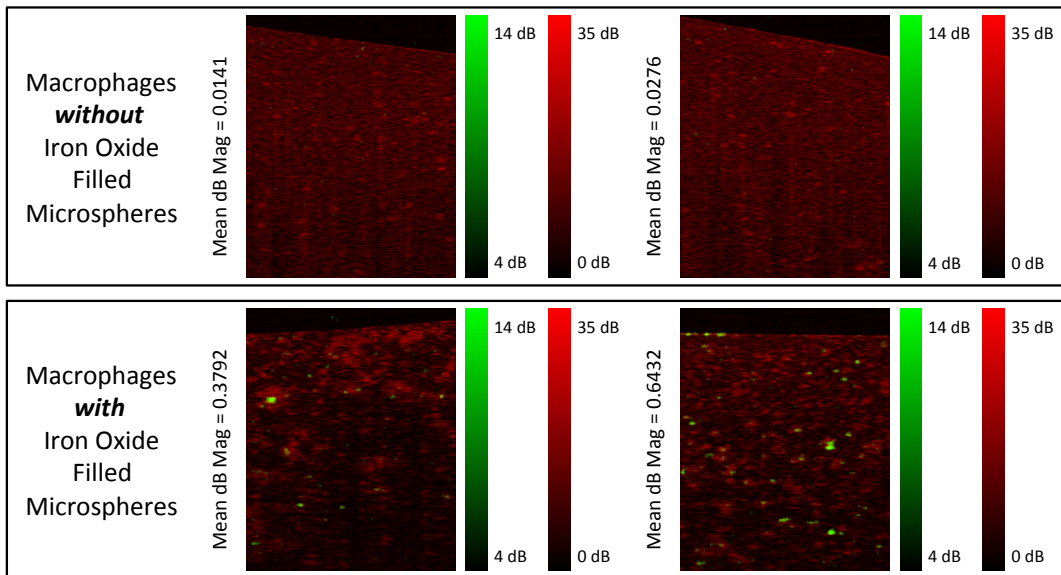


Figure 7.4: MM-OCT images of only macrophages (top row) embedded in an agarose gel. MM-OCT images of the macrophages previously incubated with iron oxide-filled protein microspheres embedded in an agarose gel.

Further preliminary studies were also performed in an atherosclerotic rat animal model. The rats were fed a high-cholesterol and high-fat diet for 10 weeks. The entire ascending aorta, aortic arch, and descending aorta were resected from the rat. The aorta was incubated at 37°C in cell media with iron oxide-filled protein microspheres for 4 hours. After the incubation period, the aorta was thoroughly flushed with saline. The aorta was then incubated at 37°C for an additional 2 hours in saline to remove any loose or excess protein microspheres. The aorta was then cut open and placed between a microscope slide and coverslip for imaging. The inner lumen of the aorta was placed facing down towards the microscope slide. A series of 17 MM-OCT images were taken approximately 1 mm apart from each other along the length of the aorta. H&E histological staining on the sample was also performed. MM-OCT results and corresponding histology from a rat that was fed a normal diet is shown in Figure 7.5. The average MM-OCT signal was found to be 0.0273 dB when averaged across the 17 images taken for this sample. The MM-OCT results and corresponding histology for the aorta from a rat that was on the high-fat and high-cholesterol diet are presented in Figure 7.6. The results show a localized area with a very strong MM-OCT signal. This area correlates to an atherosclerotic lesion on the surface of the inner lumen of the aorta. When averaging the MM-OCT signal across all 17 images, the average signal was 0.329 dB. When averaging across the images with a significant MM-OCT signal (> 0.1 dB), the average MM-OCT signal was found to be 0.931 dB across 5 images corresponding to the area of the atherosclerotic lesion. The average MM-OCT signal across the remaining 12 images representing the normal areas of the aorta was found to be 0.0774 dB. This initial data was promising in demonstrating that the iron oxide-filled protein microspheres can be uptaken into the atherosclerotic lesions and can also be detected under MM-OCT.

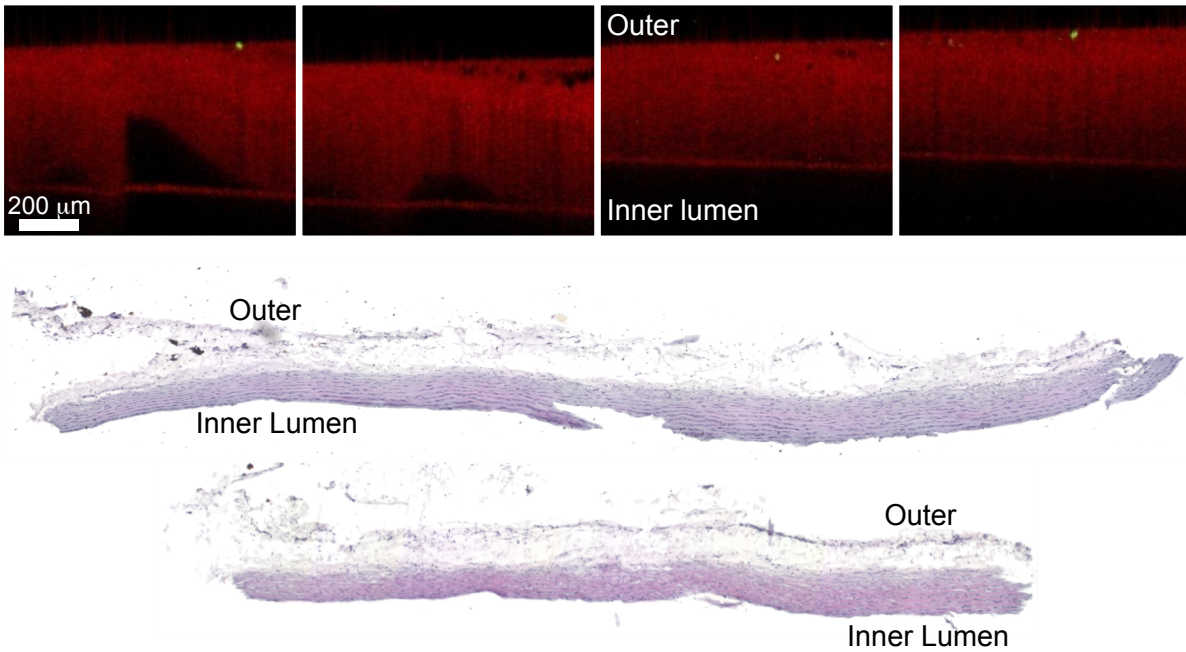


Figure 7.5: MM-OCT images of the aorta from a rat that was a fed a normal diet with corresponding histology with standard H&E staining.

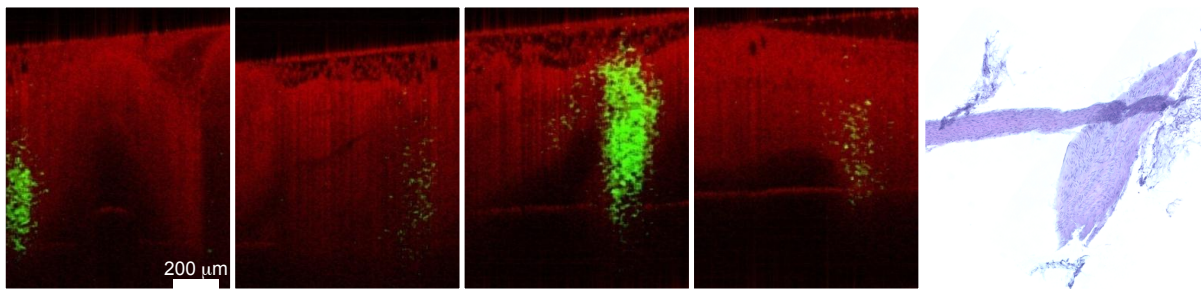


Figure 7.6: MM-OCT images of the aorta from a rat that was fed a high-fat and high-cholesterol diet with corresponding histology with standard H&E staining.

7.6 Conclusions

The overall goal of this thesis was to initially determine the utility of OCT for the intraoperative detection and assessment of cancer, particularly breast cancer. OCT was successfully demonstrated as a method for the intraoperative assessment of resected tumor margins [17, 18] and the visualization of axillary lymph nodes [19, 20]. An equally important goal of this thesis was to extend the utility of OCT for broader applications by coupling it with the development of a novel, targeted multi-modal contrast agent. With the RGD-coated magnetic and fluorescent microspheres, MM-OCT can be coupled with MRI and fluorescence imaging. By targeting the $\alpha_v\beta_3$ integrin receptor, MM-OCT can be used to image earlier stages of the tumor growth and development. I have developed the first multi-modal protein microsphere targeted for cancer cells and angiogenesis that can be imaged using MRI, MM-OCT, and fluorescence imaging.

7.7 References

1. Zysk AM, Nguyen FT, Chaney EJ, Kotynek JG, Oliphant UJ, Bellafiore FJ, Johnson PA, Rowland KM, Boppart SA. Clinical feasibility of microscopically-guided breast needle biopsy using a fiber-optic probe with computer-aided detection. *Technology in Cancer Research & Treatment*, 2009. 8 (5): p. 315-321.
2. Zysk AM, Adie SG, Armstrong JJ, Leigh MS, Paduch A, Sampson DD, Nguyen FT, Boppart SA. Needle-based refractive index measurement using low-coherence interferometry. *Opt Lett*, 2007. 32 (4): p. 385-387.
3. Zysk AM, Boppart SA. Computational methods for analysis of human breast tumor tissue in optical coherence tomography images. *J Biomed Opt*, 2006. 11 (5): p. 054015.
4. Zysk AM, Chaney EJ, Boppart SA. Refractive index of carcinogen-induced rat mammary tumours. *Phys Med Biol*, 2006. 51 (9): p. 2165-77.
5. Fani M, Psimadas D, Zikos C, Xanthopoulos S, Loudos GK, Bouziotis P, Varvarigou AD. Comparative evaluation of linear and cyclic 99mTc-rGD peptides for targeting of integrins in tumor angiogenesis. *Anticancer Res*, 2006. 26 (1A): p. 431-4.
6. Liu S. Radiolabeled cyclic rGD peptides as integrin $\alpha(v)\beta(3)$ -targeted radiotracers: Maximizing binding affinity via bivalency. *Bioconjug Chem*, 2009. 20 (12): p. 2199-213.
7. Zhou Y, Chakraborty S, Liu S. Radiolabeled cyclic rGD peptides as radiotracers for imaging tumors and thrombosis by spect. *Theranostics*, 2011. 1: p. 58-82.
8. Liu S. Radiolabeled multimeric cyclic rGD peptides as integrin $\alpha v \beta 3$ targeted radiotracers for tumor imaging. *Mol Pharm*, 2006. 3 (5): p. 472-87.

9. Kamphuis MM, Johnston AP, Such GK, Dam HH, Evans RA, Scott AM, Nice EC, Heath JK, Caruso F. Targeting of cancer cells using click-functionalized polymer capsules. *J Am Chem Soc*, 2010. 132 (45): p. 15881-3.
10. Cortez C, Tomaskovic-Crook E, Johnston AP, Scott AM, Nice EC, Heath JK, Caruso F. Influence of size, surface, cell line, and kinetic properties on the specific binding of a33 antigen-targeted multilayered particles and capsules to colorectal cancer cells. *ACS Nano*, 2007. 1 (2): p. 93-102.
11. Boturyn D, Coll JL, Garanger E, Favrot MC, Dumy P. Template assembled cyclopeptides as multimeric system for integrin targeting and endocytosis. *J Am Chem Soc*, 2004. 126 (18): p. 5730-9.
12. Odrliin TM, Haidaris CG, Lerner NB, Simpson-Haidaris PJ. Integrin alpha v beta 3-mediated endocytosis of immobilized fibrinogen by a549 lung alveolar epithelial cells. *Am J Respir Cell Mol Biol*, 2001. 24 (1): p. 12-21.
13. Castel S, Pagan R, Mitjans F, Piulats J, Goodman S, Jonczyk A, Huber F, Vilaro S, Reina M. Rgd peptides and monoclonal antibodies, antagonists of alpha(v)-integrin, enter the cells by independent endocytic pathways. *Lab Invest*, 2001. 81 (12): p. 1615-26.
14. Dibbern EM. *Core-shell microspheres for biomedical applications* [dissertation]. Urbana, IL: University of Illinois at Urbana-Champaign; 2007.
15. Kolbeck KJ. *The biomedical applications of protein microspheres* [dissertation]. Urbana, IL: University of Illinois at Urbana-Champaign; 1999.
16. Toublan FJ. *Methods to tailor protein microspheres for biomedical applications* [dissertation]. Urbana, IL: University of Illinois at Urbana-Champaign; 2005.

17. Nguyen FT, Zysk AM, Chaney EJ, Kotynek JG, Oliphant UJ, Bellafiore FJ, Rowland KM, Johnson PA, Boppart SA. Optical coherence tomography (oct) as a diagnostic tool for the real-time intraoperative assessment of breast cancer surgical margins. *Cancer Research*, 2009. 69 (2): p. 101S-101S.
18. Nguyen FT, Zysk AM, Kotynek JG, Bellafiore FJ, Rowland KM, Johnson PA, Chaney EJ, Boppart SA. Portable real-time optical coherence tomography system for intraoperative imaging and staging of breast cancer. in *SPIE - Photonics West BiOS - Advanced Biomedical and Clinical Diagnostic Systems V*. 2007. San Jose, CA.
19. Luo W, Nguyen FT, Zysk AM, Ralston TLS, Brockenbrough J, Marks DL, Oldenburg AL, Boppart SA. Optical biopsy of lymph node morphology using optical coherence tomography. *Technology in Cancer Research & Treatment*, 2005. 4 (5): p. 539-547.
20. Nguyen FT, Zysk AM, Chaney EJ, Adie SG, Kotynek JG, Oliphant UJ, Bellafiore FJ, Rowland KM, Johnson PA, Boppart SA. Optical coherence tomography: The intraoperative assessment of lymph nodes in breast cancer. *IEEE Eng Med Biol Mag*, 2010. 29 (2): p. 63-70.